From imaging to modulating the human locus coeruleus along healthy aging and the Alzheimer's disease continuum

Elise Beckers

From imaging to modulating the human locus coeruleus along healthy aging and the Alzheimer's disease continuum

Elise Beckers

The research described in this thesis was performed at the Department of Psychiatry and Neuropsychology, Mental Health and Neuroscience Research Institute, Maastricht University, Alzheimer Centrum Limburg, The Netherlands; and at the GIGA Institute - Cyclotron Research Center Human Imaging Unit, University of Liège, Belgium.
Printing of this thesis was kindly supported by Alzheimer Nederland.

Cover design	Nynke Dijkstra
Layout and printing	Ridderprint | ridderprint.nl
ISBN	978-94-6506-730-8

From imaging to modulating the human locus coeruleus along healthy aging and the Alzheimer's disease continuum

DISSERTATION

To obtain the degree of Doctor at Maastricht University,
on the authority of the Rector Magnificus, Prof. Dr. Pamela Habibović,
and the degree of Doctorate in Biomedical and Pharmaceutical Sciences
(*Doctorat en Sciences biomédicales et pharmaceutiques*) at the University of Liège,
on the authority of the Rector Magnificus, Prof. Dr. Anne-Sophie Nyssen,
in accordance with the decision of the Board of Deans,
to be defended in public
on Monday, 3rd of February 2025, at 16.00 hours

by

Elise Chantal Jeanne Beckers

Supervisors

Dr. Heidi IL Jacobs, Maastricht University
Dr. Gilles Vandewalle, University of Liège

Assessment Committee

Prof. Dr. Walter Backes (Chair), Maastricht University
Dr. Christine Bastin, University of Liège
Prof. Dr. Dorothea Hämmerer, University of Innsbruck, Austria
Prof. Dr. Sander Nieuwenhuis, Leiden University
Dr. Christophe Phillips, University of Liège
Prof. Dr. Alexander Sack, Maastricht University

TABLE OF CONTENTS

Chapter 1

General introduction, thesis aims and outline

GENERAL INTRODUCTION

Among the multiple challenges our society is facing today, one of the biggest is the global aging of the world population occurring at an unprecedented pace, and resulting in an important public health and economic burden. By 2050, the proportion of people aged 60 years and older is expected to double, and triple for people aged above 80 years [1]. At the same time, aging is reported as the primary risk factor for developing neurodegenerative diseases, including Alzheimer's disease (AD). With more than 55 million people worldwide diagnosed with dementia today and projected to triple by 2050, AD is the most prevalent form of an age-related neurodegenerative disease contributing to about two-third of all dementia cases [2, 3].

From the pathophysiological perspective, AD is characterized by the abnormal accumulation of amyloid beta (Aβ) plaques and the aggregation of hyperphosphorylated tau proteins, contributing to neurodegeneration and cognitive decline. Clinically, AD is described as a slow and progressive deterioration in brain functions, reflected in subtle changes in memory function, alterations in attentional and executive functions such as planning or reasoning, and changes in neurobehavioral functions, such as depression, anxiety, sleep disruption. Importantly, the neuropathologic hallmarks of AD start to accumulate up to two decades before the first cognitive symptoms are evident [4, 5]. These underlying pathological processes accumulate gradually and following specific spatial- and time-ordering patterns, as described by the Thal phases of Aβ deposition [6] and the Braak stages of tau pathology [7, 8] (Figure 1). For many years, the majority of the AD research field has focused on therapies targeting Aβ plaques in cognitively impaired individuals, with modest efficacy in delaying the progression of the disease [9]. Although recent clinical trials reported positive outcomes in terms of removal of Aβ plaques and delaying cognitive decline, these were associated with adverse events. Furthermore, these treatments are not (yet) available for individuals in the earliest asymptomatic stages of the disease, emphasizing the need for further examination of these anti-Aβ therapies but also to consider other treatment options [10, 11]. These moderate evidences for efficient clinical trials have ushered the AD field into an era of preventive intervention, shifting the focus

from the symptomatic toward the pre-symptomatic phase of the disease, where pathologic markers accumulate gradually while individuals remain asymptomatic [12]. Being able to prevent or slow down the progression of AD pathology through a better understanding and dissociation of age-related and pre-symptomatic neurodegenerative processes holds great promise for the development of effective therapeutics.

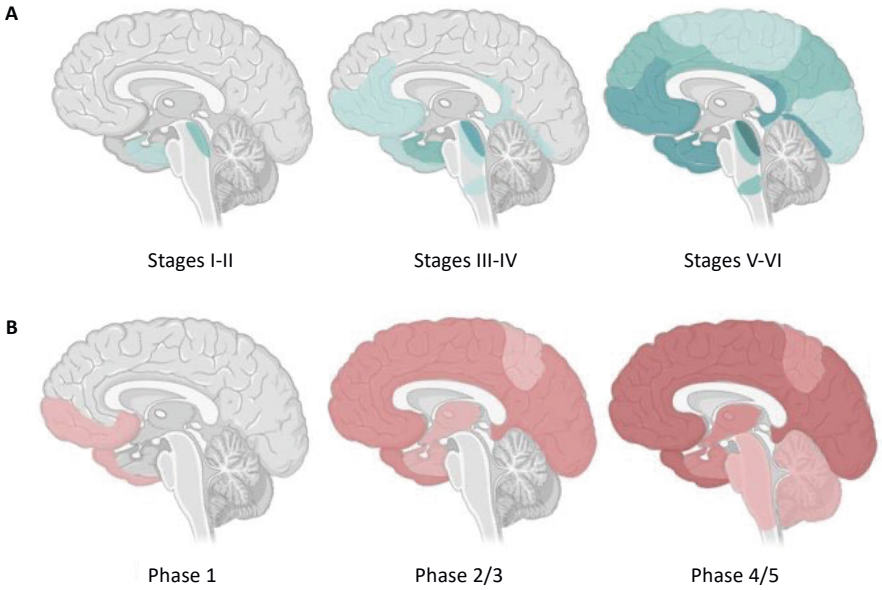

Figure 1. Schematic representation of the spatial and temporal progression of AD pathological biomarkers. **A)** Braak stages describing the progression of tau pathology in the brain, from abnormal tau observed in brainstem nuclei, mainly in the locus coeruleus (Braak stage 0, not shown on the figure), followed by the presence of pathological neurofibrillary tangles in the transentorhinal region (Stages I-II, or transentorhinal stages), to the medial temporal lobe (hippocampus) and limbic neocortical areas (Stages III-IV or limbic stages) and finally in widespread isocortical regions (Stages V-VI or isocortical stages). **B)** Thal phases describing the progression of amyloid pathology in the brain, from Aβ plaques appearing in the neocortex (Phase 1), to the allocortex, striatum and diencephalon (Phases 2/3), and finally to the midbrain, brainstem, including the locus coeruleus, and cerebellum (Phases 4/5). *Reprinted and adapted with permission from International Journal of Molecular Sciences, 22(4):2110, van Oostveen and de Lange (2021), "Imaging techniques in Alzheimer's disease: a review of applications in early diagnosis and longitudinal monitoring" under CC BY 4.0 license [13].*

Post-mortem studies have pointed toward the locus coeruleus (LC) as one of the first brain structures to accumulate hyperphosphorylated tau aggregates as early as the first decades of life, before spreading toward other brain regions [8, 14], and therefore may hold promise as a relevant marker of the earliest stages of AD. The LC was first described in the late 18th century by a French anatomist Félix Vicq-d'Azyr and later named *locus coeruleus*, or blue spot in Latin, after its dark pigmented appearance on post-mortem samples. It is a small, elongated, rod-like shaped bilateral brainstem nucleus located in the dorsal edge of the pons, at the floor of the 4th ventricle and composed of densely packed noradrenergic neurons (Figure 2). With an average size of 14.5 mm in length and 2.5 mm^2 in section [15], and around 22 to 50 thousands pigmented neurons [16, 17], the LC is the main source of norepinephrine (NE) in the brain and a key structure in the modulation of numerous physiological and cognitive functions such as memory, arousal and attention through its extensive projections to multiple brain regions [18, 19].

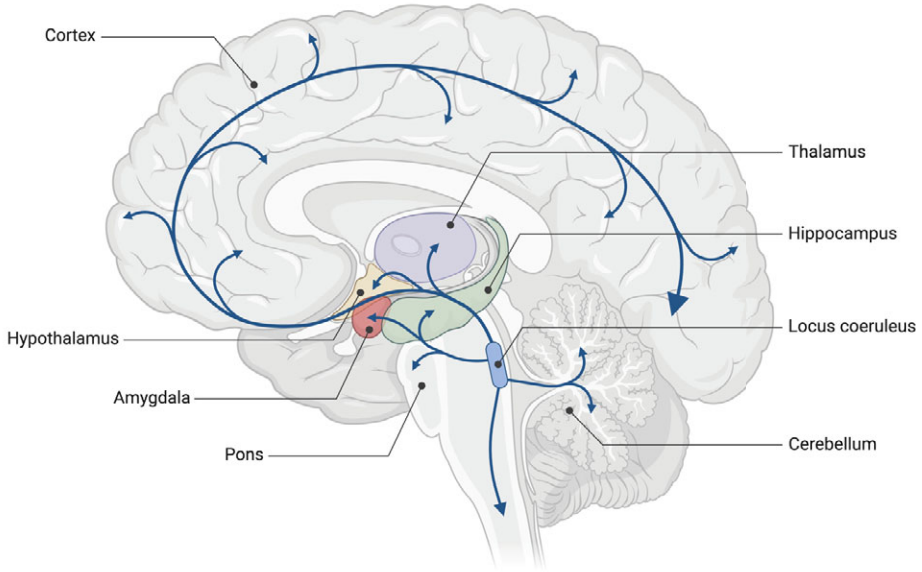

Figure 2. Visualization of the locus coeruleus and its main noradrenergic projections to subcortical and cortical brain regions. *Created with BioRender.com.*

In vivo and ex vivo quantifications of the locus coeruleus structure

Because of its deep location in the brain and small size, the in vivo visualization of the LC in humans has been and remains a major challenge in the field. The development of new imaging techniques, such as ultra-high field magnetic resonance imaging (MRI), has allowed for a highly detailed visualization of the brain and its smallest structures. The macro-, micro-structural and functional properties of the LC can now be better quantified in vivo and at high resolution through the combined use of LC-dedicated MRI sequences [20], functional MRI (fMRI) and advanced diffusion-weighted MRI models, such as neurite orientation dispersion and density imaging (NODDI) (Box 1).

Box 1.

fMRI (functional magnetic resonance imaging) is an in vivo technique providing an indirect measure of the regional and time-varying change in neuronal activity, most often in response to task stimuli or ongoing brain processes, through the detection of changes in blood-level oxygenation [21].

NODDI (neurite orientation dispersion and density imaging) is an advanced diffusion MRI technique that quantifies the microstructural properties of dendrites and axons in vivo via the characterization of their orientation dispersion and density [22].

A putative structural measure of the LC with increasing interest is its integrity, which can be derived in vivo from the hyperintense signal observed on LC-specific MRI sequences. Converging evidence emphasizes its close correlation with cognition, AD-related processes and tau pathology [23-30], suggesting that LC integrity could be a marker of early AD-related changes. However, the biological interpretation for the LC integrity metric remains a topic of debate. While at first, MRI-derived LC integrity measures were assumed to reflect neuromelanin cell density, animal and MRI studies have

now suggested that other neural components may also contribute to the MRI signal, including water, lipids, copper and possibly tau tangles [24, 31]. Accurately interpreting LC integrity findings as being reflective of degenerative or compensatory processes requires a better understanding of the underlying biological sources by comparing it to post-mortem studies. The neuroimaging literature reports inconsistencies in lateralization of LC integrity differences, with higher left LC integrity as compared to right in asymptomatic individuals [28, 30, 32], and ambiguous findings in the AD population [32, 33]. **Further insights into the pattern of AD pathology across the left and right LC will contribute to a better understanding of the disease progression, crucial for the development of future AD-related research focused on the LC.**

As we age and during the earliest stages of the disease, the LC undergoes important morphological and physiological changes that impact its function and, as a result, affect overall brain health and cognitive abilities, and increase the susceptibility to neurodegenerative diseases [8, 34]. In addition to the progressive accumulation of tau, other LC changes include partial dendritic atrophy, reduction of the density of the projections to the target brain regions [35] and increase in glial cell activation contributing to neuroinflammation, neuronal damage and ultimately reduction in NE release [36]. Together, these morphological and physiological changes are assumed to affect the macro- and micro-structural integrity of the cortical and subcortical target regions of the LC, contributing to cognitive and behavioral changes as well as neurodegenerative processes. **A careful characterization and early detection of these LC microstructural changes in vivo together with its downstream effects on the brain would facilitate the identification of age-related versus AD-related changes in the LC.**

Functional properties of the LC are usually investigated using fMRI, taking advantage of the measurement in change of blood-oxygen level-dependent (BOLD) signal, while often limited by its spatial resolution. Another method becoming increasingly popular is the use of pupillometry as an indirect measure of LC function, benefiting from advances in eye-tracking technology. Animals and human studies reported a strong correlation between changes in pupil

size and LC activity [37-39], although the underlying brain mechanisms remain unclear. While pupil size continuously fluctuates in response to light, referred to as the pupillary light response (PLR), it can also be modulated by cognitive processes and arousal states [40-43], the so-called task-evoked or transient pupil response, through a complementary activation of the parasympathetic constriction and the sympathetic dilation pathways. Importantly, the existence of a direct LC-pupil coupling is controversial as pupil regulation would not directly be governed by the LC but rather influenced by its interaction with a wide network of other brain structures along the parasympathetic and sympathetic pathways [44]. These important, although indirect, relationships emphasize the relevance of pupil dynamics (Box 2) as despite a slower temporal resolution, they can provide a proxy of phasic and tonic modes of LC-NE activity [45].

Box 2.

Pupil dynamics in response to external stimuli can be described by two distinct phases related to phasic and tonic changes in pupil. The **transient phase** (phasic) is occurring first and is reflected by a short and rapid variation in pupil size as a direct response to the stimuli. Then, the pupil response enters a **sustained phase** (tonic), about two seconds after the stimulus onset and until the sequence offset.

Modulating the locus coeruleus function: non-invasive and non-pharmacological interventions

Beside the efforts toward imaging and quantifying the LC structure and function in vivo to provide more insights on the underlying age-related and neurodegenerative processes, several studies have focused on targeting the LC-NE system as a potential therapeutic intervention that may promote cognition but also slow down or prevent cognitive decline through the modulation of noradrenergic pathways. While pharmacological or invasive

interventions are being developed [46, 47], these are often accompanied with undesired side-effects and high costs. In this thesis, we have focused on two distinct non-invasive and non-pharmacological stimulation techniques hypothesized to modulate the LC-NE system: the exposure to blue-enriched light and transcutaneous vagus nerve stimulation (tVNS) (Figure 3). In particular, we investigated their neural, physiological and behavioral correlates with the aim to provide a better understanding of their underlying mechanisms and further relevance to their potential use in clinical settings.

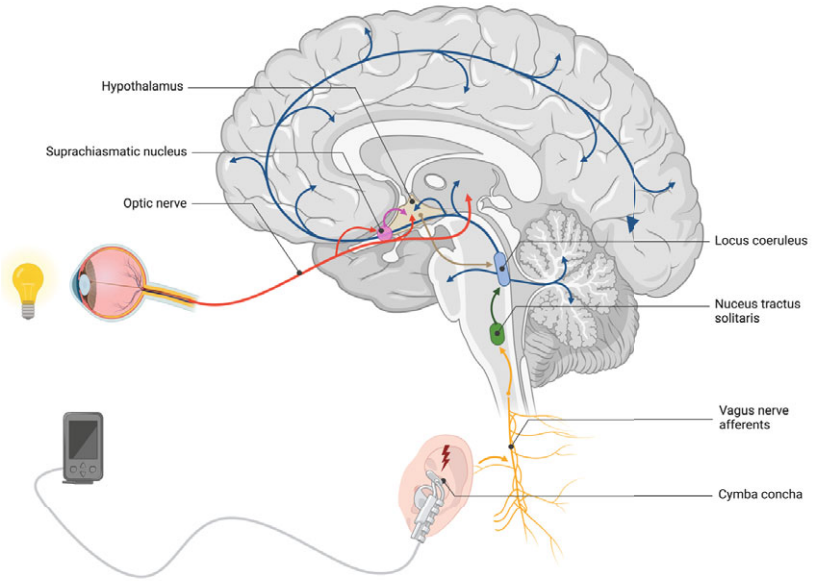

Figure 3. Simplified representation of the suggested brain pathways of light exposure and tVNS as non-invasive and non-pharmacological stimulation techniques in modulating the LC function. *Created with BioRender.com.*

In addition to allowing vision, exposure to light is known to induce non-image-forming (NIF) effects, including circadian entrainment [48], PLR [49] and the modulation of alertness and cognition [50, 51]. These responses are mainly mediated by intrinsically photosensitive retinal ganglions cells (ipRGCs), which form a third class of retinal photoreceptors because of their expression of the photopigment melanopsin [52]. IpRGCs combine their intrinsic responses to light to inputs from rods and cones, to modulate the activity of their brain projections with increased sensitivity in the blue portion of the visible light

spectrum (460-480 nm), given the maximal sensitivity of melanopsin at about 480 nm [53, 54]. The stimulating effects of blue-enriched light have been extensively reported in both younger and older adults, through increased alertness and impacts on emotion processing, executive performances and memory [50, 55-58], but also in AD patients through improvement of subjective sleep quality and cognition [59, 60]. The diverse nature in NIF responses arise from the broad projections of ipRGCs to several cortical but also subcortical regions, including the suprachiasmatic nucleus (SCN), site of the master circadian clock, and the olivary pretectal nucleus, highly involved in PLR [61]. For many years, the underlying neural mechanisms of the stimulating impact of light have been investigated, notably using fMRI. While the exact neural pathways involved remains unclear, human studies suggest that the LC partly mediates these NIF responses, potentially through its indirect input from the SCN (Figure 3) [62, 63]. **Whether blue-enriched light could have a stimulating effect on the LC, and in turn on its modulating role in cognitive processes is not established.**

As previously mentioned, imaging the LC function in vivo remains an important challenge in the field but is crucial for improving our understanding of NIF effects of light on cognition and the involvement of the LC. While most of the fMRI studies investigating the stimulating impact of light in humans used repeated short light exposures (with a block length of 1 min or less) alternating between different spectral composition [63-67], **it is unclear whether the effect of one light block carries over onto the following, hence potentially biasing the observed fMRI results**. In this context, the variation in sustained PLR under this light protocol is an easily accessible readout of the NIF impacts of light on the brain that could provide more insight on the reliability of the protocol used. Resolving this issue may not be anecdotical when focusing on small structures such as the LC which, inherently, can only induce relatively subtle changes in fMRI signal.

Transcutaneous vagus nerve stimulation (tVNS) is a neuromodulatory technique stimulating the auricular branch of the vagus nerve in the cymba conchae of the inner ear. It is non-invasive, non-pharmacological, available at

low-cost, and holds great promise at targeting the LC. Activation of the vagus nerve is thought to stimulate the LC-NE system, in turn modulating several brain functions, via its fibers connecting to the nucleus tractus solitaris and projecting to the brainstem LC (Figure 3) [68]. Accumulating evidence has shown that tVNS can modulate a variety of cognitive processes such as emotion recognition [69], episodic and working memory [70, 71] and cognitive control [72], through tVNS-induced activity in the LC and other cortical and subcortical regions, including the amygdala, thalamus and hippocampus [73-75]. However, the exact underlying neural pathways remain unclear and inconsistencies in the findings have been reported, preventing the generalizability of tVNS neuromodulatory effects on cognition [76, 77]. **Whether these mixed findings could be explained, in part, by inter-individual differences in structural integrity of the LC-NE system, hence modifying the impact of tVNS on LC-related brain pathways and resulting attentional cognitive performances, is not known.** Further insights on the potential link between tVNS-induced LC activity and attentional processes, and factors influencing this relationship, are important to shape future research on the development of non-invasive and non-pharmacological treatments in AD population.

THESIS AIMS AND OUTLINE

Recent evidence has emphasized the brainstem LC as a key structure in the brain, from its modulating role in cognitive and behavioral functions, to supporting brain health along the lifespan, but also for its specific vulnerability early on in neurodegenerative disorders including AD. The general aim of this thesis is to contribute to a better understanding of LC structural and functional properties in healthy aging and along the AD continuum, and to further test the effectiveness of non-invasive and non-pharmacological stimulation techniques in modulating LC function. These findings will contribute to the larger effort of developing LC-focused interventions to boost cognition in aging and for preventing or delaying AD progression. The associated research questions explored in this thesis are presented below.

Part I: In vivo and ex vivo quantifications of the locus coeruleus structure

Chapter 2 *- Are there microstructural associations between the LC, cortical and subcortical regions, and is astrocyte reactivity modulating these relationships?*
The LC-NE system plays a key role in supporting brain health along the lifespan, notably through its modulatory effects on neuroinflammation. In this chapter, we investigated the association between microstructural properties in the LC and in cortical or subcortical regions measured through 7T MRI in combination with NODDI diffusion models, in a healthy adult lifespan cohort. We further explored the modifying role of astrocyte reactivity on these microstructural relationships.

Chapter 3 *- Is the LC characterized by an asymmetrical pattern in AD pathology?*
Autopsy and imaging studies established that the LC is one of the first brain structures to accumulate hyperphosphorylated tau and to undergo morphological changes early in AD. However, it is not clear whether these modifications occur symmetrically across the LC length. In this study, we aimed to investigate whether tangle and neuronal LC density were characterized by an asymmetric pattern in autopsy cases across the AD continuum.

Part II: Modulating the locus coeruleus function: non-invasive and non-pharmacological interventions

Chapter 4 *- What is the impact of light on the LC in mediating cognitive processes, when assessed by task-evoked pupil responses?*
Imaging studies have suggested that the LC may be partly involved in mediating the NIF impacts of light on brain functions. However, the small size and deep location of the LC create important challenges for assessing in vivo its role in this process and more accessible proxy measures of LC activity may already provide important insights on the underlying mechanisms. Here, we used the variation in pupil size as an easily accessible and indirect proxy of LC activity to investigate whether task-evoked pupil responses during different cognitive contexts were impacted by NIF effects of light in healthy young adults.

Chapter 5 *- Are fMRI studies using short light exposures of different spectral composition biased by their light sequence protocol?*

The brain mechanisms underlying the stimulating effect of blue wavelength light, potentially mediated by subcortical regions such as the LC, have been investigated in humans using fMRI techniques with repeated short light exposures alternating between different spectral composition. So far, it was unclear whether the fMRI results could be biased by the light protocol such as the effect of light in one block carries over onto the following ones. With this study, we aimed to characterize the sustained pupil response to various short light exposures during an fMRI protocol and to further inform on the validity of the methodology employed in current and future research.

Chapter 6 *- Is there a relationship between LC structure, tVNS-induced LC activity and attention?*

tVNS is a non-invasive neuromodulatory technique that was associated with increased LC-NE activity through the afferent fibers of the vagus nerve to the nucleus tractus solitaris, which in turn projects to the LC. Furthermore, tVNS has been associated with improved cognitive performance, although these effects are not observed in every cohort. This chapter aimed at investigating the potential predictive role of LC integrity in determining who benefits from tVNS' effects on attentional performance in a cohort of healthy older individuals using 7T MRI.

Chapter 7 *- General discussion*

The thesis will close with a summary and a general discussion of the main findings, together with its methodological considerations, the implications for future research and the clinical perspective.

REFERENCES

1. World Health Organization. Aging and health 2022 [updated October 1. Available from: https://www.who.int/news-room/fact-sheets/detail/ageing-and-health.
2. World Health Organization. Dementia 2023 [updated March 15. Available from: https://www.who.int/news-room/fact-sheets/detail/dementia.
3. Alzheimer's Association. 2024 Alzheimer's Disease Facts and Figures. Alzheimer's & Dementia. 2024;20(5):3708-821.
4. Jansen WJ, et al. Prevalence Estimates of Amyloid Abnormality Across the Alzheimer Disease Clinical Spectrum. JAMA Neurol. 2022;79(3):228-43.
5. Jack CR, Jr., et al. NIA-AA Research Framework: Toward a biological definition of Alzheimer's disease. Alzheimers Dement. 2018;14(4):535-62.
6. Thal DR, et al. Phases of A beta-deposition in the human brain and its relevance for the development of AD. Neurology. 2002;58(12):1791-800.
7. Braak H and Braak E. Neuropathological stageing of Alzheimer-related changes. Acta Neuropathol. 1991;82(4):239-59.
8. Braak H, et al. Stages of the pathologic process in Alzheimer disease: age categories from 1 to 100 years. *J Neuropathol Exp Neurol*. 2011;70(11):960-9.
9. Zhang Y, et al. Amyloid β-based therapy for Alzheimer's disease: challenges, successes and future. *Signal Transduct Target Ther*. 2023;8(1):248.
10. van Dyck CH, et al. Lecanemab in Early Alzheimer's Disease. *N Engl J Med*. 2023;388(1):9-21.
11. Yadollahikhales G and Rojas JC. Anti-Amyloid Immunotherapies for Alzheimer's Disease: A 2023 Clinical Update. *Neurotherapeutics*. 2023;20(4):914-31.
12. Sperling R, Mormino E, and Johnson K. The evolution of preclinical Alzheimer's disease: implications for prevention trials. *Neuron*. 2014;84(3):608-22.
13. van Oostveen WM and de Lange ECM. Imaging Techniques in Alzheimer's Disease: A Review of Applications in Early Diagnosis and Longitudinal Monitoring. *Int J Mol Sci*. 2021;22(4).
14. Braak H and Del Tredici K. The preclinical phase of the pathological process underlying sporadic Alzheimer's disease. *Brain*. 2015;138(Pt 10):2814-33.
15. Fernandes P, et al. The human locus coeruleus 3-D stereotactic anatomy. *Surg Radiol Anat*. 2012;34(10):879-85.
16. Beardmore R, et al. The Locus Coeruleus in Aging and Alzheimer's Disease: A Postmortem and Brain Imaging Review. *J Alzheimers Dis*. 2021;83(1):5-22.
17. German DC, et al. The human locus coeruleus: computer reconstruction of cellular distribution. *J Neurosci*. 1988;8(5):1776-88.
18. Poe GR, et al. Locus coeruleus: a new look at the blue spot. *Nat Rev Neurosci*. 2020;21(11):644-59.
19. Sara SJ. The locus coeruleus and noradrenergic modulation of cognition. *Nat Rev Neurosci*. 2009;10(3):211-23.

20. Priovoulos N, et al. High-resolution in vivo imaging of human locus coeruleus by magnetization transfer MRI at 3T and 7T. *Neuroimage*. 2018;168:427-36.

21. Ogawa S, et al. Brain magnetic resonance imaging with contrast dependent on blood oxygenation. *Proc Natl Acad Sci U S A*. 1990;87(24):9868-72.

22. Zhang H, et al. NODDI: practical in vivo neurite orientation dispersion and density imaging of the human brain. *Neuroimage*. 2012;61(4):1000-16.

23. Bueichekú E, et al. Spatiotemporal patterns of locus coeruleus integrity predict cortical tau and cognition. *Nat Aging*. 2024.

24. Jacobs HIL, et al. In vivo and neuropathology data support locus coeruleus integrity as indicator of Alzheimer's disease pathology and cognitive decline. *Sci Transl Med*. 2021;13(612):eabj2511.

25. Jacobs HIL, et al. Waning locus coeruleus integrity precedes cortical tau accrual in preclinical autosomal dominant Alzheimer's disease. *Alzheimers Dement*. 2023;19(1):169-80.

26. Van Egroo M, et al. Ultra-high field imaging, plasma markers and autopsy data uncover a specific rostral locus coeruleus vulnerability to hyperphosphorylated tau. *Mol Psychiatry*. 2023:1-11.

27. Bachman SL, et al. Locus coeruleus MRI contrast is associated with cortical thickness in older adults. *Neurobiol Aging*. 2021;100:72-82.

28. Dahl MJ, et al. Rostral locus coeruleus integrity is associated with better memory performance in older adults. *Nat Hum Behav*. 2019;3(11):1203-14.

29. Dahl MJ, et al. Locus coeruleus integrity is related to tau burden and memory loss in autosomal-dominant Alzheimer's disease. *Neurobiol Aging*. 2022;112:39-54.

30. Elman JA, et al. Associations between MRI-assessed locus coeruleus integrity and cortical gray matter microstructure. *Cereb Cortex*. 2022;32(19):4191-203.

31. Priovoulos N, et al. Unraveling the contributions to the neuromelanin-MRI contrast. *Brain Struct Funct*. 2020;225(9):2757-74.

32. Betts MJ, et al. In vivo MRI assessment of the human locus coeruleus along its rostrocaudal extent in young and older adults. *Neuroimage*. 2017;163:150-9.

33. Cassidy CM, et al. Association of locus coeruleus integrity with Braak stage and neuropsychiatric symptom severity in Alzheimer's disease. *Neuropsychopharmacology*. 2022;47(5):1128-36.

34. Wilson RS, et al. Neural reserve, neuronal density in the locus ceruleus, and cognitive decline. *Neurology*. 2013;80(13):1202-8.

35. Chan-Palay V and Asan E. Alterations in catecholamine neurons of the locus coeruleus in senile dementia of the Alzheimer type and in Parkinson's disease with and without dementia and depression. *J Comp Neurol*. 1989;287(3):373-92.

36. Heneka MT, et al. Locus ceruleus degeneration promotes Alzheimer pathogenesis in amyloid precursor protein 23 transgenic mice. *J Neurosci*. 2006;26(5):1343-54.

37. Joshi S, et al. Relationships between Pupil Diameter and Neuronal Activity in the Locus Coeruleus, Colliculi, and Cingulate Cortex. *Neuron*. 2016;89(1):221-34.

38. Murphy PR, et al. Pupil diameter covaries with BOLD activity in human locus coeruleus. *Hum Brain Mapp*. 2014;35(8):4140-54.

39. de Gee JW, et al. Dynamic modulation of decision biases by brainstem arousal systems. *Elife*. 2017;6.

40. Nassar MR, et al. Rational regulation of learning dynamics by pupil-linked arousal systems. *Nat Neurosci*. 2012;15(7):1040-6.

41. Jepma M and Nieuwenhuis S. Pupil diameter predicts changes in the exploration-exploitation trade-off: evidence for the adaptive gain theory. *J Cogn Neurosci*. 2011;23(7):1587-96.

42. Granholm E and Steinhauer SR. Pupillometric measures of cognitive and emotional processes. *Int J Psychophysiol*. 2004;52(1):1-6.

43. Kahneman D and Beatty J. Pupil diameter and load on memory. *Science*. 1966;154(3756):1583-5.

44. Megemont M, McBurney-Lin J, and Yang H. Pupil diameter is not an accurate real-time readout of locus coeruleus activity. *eLife*. 2022;11:e70510.

45. Mathôt S. Pupillometry: Psychology, Physiology, and Function. *J Cogn*. 2018;1(1):16.

46. Gutiérrez IL, et al. Noradrenaline in Alzheimer's Disease: A New Potential Therapeutic Target. *Int J Mol Sci*. 2022;23(11).

47. David M and Malhotra PA. New approaches for the quantification and targeting of noradrenergic dysfunction in Alzheimer's disease. *Ann Clin Transl Neurol*. 2022;9(4):582-96.

48. Hughes S, et al. Photic regulation of clock systems. *Methods Enzymol*. 2015;552:125-43.

49. Gamlin PD, et al. Human and macaque pupil responses driven by melanopsin-containing retinal ganglion cells. *Vision Res*. 2007;47(7):946-54.

50. Vandewalle G, Maquet P, and Dijk DJ. Light as a modulator of cognitive brain function. *Trends Cogn Sci*. 2009;13(10):429-38.

51. Cajochen C, et al. High sensitivity of human melatonin, alertness, thermoregulation, and heart rate to short wavelength light. *J Clin Endocrinol Metab*. 2005;90(3):1311-6.

52. Berson DM, Dunn FA, and Takao M. Phototransduction by retinal ganglion cells that set the circadian clock. *Science*. 2002;295(5557):1070-3.

53. Güler AD, et al. Melanopsin cells are the principal conduits for rod-cone input to non-image-forming vision. *Nature*. 2008;453(7191):102-5.

54. Brainard GC, et al. Action spectrum for melatonin regulation in humans: evidence for a novel circadian photoreceptor. *J Neurosci*. 2001;21(16):6405-12.

55. Cajochen C, et al. Dose-response relationship for light intensity and ocular and electroencephalographic correlates of human alertness. *Behav Brain Res*. 2000;115(1):75-83.

56. Grant LK, et al. Daytime Exposure to Short Wavelength-Enriched Light Improves Cognitive Performance in Sleep-Restricted College-Aged Adults. *Front Neurol*. 2021;12:624217.

57. Alkozei A, et al. Exposure to Blue Wavelength Light Is Associated With Increases in Bidirectional Amygdala-DLPFC Connectivity at Rest. *Front Neurol*. 2021;12:625443.

58. Alkozei A, et al. Exposure to Blue Light Increases Subsequent Functional Activation of the Prefrontal Cortex During Performance of a Working Memory Task. *Sleep*. 2016;39(9):1671-80.

59. Cremascoli R, et al. Effects of Circadian Phase Tailored Light Therapy on Sleep, Mood, and Cognition in Alzheimer's Disease: Preliminary Findings in a Pivotal Study. *Front Physiol*. 2021;12:755322.

60. Kim SJ, et al. Positive effect of timed blue-enriched white light on sleep and cognition in patients with mild and moderate Alzheimer's disease. *Sci Rep*. 2021;11(1):10174.

61. Hattar S, et al. Central projections of melanopsin-expressing retinal ganglion cells in the mouse. *J Comp Neurol*. 2006;497(3):326-49.

62. Aston-Jones G, et al. A neural circuit for circadian regulation of arousal. *Nat Neurosci*. 2001;4(7):732-8.

63. Vandewalle G, et al. Brain responses to violet, blue, and green monochromatic light exposures in humans: prominent role of blue light and the brainstem. *PLoS One*. 2007;2(11):e1247.

64. Daneault V, et al. Aging reduces the stimulating effect of blue light on cognitive brain functions. *Sleep*. 2014;37(1):85-96.

65. McGlashan EM, et al. Afraid of the dark: Light acutely suppresses activity in the human amygdala. *PLoS One*. 2021;16(6):e0252350.

66. Vandewalle G, et al. Effects of light on cognitive brain responses depend on circadian phase and sleep homeostasis. *J Biol Rhythms*. 2011;26(3):249-59.

67. Vandewalle G, et al. Spectral quality of light modulates emotional brain responses in humans. *Proc Natl Acad Sci U S A*. 2010;107(45):19549-54.

68. Ruffoli R, et al. The chemical neuroanatomy of vagus nerve stimulation. *J Chem Neuroanat*. 2011;42(4):288-96.

69. Colzato LS, Sellaro R, and Beste C. Darwin revisited: The vagus nerve is a causal element in controlling recognition of other's emotions. *Cortex*. 2017;92:95-102.

70. Jacobs HI, et al. Transcutaneous vagus nerve stimulation boosts associative memory in older individuals. *Neurobiol Aging*. 2015;36(5):1860-7.

71. Zhao R, et al. Transcutaneous auricular vagus stimulation (taVNS) improves human working memory performance under sleep deprivation stress. *Behav Brain Res*. 2023;439:114247.

72. Fischer R, et al. Transcutaneous vagus nerve stimulation (tVNS) enhances conflict-triggered adjustment of cognitive control. *Cogn Affect Behav Neurosci*. 2018;18(4):680-93.

73. Yakunina N, Kim SS, and Nam EC. Optimization of Transcutaneous Vagus Nerve Stimulation Using Functional MRI. *Neuromodulation*. 2017;20(3):290-300.

74. Dietrich S, et al. A novel transcutaneous vagus nerve stimulation leads to brainstem and cerebral activations measured by functional MRI. *Biomed Tech (Berl)*. 2008;53(3):104-11.

75. Kraus T, et al. CNS BOLD fMRI effects of sham-controlled transcutaneous electrical nerve stimulation in the left outer auditory canal - a pilot study. *Brain Stimul*. 2013;6(5):798-804.

76. Mertens A, et al. Transcutaneous Vagus Nerve Stimulation Does Not Affect Verbal Memory Performance in Healthy Volunteers. *Front Psychol*. 2020;11:551.

77. Verkuil B and Burger AM. Transcutaneous vagus nerve stimulation does not affect attention to fearful faces in high worriers. *Behav Res Ther*. 2019;113:25-31.

Part I

In vivo and ex vivo quantifications of the locus coeruleus structure

Chapter 2

Microstructural associations between locus coeruleus, cortical and subcortical regions are modulated by astrocyte reactivity: a 7T MRI adult lifespan study

Elise Beckers
Maxime Van Egroo
Nicholas J Ashton
Kaj Blennow
Gilles Vandewalle
Henrik Zetterberg
Benedikt A Poser
Heidi IL Jacobs

Published in Cerebral Cortex, 2024

ABSTRACT

The locus coeruleus-norepinephrine (LC-NE) system plays a key role in supporting brain health along the lifespan, notably through its modulatory effects on neuroinflammation. Using ultra-high field diffusion MRI, we examined whether microstructural properties (neurite density index (NDI) and orientation dispersion index (ODI)) in the LC were related to those in cortical and subcortical regions, and whether this was modulated by plasma glial fibrillary acidic protein (GFAP) levels, as a proxy of astrocyte reactivity. In our cohort of 60 healthy individuals (30–85 years, 50% female), higher GFAP correlated with lower NDI in frontal cortical regions, the hippocampus and the amygdala. Furthermore, under higher levels of GFAP (above ~150 pg/mL for cortical and ~145 pg/mL for subcortical regions), lower LC ODI was associated with lower ODI in fronto-temporal cortical regions and in subcortical regions. Interestingly, individuals with higher LC ODI exhibited higher ODI in these (sub) cortical regions, despite having higher GFAP levels. Together, these results suggest that the interaction between LC-NE cells and astrocytes can signal a detrimental or neuroprotective pathway for brain integrity and support the importance of maintaining LC neuronal health in aging and in the prevention of age-related neurodegenerative diseases.

INTRODUCTION

The locus coeruleus (LC) is a small, elongated nucleus in the pons that provides norepinephrine (NE) to the entire brain through its widespread projections, and thus has important functions in normal physiology, including the regulation of arousal and the sleep-wake cycle, and the modulation of cognition and behavior [1-3]. Despite its small size, several neuroimaging and autopsy studies have highlighted its critical role in supporting brain health through the lifespan, as reflected by brain micro- and macro-structure [4-6], but also its vulnerability to Alzheimer's disease (AD)-related pathologic changes starting early in adulthood [7-10]. Thus, identifying processes that contribute to the impact of LC neurons on the neuroaxis will be critical in our attempt to promote brain health.

An important pathway contributing to brain health in aging is the involvement of the LC-NE system in the regulation of neuroinflammatory processes. Animal studies showed that endogenous NE exerts anti-inflammatory and neuroprotective effects onto the brain by downregulating the microglial functions and the transcription of pro-inflammatory genes in astrocytes [11-13]. By contrast, destroying LC neurons with the selective noradrenergic neurotoxin N-(2-chloroethyl)-N-ethyl-2-bromobenzylamine (DSP-4) resulted in NE depletion, exacerbated neuroinflammatory responses and astrocyte reactivity [14]. When dysregulated, these reactive astrocytes are characterized by the overexpression of the intermediate filament glial fibrillary acidic protein (GFAP) and if sustained, can have detrimental effects on overall brain health. Both animal studies as well as human neuropathology studies reported that GFAP levels increase with aging [15], may contribute to reduced clearance of beta-amyloid [13], and are associated with the presence of both neurofibrillary tangles and beta-amyloid plaques [16]. It is important to note that the DSP-4 neurotoxin used in animal studies destroys a high proportion of LC neurons (up to 80%), while in humans, loss of LC neurons is a less extensive, gradual, and delayed process. Autopsy studies demonstrated that LC neurons remain sturdy, even when early hyperphosphorylated tau accumulates [17, 18]. However, while neuronal death seems to occur later in the disease progression, LC cells do undergo morphological changes during aging and the earliest disease stages, including partial dendritic atrophy, sometimes combined with

swollen dendritic trees, and a reduction in the density of their projections to the cortex [19]. These morphological changes are also detected in the precortical Braak stages of AD, with cell bodies and neurites staining positive for tau pathology starting at the precortical Braak stages of tau pathology [20].

Thus, while animal studies suggest that loss of LC neurons contributes to greater AD-related pathology via increased astrocyte reactivity, autopsy data indicates that these events may already be occurring during normal aging with more subtle changes to cytoskeletal components of LC neurons. Detecting these early changes could facilitate the early detection of processes associated with declining brain health in aging and could open up opportunities to develop preventive interventions targeting the LC-NE system in age-related diseases, starting before the emergence of cognitive decline. Measuring the LC in vivo has been challenging due to its small size and hidden location deep in the brain. But with the development of specific magnetic resonance imaging (MRI) sequences sensitive to LC contrast, recent work revealed that compared to younger individuals, older individuals retaining higher LC integrity presented a larger cortical thickness in parietal, frontal and occipital regions [5]. Such macrostructural associations were not observed within an older male population of a narrow age range, but better microstructural cortical gray matter properties in the salience network and fronto-parietal regions were associated with higher LC integrity [6]. These findings suggest that microstructural brain properties, as measured with diffusion-weighted imaging (DWI), provide more sensitivity to detect early LC-related brain structural changes in healthy individuals. So far, only a handful of studies examined diffusion in the LC and reported unexpected lower diffusivity and higher fractional anisotropy (FA) in the LC in older individuals relative to younger ones [21, 22]. These unexpected findings in LC diffusion metrics may result from partial volume effects due to the large voxel size or a slightly biased delineation of the LC due to the use of non-study specific templates in standard space that do not take into account individual anatomic variability [23].

Ultra-high field (UHF) MRI has ushered in an era of more detailed visualization of the brain, allowing to image the LC in great detail at the individual level [24]. The implementation of the aforementioned LC-specific sequences at UHF MRI in combination with advanced biophysical diffusion

models such as neurite orientation dispersion and density imaging (NODDI) allows for detailed assessment of complex microstructural properties within the LC. Compared to standard diffusion models, NODDI provides a more sensitive detection of subtle age-related microstructural changes in neurite density and organization, that are preceding macrostructural changes [25, 26]. Taking advantage of these new UHF MRI developments, we set out to relate microstructural NODDI properties of the LC to those extracted in cortical gray matter and subcortical brain regions in 60 individuals across the adult lifespan. We further investigated the moderating effect of reactive astrocytes, indexed by plasma GFAP levels, on these relationships. Finally, because the LC can shape cognitive functions through its interactions with the cortex and subcortex, we also explored potential associations with cognition. Guided by the literature, we hypothesized that lower LC microstructural properties will be associated with both lower cortical and lower subcortical microstructural properties, and that this effect will be more pronounced under elevated plasma GFAP levels.

METHODS

Participants

Our study population is composed of a subgroup of cognitively unimpaired individuals across the adult lifespan (N = 62, age range = 30–85 years; 30 women [50%]) from the 7T adult lifespan study [8, 27]. Individuals were included into the current study if they had availability of the diffusion scan. Participants were right-handed and recruited from the Dutch population through advertisements in the South of the Netherlands. Exclusion criteria included contraindications for UHF MRI scanning, history of major psychiatric or neurological disorders, history of cardiac disorders, use of drugs or psychoactive medication, and excessive alcohol consumption (>15 units/week). All participants provided written informed consent, and the experimental protocol was approved by the local Medical Ethics Committee of the Maastricht University Medical Center.

MRI data acquisition

The imaging protocol was performed on a 7T MAGNETOM whole-body MR system (Siemens Healthineers, Erlangen, Germany) with a 32-channel (1TX/32RX) head coil (Nova Medical, Wilmington, MA, USA). A whole-brain structural T1-weighted image was acquired using a Magnetization Prepared 2 Rapid Gradient Echoes (MP2RAGE) sequence [28] (TR = 5000 ms, TE = 2.47 ms, flip angle = 5°/3°, voxel size = 0.7 mm isotropic, number of slices = 240). The LC was imaged at high resolution with an in-house developed magnetization transfer-weighted turbo flash (MT-TFL) sequence [24], consisting of a multi-shot 3D readout (TR = 538 ms, TE = 4.08, flip angle = 8°, voxel size = 0.4 × 0.4 × 0.5 mm^3, number of slices = 60) with center-out k-space sampling, preceded by 20 long off-resonant Gaussian sinc pulses (pulse length = 5.12 ms, bandwidth = 250 Hz, B_1 = 0.25 μT). The field of view of the MT-TFL sequence was placed perpendicular to the dorsal surface of the pons and covered an area between the inferior colliculi and the caudal border of the pons. Diffusion data were acquired using a multi-shell DWI sequence (66 directions, b = 2000 s/mm^2; 35 directions, b = 700 s/mm^2; 6 directions, b = 20 s/mm^2; b = 0 in opposite phase-encoding direction; TR = 5000 ms, TE = 60.8 ms, voxel size = 1.25 mm isotropic, number of slices = 72). Because of our focus on the brainstem, the field of view of the DWI acquisitions excluded the most dorsal portion of the fronto-parietal lobe (Supplementary Figure 1).

Structural MRI processing

Whole-brain structural MR images were processed in FreeSurfer version 6.0 [29] using the default cortical and subcortical reconstruction protocol as previously described [30] with the appropriate configuration for 7T data, i.e. including the *"-highres"* flag and the expert options file. In brief, this processing pipeline entails intensity normalization, bias field correction and skull stripping of each individual T1-weighted image. White and pial surfaces were delineated and the resulting cortical area was parcellated in 34 distinct regions per hemisphere, according to the Desikan-Killiany atlas [31]. Six subcortical structures labeled according to the *Aseg* atlas were included in the analysis: amygdala, caudate, hippocampus, pallidum, putamen, and thalamus. Note that we follow the labelling of FreeSurfer even though hippocampus is cytoarchitectonically

allocortex. All processed images were visually inspected for over- or under-estimation of the gray/white matter boundaries and, if necessary, manually corrected. Finally, the parcellated cortical and subcortical regions were registered to the MP2RAGE space using the function *Estimate and Reslice* with the *nearest neighbour* interpolation option in SPM12 software (https://www.fil.ion.ucl.ac.uk/spm/software/spm12/), under MATLAB R2023a (version 9.14.0, MathWorks, Natick, MA).

The MT-TFL images were preprocessed following our in-house developed 7T LC pipeline, as described previously [27]. All LC scans were intensity-normalized using the subject-specific mean intensity of a 10 × 10 voxels reference region located in the pontine tegmentum. A study-specific template was created using an iterative diffeomorphic warp estimate in ANTs. The LC mask was then manually delineated on the template by an expert (MVE), based on voxel intensities and prior knowledge on LC anatomy. Subject-specific median LC MRI signal intensity values across each slice were extracted per hemisphere by applying the LC mask onto each individual intensity-normalized MT-TFL images registered to the study-specific template. An illustration of the delineated LC mask in the standard MNI space (0.5 mm resolution) together with its overlap on the published meta-mask [32] is presented in Supplementary Figure 2.

Diffusion MRI processing

Diffusion-weighted images were preprocessed to correct for B_0 susceptibility-induced and eddy current-induced distortions, as well as participant's motion, using *topup* and *eddy* tools of the FSL software version 5.0.9 [33]. Whole-brain NODDI parameter maps of neurite density index (NDI) and orientation dispersion index (ODI), were then computed using the Microstructure Diffusion Toolbox (v1.2.6, https://github.com/robbert-harms/MDT). NDI values range from 0 to 1, with 0 reflecting low neurite density (i.e., mostly extracellular diffusion) and 1 reflecting high neurite density (i.e., mostly intracellular diffusion). ODI values range from 0 to 1, with 0 reflecting low arborization (i.e., parallel neurites) and 1 reflecting high arborization (i.e., highly dispersed neurites) [34]. Axial and coronal views of NODDI maps with and without the

LC mask overlaid are presented in Supplementary Figure 3 for illustrative purposes.

Cortical, subcortical and LC NODDI parameters extraction

Individual structural MP2RAGE images were registered to the individual mean diffusion-weighted b0 volume using SPM12 *Estimate and Reslice* function with the *nearest neighbour* interpolation option. The resulting transformation matrices were subsequently applied to the individual LC masks and the parcellated cortical and subcortical regions, previously resliced to the MP2RAGE space. For each individual, registrations of the LC mask and the parcellated cortical and subcortical regions to the diffusion space were visually inspected, and data was excluded in case of poor registration quality (N = 2). To prevent a calculation bias due to the partial diffusion field of view, cortical regions for which at least 90% of their voxels in at least 80% of the participants were not mapped into the diffusion space were excluded from the analyses. As a result, eleven cortical regions were excluded: caudal middle frontal, cuneus, inferior parietal, paracentral, postcentral, posterior cingulate, precentral, precuneus, superior frontal, superior parietal and supramarginal.

Microstructure NODDI estimates (i.e., NDI and ODI) were computed by taking the median of values from each region of interest, i.e. the LC and the parcellated cortical and subcortical regions. As we had no a priori hypothesis on asymmetry, median diffusion metric estimates were averaged across left and right hemispheres.

Plasma measurements

Fasted EDTA plasma samples were obtained in the morning through venipuncture from the antecubital vein and processed according to the SOP stipulated by the central biobank of Maastricht University Medical Center. Samples were centrifuged at 2000 × g, aliquoted in polypropylene tubes, and stored at -80 °C in our biobank within 60 min of collection. Plasma GFAP levels were analyzed in randomized order using a commercially available ultra-sensitive Single molecule array (Simoa) assay kit on an HD-X instrument (Quanterix, Inc) at the University of Gothenburg, Sweden. Intra- and inter-assay coefficients of variation for GFAP in this study were 5.6% and 7.8%, respectively.

Apolipoprotein (*APOE*) genotyping was performed using polymerase chain reaction on DNA extracted from whole blood samples. Participants' *APOE* status was defined as "ε4 carrier" if they carried at least one ε4 allele. Technicians handling the blood samples were blinded to the participant cognitive and imaging data, and staff collecting cognitive or imaging data were blinded to blood results.

Neuropsychological assessment

Participants underwent a comprehensive neuropsychological test battery including the Mini-Mental State Examination (MMSE), the logical memory delayed recall test, the digit symbol substitution test, the Rey-auditory verbal learning test (total and delayed free recall) and the category fluency test. From these 5 available cognitive tests, we derived the preclinical Alzheimer's cognitive composite (PACC), sensitive to cognitive change among individuals with preclinical AD, by averaging the z-scores of the tests' performance [35].

Statistical analyses

All analyses were performed using R statistical software (version 4.1.2, http://www.r-project.org/). Group characteristics are represented in mean and standard deviation for continuous variables and proportions for dichotomous variables. Zero-order correlations across all relevant variables were examined with Pearson's correlations for continuous variables and point-biserial correlations for dichotomous variables. All the following regression models were bootstrapped (5,000 iterations) to approximate a normal distribution for our statistical testing.

First, we examined associations between our key variables for demographics (age, sex, or *APOE* status) and plasma GFAP, LC intensity, and NODDI parameters in the LC, in the averaged 23 cortical regions and in the averaged 6 subcortical regions using bootstrapped linear regression.

Following our main hypotheses, we then examined the relationship between NODDI metrics in the LC to NODDI metrics in each of the 23 included cortical regions or in each of the 6 subcortical regions using bootstrapped linear regression analyses. In a second step, we related GFAP plasma concentrations to NODDI metrics in each cortical or subcortical region.

We then combined these models, by examining the interactive effect between LC NODDI parameters and GFAP plasma concentrations on NODDI metrics in each individual cortical or subcortical region. Models were corrected for age and sex and statistical results were adjusted for multiple comparison per model (across cortical or subcortical regions) using a false discovery rate (FDR) approach with a statistical significance threshold set to $\alpha < 0.05$. Using the FDR corrected Johnson-Neyman approach, we determined the range of values where the plasma GFAP marker modified the relationship between LC NODDI metrics and cortical or subcortical region-specific NODDI metrics. To reduce the number of comparisons and the risk for Type I errors in the Johnson-Neyman analyses, we averaged all regions where we found significant associations in the model interacting LC NODDI parameters by GFAP plasma concentrations on (sub)cortical NODDI parameters. Regions of interest (ROIs) were displayed using the *ggseg* package [36]. In order to test for potential shared method-related variance effects in models involving LC NODDI parameters, we performed specificity analyses replicating the previous models yielding significant associations but replacing LC NODDI metrics by LC intensity, as this represents a distinct imaging method, but is still closely related to our original aim. Sensitivity analyses were performed by repeating our initial models in individuals of age 50 or older, and by adding *APOE* status, or LC intensity (used as a proxy of LC structural integrity) as covariate to the interaction model to control for AD-related genetic risk and for LC MRI-integrity.

Finally, to examine the associations with cognition, we used bootstrapped linear regression to examine the main and interactive associations of GFAP and our imaging NODDI metrics (in the LC, the cortex and the subcortex) with PACC-score, while correcting for age, sex, and education.

RESULTS

Sample characteristics

Our study cohort consisted of 60 participants with a mean age of 59 years (range 30–85 years), 30 (50%) were female and 17 (28%) carried at least one

APOE ε4 allele. All participants were cognitively healthy (mean MMSE score: 28.95) and had a mean plasma GFAP level of 152 pg/mL (Table 1).

Table 1. Demographics

N = 60	
Age (years)	58.90 (14.70), range: 30-85
Female (No. (%))	30 (50%)
Education (years)	14.58 (2.24)
MMSE (score)	28.95 (1.14)
PACC (z-score)	0.09 (0.70)
Plasma GFAP (pg/mL)	152 (65)
APOE ε4 carrier (No. (%))	17 (28.33%)
LC intensity (a.u.)	0.12 (0.04)
NDI LC	0.54 (0.05)
ODI LC	0.10 (0.03)
NDI cortex[#]	0.53 (0.02)
ODI cortex[#]	0.39 (0.04)
NDI subcortex[#]	0.59 (0.04)
ODI subcortex[#]	0.35 (0.05)

Participants' characteristics are presented as mean and standard deviation, or proportion. [#]: These values refer to the average of median NODDI parameters values in the 23 cortical or in the 6 subcortical regions included in the analyses. MMSE = mini-mental state examination, PACC = preclinical Alzheimer's cognitive composite, GFAP = glial fibrillary acidic protein, LC = locus coeruleus, *APOE* ε4 = apolipoprotein ε4, NDI = neurite density index, ODI = orientation dispersion index.

Zero-order correlations between demographics, GFAP, LC intensity, and NODDI parameters in the LC and in the averaged cortical or subcortical regions, are provided in Supplementary Table 1. We first assessed the effect of age, sex, or *APOE* status on plasma GFAP, LC intensity, and NODDI metrics in the LC and in the averaged cortical and subcortical regions (Figure 1). Older age was associated with higher plasma GFAP ($\beta = 2.463$, CI = [1.486; 3.399], $p < 0.001$), lower cortical NDI ($\beta = -0.0005$, CI = [-0.0009; -0.0002], $p = 0.0028$), lower cortical ODI ($\beta = -0.0015$, CI = [-0.0020; -0.0009], $p < 0.001$), lower subcortical NDI ($\beta = -0.0017$, CI = [-0.0023; -0.0012], $p < 0.001$) and lower subcortical ODI ($\beta = -0.0021$, CI = [-0.0028; -0.0015], $p < 0.001$). As compared to males, females

exhibited higher cortical ODI (β = 0.037, CI = [0.020; 0.055], p < 0.001), higher subcortical ODI (β = 0.044, CI = [0.023; 0.066], p < 0.001) and at trend-level higher subcortical NDI (β = 0.0198, CI = [-0.0006; 0.0406], p = 0.0562). Carrying at least one ε4 allele was associated with lower plasma GFAP (β = -38.507, CI = [-71.645; -2.061], p = 0.042) and with higher subcortical NDI (β = 0.028, CI = [0.006; 0.049], p = 0.013). No other age-, sex-, or *APOE*-relationships were detected (all p > 0.105).

As for the imaging variables, higher plasma GFAP was associated with both lower NDI (β = -0.00015, CI = [-0.00023; -0.00007], p < 0.001) and lower ODI (β = -0.00020, CI = [-0.00036; -0.00007], p = 0.0036) in the cortex, and both lower NDI (β = -0.0003, CI = [-0.0005; -0.0002], p < 0.001) and lower ODI (β = -0.0003, CI = [-0.0005; -0.0002], p < 0.001) in the subcortex. Higher ODI in the LC was associated with higher ODI in the subcortex (β = 0.467, CI = [0.028; 0.872], p = 0.037). NDI and ODI metrics were positively correlated in the cortex (β = 1.287, CI = [0.989; 1.588], p < 0.001), in the subcortex (β = 0.920, CI = [0.747; 1.101], p < 0.001), and also in the LC (β = 0.181, CI = [0.056; 0.304], p = 0.004), such that higher NDI was associated with higher ODI. In addition, higher cortical NDI was associated with both higher NDI (β = 1.442, CI = [1.133; 1.767], p < 0.001) and ODI (β = 1.508, CI = [1.104; 1.907], p < 0.001) in the subcortex, and similarly higher cortical ODI was associated with both higher NDI (β = 0.754, CI = [0.557; 0.963], p < 0.001) and ODI (β = 1.104, CI = [0.956; 1.253], p < 0.001) in the subcortex. We observed a negative trend-level association between LC intensity and LC ODI (β = -0.277, CI = [-0.589; 0.063], p = 0.092). No other association between plasma GFAP, LC intensity or NODDI parameters in the cortex, subcortex and the LC were detected (all p > 0.137).

Region-based relationships between cortical or subcortical and LC microstructural properties

We found that higher NDI in the rostral anterior cingulate region was associated with higher NDI in the LC (p_{FDR} = 0.028, Supplementary Figure 4A). No other cortical or subcortical regions survived adjustment for multiple comparisons (Supplementary Table 2-4). We further observed that higher LC ODI estimate was associated with higher ODI in the pallidum (p_{FDR} = 0.042, Supplementary Figure 4B), and no other cortical or subcortical regions survived correction

for multiple comparisons (Supplementary Table 3-5). Our specificity analyses, replacing LC NODDI metrics by LC intensity in models that showed significant associations in our previous analyses, revealed no association surviving correction for multiple comparisons between NDI metrics in the cortex and LC intensity and between ODI metrics in subcortical regions and LC intensity (Supplementary Table 6-7).

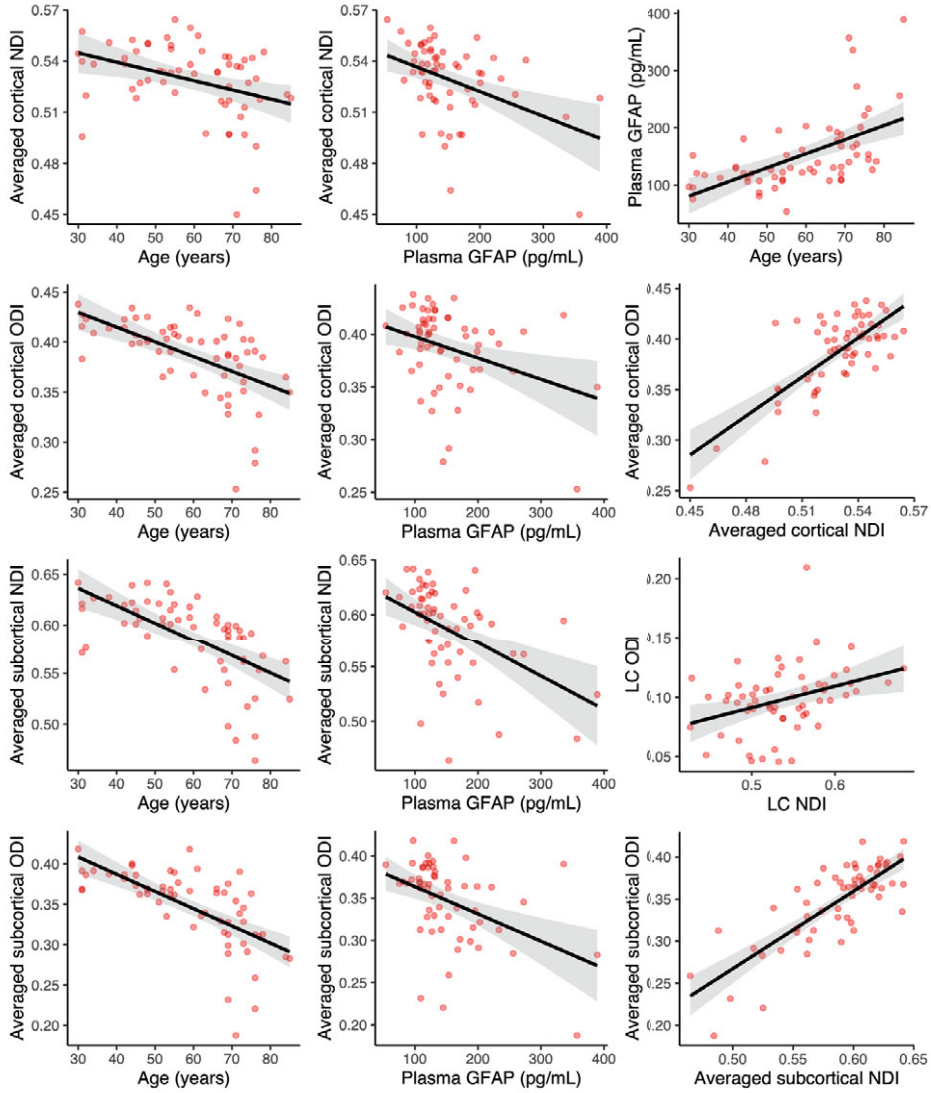

Figure 1. Associations between NODDI parameters, plasma GFAP and demographics. Regression lines and boxplots depicting the significant associations between variables in the entire cohort. Cortical and subcortical NODDI parameters are computed as the average of the NODDI estimates in the 23 cortical or in the 6 subcortical regions included in the analysis. Shaded areas surrounding the regression lines represent the 95% confidence interval of the regression fit. See also Supplementary Table 1 for zero-order correlation coefficients between all variables.

Region-based relationships between cortical or subcortical microstructural properties and plasma GFAP levels

Higher NDI and ODI cortical diffusion estimates were both associated with lower plasma GFAP levels (Supplementary Table 8-9). While none of the four significant regions survived FDR correction in the ODI model, seven cortical regions survived adjustment for multiple comparisons in the NDI model (all $p_{FDR} < 0.01$, Figure 2A). These regions were mainly located in the frontal cortex. To limit the number of figures, we provide a scatterplot relating GFAP to the average of the seven significant cortical regions in Figure 2B. For the subcortical models, lower NDI in the hippocampus and the amygdala was associated with higher GFAP ($p_{FDR} = 0.042$, Supplementary Table 10, Figure 2C-E). We further observed that lower ODI in the amygdala was associated with higher plasma GFAP, although not surviving adjustment for multiple comparisons (Supplementary Table 11).

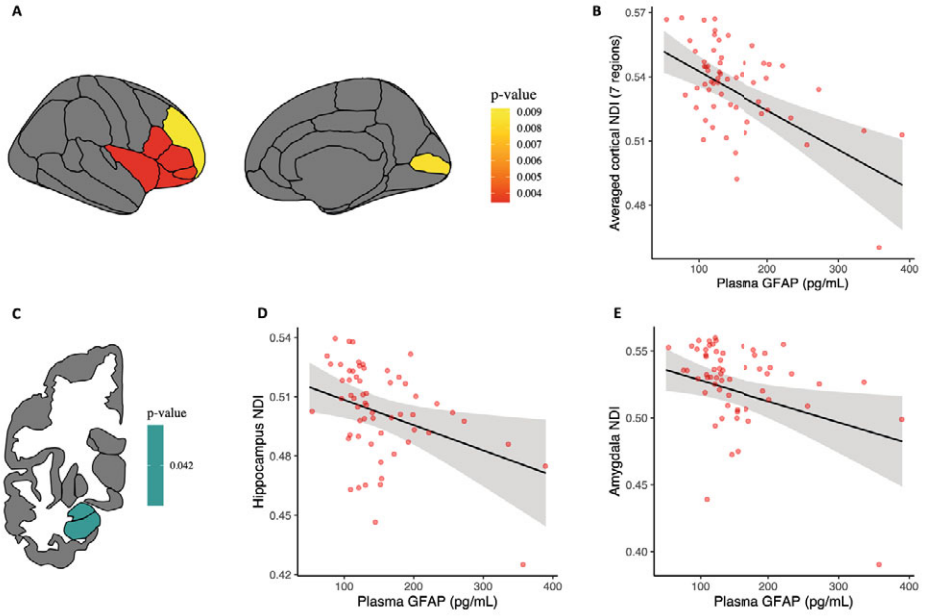

Figure 2. Plasma GFAP associations with regional cortical and subcortical NDI values. **A)** Illustrative map of cortical regions with significant associations ($p_{FDR} < 0.05$) between cortical NDI values and plasma GFAP levels. Left and right hemispheres values were averaged for each cortical region. **B)** Relationship between the average of NDI values in the 7 significant cortical regions surviving correction for multiple comparisons and plasma GFAP levels. **C)** Illustrative map of subcortical regions showing significant associations ($p_{FDR} < 0.05$) between subcortical NDI values and plasma GFAP levels. Left and right hemispheres values were averaged for each subcortical region. **D)** and **E)** Relationships between NDI in the hippocampus/amygdala and plasma GFAP ($p_{FDR} = 0.042$). All models used bootstrapped (5,000 iterations) linear regression analyses and were corrected for age and sex. Raw data points are overlayed to the predicted regression line. Shaded areas surrounding the regression lines represent the 95% confidence interval of the regression fit.

Region-based interactive relationships of LC microstructural properties and plasma GFAP levels on (sub)cortical microstructural properties

Finally, we investigated whether the interaction between LC NODDI and plasma GFAP concentrations was associated with cortical or subcortical NODDI parameters. First looking at the cortical regions, no interaction effect survived correction for multiple comparisons when considering the NDI models

(Supplementary Table 12). In contrast, at levels of plasma GFAP above 150.84 pg/mL, a positive LC-cortical ODI association emerged in 13 frontal-temporal regions (all $p_{FDR} < 0.04$, Figure 3A-B, Supplementary Table 13). Above the GFAP threshold, lower LC ODI was associated with lower cortical ODI in fronto-temporal cortical regions and conversely, higher ODI in the LC was associated with higher ODI in the same regions. Interestingly, similar patterns emerged when looking at the subcortical regions. While no interaction effect of LC NDI and GFAP on subcortical NDI was observed (Supplementary Table 14), all 6 subcortical regions showed significant ODI interaction effects at levels of plasma GFAP above 145.55 pg/mL such that lower LC ODI was associated with lower subcortical ODI and conversely, higher LC ODI was associated with higher subcortical ODI above the GFAP threshold (all $p_{FDR} < 0.036$, Figure 3C-D, Supplementary Table 15). In our specificity analyses, replacing LC NODDI metrics by LC intensity in the significant cortical and subcortical ODI models in interaction with GFAP, we observed that no cortical or subcortical region survived correction for multiple comparisons (Supplementary Table 16-17).

Sensitivity analyses confirmed these interaction results for both NODDI cortical and subcortical parameters when controlling for LC intensity, except for the banks region becoming significant in the ODI cortical model (Supplementary Table 18-21), or when controlling for *APOE* ε4 carriership (Supplementary Table 22-25). Running all the previous models in a subsample of individuals aged 50 and older yielded similar results, although in a more restricted set of regions likely due to the smaller sample size (N = 43): plasma GFAP was negatively associated to cortical NDI in two regions (pericalcarine and insula). However, no association was observed between plasma GFAP and subcortical NODDI metrics after adjusting for multiple comparisons. The interaction between LC ODI and plasma GFAP was associated with cortical ODI in the same regions, and in 2 additional regions (lingual and frontal pole), and with subcortical ODI in the same regions but the thalamus.

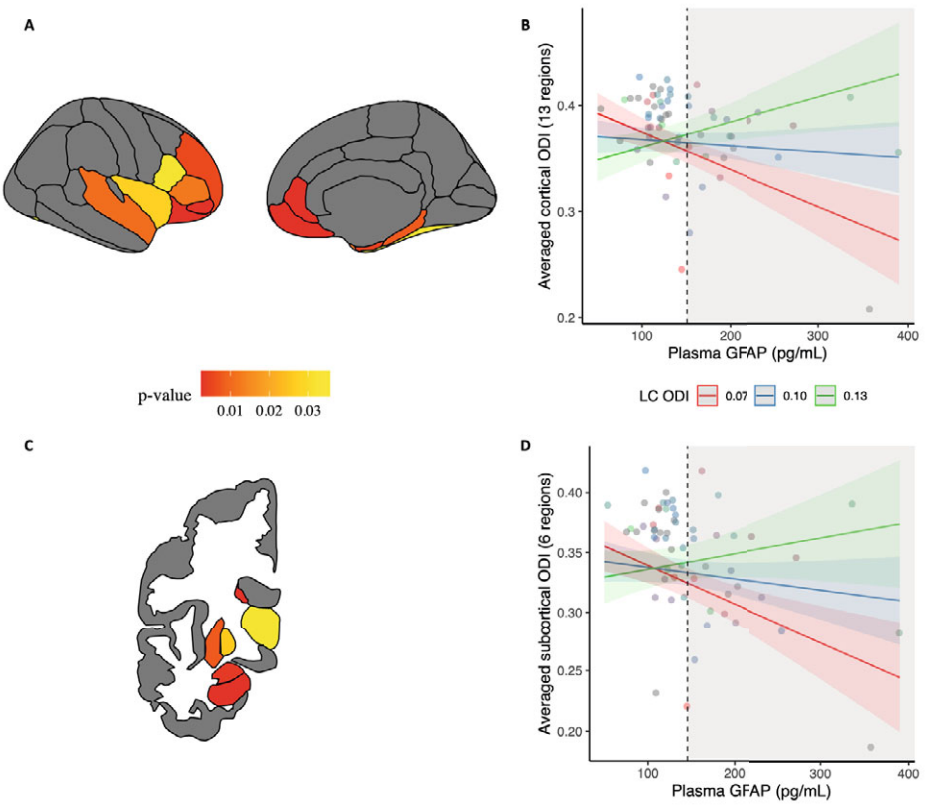

Figure 3. Interactive effects among ODI in the (sub)cortex, ODI in the LC, and plasma GFAP. **Left**: Illustrative maps of cortical (**A**) and subcortical (**C**) regions with significant interactive effects ($p_{FDR} < 0.05$) between LC ODI values and plasma GFAP on (sub) cortical ODI values using bootstrapped linear regression models (5,000 replicates) corrected for age and sex. Left and right hemispheres were averaged for each ROI. **Right**: Scatterplots showing the interactive relationship between LC ODI and plasma GFAP on the average of ODI in all 13 significant cortical regions (**B**) and the average of ODI in all 6 significant subcortical regions (**D**). The gray area represents the range of GFAP values (above 150.84 pg/mL (**B**) or above 145.55 pg/ml (**D**)) where LC ODI was positively associated with (sub)cortical ODI. For visualization purposes, LC ODI values are shown as mean, + and – 1 standard deviation, but analyses were performed continuously. Raw data points are overlayed to the predicted regression line. Shaded areas surrounding the regression lines represent the 95% confidence interval of the regression fit.

Independent and interactive relationships of imaging metrics and GFAP on PACC

After averaging the NODDI metrics across the 23 cortical or the 6 subcortical regions included, higher PACC-score was associated with higher NDI in the cortex ($p = 0.009$) and subcortex ($p = 0.001$), and with higher subcortical ODI ($p = 0.016$) (Figure 4). We observed trend-level associations between cortical ODI and PACC ($p = 0.05$), and between GFAP and PACC ($p = 0.09$), such that higher PACC was associated with higher cortical ODI and lower GFAP levels. We found no association between the LC NODDI metrics or LC intensity and PACC performance (all $p > 0.47$). Given that the cortical and subcortical NODDI relationships with LC NODDI metrics were dependent on GFAP, we also explored the interactive relationships of GFAP with cortical, subcortical and LC NODDI metrics and found no evidence for GFAP moderating the NODDI measures to cognition relationships (all $p > 0.53$; Supplementary Table 26).

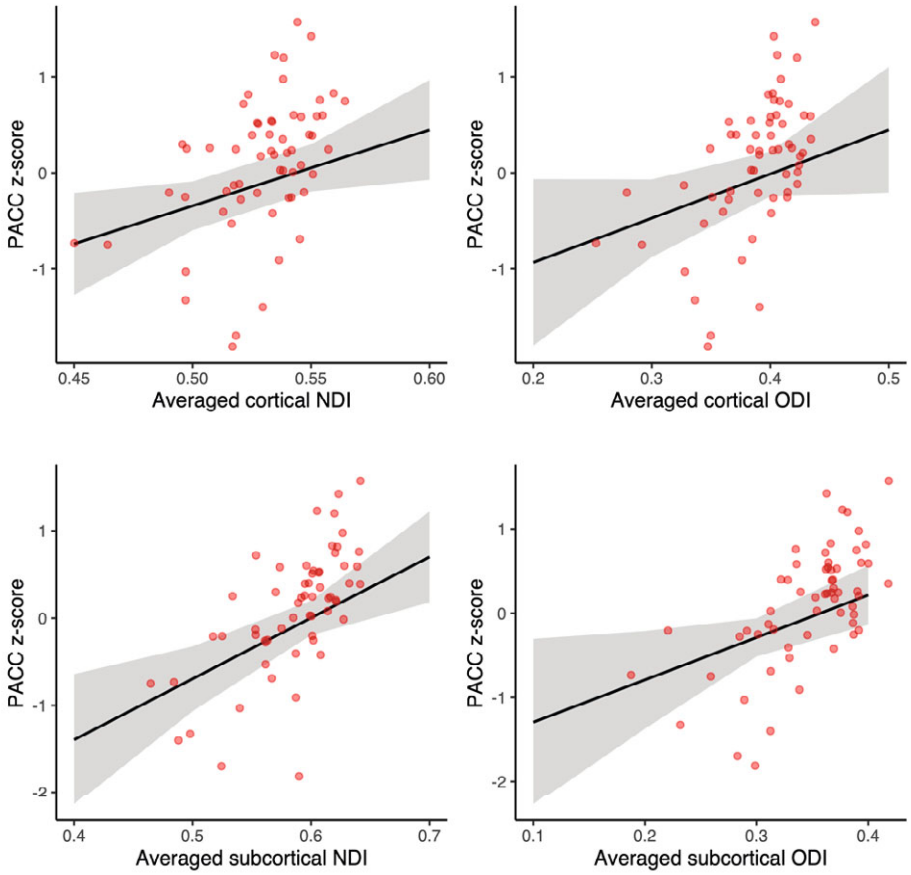

Figure 4. Association between (sub)cortical NODDI metrics and PACC-score. Relationships between the averaged cortical (23 regions) or subcortical (6 regions) NODDI metrics and PACC z-score: higher PACC is associated with higher NDI in the cortex (p = 0.009) and the subcortex (p = 0.001), and higher ODI in the subcortex (p = 0.016) and the cortex at a trend-level (p = 0.05). PACC = preclinical Alzheimer's cognitive composite. Bootstrapped (5,000 iterations) linear regression models are corrected for age, sex, and education. Raw data points are overlayed to the predicted regression line. Shaded areas surrounding the regression lines represent the 95% confidence interval of the regression fit.

DISCUSSION

Accumulating evidence implicates the LC-NE system in age-related brain changes, in particular through its modulation of neuroinflammation [4, 13, 37]. Furthermore, morphological changes to the LC neurons and projections, and the associated loss in noradrenergic input have been related to advanced brain aging processes, reduced neuroimmune mechanisms and the progression of pathologic changes associated with neurodegenerative diseases such as AD [38, 39]. Here, we related indices of neurite density (i.e., NDI) and organization (i.e., ODI) in the LC to those of cortical and subcortical regions using 7T MRI and examined the impact of astroglial activation on these relationships. Consistent with previous animal studies, lower arborization complexity (as indexed by ODI metrics) in LC neurites was associated with lower arborization complexity in fronto-temporal cortical regions and in all the 6 subcortical regions, in particular under elevated astrocyte reactivity (above ~150 or ~145 pg/mL). Interestingly, among individuals with higher LC neurite arborization complexity, the negative effect of elevated astrocyte reactivity on (sub)cortical microstructure was attenuated. These findings support that the health of LC neurites play a critical role in supporting cortical and subcortical regions, even in the context of elevated astrocyte reactivity. While we cannot establish causality, animal studies suggest that the health of LC neurites may possibly modulate astrocyte profiles toward a detrimental or protective signal. These findings underscore the importance of supporting LC neuronal health in adulthood before the emergence of age-related neurodegenerative processes.

We confirmed previous animal and human studies that older age was associated with worse microstructural properties in the brain [40, 41] and with higher astrocyte reactivity [15]. Astrocytes interact directly with neuritic processes and are involved in neuroinflammatory mechanisms. They play an important role in pruning synapses and maintaining the connections between presynaptic terminals and dendritic spines, but can become reactive during aging and in response to pathology [42]. This overexpression of GFAP is considered an early process in the preclinical stages of AD [43-45]. Recently, Bettcher and colleagues (2021) showed that among the entire spectrum of cognitively normal individuals to AD patients, elevated plasma GFAP levels

were associated with lower white matter integrity as indexed by FA in a medial temporal white matter aggregate and a white matter AD vulnerable aggregate, consisting of the hippocampal portion of the cingulum, dorsal portion of the cingulum, fornix crus, sagittal stratum, and corpus callosum [46]. Given that astrocyte reactivity has been associated with dendritic damage [42], we evaluated the relationship between gray matter neurites and astrocyte reactivity and observed that higher astrocyte reactivity was associated with lower density of neurites (i.e., NDI) in the hippocampus, the amygdala and frontal brain regions. Interestingly, Thaker and colleagues (2023) reported that higher GFAP levels were related to lower neurite orientation dispersion (i.e., ODI) in regions vulnerable to AD, an effect strongly driven by women, but found no association with neurite density [47]. Astrocyte reactivity was also related to a steeper increase in temporal and parietal mean diffusivity, possibly reflecting the microstructural changes occurring during AD-related neuroinflammatory processes [48]. While our dispersion metrics demonstrated the opposite, a negative relationship – higher GFAP was associated with lower neurites orientation dispersion in the parahippocampal and frontal regions, these models did not survive correction for multiple comparisons. Importantly, these regions are well known for their structural and functional vulnerability in aging [49]. Astrocytes can exhibit both aberrant disease-related as well as beneficial changes in the earliest stages of the disease, and thus it is possible that these opposing relationships reflect different functional aspects of GFAP or disease stages. This will require a more in-depth investigation in larger cohorts covering the entire spectrum of the disease. Together, our results are largely consistent with the previous AD literature and extend these findings to the adult lifespan, showing that astrocyte reactivity is linked to microstructural brain damage during aging.

It is possible that these astrocyte-related microstructural brain changes may reflect, spur, or interact with other early AD-related processes [50]. One of the earliest sites of hyperphosphorylated tau pathology in early adulthood is the LC. While several studies have investigated LC integrity using dedicated MRI techniques, only a handful of them have investigated microstructural properties of the LC, such as neurite morphology and organization during aging or the preclinical stages of AD. Studies using standard diffusion methods

demonstrated that diffusivity was lower and FA higher in the LC of older individuals compared to younger individuals [21, 22]. They speculated that this association reflected increased neuroinflammation, as microglia activation and therefore increased microglia density is known to restrict diffusivity. Even though we did not observe a direct relationship between LC integrity and astrocyte reactivity, we indeed found a synergistic effect between the LC NODDI metrics and microglial activation, as lower arborization complexity in the LC was associated with lower arborization complexity in widespread frontal and temporal cortical regions, when GFAP level was above ~150 pg/mL. Similar interactive relationships were found in the hippocampus, caudate, amygdala, putamen, pallidum, and thalamus, when GFAP level was above ~145 pg/mL. When the LC displays a higher arborization complexity, we find that arborization complexity in the (sub)cortex remains high despite the presence of elevated levels of astrocyte reactivity. The fact that both the LC and the (sub)cortex exhibit higher levels of arborization complexity indicates that astrocyte reactivity has no instantaneous negative effect on brain health or that the LC is able to provide neural resilience. Animal work demonstrated that LC-NE neurons can alter cortical responses and neural network dynamics via its influence on astrocytes [51]. Whether the LC-NE system counterbalances the detrimental effects of elevated astrocyte reactivity, possibly through glutamate-related co-activation, or may steer astrocyte signaling in neuroprotective pathways remains unclear [52]. Topographically, these GFAP-dependent associations between the LC and (sub)cortex were observed in the prefrontal, temporal, entorhinal cortices, hippocampus, thalamus and amygdala regions that are known to be highly connected to and regulated by the LC-NE system [1, 53, 54]. In addition, these regions are specifically vulnerable to aging and the earliest stages of AD [55-57]. Importantly, these findings highlight the neuroprotective effects the LC-NE system can have on brain health and stress the importance of maintaining LC neuronal health early in adulthood and in the prevention of age-related neurodegenerative diseases [4, 58, 59].

It is worth noting that these findings were independent of both *APOE* ε4 status and LC macrostructural integrity, as measured with the MT-TFL sequence, indicating that they are capturing different underlying biological processes. The negative trend-level relationship between LC integrity and LC

neurite orientation dispersion was unexpected, but may indicate that higher neuronal integrity is associated with dendrites in a less sprawling, more organized pattern. The distribution of neurons in the LC is characterized by a densely packed clustering of dendro-dendritic opposed neurons [60]. It is conceivable that under the influence of pathologic processes, this organization becomes more dispersed due to neuronal swelling or changes in dendritic arborization. In gray matter, the ODI parameter is thought to reflect dendritic arborization complexity, while the source of the commonly used structural LC contrast scans remains largely unknown, with hypothesized contributions from neuromelanin cells density, copper, water, and tau pathology [55, 61]. As our cohort consists of cognitively normal individuals along the adult lifespan, we are not able to examine how the contribution of these different LC markers evolves from healthy aging to AD. However, as our findings are similar in the entire cohort as in the ≥50-year-old individuals, and our GFAP threshold was equivalent to that identified in larger cohorts examining preclinical AD [45], we speculate that the NODDI parameters in the LC capture earlier, subtle changes compared to the LC macrostructural integrity metrics, and may presage the earliest processes related to age-related neurodegenerative diseases.

The LC is known to shape cognition through its modulatory effect on the cortex and subcortex. While we found no direct associations between LC NODDI metrics and cognition, we did see that higher cortical NDI values (and ODI at trend-level) and higher subcortical NDI and ODI values were associated with higher PACC performance. Cortical neurite density has been reported to be a sensitive marker of cortical changes that precede cognitive impairments [62]. The patterns for ODI versus NDI that we observed between the LC and supratentorial regions were very similar for the cortex and the subcortex. Even though GFAP modulated the relationship between LC and (sub)cortical NODDI metrics, we did not see an interaction between GFAP and NODDI metrics in association with cognition. This is not surprising given the moderate size of our sample and the fact that all our individuals are cognitively normal. Detecting complex behavioral associations may require longitudinal observations, as cognitive changes are expected to occur downstream of the AD-related brain changes. Future studies should also include cognitively impaired individuals

as well as longitudinal data to better understand the temporal ordering of the brain-behavior events in aging and disease-related processes.

The strengths of our study include innovative in vivo investigation of the LC microstructure through the combination of a LC-specific sequence at UHF MRI and advanced NODDI, providing more sensitive detection of subtle age-related changes. However, our study has limitations. First, the sample size is relatively moderate due to the strict inclusion criteria at 7T and only includes cognitively healthy individuals, limiting the generalizability of our findings. Considering larger cohorts with patients at different stages of AD and longitudinal follow-up will provide replication of our findings and more insight into the evolution of these LC-astrocyte relationships with cortical health across disease progression. Second, DWI is limited by its spatial resolution and its partial field of view. While the use of 7T NODDI MRI along with the MT-weighted sequence increased the reliability of our anatomic localization of the LC, 11 cortical regions out of 34 had to be excluded from the analyses. Enlarging the field of view would be at the cost of increased acquisition time and could introduce motion artifacts but would allow for a complete investigation of the cortex. Finally, we measured GFAP in blood and not in the cerebrospinal fluid. It has been reported that blood measures of GFAP exhibit a low variability and were superior in predicting AD-pathology in preclinical AD, compared to its CSF counterpart [45, 63]. Furthermore, the GFAP marker only stains sub-population of astrocytes, limiting the generalizability of our findings to the entire astrocyte population.

To conclude, our findings show that lower neurite arborization complexity of the LC was associated with lower cortical and subcortical arborization complexity in the context of astrocyte reactivity. Interestingly, individuals with higher neurite arborization in the LC also displayed higher (sub)cortical arborization, despite the presence of astrocyte reactivity, indicating that the LC-NE cells and astrocytes are closely intertwined, and their interaction may set off either a detrimental or neuroprotective pathway in aging. These findings signal the importance of maintaining LC neuronal health early in adult life and suggest that microstructural measures of the LC may detect potentially very early age-related neurodegenerative disease changes. Future research is needed to elucidate the temporal sequence of these processes and how the support of the LC-NE system could be used in interventions delaying the progression of AD.

REFERENCES

1. Samuels ER and Szabadi E. Functional neuroanatomy of the noradrenergic locus coeruleus: its roles in the regulation of arousal and autonomic function part I: principles of functional organisation. *Curr Neuropharmacol*. 2008;6(3):235-53.
2. Sara SJ. The locus coeruleus and noradrenergic modulation of cognition. *Nat Rev Neurosci*. 2009;10(3):211-23.
3. Van Egroo M, et al. Importance of the locus coeruleus-norepinephrine system in sleep-wake regulation: Implications for aging and Alzheimer's disease. *Sleep Med Rev*. 2022;62:101592.
4. Mather M and Harley CW. The Locus Coeruleus: Essential for Maintaining Cognitive Function and the Aging Brain. *Trends Cogn Sci*. 2016;20(3):214-26.
5. Bachman SL, et al. Locus coeruleus MRI contrast is associated with cortical thickness in older adults. *Neurobiol Aging*. 2021;100:72-82.
6. Elman JA, et al. Associations between MRI-assessed locus coeruleus integrity and cortical gray matter microstructure. *Cereb Cortex*. 2022;32(19):4191-203.
7. Braak H, et al. Stages of the pathologic process in Alzheimer disease: age categories from 1 to 100 years. *J Neuropathol Exp Neurol*. 2011;70(11):960-9.
8. Van Egroo M, et al. Ultra-high field imaging, plasma markers and autopsy data uncover a specific rostral locus coeruleus vulnerability to hyperphosphorylated tau. *Mol Psychiatry*. 2023:1-11.
9. Jacobs HIL, et al. Waning locus coeruleus integrity precedes cortical tau accrual in preclinical autosomal dominant Alzheimer's disease. *Alzheimers Dement*. 2023;19(1):169-80.
10. Kang SS, et al. Tau modification by the norepinephrine metabolite DOPEGAL stimulates its pathology and propagation. *Nat Struct Mol Biol*. 2022;29(4):292-305.
11. Braun D, Madrigal JL, and Feinstein DL. Noradrenergic regulation of glial activation: molecular mechanisms and therapeutic implications. *Curr Neuropharmacol*. 2014;12(4):342-52.
12. Finnell JE, et al. The contribution of the locus coeruleus-norepinephrine system in the emergence of defeat-induced inflammatory priming. *Brain Behav Immun*. 2019;79:102-13.
13. Heneka MT, et al. Locus ceruleus controls Alzheimer's disease pathology by modulating microglial functions through norepinephrine. *Proceedings of the National Academy of Sciences*. 2010;107(13):6058-63.
14. Heneka MT, et al. Locus ceruleus degeneration promotes Alzheimer pathogenesis in amyloid precursor protein 23 transgenic mice. *J Neurosci*. 2006;26(5):1343-54.
15. Nichols NR, et al. GFAP mRNA increases with age in rat and human brain. *Neurobiol Aging*. 1993;14(5):421-9.
16. Porchet R, et al. Analysis of glial acidic fibrillary protein in the human entorhinal cortex during aging and in Alzheimer's disease. *Proteomics*. 2003;3(8):1476-85.

17. Theofilas P, et al. Locus coeruleus volume and cell population changes during Alzheimer's disease progression: A stereological study in human postmortem brains with potential implication for early-stage biomarker discovery. *Alzheimers Dement*. 2017;13(3):236-46.

18. Ehrenberg AJ, et al. Quantifying the accretion of hyperphosphorylated tau in the locus coeruleus and dorsal raphe nucleus: the pathological building blocks of early Alzheimer's disease. *Neuropathol Appl Neurobiol*. 2017;43(5):393-408.

19. Chan-Palay V and Asan E. Alterations in catecholamine neurons of the locus coeruleus in senile dementia of the Alzheimer type and in Parkinson's disease with and without dementia and depression. *J Comp Neurol*. 1989;287(3):373-92.

20. Gilvesy A, et al. Spatiotemporal characterization of cellular tau pathology in the human locus coeruleus-pericoerulear complex by three-dimensional imaging. *Acta Neuropathol*. 2022;144(4):651-76.

21. Langley J, et al. Characterization of age-related microstructural changes in locus coeruleus and substantia nigra pars compacta. *Neurobiol Aging*. 2020;87:89-97.

22. Porat S, et al. Age differences in diffusivity in the locus coeruleus and its ascending noradrenergic tract. *Neuroimage*. 2022;251:119022.

23. Engels-Domínguez N, et al. State-of-the-art imaging of neuromodulatory subcortical systems in aging and Alzheimer's disease: Challenges and opportunities. *Neurosci Biobehav Rev*. 2023;144:104998.

24. Priovoulos N, et al. High-resolution in vivo imaging of human locus coeruleus by magnetization transfer MRI at 3T and 7T. *Neuroimage*. 2018;168:427-36.

25. Schiavone F, et al. Imaging age-related cognitive decline: A comparison of diffusion tensor and magnetization transfer MRI. *J Magn Reson Imaging*. 2009;29(1):23-30.

26. Kamiya K, Hori M, and Aoki S. NODDI in clinical research. *J Neurosci Methods*. 2020;346:108908.

27. Van Egroo M, van Hooren RWE, and Jacobs HIL. Associations between locus coeruleus integrity and nocturnal awakenings in the context of Alzheimer's disease plasma biomarkers: a 7T MRI study. *Alzheimers Res Ther*. 2021;13(1):159.

28. Marques JP, et al. MP2RAGE, a self bias-field corrected sequence for improved segmentation and T1-mapping at high field. *Neuroimage*. 2010;49(2):1271-81.

29. Fischl B. FreeSurfer. *Neuroimage*. 2012;62(2):774-81.

30. Dale AM, Fischl B, and Sereno MI. Cortical Surface-Based Analysis: I. Segmentation and Surface Reconstruction. *NeuroImage*. 1999;9(2):179-94.

31. Desikan RS, et al. An automated labeling system for subdividing the human cerebral cortex on MRI scans into gyral based regions of interest. *NeuroImage*. 2006;31(3):968-80.

32. Dahl MJ, et al. Locus coeruleus integrity is related to tau burden and memory loss in autosomal-dominant Alzheimer's disease. *Neurobiol Aging*. 2022;112:39-54.

33. Jenkinson M, et al. FSL. *Neuroimage*. 2012;62(2):782-90.

34. Zhang H, et al. NODDI: practical in vivo neurite orientation dispersion and density imaging of the human brain. *Neuroimage*. 2012;61(4):1000-16.

35. Papp KV, et al. Optimizing the preclinical Alzheimer's cognitive composite with semantic processing: The PACC5. *Alzheimers Dement (N Y)*. 2017;3(4):668-77.

36. Mowinckel AM and Vidal-Piñeiro D. Visualization of brain statistics with R packages ggseg and ggseg3d. *Advances in Methods and Practices in Psychological Science*. 2020;3(4):466-83.

37. Feinstein DL, et al. Noradrenergic regulation of inflammatory gene expression in brain. *Neurochem Int*. 2002;41(5):357-65.

38. Evans AK, Defensor E, and Shamloo M. Selective Vulnerability of the Locus Coeruleus Noradrenergic System and its Role in Modulation of Neuroinflammation, Cognition, and Neurodegeneration. *Front Pharmacol*. 2022;13:1030609.

39. Feinstein DL, Kalinin S, and Braun D. Causes, consequences, and cures for neuroinflammation mediated via the locus coeruleus: noradrenergic signaling system. *J Neurochem*. 2016;139 Suppl 2:154-78.

40. Dickstein DL, et al. Dendritic spine changes associated with normal aging. *Neuroscience*. 2013;251:21-32.

41. Pannese E. Morphological changes in nerve cells during normal aging. *Brain Struct Funct*. 2011;216(2):85-9.

42. Price BR, Johnson LA, and Norris CM. Reactive astrocytes: The nexus of pathological and clinical hallmarks of Alzheimer's disease. *Ageing Res Rev*. 2021;68:101335.

43. Chatterjee P, et al. Plasma glial fibrillary acidic protein is elevated in cognitively normal older adults at risk of Alzheimer's disease. *Transl Psychiatry*. 2021;11(1):27.

44. Asken BM, et al. Plasma Glial Fibrillary Acidic Protein Levels Differ Along the Spectra of Amyloid Burden and Clinical Disease Stage. *J Alzheimers Dis*. 2020;78(1):265-76.

45. Benedet AL, et al. Differences Between Plasma and Cerebrospinal Fluid Glial Fibrillary Acidic Protein Levels Across the Alzheimer Disease Continuum. *JAMA Neurol*. 2021;78(12):1471-83.

46. Bettcher BM, et al. Astrogliosis and episodic memory in late life: higher GFAP is related to worse memory and white matter microstructure in healthy aging and Alzheimer's disease. *Neurobiol Aging*. 2021;103:68-77.

47. Thaker AA, et al. Astrogliosis, neuritic microstructure, and sex effects: GFAP is an indicator of neuritic orientation in women. *Brain Behav Immun*. 2023;113:124-35.

48. Spotorno N, et al. Diffusion MRI tracks cortical microstructural changes during the early stages of Alzheimer's disease. *Brain*. 2023.

49. Salat DH, et al. Thinning of the cerebral cortex in aging. *Cereb Cortex*. 2004;14(7):721-30.

50. Jacobs HIL, et al. Alzheimer's disease pathology: pathways between central norepinephrine activity, memory, and neuropsychiatric symptoms. *Mol Psychiatry*. 2021;26(3):897-906.

51. Bekar LK, He W, and Nedergaard M. Locus coeruleus alpha-adrenergic-mediated activation of cortical astrocytes in vivo. *Cereb Cortex*. 2008;18(12):2789-95.

52. Garwood CJ, et al. Review: Astrocytes in Alzheimer's disease and other age-associated dementias: a supporting player with a central role. *Neuropathol Appl Neurobiol*. 2017;43(4):281-98.

53. Chandler DJ, Gao WJ, and Waterhouse BD. Heterogeneous organization of the locus coeruleus projections to prefrontal and motor cortices. *Proc Natl Acad Sci U S A*. 2014;111(18):6816-21.

54. Dahl MJ, Mather M, and Werkle-Bergner M. Noradrenergic modulation of rhythmic neural activity shapes selective attention. *Trends Cogn Sci*. 2022;26(1):38-52.

55. Jacobs HIL, et al. In vivo and neuropathology data support locus coeruleus integrity as indicator of Alzheimer's disease pathology and cognitive decline. *Sci Transl Med*. 2021;13(612):eabj2511.

56. van der Velpen IF, et al. Subcortical brain structures and the risk of dementia in the Rotterdam Study. *Alzheimers Dement*. 2023;19(2):646-57.

57. Eustache P, et al. Multimodal Magnetic Resonance Imaging in Alzheimer's Disease Patients at Prodromal Stage. *J Alzheimers Dis*. 2016;50(4):1035-50.

58. Wilson RS, et al. Neural reserve, neuronal density in the locus ceruleus, and cognitive decline. *Neurology*. 2013;80(13):1202-8.

59. Dahl MJ, et al. Rostral locus coeruleus integrity is associated with better memory performance in older adults. *Nat Hum Behav*. 2019;3(11):1203-14.

60. Totah NK, et al. The Locus Coeruleus Is a Complex and Differentiated Neuromodulatory System. *Neuron*. 2018;99(5):1055-68.e6.

61. Priovoulos N, et al. Unraveling the contributions to the neuromelanin-MRI contrast. *Brain Struct Funct*. 2020;225(9):2757-74.

62. Vogt NM, et al. Interaction of amyloid and tau on cortical microstructure in cognitively unimpaired adults. *Alzheimers Dement*. 2022;18(1):65-76.

63. Simrén J, et al. Differences between blood and cerebrospinal fluid glial fibrillary Acidic protein levels: The effect of sample stability. *Alzheimers Dement*. 2022;18(10):1988-92.

SUPPLEMENTARY MATERIAL

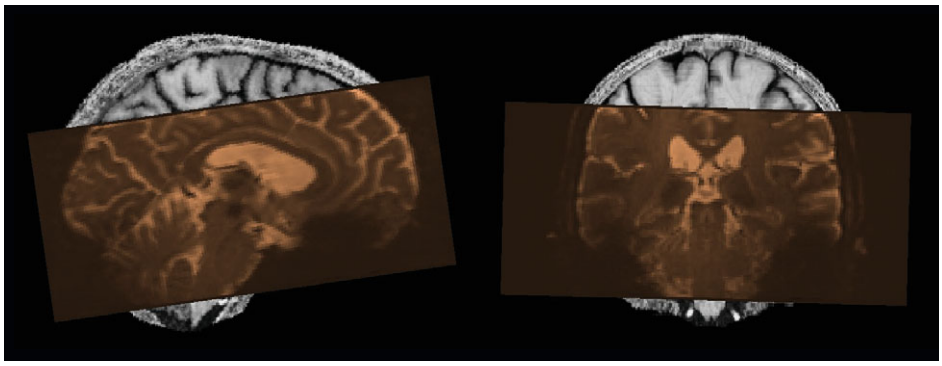

Figure S1. Visualization of the partial field of view for diffusion-weighted (DW) acquisitions. Whole brain structural image of one participant overlayed with diffusion-weighted image (in brown), illustrating the restricted field of view of the DW acquisitions.

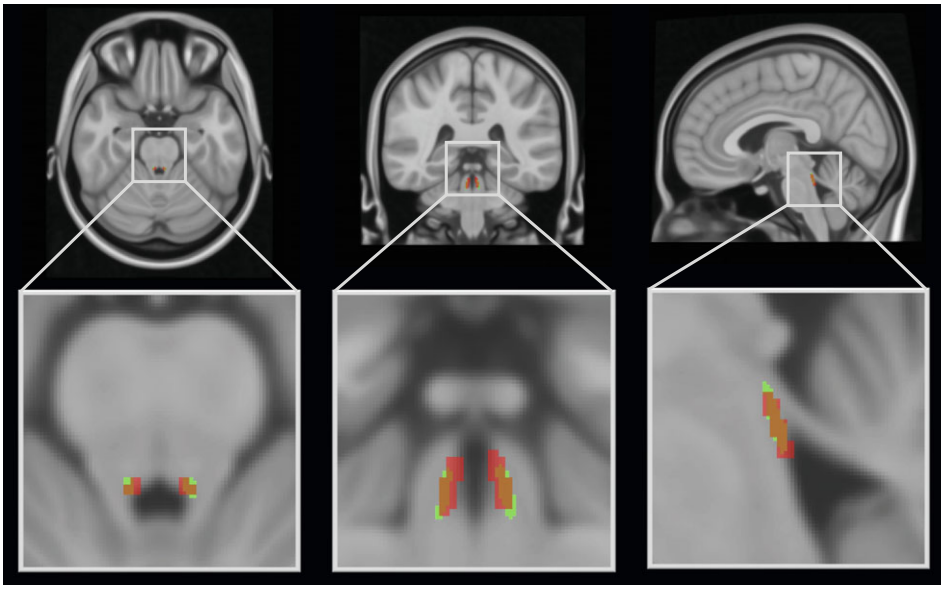

Figure S2. Overlap between our LC mask and the published LC meta mask. Axial, coronal and sagittal views of our LC mask (in red) overlayed with the LC meta mask [1] (in green) and the overlap between the two (in orange). Visualization in the standard MNI space (0.5 mm resolution).

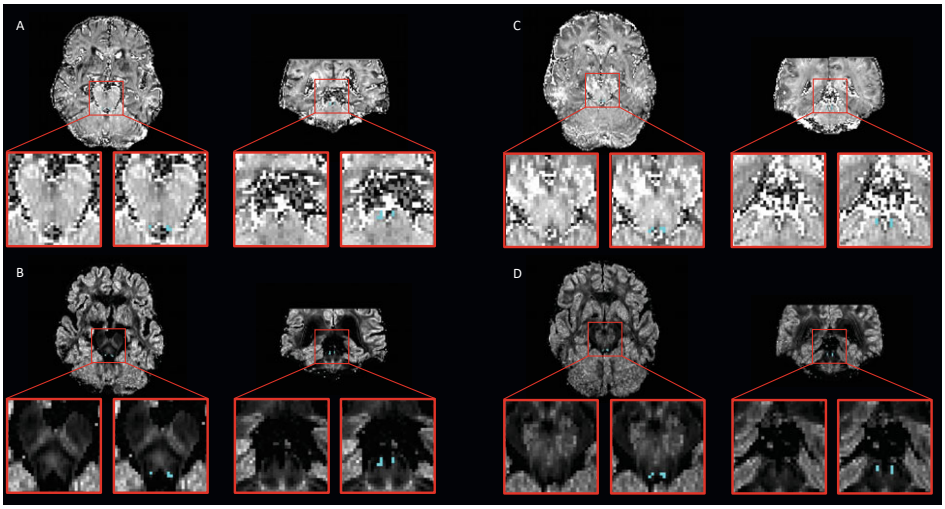

Figure S3. Illustration of NODDI maps overlaid with the LC mask. Axial and coronal views of (**A, C**) NDI and (**B, D**) ODI maps overlaid with the LC mask (depicted in blue), and zoomed in on the LC region (red square). Data is shown for (**A, B**) an older individual (76 years old) and (**C, D**) a younger individual (31 years old).

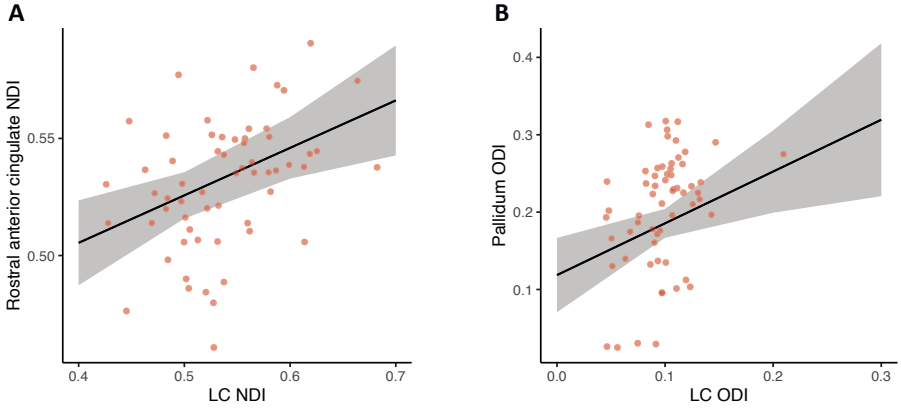

Figure S4. Significant associations between (sub)cortical and LC microstructure. Relationships between **A)** NDI in the rostral anterior cingulate and LC NDI (p_{FDR} = 0.028), and **B)** ODI in the pallidum and LC ODI (p_{FDR} = 0.042). Bootstrapped (5,000 iterations) linear regression models controlling for age and sex. Raw data points are overlayed to the predicted regression line. Shaded areas surrounding the regression lines represent the 95% confidence interval of the regression fit.

Table S1. Zero-order correlations between GFAP, LC intensity, cortical, subcortical and LC NODDI parameters, and demographics

	Age	Sex	*APOE*	GFAP	$LC_{intensity}$	NDI_{LC}	ODI_{LC}	NDI_{cortex}	ODI_{cortex}	$NDI_{subcortex}$
Sex	-0.20									
APOE	**-0.40****	-0.11								
GFAP	**0.56*****	0.02	**-0.27***							
$LC_{intensity}$	-0.10	0.15	-0.04	-0.16						
NDI_{LC}	0.02	0.20	-0.10	-0.08	-0.01					
ODI_{LC}	-0.15	0.17	0.13	-0.09	-0.22$^{\#}$	**0.35****				
NDI_{cortex}	**-0.36****	0.19	0.19	**-0.43*****	0.12	0.02	0.20			
ODI_{cortex}	**-0.57*****	**0.49*****	0.21$^{\#}$	**-0.34****	0.09	0.08	0.19	**0.74*****		
$NDI_{subcortex}$	**-0.61*****	0.24$^{\#}$	**0.31***	**-0.48*****	0.0001	0.10	0.17	**0.77*****	**0.70*****	
$ODI_{subcortex}$	**-0.66*****	**0.47*****	0.18	**-0.44*****	0.06	0.16	**0.28***	**0.70*****	**0.89*****	**0.80*****

Correlation matrix showing Pearson's product-moment correlation coefficients (continuous variables) or point-biserial correlation coefficients (dichotomous variables). Cortical NODDI parameters are calculated as the average of NODDI parameters in the 23 cortical regions included in the analysis. Subcortical NODDI parameters are calculated as the average of NODDI parameters in the 6 subcortical regions included in the analysis. Sex variable was coded as 0 for males and 1 for females. Statistical trend or significance is indicated as $^{\#}$: $p < 0.10$, *: $p < 0.05$, **: $p < 0.01$, ***: $p < 0.001$.

Table S2. Associations between NDI in cortical regions and in the LC

Cortical region	Coefficient	CI	p-value	p-value$_{FDR}$
Rostral anterior cingulate	0.2027	[0.0838; 0.3193]	**0.0012**	**0.0276**
Medial orbitofrontal	0.1233	[-0.0024; 0.2419]	0.0546	0.4439
Transverse temporal	-0.1673	[-0.3418; 0.0068]	0.0598	0.4439
Lateral orbitofrontal	0.1301	[-0.0168; 0.2735]	0.0772	0.4439
Temporal pole	-0.2169	[-0.4715; 0.0399]	0.1058	0.4867
Pars orbitalis	0.0798	[-0.0317; 0.1906]	0.1612	0.6179
Entorhinal	-0.1354	[-0.4081; 0.1263]	0.2936	0.9020
Pars triangularis	0.0481	[-0.0562; 0.1487]	0.3596	0.9020
Middle temporal	-0.0855	[-0.2796; 0.1063]	0.3722	0.9020
Superior temporal	-0.0587	[-0.2108; 0.0944]	0.4264	0.9020
Isthmus cingulate	0.0366	[-0.0529; 0.1252]	0.4314	0.9020
Fusiform	0.0517	[-0.1240; 0.2303]	0.5652	0.9698
Lingual	0.0272	[-0.1176; 0.1672]	0.7208	0.9698
Lateral occipital	-0.0221	[-0.1583; 0.1073]	0.7358	0.9698
Inferior temporal	-0.0298	[-0.2246; 0.1587]	0.7452	0.9698
Insula	0.0122	[-0.0804; 0.1064]	0.8002	0.9698
Pericalcarine	0.0201	[-0.1632; 0.1975]	0.8334	0.9698
Banks	0.0178	[-0.1295; 0.1633]	0.8388	0.9698
Pars opercularis	0.0101	[-0.0784; 0.0984]	0.8408	0.9698
Frontal pole	0.0246	[-0.2120; 0.2624]	0.8670	0.9698
Parahippocampal	-0.0066	[-0.1424; 0.1282]	0.9142	0.9698
Caudal anterior cingulate	0.0034	[-0.0790; 0.0843]	0.9276	0.9698
Rostral middle frontal	-0.0008	[-0.1015; 0.0957]	0.9792	0.9792

Results from the bootstrapped (5,000 iterations) linear regression model showing the bootstrapped coefficient, the confidence interval (CI), the p-value before (p-value) and after correction for multiple comparisons (p-value$_{FDR}$) related to the main effect of LC NDI. The 23 cortical regions included in the analysis are shown. Significant p-values are highlighted in bold. Age and sex are included as covariates in the model.

Table S3. Associations between ODI in cortical regions and in the LC

Cortical region	Coefficient	CI	p-value	$p\text{-value}_{FDR}$
Caudal anterior cingulate	-0.1784	[-0.3499; -0.0118]	**0.0356**	0.4585
Frontal pole	-0.6523	[-1.3163; -0.0286]	**0.0408**	0.4585
Rostral middle frontal	-0.1724	[-0.3616; 0.0082]	0.0598	0.4585
Insula	0.1668	[-0.0485; 0.3591]	0.1256	0.5486
Pars triangularis	-0.1458	[-0.3547; 0.0521]	0.1664	0.5486
Entorhinal	0.4542	[-0.2506; 1.0850]	0.1876	0.5486
Transverse temporal	0.2343	[-0.1677; 0.6118]	0.2492	0.5486
Inferior temporal	0.3407	[-0.2362; 0.8762]	0.2494	0.5486
Parahippocampal	0.2049	[-0.1499; 0.5437]	0.2524	0.5486
Lateral orbitofrontal	0.2258	[-0.2709; 0.6608]	0.2708	0.5486
Banks	0.1664	[-0.1554; 0.4828]	0.3238	0.5486
Fusiform	0.2609	[-0.2641; 0.7441]	0.3334	0.5486
Superior temporal	0.1962	[-0.2722; 0.6024]	0.3712	0.5486
Pars orbitalis	0.1183	[-0.1763; 0.3903]	0.3734	0.5486
Middle temporal	0.2070	[-0.2693; 0.6455]	0.3868	0.5486
Rostral anterior cingulate	0.1069	[-0.1366; 0.3514]	0.3938	0.5486
Lateral occipital	-0.1643	[-0.5963; 0.2366]	0.4284	0.5486
Temporal pole	0.2942	[-0.4490; 0.9932]	0.4442	0.5486
Isthmus cingulate	0.0780	[-0.1486; 0.2798]	0.4532	0.5486
Pars opercularis	0.0595	[-0.1444; 0.2480]	0.5874	0.6755
Lingual	0.0799	[-0.2719; 0.4103]	0.6588	0.7040
Pericalcarine	-0.0746	[-0.4469; 0.2841]	0.6734	0.7040
Medial orbitofrontal	-0.0220	[-0.5289; 0.4656]	0.9098	0.9098

Results from the bootstrapped (5,000 iterations) linear regression model showing the bootstrapped coefficient, the confidence interval (CI), the p-value before (p-value) and after correction for multiple comparisons ($p\text{-value}_{FDR}$) related to the main effect of LC ODI. The 23 cortical regions included in the analysis are shown. Significant p-values are highlighted in bold. Age and sex are included as covariates in the model.

Table S4. Associations between NDI in subcortical regions and in the LC

Subcortical region	Coefficient	CI	p-value	$p\text{-value}_{FDR}$
Thalamus	0.1152	[-0.0308; 0.2544]	0.1202	0.6211
Hippocampus	0.0555	[-0.0548; 0.1611]	0.2994	0.6211
Caudate	0.0884	[-0.1520; 0.3245]	0.4674	0.6211
Putamen	0.0849	[-0.1672; 0.3250]	0.5080	0.6211
Amygdala	0.0419	[-0.0953; 0.1725]	0.5176	0.6211
Pallidum	0.0323	[-0.2389; 0.3019]	0.8268	0.8268

Results from the bootstrapped (5,000 iterations) linear regression model showing the bootstrapped coefficient, the confidence interval (CI), the p-value before (p-value) and after correction for multiple comparisons ($p\text{-value}_{FDR}$) related to the main effect of LC NDI. The 6 subcortical regions included in the analysis are shown. Significant p-values are highlighted in bold. Age and sex are included as covariates in the model.

Table S5. Associations between ODI in subcortical regions and in the LC

Subcortical region	Coefficient	CI	p-value	$p\text{-value}_{FDR}$
Pallidum	0.6693	[0.2035; 1.1128]	**0.0060**	**0.0360**
Putamen	0.3942	[-0.1425; 0.8730]	0.1446	0.4338
Hippocampus	0.1469	[-0.1528; 0.4195]	0.3276	0.6552
Amygdala	0.1084	[-0.2762; 0.4510]	0.5590	0.7428
Thalamus	0.0287	[-0.1025; 0.1597]	0.6690	0.7428
Caudate	0.0599	[-0.2948; 0.4036]	0.7428	0.7428

Results from the bootstrapped (5,000 iterations) linear regression model showing the bootstrapped coefficient, the confidence interval (CI), the p-value before (p-value) and after correction for multiple comparisons ($p\text{-value}_{FDR}$) related to the main effect of LC ODI. The 6 subcortical regions included in the analysis are shown. Significant p-values are highlighted in bold. Age and sex are included as covariates in the model.

Table S6. Associations between NDI in cortical regions and LC intensity

Cortical region	Coefficient	CI	p-value	p-value$_{FDR}$
Temporal pole	0.3736	[-0.0202; 0.7617]	0.0658	0.9986
Medial orbitofrontal	-0.1153	[-0.3078; 0.0721]	0.2220	0.9986
Insula	0.0753	[-0.0671; 0.2168]	0.2936	0.9986
Superior temporal	0.1254	[-0.1170; 0.3562]	0.3048	0.9986
Transverse temporal	0.1341	[-0.1333; 0.4088]	0.3406	0.9986
Rostral middle frontal	0.0701	[-0.0866; 0.2249]	0.3710	0.9986
Middle temporal	0.1303	[-0.1636; 0.4229]	0.4028	0.9986
Entorhinal	0.1334	[-0.2642; 0.5363]	0.4998	0.9986
Rostral anterior cingulate	-0.0662	[-0.2656; 0.1381]	0.5284	0.9986
Caudal anterior cingulate	0.0332	[-0.1007; 0.1634]	0.6224	0.9986
Lateral occipital	-0.0475	[-0.2483; 0.1474]	0.6278	0.9986
Pars opercularis	0.0322	[-0.1041; 0.1708]	0.6494	0.9986
Isthmus cingulate	0.0254	[-0.1111; 0.1601]	0.7266	0.9986
Banks	0.0399	[-0.1854; 0.2659]	0.7406	0.9986
Inferior temporal	0.0466	[-0.2548; 0.3376]	0.7468	0.9986
Frontal pole	-0.0446	[-0.4199; 0.3102]	0.7996	0.9986
Pars triangularis	0.0204	[-0.1355; 0.1805]	0.8180	0.9986
Fusiform	0.0200	[-0.2489; 0.2856]	0.8970	0.9986
Parahippocampal	-0.0114	[-0.2202; 0.1921]	0.8984	0.9986
Lingual	0.0121	[-0.2046; 0.2284]	0.9280	0.9986
Pars orbitalis	-0.0048	[-0.1834; 0.1750]	0.9558	0.9986
Pericalcarine	0.0064	[-0.2807; 0.2698]	0.9570	0.9986
Lateral orbitofrontal	-0.0016	[-0.2378; 0.2239]	0.9986	0.9986

Results from the bootstrapped (5,000 iterations) linear regression model showing the bootstrapped coefficient, the confidence interval (CI), the p-value before (p-value) and after correction for multiple comparisons (p-value$_{FDR}$) related to the main effect of LC intensity. The 23 cortical regions included in the analysis are shown. Significant p-values are highlighted in bold. Age and sex are included as covariates in the model.

Table S7. Associations between ODI in subcortical regions and LC intensity

Subcortical region	Coefficient	CI	p-value	$p\text{-value}_{FDR}$
Pallidum	-0.1803	[-0.5745; 0.2045]	0.3688	0.8033
Thalamus	-0.0355	[-0.1379; 0.0651]	0.4858	0.8033
Amygdala	-0.0714	[-0.3593; 0.2119]	0.6154	0.8033
Putamen	-0.0920	[-0.5047; 0.3275]	0.6486	0.8033
Caudate	-0.0616	[-0.3298; 0.2099]	0.6694	0.8033
Hippocampus	-0.0046	[-0.2355; 0.2158]	0.9706	0.9706

Results from the bootstrapped (5,000 iterations) linear regression model showing the bootstrapped coefficient, the confidence interval (CI), the p-value before (p-value) and after correction for multiple comparisons ($p\text{-value}_{FDR}$) related to the main effect of LC intensity. The 6 subcortical regions included in the analysis are shown. Significant p-values are highlighted in bold. Age and sex are included as covariates in the model.

Table S8. Associations between NDI in cortical regions and plasma GFAP

Cortical region	Coefficient	CI	p-value	p-value$_{FDR}$
Pars triangularis	-0.0002	[-0.0003; -0.0001]	**0.0002**	**0.0035**
Insula	-0.0002	[-0.0002; -0.0001]	**0.0006**	**0.0035**
Lateral orbitofrontal	-0.0002	[-0.0004; -0.0001]	**0.0006**	**0.0035**
Pars opercularis	-0.0001	[-0.0002; -0.0001]	**0.0006**	**0.0035**
Pars orbitalis	-0.0002	[-0.0003; -0.0001]	**0.0008**	**0.0037**
Pericalcarine	-0.0003	[-0.0004; -0.0001]	**0.0022**	**0.0084**
Rostral middle frontal	-0.0001	[-0.0002; 0.0000]	**0.0028**	**0.0092**
Fusiform	-0.0002	[-0.0004; 0.0000]	**0.0290**	0.0834
Lingual	-0.0001	[-0.0003; 0.0000]	0.0580	0.1284
Superior temporal	-0.0001	[-0.0003; 0.0000]	0.0614	0.1284
Banks	-0.0001	[-0.0003; 0.0000]	0.0622	0.1284
Medial orbitofrontal	-0.0001	[-0.0002; 0.0000]	0.0670	0.1284
Inferior temporal	-0.0002	[-0.0004; 0.0000]	0.0744	0.1316
Transverse temporal	-0.0001	[-0.0003; 0.0000]	0.1240	0.2037
Entorhinal	-0.0002	[-0.0005; 0.0001]	0.1678	0.2547
Rostral anterior cingulate	-0.0001	[-0.0002; 0.0000]	0.1772	0.2547
Isthmus cingulate	-0.0001	[-0.0001; 0.0000]	0.2060	0.2787
Parahippocampal	-0.0001	[-0.0002; 0.0001]	0.2656	0.3394
Temporal pole	0.0001	[-0.0001; 0.0004]	0.3006	0.3639
Middle temporal	-0.0001	[-0.0003; 0.0001]	0.3348	0.3850
Lateral occipital	-0.0001	[-0.0002; 0.0001]	0.4526	0.4957
Caudal anterior cingulate	0.0000	[-0.0001; 0.0001]	0.6574	0.6873
Frontal pole	-0.0001	[-0.0003; 0.0002]	0.6918	0.6918

Results from the bootstrapped (5,000 iterations) linear regression model showing the bootstrapped coefficient, the confidence interval (CI), the p-value before (p-value) and after correction for multiple comparisons (p-value$_{FDR}$) related to the main effect of GFAP. The 23 cortical regions included in the analysis are shown. Significant p-values are highlighted in bold. Age and sex are included as covariates in the model.

Table S9. Associations between ODI in cortical regions and plasma GFAP

Cortical region	Coefficient	CI	p-value	$p\text{-value}_{FDR}$
Parahippocampal	-0.0002	[-0.0004; 0.0000]	**0.0112**	0.1679
Lateral orbitofrontal	-0.0003	[-0.0005; 0.0000]	**0.0230**	0.1679
Pars orbitalis	-0.0002	[-0.0003; 0.0000]	**0.0258**	0.1679
Insula	-0.0001	[-0.0002; 0.0000]	**0.0292**	0.1679
Pars opercularis	-0.0001	[-0.0002; 0.0000]	0.0584	0.2686
Superior temporal	-0.0002	[-0.0004; 0.0001]	0.1306	0.4094
Banks	-0.0001	[-0.0003; 0.0000]	0.1312	0.4094
Transverse temporal	-0.0002	[-0.0004; 0.0000]	0.1424	0.4094
Fusiform	-0.0002	[-0.0004; 0.0001]	0.1964	0.5019
Pars triangularis	-0.0001	[-0.0002; 0.0000]	0.2222	0.5111
Rostral anterior cingulate	-0.0001	[-0.0002; 0.0001]	0.3826	0.7976
Lateral occipital	0.0001	[-0.0002; 0.0003]	0.4598	0.7976
Inferior temporal	-0.0001	[-0.0004; 0.0002]	0.4822	0.7976
Frontal pole	0.0001	[-0.0003; 0.0004]	0.5464	0.7976
Medial orbitofrontal	0.0001	[-0.0002; 0.0003]	0.5494	0.7976
Middle temporal	-0.0001	[-0.0003; 0.0002]	0.6258	0.7976
Rostral middle frontal	0.0000	[-0.0001; 0.0001]	0.6350	0.7976
Temporal pole	0.0001	[-0.0003; 0.0005]	0.6690	0.7976
Entorhinal	-0.0001	[-0.0005; 0.0003]	0.6986	0.7976
Isthmus cingulate	0.0000	[-0.0001; 0.0001]	0.7068	0.7976
Pericalcarine	0.0000	[-0.0002; 0.0001]	0.7282	0.7976
Caudal anterior cingulate	0.0000	[-0.0001; 0.0001]	0.8574	0.8876
Lingual	0.0000	[-0.0002; 0.0002]	0.8876	0.8876

Results from the bootstrapped (5,000 iterations) linear regression model showing the bootstrapped coefficient, the confidence interval (CI), the p-value before (p-value) and after correction for multiple comparisons ($p\text{-value}_{FDR}$) related to the main effect of GFAP. The 23 cortical regions included in the analysis are shown. Significant p-values are highlighted in bold. Age and sex are included as covariates in the model.

Table S10. Associations between NDI in subcortical regions and plasma GFAP

Subcortical region	Coefficient	CI	p-value	p-value$_{FDR}$
Hippocampus	-0.00013	[-0.00023; -0.00003]	**0.0094**	**0.0420**
Amygdala	-0.00016	[-0.00030; -0.00003]	**0.0140**	**0.0420**
Putamen	-0.00024	[-0.00050; 0.00000]	**0.0460**	0.0920
Thalamus	-0.00009	[-0.00025; 0.00005]	0.2036	0.2885
Caudate	-0.00015	[-0.00041; 0.00009]	0.2404	0.2885
Pallidum	-0.00011	[-0.00040; 0.00017]	0.4272	0.4272

Results from the bootstrapped (5,000 iterations) linear regression model showing the bootstrapped coefficient, the confidence interval (CI), the p-value before (p-value) and after correction for multiple comparisons (p-value$_{FDR}$) related to the main effect of GFAP. The 6 subcortical regions included in the analysis are shown. Significant p-values are highlighted in bold. Age and sex are included as covariates in the model.

Table S11. Associations between ODI in subcortical regions and plasma GFAP

Subcortical region	Coefficient	CI	p-value	p-value$_{FDR}$
Amygdala	-0.00021	[-0.00040; -0.00003]	**0.0214**	0.1284
Caudate	-0.00016	[-0.00034; 0.00002]	0.0816	0.1644
Hippocampus	-0.00013	[-0.00028; 0.00002]	0.0958	0.1644
Putamen	-0.00021	[-0.00049; 0.00005]	0.1096	0.1644
Thalamus	-0.00002	[-0.00009; 0.00005]	0.5992	0.6666
Pallidum	-0.00006	[-0.00033; 0.00019]	0.6666	0.6666

Results from the bootstrapped (5,000 iterations) linear regression model showing the bootstrapped coefficient, the confidence interval (CI), the p-value before (p-value) and after correction for multiple comparisons (p-value$_{FDR}$) related to the main effect of GFAP. The 6 subcortical regions included in the analysis are shown. Significant p-values are highlighted in bold. Age and sex are included as covariates in the model.

Table S12. Interactive associations of NDI in the LC and plasma GFAP on cortical NDI

Cortical region	Coefficient	CI	p-value	$p\text{-value}_{FDR}$
Isthmus cingulate	-0.0018	[-0.0033; -0.0003]	**0.0234**	0.4577
Lateral occipital	-0.0026	[-0.0049; -0.0001]	**0.0398**	0.4577
Temporal pole	-0.0035	[-0.0080; 0.0010]	0.1260	0.7184
Banks	-0.0018	[-0.0043; 0.0008]	0.1636	0.7184
Pars orbitalis	0.0013	[-0.0005; 0.0032]	0.1726	0.7184
Parahippocampal	-0.0017	[-0.0042; 0.0008]	0.1874	0.7184
Inferior temporal	-0.0020	[-0.0055; 0.0015]	0.2568	0.7562
Fusiform	-0.0016	[-0.0047; 0.0015]	0.3118	0.7562
Transverse temporal	0.0015	[-0.0016; 0.0047]	0.3438	0.7562
Lingual	-0.0011	[-0.0036; 0.0014]	0.4032	0.7562
Caudal anterior cingulate	-0.0006	[-0.0021; 0.0009]	0.4520	0.7562
Middle temporal	-0.0013	[-0.0047; 0.0024]	0.4662	0.7562
Entorhinal	-0.0016	[-0.0065; 0.0031]	0.4700	0.7562
Superior temporal	-0.0009	[-0.0037; 0.0019]	0.4846	0.7562
Rostral anterior cingulate	0.0006	[-0.0015; 0.0028]	0.5652	0.7562
Medial orbitofrontal	0.0006	[-0.0017; 0.0029]	0.5776	0.7562
Lateral orbitofrontal	0.0005	[-0.0020; 0.0033]	0.6464	0.7562
Pericalcarine	-0.0007	[-0.0036; 0.0024]	0.6658	0.7562
Frontal pole	-0.0009	[-0.0052; 0.0037]	0.6674	0.7562
Insula	-0.0003	[-0.0019; 0.0012]	0.6896	0.7562
Pars triangularis	0.0003	[-0.0014; 0.0021]	0.6904	0.7562
Rostral middle frontal	0.0001	[-0.0016; 0.0019]	0.8642	0.9035
Pars opercularis	0.0001	[-0.0014; 0.0015]	0.9146	0.9146

Results from the bootstrapped (5,000 iterations) linear regression model showing the bootstrapped coefficient, the confidence interval (CI), the p-value before (p-value) and after correction for multiple comparisons ($p\text{-value}_{FDR}$) related to the interaction term. The 23 cortical regions included in the analysis are shown. Significant p-values are highlighted in bold. Age and sex are included as covariates in the model.

Table S13. Interactive associations of ODI in the LC and plasma GFAP on cortical ODI

Cortical region	Coefficient	CI	p-value	p-value$_{FDR}$
Lateral orbitofrontal	0.0185	[0.0138; 0.0237]	**0.0000**	**0.0000**
Medial orbitofrontal	0.0159	[0.0095; 0.0227]	**0.0000**	**0.0000**
Pars orbitalis	0.0102	[0.0067; 0.0135]	**0.0000**	**0.0000**
Rostral anterior cingulate	0.0079	[0.0047; 0.0113]	**0.0000**	**0.0000**
Entorhinal	0.0175	[0.0083; 0.0278]	**0.0006**	**0.0028**
Rostral middle frontal	0.0047	[0.0021; 0.0075]	**0.0010**	**0.0038**
Parahippocampal	0.0078	[0.0031; 0.0129]	**0.0020**	**0.0066**
Superior temporal	0.0095	[0.0035; 0.0161]	**0.0034**	**0.0098**
Pars triangularis	0.0045	[0.0014; 0.0076]	**0.0046**	**0.0118**
Temporal pole	0.0146	[0.0042; 0.0259]	**0.0052**	**0.0120**
Insula	0.0040	[0.0010; 0.0071]	**0.0142**	**0.0297**
Pars opercularis	0.0035	[0.0006; 0.0065]	**0.0220**	**0.0393**
Fusiform	0.0090	[0.0014; 0.0168]	**0.0222**	**0.0393**
Banks	0.0047	[-0.0001; 0.0096]	0.0552	0.0907
Lingual	0.0050	[-0.0002; 0.0106]	0.0600	0.0920
Transverse temporal	0.0049	[-0.0009; 0.0112]	0.1056	0.1518
Frontal pole	0.0064	[-0.0035; 0.0175]	0.1798	0.2433
Caudal anterior cingulate	0.0017	[-0.0009; 0.0043]	0.2236	0.2677
Lateral occipital	0.0041	[-0.0024; 0.0110]	0.2238	0.2677
Middle temporal	0.0044	[-0.0025; 0.0119]	0.2328	0.2677
Pericalcarine	0.0018	[-0.0039; 0.0080]	0.5506	0.6030
Inferior temporal	0.0017	[-0.0071; 0.0110]	0.7282	0.7613
Isthmus cingulate	-0.0003	[-0.0037; 0.0034]	0.8398	0.8398

Results from the bootstrapped (5,000 iterations) linear regression model showing the bootstrapped coefficient, the confidence interval (CI), the p-value before (p-value) and after correction for multiple comparisons (p-value$_{FDR}$) related to the interaction term. The 23 cortical regions included in the analysis are shown. Significant p-values are highlighted in bold. Age and sex are included as covariates in the model.

Table S14. Interactive associations of NDI in the LC and plasma GFAP on subcortical NDI

Subcortical region	Coefficient	CI	p-value	p-value$_{FDR}$
Putamen	0.0041	[-0.0003; 0.0084]	0.0660	0.1998
Caudate	0.0041	[-0.0003; 0.0083]	0.0666	0.1998
Thalamus	0.0020	[-0.0007; 0.0045]	0.1300	0.2600
Pallidum	0.0010	[-0.0040; 0.0061]	0.6940	0.8318
Amygdala	0.0002	[-0.0022; 0.0027]	0.8232	0.8318
Hippocampus	-0.0002	[-0.0021; 0.0016]	0.8318	0.8318

Results from the bootstrapped (5,000 iterations) linear regression model showing the bootstrapped coefficient, the confidence interval (CI), the p-value before (p-value) and after correction for multiple comparisons (p-value$_{FDR}$) related to the interaction term. The 6 subcortical regions included in the analysis are shown. Significant p-values are highlighted in bold. Age and sex are included as covariates in the model.

Table S15. Interactive associations of ODI in the LC and plasma GFAP on subcortical ODI

Subcortical region	Coefficient	CI	p-value	p-value$_{FDR}$
Hippocampus	0.0072	[0.0030; 0.0114]	**0.0006**	**0.0024**
Caudate	0.0086	[0.0037; 0.0138]	**0.0008**	**0.0024**
Amygdala	0.0084	[0.0033; 0.0139]	**0.0016**	**0.0032**
Putamen	0.0110	[0.0037; 0.0188]	**0.0052**	**0.0078**
Pallidum	0.0080	[0.0009; 0.0155]	**0.0216**	**0.0259**
Thalamus	0.0020	[0.0002; 0.0041]	**0.0356**	**0.0356**

Results from the bootstrapped (5,000 iterations) linear regression model showing the bootstrapped coefficient, the confidence interval (CI), the p-value before (p-value) and after correction for multiple comparisons (p-value$_{FDR}$) related to the interaction term. The 6 subcortical regions included in the analysis are shown. Significant p-values are highlighted in bold. Age and sex are included as covariates in the model.

Table S16. Interactive associations of LC intensity and plasma GFAP on cortical ODI

Cortical region	Coefficient	CI	p-value	$p\text{-value}_{FDR}$
Lateral orbitofrontal	-0.0064	[-0.0101; -0.0018]	**0.0202**	0.4646
Pars orbitalis	-0.0027	[-0.0051; -0.0001]	**0.0470**	0.5382
Isthmus cingulate	0.0017	[-0.0002; 0.0038]	0.0792	0.5382
Rostral anterior cingulate	-0.0020	[-0.0041; 0.0004]	0.0936	0.5382
Entorhinal	-0.0052	[-0.0112; 0.0027]	0.1248	0.5741
Temporal pole	-0.0051	[-0.0117; 0.0023]	0.1626	0.5947
Medial orbitofrontal	-0.0031	[-0.0074; 0.0020]	0.1810	0.5947
Superior temporal	-0.0018	[-0.0056; 0.0031]	0.3296	0.8864
Pericalcarine	0.0015	[-0.0019; 0.0051]	0.3940	0.8864
Caudal anterior cingulate	-0.0007	[-0.0024; 0.0009]	0.3988	0.8864
Parahippocampal	-0.0012	[-0.0042; 0.0024]	0.4274	0.8864
Pars opercularis	-0.0007	[-0.0025; 0.0012]	0.4644	0.8864
Frontal pole	0.0020	[-0.0035; 0.0094]	0.5010	0.8864
Transverse temporal	-0.0006	[-0.0042; 0.0035]	0.6920	0.9351
Pars triangularis	-0.0004	[-0.0024; 0.0017]	0.7274	0.9351
Rostral middle frontal	-0.0002	[-0.0020; 0.0017]	0.7610	0.9351
Insula	-0.0002	[-0.0021; 0.0021]	0.8112	0.9351
Inferior temporal	0.0007	[-0.0044; 0.0064]	0.8170	0.9351
Banks	-0.0003	[-0.0034; 0.0027]	0.8402	0.9351
Middle temporal	-0.0003	[-0.0045; 0.0045]	0.8470	0.9351
Fusiform	0.0005	[-0.0043; 0.0059]	0.8538	0.9351
Lingual	-0.0001	[-0.0032; 0.0034]	0.9274	0.9434
Lateral occipital	-0.0001	[-0.0039; 0.0042]	0.9434	0.9434

Results from the bootstrapped (5,000 iterations) linear regression model showing the bootstrapped coefficient, the confidence interval (CI), the p-value before (p-value) and after correction for multiple comparisons ($p\text{-value}_{FDR}$) related to the interaction term. The 23 cortical regions included in the analysis are shown. Significant p-values are highlighted in bold. Age and sex are included as covariates in the model.

Table S17. Interactive associations of LC intensity and plasma GFAP on subcortical ODI

Subcortical region	Coefficient	CI	p-value	$p\text{-value}_{FDR}$
Thalamus	-0.0008	[-0.0019; 0.0005]	0.1952	0.4425
Caudate	-0.0017	[-0.0049; 0.0017]	0.2750	0.4425
Hippocampus	-0.0014	[-0.0042; 0.0015]	0.2808	0.4425
Amygdala	-0.0018	[-0.0050; 0.0018]	0.2950	0.4425
Pallidum	0.0010	[-0.0035; 0.0063]	0.6862	0.8160
Putamen	-0.0005	[-0.0052; 0.0050]	0.8160	0.8160

Results from the bootstrapped (5,000 iterations) linear regression model showing the bootstrapped coefficient, the confidence interval (CI), the p-value before (p-value) and after correction for multiple comparisons ($p\text{-value}_{FDR}$) related to the interaction term. The 6 subcortical regions included in the analysis are shown. Significant p-values are highlighted in bold. Age and sex are included as covariates in the model.

Table S18. Sensitivity analysis: Interactive associations of NDI in the LC and plasma GFAP on cortical NDI, controlling for LC intensity

Cortical region	Coefficient	CI	p-value	p-value$_{LC}$	p-value$_{FDR}$	p-value$_{LC,FDR}$
Lateral occipital	-0.0028	[-0.0052; -0.0003]	**0.0256**	0.3226	0.3151	0.9392
Isthmus cingulate	-0.0018	[-0.0034; -0.0002]	**0.0274**	0.8984	0.3151	0.9392
Banks	-0.0018	[-0.0045; 0.0008]	0.1694	0.8980	0.7835	0.9392
Parahippocampal	-0.0018	[-0.0044; 0.0007]	0.1744	0.6012	0.7835	0.9392
Temporal pole	-0.0029	[-0.0074; 0.0017]	0.1976	0.0688	0.7835	0.9392
Pars orbitalis	0.0012	[-0.0006; 0.0032]	0.2044	0.7114	0.7835	0.9392
Inferior temporal	-0.0021	[-0.0058; 0.0016]	0.2570	0.8930	0.7886	0.9392
Transverse temporal	0.0017	[-0.0015; 0.0049]	0.2906	0.4276	0.7886	0.9392
Fusiform	-0.0017	[-0.0050; 0.0016]	0.3086	0.7634	0.7886	0.9392
Lingual	-0.0012	[-0.0038; 0.0014]	0.3856	0.7488	0.8306	0.9392
Caudal anterior cingulate	-0.0006	[-0.0022; 0.0010]	0.4936	0.7508	0.8306	0.9392
Entorhinal	-0.0015	[-0.0065; 0.0033]	0.5220	0.7698	0.8306	0.9392
Middle temporal	-0.0011	[-0.0047; 0.0025]	0.5404	0.5778	0.8306	0.9392
Superior temporal	-0.0008	[-0.0036; 0.0020]	0.5632	0.5150	0.8306	0.9392
Pericalcarine	-0.0008	[-0.0039; 0.0023]	0.6124	0.6090	0.8306	0.9392
Frontal pole	-0.0011	[-0.0055; 0.0035]	0.6360	0.7100	0.8306	0.9392
Rostral anterior cingulate	0.0004	[-0.0017; 0.0027]	0.6514	0.5042	0.8306	0.9392
Lateral orbitofrontal	0.0005	[-0.0021; 0.0032]	0.6926	0.7042	0.8306	0.9392
Pars triangularis	0.0003	[-0.0015; 0.0021]	0.7158	0.8942	0.8306	0.9392

Table S18. Continued

Cortical region	Coefficient	CI	p-value	$p\text{-value}_{LC}$	$p\text{-value}_{FDR}$	$p\text{-value}_{LC,FDR}$
Medial orbitofrontal	0.0003	[-0.0019; 0.0027]	0.7380	0.1680	0.8306	0.9392
Insula	-0.0003	[-0.0018; 0.0013]	0.7584	0.6028	0.8306	0.9392
Rostral middle frontal	0.0002	[-0.0015; 0.0020]	0.8010	0.6004	0.8374	0.9392
Pars opercularis	0.0000	[-0.0015; 0.0016]	0.9202	0.9804	0.9202	0.9804

Results from the bootstrapped (5,000 iterations) linear regression model showing the bootstrapped coefficient, the confidence interval (CI), the p-value before (p-value) and after correction for multiple comparisons ($p\text{-value}_{FDR}$) related to the interaction term, and the p-value before ($p\text{-value}_{LC}$) and after correction for multiple comparisons ($p\text{-value}_{LC,FDR}$) related to the main effect of LC intensity as covariate. The 23 cortical regions included in the analysis are shown. Significant p-values are highlighted in bold. Age, sex and LC intensity are included as covariates in the model.

Table S19. Sensitivity analysis: Interactive associations of ODI in the LC and plasma GFAP on cortical ODI, controlling for LC intensity

Cortical region	Coefficient	CI	p-value	p-value$_{LC}$	p-value$_{FDR}$	p-value$_{LC,FDR}$
Lateral orbitofrontal	0.0188	[0.0139; 0.0239]	**0.0000**	0.5494	**0.0000**	0.7972
Medial orbitofrontal	0.0153	[0.0088; 0.0220]	**0.0000**	0.2002	**0.0000**	0.7930
Pars orbitalis	0.0100	[0.0065; 0.0134]	**0.0000**	0.4482	**0.0000**	0.7930
Rostral anterior cingulate	0.0077	[0.0044; 0.0110]	**0.0000**	0.2740	**0.0000**	0.7930
Entorhinal	0.0181	[0.0086; 0.0288]	**0.0006**	0.4224	**0.0028**	0.7930
Rostral middle frontal	0.0046	[0.0019; 0.0074]	**0.0008**	0.5148	**0.0031**	0.7972
Superior temporal	0.0098	[0.0038; 0.0165]	**0.0022**	0.4250	**0.0069**	0.7930
Parahippocampal	0.0078	[0.0031; 0.0130]	**0.0024**	0.8166	**0.0069**	0.8980
Temporal pole	0.0162	[0.0059; 0.0275]	**0.0030**	**0.0384**	**0.0077**	0.6072
Pars triangularis	0.0044	[0.0012; 0.0075]	**0.0058**	0.6654	**0.0133**	0.8980
Insula	0.0041	[0.0010; 0.0072]	**0.0152**	0.7788	**0.0318**	0.8980
Banks	0.0054	[0.0007; 0.0101]	**0.0198**	0.0528	**0.0380**	0.6072
Pars opercularis	0.0036	[0.0006; 0.0066]	**0.0250**	0.8590	**0.0414**	0.8980
Fusiform	0.0090	[0.0011; 0.0170]	**0.0252**	0.9776	**0.0414**	0.9776
Lingual	0.0047	[-0.0006; 0.0103]	0.0912	0.3566	0.1398	0.7930
Transverse temporal	0.0050	[-0.0010; 0.0114]	0.1066	0.8494	0.1532	0.8980
Middle temporal	0.0048	[-0.0022; 0.0123]	0.1804	0.3628	0.2441	0.7930
Frontal pole	0.0058	[-0.0041; 0.0169]	0.2390	0.3668	0.2992	0.7930
Caudal anterior cingulate	0.0016	[-0.0010; 0.0043]	0.2472	0.7670	0.2992	0.8980

Table S19. Continued

Cortical region	Coefficient	CI	p-value	$p\text{-value}_{LC}$	$p\text{-value}_{FDR}$	$p\text{-value}_{LC,FDR}$
Lateral occipital	0.0036	[-0.0031; 0.0106]	0.2912	0.3086	0.3349	0.7930
Inferior temporal	0.0024	[-0.0064; 0.0115]	0.6150	0.2864	0.6593	0.7930
Pericalcarine	0.0014	[-0.0044; 0.0076]	0.6306	0.3852	0.6593	0.7930
Isthmus cingulate	-0.0004	[-0.0039; 0.0033]	0.7884	0.5546	0.7884	0.7972

Results from the bootstrapped (5,000 iterations) linear regression model showing the bootstrapped coefficient, the confidence interval (CI), the p-value before (p-value) and after correction for multiple comparisons ($p\text{-value}_{FDR}$) related to the interaction term, and the p-value before ($p\text{-value}_{LC}$) and after correction for multiple comparisons ($p\text{-value}_{LC,FDR}$) related to the main effect of LC intensity as covariate. The 23 cortical regions included in the analysis are shown. Significant p-values are highlighted in bold. Age, sex and LC intensity are included as covariates in the model.

Table S20. Sensitivity analysis: Interactive associations of NDI in the LC and plasma GFAP on subcortical NDI, controlling for LC intensity

Subcortical region	Coefficient	CI	p-value	p-value$_{LC}$	p-value$_{FDR}$	p-value$_{LC,FDR}$
Putamen	0.0037	[-0.0008; 0.0081]	0.1046	0.3188	0.3216	0.6472
Caudate	0.0036	[-0.0008; 0.0079]	0.1072	0.1818	0.3216	0.6472
Thalamus	0.0019	[-0.0008; 0.0045]	0.1678	0.6688	0.3356	0.9772
Pallidum	0.0010	[-0.0041; 0.0062]	0.6940	0.9080	0.9550	0.9772
Hippocampus	-0.0002	[-0.0021; 0.0017]	0.8330	0.9772	0.9550	0.9772
Amygdala	0.0001	[-0.0025; 0.0024]	0.9550	0.3236	0.9550	0.6472

Results from the bootstrapped (5,000 iterations) linear regression model showing the bootstrapped coefficient, the confidence interval (CI), the p-value before (p-value) and after correction for multiple comparisons (p-value$_{FDR}$) related to the interaction term, and the p-value before (p-value$_{LC}$) and after correction for multiple comparisons (p-value$_{LC, FDR}$) related to the main effect of LC intensity as covariate. The 6 subcortical regions included in the analysis are shown. Significant p-values are highlighted in bold. Age, sex and LC intensity are included as covariates in the model.

Table S21. Sensitivity analysis: Interactive associations of ODI in the LC and plasma GFAP on subcortical ODI, controlling for LC intensity

Subcortical region	Coefficient	CI	p-value	$p\text{-value}_{LC}$	$p\text{-value}_{FDR}$	$p\text{-value}_{LC,FDR}$
Hippocampus	0.0073	[0.0030; 0.0116]	**0.0010**	0.6784	**0.0042**	0.9934
Caudate	0.0085	[0.0036; 0.0138]	**0.0014**	0.7838	**0.0042**	0.9934
Amygdala	0.0082	[0.0030; 0.0138]	**0.0028**	0.6988	**0.0056**	0.9934
Putamen	0.0111	[0.0036; 0.0191]	**0.0058**	0.9506	**0.0087**	0.9934
Pallidum	0.0080	[0.0007; 0.0155]	**0.0286**	0.9934	**0.0343**	0.9934
Thalamus	0.0020	[0.0000; 0.0041]	**0.0452**	0.6836	**0.0452**	0.9934

Results from the bootstrapped (5,000 iterations) linear regression model showing the bootstrapped coefficient, the confidence interval (CI), the p-value before (p-value) and after correction for multiple comparisons ($p\text{-value}_{FDR}$) related to the interaction term, and the p-value before ($p\text{-value}_{LC}$) and after correction for multiple comparisons ($p\text{-value}_{LC,FDR}$) related to the main effect of LC intensity as covariate. The 6 subcortical regions included in the analysis are shown. Significant p-values are highlighted in bold. Age, sex and LC intensity are included as covariates in the model.

Table S22. Sensitivity analysis: Interactive associations of NDI in the LC and plasma GFAP on cortical NDI, controlling for *APOE* ε4 status

Cortical region	Coefficient	CI	p-value	p-value$_{\varepsilon 4}$	p-value$_{FDR}$	p-value$_{\varepsilon 4,FDR}$
Isthmus cingulate	-0.0018	[-0.0034; -0.0002]	**0.0242**	0.8874	0.2898	0.9324
Lateral occipital	-0.0028	[-0.0051; -0.0003]	**0.0252**	0.2502	0.2898	0.9210
Pars orbitalis	0.0014	[-0.0004; 0.0033]	0.1250	0.1324	0.7215	0.8384
Temporal pole	-0.0034	[-0.0080; 0.0011]	0.1380	0.7176	0.7215	0.9210
Parahippocampal	-0.0017	[-0.0042; 0.0008]	0.1992	0.8324	0.7215	0.9324
Banks	-0.0016	[-0.0041; 0.0010]	0.2096	0.1458	0.7215	0.8384
Inferior temporal	-0.0019	[-0.0055; 0.0017]	0.2964	0.4426	0.7215	0.9210
Transverse temporal	0.0016	[-0.0015; 0.0048]	0.3158	0.6048	0.7215	0.9210
Fusiform	-0.0015	[-0.0047; 0.0016]	0.3396	0.5312	0.7215	0.9210
Lingual	-0.0012	[-0.0037; 0.0014]	0.3910	0.7638	0.7215	0.9246
Entorhinal	-0.0018	[-0.0067; 0.0030]	0.4320	0.5280	0.7215	0.9210
Caudal anterior cingulate	-0.0006	[-0.0021; 0.0010]	0.4738	0.7208	0.7215	0.9210
Middle temporal	-0.0012	[-0.0047; 0.0024]	0.4878	0.7184	0.7215	0.9210
Superior temporal	-0.0009	[-0.0036; 0.0019]	0.5308	0.5636	0.7215	0.9210
Pars triangularis	0.0005	[-0.0012; 0.0022]	0.5616	0.1078	0.7215	0.8384
Lateral orbitofrontal	0.0007	[-0.0019; 0.0034]	0.5706	0.3510	0.7215	0.9210
Rostral anterior cingulate	0.0005	[-0.0016; 0.0028]	0.5936	0.6818	0.7215	0.9210

Table S22. Continued

Cortical region	Coefficient	CI	p-value	p-value$_{\varepsilon4}$	p-value$_{FDR}$	p-value$_{\varepsilon4,FDR}$
Medial orbitofrontal	0.0005	[-0.0017; 0.0029]	0.5954	0.9170	0.7215	0.9324
Frontal pole	-0.0012	[-0.0054; 0.0034]	0.5960	0.3446	0.7215	0.9210
Pericalcarine	-0.0007	[-0.0037; 0.0024]	0.6598	0.9324	0.7588	0.9324
Pars opercularis	0.0002	[-0.0013; 0.0017]	0.7582	0.0510	0.7894	0.8384
Insula	-0.0003	[-0.0018; 0.0013]	0.7598	0.4228	0.7894	0.9210
Rostral middle frontal	0.0002	[-0.0015; 0.0020]	0.7894	0.3204	0.7894	0.9210

Results from the bootstrapped (5,000 iterations) linear regression model showing the bootstrapped coefficient, the confidence interval (CI), the p-value before (p-value) and after correction for multiple comparisons (p-value$_{FDR}$) related to the interaction term, and the p-value before (p-value$_{\varepsilon4}$) and after correction for multiple comparisons (p-value$_{\varepsilon4,FDR}$) related to the main effect of *APOE* ε4 as covariate. The 23 cortical regions included in the analysis are shown. Significant p-values are highlighted in bold. Age, sex and *APOE* ε4 carriership are included as covariates in the model.

Table S23. Sensitivity analysis: Interactive associations of ODI in the LC and plasma GFAP on cortical ODI, controlling for *APOE* ε4 status

Cortical region	Coefficient	CI	p-value	p-value$_{\varepsilon 4}$	p-value$_{FDR}$	p-value$_{\varepsilon 4,FDR}$
Entorhinal	0.0179	[0.0088; 0.0283]	**0.0000**	0.3140	**0.0000**	0.7208
Lateral orbitofrontal	0.0187	[0.0139; 0.0239]	**0.0000**	0.4102	**0.0000**	0.7208
Medial orbitofrontal	0.0160	[0.0096; 0.0229]	**0.0000**	0.6268	**0.0000**	0.7208
Pars orbitalis	0.0104	[0.0070; 0.0137]	**0.0000**	0.1022	**0.0000**	0.7208
Rostral anterior cingulate	0.0080	[0.0048; 0.0114]	**0.0000**	0.6070	**0.0000**	0.7208
Rostral middle frontal	0.0048	[0.0021; 0.0076]	**0.0000**	0.4510	**0.0000**	0.7208
Parahippocampal	0.0078	[0.0031; 0.0129]	**0.0018**	0.7788	**0.0059**	0.8142
Superior temporal	0.0097	[0.0037; 0.0161]	**0.0022**	0.2672	**0.0063**	0.7208
Pars triangularis	0.0046	[0.0015; 0.0077]	**0.0030**	0.1318	**0.0077**	0.7208
Temporal pole	0.0152	[0.0046; 0.0262]	**0.0048**	0.1554	**0.0110**	0.7208
Pars opercularis	0.0037	[0.0008; 0.0066]	**0.0132**	0.1088	**0.0276**	0.7208
Insula	0.0041	[0.0010; 0.0072]	**0.0154**	0.6192	**0.0295**	0.7208
Fusiform	0.0091	[0.0013; 0.0170]	**0.0200**	0.7334	**0.0354**	0.8032
Banks	0.0048	[-0.0001; 0.0097]	0.0532	0.5738	0.0874	0.7208
Lingual	0.0049	[-0.0004; 0.0106]	0.0720	0.5950	0.1104	0.7208
Transverse temporal	0.0051	[-0.0007; 0.0114]	0.0848	0.3206	0.1219	0.7208
Frontal pole	0.0067	[-0.0031; 0.0182]	0.1588	0.4120	0.2148	0.7208

Table S23. Continued

Cortical region	Coefficient	CI	p-value	p-value$_{\varepsilon4}$	p-value$_{FDR}$	p-value$_{\varepsilon4,FDR}$
Caudal anterior cingulate	0.0018	[-0.0008; 0.0044]	0.1866	0.2590	0.2370	0.7208
Middle temporal	0.0046	[-0.0022; 0.0121]	0.1958	0.3430	0.2370	0.7208
Lateral occipital	0.0039	[-0.0026; 0.0109]	0.2490	0.4826	0.2864	0.7208
Pericalcarine	0.0017	[-0.0041; 0.0078]	0.5918	0.5264	0.6482	0.7208
Inferior temporal	0.0017	[-0.0072; 0.0110]	0.7352	0.9942	0.7686	0.9942
Isthmus cingulate	-0.0002	[-0.0035; 0.0035]	0.9016	0.4032	0.9016	0.7208

Results from the bootstrapped (5,000 iterations) linear regression model showing the bootstrapped coefficient, the confidence interval (CI), the p-value before (p-value) and after correction for multiple comparisons (p-value$_{FDR}$) related to the interaction term, and the p-value before (p-value$_{\varepsilon4}$) and after correction for multiple comparisons (p-value$_{\varepsilon4,FDR}$) related to the main effect of *APOE* ε4 as covariate. The 23 cortical regions included in the analysis are shown. Significant p-values are highlighted in bold. Age, sex and *APOE* ε4 carriership are included as covariates in the model.

Table S24. Sensitivity analysis: Interactive associations of NDI in the LC and plasma GFAP on subcortical NDI, controlling for *APOE* ε4 status

Subcortical region	Coefficient	CI	p-value	p-value$_{\varepsilon 4}$	p-value$_{FDR}$	p-value$_{\varepsilon 4,FDR}$
Putamen	0.0045	[0.0001; 0.0088]	**0.0450**	0.1108	0.1524	0.3324
Caudate	0.0044	[0.0000; 0.0086]	0.0508	0.1996	0.1524	0.3681
Thalamus	0.0022	[-0.0004; 0.0047]	0.1004	0.1106	0.2008	0.3324
Pallidum	0.0009	[-0.0041; 0.0061]	0.7020	0.8596	0.9304	0.8596
Amygdala	0.0003	[-0.0022; 0.0027]	0.8012	0.7498	0.9304	0.8596
Hippocampus	-0.0001	[-0.0020; 0.0018]	0.9304	0.2454	0.9304	0.3681

Results from the bootstrapped (5,000 iterations) linear regression model showing the bootstrapped coefficient, the confidence interval (CI), the p-value before (p-value) and after correction for multiple comparisons (p-value$_{FDR}$) related to the interaction term, and the p-value before (p-value$_{\varepsilon 4}$) and after correction for multiple comparisons (p-value$_{\varepsilon 4,FDR}$) related to the main effect of *APOE* ε4 as covariate. The 6 subcortical regions included in the analysis are shown. Significant p-values are highlighted in bold. Age, sex and *APOE* ε4 carriership are included as covariates in the model.

Table S25. Sensitivity analysis: Interactive associations of ODI in the LC and plasma GFAP on subcortical ODI, controlling for *APOE* ε4 status

Subcortical region	Coefficient	CI	p-value	p-value$_{\varepsilon4}$	p-value$_{FDR}$	p-value$_{\varepsilon4,FDR}$
Hippocampus	0.0073	[0.0031; 0.0115]	**0.0000**	0.4128	**0.0000**	0.6413
Amygdala	0.0086	[0.0036; 0.0140]	**0.0012**	0.3156	**0.0028**	0.6413
Caudate	0.0085	[0.0036; 0.0137]	**0.0014**	0.7336	**0.0028**	0.7336
Putamen	0.0108	[0.0034; 0.0187]	**0.0070**	0.4492	**0.0105**	0.6413
Pallidum	0.0078	[0.0007; 0.0153]	**0.0284**	0.5344	**0.0341**	0.6413
Thalamus	0.0020	[0.0001; 0.0040]	**0.0424**	0.2918	**0.0424**	0.6413

Results from the bootstrapped (5,000 iterations) linear regression model showing the bootstrapped coefficient, the confidence interval (CI), the p-value before (p-value) and after correction for multiple comparisons (p-value$_{FDR}$) related to the interaction term, and the p-value before (p-value$_{\varepsilon4}$) and after correction for multiple comparisons (p-value$_{\varepsilon4,FDR}$) related to the main effect of *APOE* ε4 as covariate. The 6 subcortical regions included in the analysis are shown. Significant p-values are highlighted in bold. Age, sex and *APOE* ε4 carriership are included as covariates in the model.

Table S26. Main and interactive associations of imaging metrics and GFAP on PACC performance

	Coefficient	CI	p-value
NDI_{LC}	-0.9171	[-3.4869; 1.5706]	0.4662
ODI_{LC}	-0.4685	[-5.5337; 4.2323]	0.8558
NDI_{cortex}	7.9236	[1.7810; 14.5268]	**0.0092**
ODI_{cortex}	4.6106	[-0.0034; 9.6285]	0.0504
$NDI_{subcortex}$	6.9828	[2.9976; 11.0061]	**0.0012**
$ODI_{subcortex}$	5.0346	[1.0970; 9.1505]	**0.0164**
$LC_{intensity}$	0.4440	[-3.5274; 4.2930]	0.8424
GFAP	-0.0022	[-0.0048; 0.0003]	0.0936
NDI_{LC} x GFAP	0.0047	[-0.0423; 0.0499]	0.8478
ODI_{LC} x GFAP	-0.0005	[-0.0789; 0.0799]	0.9822
NDI_{cortex} x GFAP	-0.0214	[-0.0875; 0.0526]	0.5290
ODI_{cortex} x GFAP	0.0001	[-0.0414; 0.0451]	0.9730
$NDI_{subcortex}$ x GFAP	0.0073	[-0.0357; 0.0543]	0.7724
$ODI_{subcortex}$ x GFAP	-0.0034	[-0.0373; 0.0316]	0.8256

Results from the bootstrapped (5,000 iterations) linear regression models showing the bootstrapped coefficient, the confidence interval (CI), the p-value (p-value) related to the main and interactive relationships between imaging metrics (LC intensity, cortical, subcortical and LC NODDI metrics) and plasma GFAP in association with PACC performance, controlling for age, sex and education. Cortical and subcortical NODDI parameters are respectively calculated as the average of NODDI values in the 23 cortical and the 6 subcortical regions included in the analysis. PACC = preclinical Alzheimer's cognitive composite.

REFERENCES

1. Dahl MJ, et al. Locus coeruleus integrity is related to tau burden and memory loss in autosomal-dominant Alzheimer's disease. *Neurobiol Aging*. 2022;112:39-54.

Chapter 3

Sparse asymmetry in locus coeruleus pathology in Alzheimer's disease

Elise Beckers
Joost M Riphagen
Maxime Van Egroo
David A Bennett
Heidi IL Jacobs

Published in Journal of Alzheimer's Disease, 2024

ABSTRACT

Tau accumulation in and neurodegeneration of locus coeruleus (LC) neurons is observed in Alzheimer's disease (AD). We investigated whether tangle and neuronal density in the rostral and caudal LC is characterized by an asymmetric pattern in 77 autopsy cases of the Rush Memory and Aging Project. We found left-right equivalence for tangle density across individuals with and without AD pathology. However, neuronal density, particularly in the caudal-rostral axis of the LC, is asymmetric among individuals with AD pathology. Asymmetry in LC neuronal density may signal advanced disease progression and should be considered in AD neuroimaging studies of LC neurodegeneration.

INTRODUCTION

Findings from autopsy and imaging studies established that the locus coeruleus (LC) accumulates hyperphosphorylated tau and undergoes morphological changes early in Alzheimer's disease (AD) progression, supporting a critical role for the LC in early detection of AD [1-4]. Even though, the LC modulates many cognitive functions and behaviors, including those affected in AD [5], the evidence regarding potential asymmetry in LC pathology remains ambiguous as autopsy studies often examine only one side of the brain. Immunohistochemistry studies report no morphological asymmetry in LC shape or length in clinically normal cases [6], but reported length differences up to 15.2% in AD cases [7]. Similarly, the count of LC neurons is overall symmetric [8, 9], but neuronal loss becomes more asymmetric in AD (left-right differences in neuronal count up to 8% in clinically normal and 17% in AD; Figure 1) [7]. Neuronal degeneration occurs as the disease progresses, but importantly, are preceded by accumulation of hyperphosphorylated tau. Beyond the anecdotal report of Braak and Del Tredici (2015) that an asymmetrical pattern of abnormal tau inclusions is seldom observed [10], no quantitative data on (a)symmetry of tau in the LC in AD is available. Recently developed MRI-based measures of LC integrity presumably reflect neuronal density and tangle-related processes [3, 11]. In asymptomatic individuals the left LC exhibited higher integrity values than the right [12-14], but inconsistencies exist in the AD neuroimaging literature, ranging from higher right dorsal LC integrity [12], to no left-right differences [15]. Thus, understanding patterns of pathology in the LC will facilitate the interpretation of MRI-based LC findings during AD progression [3], and contribute to understanding disease heterogeneity, contralateral functional compensation [16], and neuroanatomical correlates underlying resilience [17] or correlations with specific behavioral outcomes. Leveraging the neuropathologic data from the Rush Memory and Aging Project (MAP), we set out to determine whether asymmetry in LC tangle or neuronal density was present in older individuals with and without evidence of AD pathology.

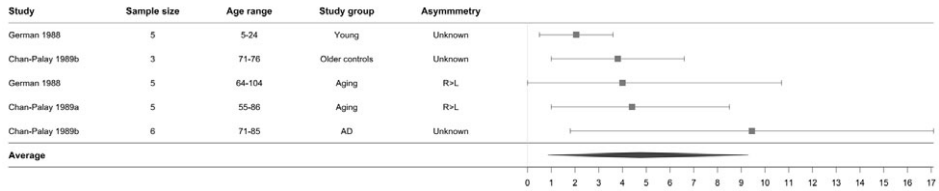

Figure 1. Overview of asymmetry in locus coeruleus in neuronal count in autopsy studies. Visualization of the reported left-right differences in neuronal count in the LC in autopsy studies [7-9]. The square indicates the mean percentage left-right difference in neuronal count with the bars representing the minimum and maximum reported percentage asymmetry in neuronal count of the LC. The diamond provides the average of all studies (4.74%, range: 0.86% - 9.30%). Unknown asymmetry means that percentage difference in asymmetry was reported without providing the directionality. The reference of Chan-Palay 1989a refers to [8], while Chan-Palay 1989b refers to [7].

METHODS

Participants

The dataset included 77 older participants from the Rush Memory and Aging Project (MAP), a clinical-pathologic observational cohort that started in 1997 [18]. Eligibility criteria included older age, absence of a previous dementia diagnosis and consent to annual clinical evaluation and brain autopsy at death. This sample included individuals for whom detailed LC neuropathology data was available and consisted of individuals with no cognitive impairment (N = 29), mild cognitive impairment (N = 27) or AD dementia (N = 21). At time of death, select clinical data (cognitive history, neuropsychological evaluation and clinical judgment) was reviewed by a neurologist, blinded to post-mortem data, who provided a clinical diagnosis based on the National Institute of Neurological and Communicative Disorders and Stroke and the AD and Related Disorders Association (NINCDS/ADRDA) criteria [19-21]. The average time between the last visit and death was 0.77 years (SD = 0.60). All data were de-identified and shared with a Data User Agreement. The study was approved by an Institutional Review Board of Rush University Medical Center. All participants signed an

informed consent, an Anatomical Gift Act, and a repository consent which allowed their data to be shared.

Neuropathological measures

Neuronal density (per mm^2) and paired helical filaments (PHF) tau tangle density of the LC were examined using immunohistochemistry with a monoclonal anti-tyrosine hydroxylase antibody and an anti-PHF tau antibody AT8, respectively, each at the left or right side of the pons and two levels of the LC, rostral and caudal [22-24]. In addition, tangle density was divided by neuronal density and expressed as percentage. We selected participants who had neuropathologic data on both sides of the LC and both sections (N = 77). Using available information on cortical neurofibrillary tangles (Braak) and neuritic plaques (CERAD), the likelihood of AD pathology was identified according to the modified National Institute of Aging (NIA)-Reagan diagnosis of AD and grouped into not present (no or low likelihood) and present (intermediate or high likelihood). This evaluation was performed independent of clinical information [21].

Statistical analyses

Statistical analyses were performed in R (version 4.1.2, http://www.r-project.org/). Group characteristics are represented in mean and standard deviation or proportion. Asymmetry in tangle density, neuronal density or relative tangle density were related to age, post-mortem interval and sex with repeated measures ANOVA interacting the relevant variable with the within-factor (hemisphere), including Greenhouse-Geiser correction. Asymmetry in LC pathology measures was tested with paired t-tests per LC section (False-Discovery Rate adjustment at $\alpha = 0.05$ per section) and if non-significant, followed up with the bootstrapped two one-sided test (TOST) procedure for pairwise comparisons (5,000 bootstrap replicates) at $\alpha = 0.05$. Given that absence of asymmetry evidence (non-significance) does not equate evidence of symmetry, the TOST evaluates whether left and right differences in LC pathology can be considered statistically equivalent to zero or below the smallest effect meaningful for asymmetry (Supplementary Figure 1, [25]). Because of the lack of literature on left-right meaningful differences in LC

pathology, we tested left-right differences iteratively across a range of values to detect the highest bound at which equivalence was no longer met: 1 to 10 tangles, 1 to 77 neurons per mm^2, and 1 to 30% relative difference. Upper limit of the asymmetry equivalence bound was determined by the maximum observed difference for that measure. Tests for asymmetry were performed for the entire LC and for rostral and caudal sections. We then assessed whether left-right asymmetry was equivalent between rostral and caudal LC sections using repeated measures ANOVA with two levels (hemisphere and section) with Greenhouse-Geiser and Tukey-adjustment. If non-significant, these analyses were followed up by the TOST. Sensitivity analyses tested asymmetry differences within individuals with and without evidence of AD pathology (NIA-Reagan diagnosis of AD).

RESULTS

The average age at death was 88.6 years (range 74.8 – 99.7), and participants were highly educated, with the majority being female (72%) and 13% carrying one or more *APOE* ε4 alleles (Table 1).

Table 1. Demographics

		MAP (N = 77)
Age at death (years)		88.59 (5.84)
	Range	74.83 – 99.67
Sex (F; n, %)		56 (72.27%)
Education (years)		14.44 (2.66)
Post-mortem interval (hours)		7.09 (3.88)
***APOE* ε4 (n, %)**		10 (12.99%)
Diagnosis (n, %)	*CN*	29 (37.66%)
	MCI	27 (35.07%)
	AD	21 (27.27%)
AD-Reagan diagnosis of AD (n, %)	*No to low*	30 (38.96%)
	Intermediate to high	47 (61.04%)
LC tangle density	*Left*	3.48 (3.39)
	Right	3.82 (3.73)
LC neuronal density	*Left*	77.11 (25.02)
	Right	75.53 (23.99)

Demographics are provided in mean and standard deviation for continuous variables, or as proportion for categorical variables. AD = Alzheimer's disease, *APOE* = Apolipoprotein E, LC = locus coeruleus, CN = control, MCI = mild cognitive impairment.

Left-right differences in LC pathology measures were not associated with age, post-mortem interval, or sex (Supplementary Table 1). There was no difference between left and right LC in terms of tangle density, neuronal density, or relative tangle density for the entire LC, the rostral or caudal sections (Supplementary Table 2 for statistical details). Sensitivity analyses revealed no differences in LC measures for individuals with or without evidence of underlying AD pathology, except for an at trend-level asymmetry in caudal LC neuronal density in individuals with AD pathology (on average 7.32 fewer neurons per mm^2 in the right caudal LC (mean difference: 7.32, $t_{46} = 2.24$, $p = 0.03$, $p_{FDR} = 0.09$); Figure 2, Supplementary Table 2). Based on the literature (Figure 1), >9.30% difference between left and right would represent an above average asymmetry in older individuals and AD patients, which translates to an asymmetry difference of about 7 neurons per mm^2; 74.47% of the individuals with AD pathology exhibited a left-right difference of at least 7.32 neurons per mm^2. TOST-evaluation indicated that rostral tangle density asymmetry was no longer equivalent at [-1,1] tangle density. For the neuronal density, left

and right was not equivalent at [-5,5] for the entire LC, [-6,6] for the rostral LC and [-9,9] for the caudal LC. For relative tangle density, the null hypothesis of equivalence was rejected at [-1%, 1%] for the entire LC and [-2%, 2%] for the rostral LC (Supplementary Figure 2). Equivalence bounds for the entire LC and its sections were similar for both the group with and without evidence of underlying AD pathology. These results provide evidence for equivalence (no asymmetry) in LC pathology, except for the caudal neuronal density where the effect exceeded the smallest meaningful difference of 7 neurons per mm^2.

While the neuroimaging literature reported inconsistencies in rostro-caudal asymmetry, we found no evidence for asymmetry in LC pathology between rostral and caudal sections for the entire sample and among individuals with and without AD pathology (Supplementary Table 3), except for a lower neuronal density in the right caudal than left caudal LC section among individuals with AD pathology, relative to the rostral LC ($p_{Tukey} = 0.03$, Supplementary Figure 3). The TOST (Supplementary Figure 4) showed left-right equivalence across rostro-dorsal sections for LC tangle density up to [-1,1] and relative tangle density, up to [-3%, 3%]. Equivalence bounds of left-right differences in neuronal density across rostro-caudal sections exceeded the smallest meaningful difference and varied between [-11,11] (entire sample) and [-19,19] (with AD pathology), indicative of asymmetry as also supported by the repeated measures ANOVA.

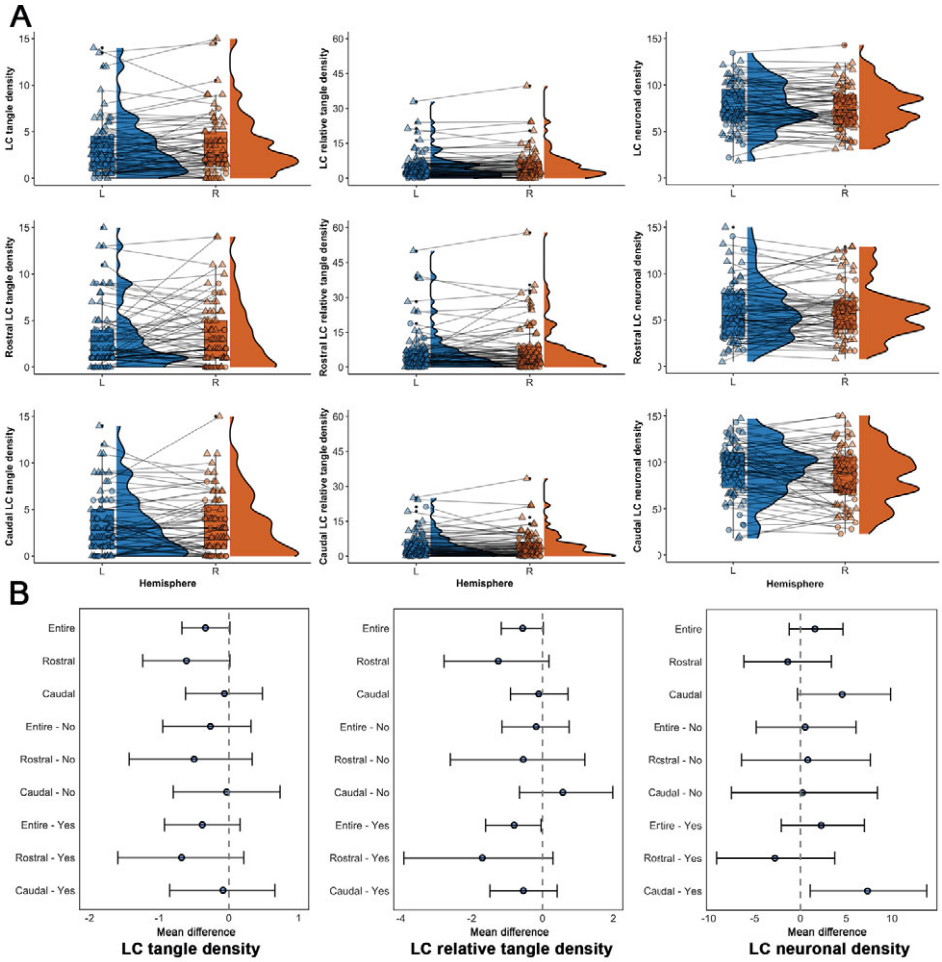

Figure 2. Distribution and effect sizes of left-right differences in the LC measures. **A)** Boxplots (with median and interquartile range indicated with the horizontal line and bars) and distributions (half violin) depicting the left and right distribution of the LC pathology measures (tangle density, relative tangle density, neuronal density) across the entire LC and its rostral and caudal sections. Triangle shapes indicate individuals with underlying AD pathology according to the NIA-Reagan criteria, whereas circles are those individuals without evidence. **B)** Mean difference in asymmetry (left-right) for every pathology measure, LC section and group (Yes: evidence of underlying AD pathology; No: no evidence of underlying AD pathology). Error bars represent the 95% confidence intervals (Bootstrapped at 5,000 replicates; α = 0.05).

DISCUSSION

Neuropathology studies reported LC neurodegeneration during the course of AD, with modestly increasing asymmetry relative to neurologically healthy individuals [7-9]. Because accumulation of hyperphosphorylated tau in the LC emerges early in adulthood and starts two to three decades prior to neuronal changes [1], the LC has become an important target for early detection of AD, motivating the development of in vivo neuroimaging methods of LC integrity [3]. These neuroimaging-based LC metrics covary with tau pathology measured with PET-imaging or blood-based markers [3, 24]. Despite the LC's early involvement in AD and its critical role in modulating cognition and behavior [3, 5], the clinical relevance of potential asymmetry in LC measures remains unknown. We addressed this gap of knowledge by determining if asymmetry of pathology occurs in the LC across different disease stages, as this will inform the granularity of planned analytical approaches, the interpretation of MRI-based LC findings during AD progression and in the context of clinical heterogeneity. We found that the amount of tangle density as well as relative tangle density were equivalent in the left and right LC, both when considering the rostral or caudal sections separately or when analyzing individuals with or without evidence of underlying AD pathology. However, considering the range of reported percent differences in neuronal count in AD [7], our results indicate that the left versus right neuronal density in the caudal LC is different from the pattern of neuronal density in the rostral LC among individuals with underlying AD pathology.

Interestingly, the caudal LC contains very tightly clustered cells, but relatively fewer large multipolar cells compared to the rostral LC, which consists of a scattered pattern of both large and small cells. During disease progression, the small, fusiform cells in the dorsal-middle LC are most vulnerable to accumulate tau and show neurodegeneration from Braak stage III-IV [1, 7]. Our data indicates that in older individuals in whom the downstream effects of tau may have been unfolding over several decades, particularly in rostral-middle sections, a more symmetrical pattern of rostral neurodegeneration can be observed. We speculate that as the disease progresses, cells in the caudal section degenerate and become more dispersed. Caudal asymmetry

in neuronal degeneration (relative to rostral) may thus signal progression to a more advanced disease stage (above Braak stage IV and Thal stage 3) and possibly correspond to late-stage symptoms including motor-related or autonomic dysfunctions – reflective of its projections to the cerebellum and spinal cord affected earlier in Parkinson's disease [7, 26]. This does not preclude potential asymmetry in neuronal degeneration of the rostral part earlier in life. We were not able to examine this hypothesis, as the age range in this cohort is older than what is typical for observational studies. An older age range is inherent to autopsy studies but can introduce survival biases and limit the generalizability of our findings to younger populations who likely harbor tau pathology in the LC. In addition to examining a broader age span, it would be valuable for future studies to use more comprehensive methods such as unbiased stereological evaluations, relate asymmetries in neuronal density to symptoms and loss of projection density to cortical target regions [27], and to examine if asymmetry in other read-outs of LC function relate to pathologic asymmetry of the LC [28].

Imaging the LC in vivo is feasible with dedicated procedures [3, 29, 30], but often the LC seems shorter in length than what is observed in neuropathology studies. This is most likely because the LC's cylindrical shape widens along the caudal direction resulting in worse caudal signal-to-noise ratio [6]. The findings of this study hold important implications for in vivo imaging studies, as they suggest that in individuals with advanced underlying AD pathologic change neurodegenerative measures of the LC should be investigated in detail, preferably considering both sides separately and examining different sections of the LC. In contrast, our null-findings indicate that tau-related measures may not require this level of detail, facilitating clinical translation of these markers.

REFERENCES

1. Ehrenberg AJ, et al. Quantifying the accretion of hyperphosphorylated tau in the locus coeruleus and dorsal raphe nucleus: the pathological building blocks of early Alzheimer's disease. *Neuropathol Appl Neurobiol*. 2017;43(5):393-408.
2. Theofilas P, et al. Locus coeruleus volume and cell population changes during Alzheimer's disease progression: A stereological study in human postmortem brains with potential implication for early-stage biomarker discovery. *Alzheimers Dement*. 2017;13(3):236-46.
3. Jacobs HIL, et al. In vivo and neuropathology data support locus coeruleus integrity as indicator of Alzheimer's disease pathology and cognitive decline. *Sci Transl Med*. 2021;13(612):eabj2511.
4. Jacobs HIL, et al. Waning locus coeruleus integrity precedes cortical tau accrual in preclinical autosomal dominant Alzheimer's disease. *Alzheimers Dement*. 2023;19(1):169-80.
5. Ehrenberg AJ, et al. Priorities for research on neuromodulatory subcortical systems in Alzheimer's disease: Position paper from the NSS PIA of ISTAART. *Alzheimers Dement*. 2023;19(5):2182-96.
6. Fernandes P, et al. The human locus coeruleus 3-D stereotactic anatomy. *Surg Radiol Anat*. 2012;34(10):879-85.
7. Chan-Palay V and Asan E. Alterations in catecholamine neurons of the locus coeruleus in senile dementia of the Alzheimer type and in Parkinson's disease with and without dementia and depression. *J Comp Neurol*. 1989;287(3):373-92.
8. Chan-Palay V and Asan E. Quantitation of catecholamine neurons in the locus coeruleus in human brains of normal young and older adults and in depression. *J Comp Neurol*. 1989;287(3):357-72.
9. German DC, et al. The human locus coeruleus: computer reconstruction of cellular distribution. *J Neurosci*. 1988;8(5):1776-88.
10. Braak H and Del Tredici K. Neuroanatomy and pathology of sporadic Alzheimer's disease. Böckers TM, Clascá F, Kmiec Z, Singh B, Sutovsky P, Timmermans JP, editors. Switzerland: Springer International Publishing; 2015.
11. Engels-Domínguez N, et al. State-of-the-art imaging of neuromodulatory subcortical systems in aging and Alzheimer's disease: Challenges and opportunities. *Neurosci Biobehav Rev*. 2023;144:104998.
12. Betts MJ, et al. In vivo MRI assessment of the human locus coeruleus along its rostrocaudal extent in young and older adults. *Neuroimage*. 2017;163:150-9.
13. Dahl MJ, et al. Higher rostral locus coeruleus density is associated with better memory performance in older adults. *Nature Human Behaviour*. 2019.
14. Elman JA, et al. MRI-assessed locus coeruleus integrity is heritable and associated with multiple cognitive domains, mild cognitive impairment, and daytime dysfunction. *Alzheimers Dement*. 2021;17(6):1017-25.
15. Cassidy CM, et al. Association of locus coeruleus integrity with Braak stage and neuropsychiatric symptom severity in Alzheimer's disease. *Neuropsychopharmacology*. 2022;47(5):1128-36.

16. Jacobs HI, et al. Relevance of parahippocampal-locus coeruleus connectivity to memory in early dementia. *Neurobiol Aging*. 2015;36(2):618-26.

17. Mather M and Harley CW. The Locus Coeruleus: Essential for Maintaining Cognitive Function and the Aging Brain. *Trends Cogn Sci*. 2016;20(3):214-26.

18. Bennett DA, et al. Religious Orders Study and Rush Memory and Aging Project. *J Alzheimers Dis*. 2018;64(s1):S161-S89.

19. Bennett DA, et al. Decision rules guiding the clinical diagnosis of Alzheimer's disease in two community-based cohort studies compared to standard practice in a clinic-based cohort study. *Neuroepidemiology*. 2006;27(3):169-76.

20. Bennett DA, et al. Natural history of mild cognitive impairment in older persons. *Neurology*. 2002;59(2):198-205.

21. Bennett DA, et al. Neuropathology of older persons without cognitive impairment from two community-based studies. *Neurology*. 2006;66(12):1837-44.

22. Buchman AS, et al. Locus coeruleus neuron density and parkinsonism in older adults without Parkinson's disease. *Mov Disord*. 2012;27(13):1625-31.

23. Wilson RS, et al. Neural reserve, neuronal density in the locus ceruleus, and cognitive decline. *Neurology*. 2013;80(13):1202-8.

24. Van Egroo M, et al. Ultra-high field imaging, plasma markers and autopsy data uncover a specific rostral locus coeruleus vulnerability to hyperphosphorylated tau. *Mol Psychiatry*. 2023:1-11.

25. Lakens D, Scheel AM, and Isager PM. Equivalence testing for psychological research: a tutorial. *Advances in Methods and Practices in Psychological Sciences*. 2018;1(2):259-69.

26. O'Callaghan C, et al. Locus coeruleus integrity and the effect of atomoxetine on response inhibition in Parkinson's disease. *Brain*. 2021;144(8):2513-26.

27. Gilvesy A, et al. Spatiotemporal characterization of cellular tau pathology in the human locus coeruleus-pericoerulear complex by three-dimensional imaging. *Acta Neuropathol*. 2022;144(4):651-76.

28. Liu Y, et al. Dynamic Lateralization of Pupil Dilation Evoked by Locus Coeruleus Activation Results from Sympathetic, Not Parasympathetic, Contributions. *Cell Rep*. 2017;20(13):3099-112.

29. Priovoulos N, et al. High-resolution in vivo imaging of human locus coeruleus by magnetization transfer MRI at 3T and 7T. *Neuroimage*. 2018;168:427-36.

30. Van Egroo M, van Hooren RWE, and Jacobs HIL. Associations between locus coeruleus integrity and nocturnal awakenings in the context of Alzheimer's disease plasma biomarkers: a 7T MRI study. *Alzheimers Res Ther*. 2021;13(1):159.

SUPPLEMENTARY MATERIAL

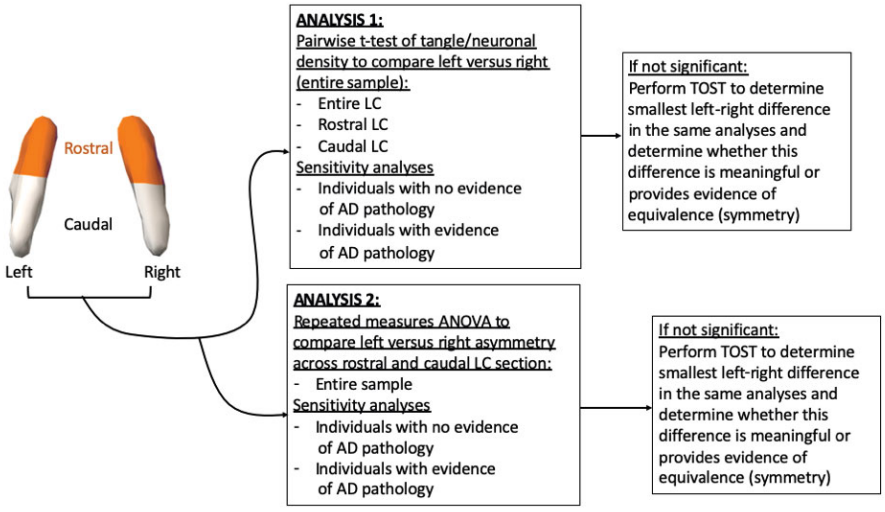

Figure S1. Flow chart depicting the key statistical analyses in the manuscript. Pairwise t-test were adjusted for multiple comparisons using the False Discovery Rate. Repeated measures ANOVA were adjusted using Tukey.

Table S1. Association between left-right differences in locus coeruleus pathology measures and age, sex or post-mortem interval

Hemisphere x covariate	F-value	p-value	Effect size (partial η^2)
Interactions with age as between subject factor (N = 77)			
Tangle density asymmetry by age	0.015	0.90	<0.001
Neuronal density asymmetry by age	0.381	0.54	0.005
Relative tangle density asymmetry by age	0.109	0.74	0.001
Interactions with sex as between subject factor (N = 77)			
Tangle density asymmetry by sex	0.001	0.99	<0.001
Neuronal density asymmetry by sex	0.294	0.59	0.003
Relative tangle density asymmetry by sex	0.163	0.69	0.002
Interactions with post-mortem interval (pmi) as between subject factor (N = 77)			
Tangle density asymmetry by pmi	0.506	0.95	0.75
Neuronal density asymmetry by pmi	0.808	0.72	0.83
Relative tangle density asymmetry by pmi	0.725	0.80	0.81

Repeated measures ANOVA with hemisphere (left, right) as repeated levels (with Greenhous-Geiser correction) in interaction with age or sex or post-mortem interval time (between-subject level).

Table S2. Left-right differences in locus coeruleus pathology measures

	Mean difference	T-value (df = 76)	p-value
Entire sample (N = 77)			
Entire LC			
Tangle density	-0.34	-1.61	0.11
Neuronal density	1.58	0.89	0.38
Relative tangle density	-0.56	-1.80	0.075
Rostral LC			
Tangle density	-0.61	-1.84	0.07
Neuronal density	-1.39	-0.56	0.57
Relative tangle density	-1.25	-1.66	0.10
Caudal LC			
Tangle density	-0.06	-0.23	0.82
Neuronal density	4.55	1.75	0.08
Relative tangle density	-0.11	-0.25	0.80
Sensitivity analyses: Without evidence of AD pathology (N = 30)			
Entire LC			
Tangle density	0.27	0.83	0.42
Neuronal density	0.52	0.19	0.85
Relative tangle density	-0.18	-0.37	0.71
Rostral LC			
Tangle density	-0.5	-1.07	0.29
Neuronal density	0.8	0.22	0.83
Relative tangle density	-0.54	-0.55	0.59
Caudal LC			
Tangle density	-0.03	-0.08	0.94
Neuronal density	0.23	0.06	0.96
Relative tangle density	0.57	0.82	0.42
Sensitivity analyses: With evidence of AD pathology (N = 47)			
Entire LC			
Tangle density	-0.38	-1.37	0.18
Neuronal density	2.27	0.97	0.34
Relative tangle density	-0.80	-1.98	**0.05**
Rostral LC			
Tangle density	-0.68	-1.48	0.15
Neuronal density	-2.79	-0.85	0.40
Relative tangle density	-1.70	-1.59	0.12
Caudal LC			
Tangle density	-0.09	-0.22	0.82
Neuronal density	7.32	2.24	**0.03**
Relative tangle density	-0.54	-1.07	0.29

Observed left-right differences for the entire LC, rostral LC and caudal LC and for the tangle density, neuronal density and relative tangle density measures within the entire sample, individuals with and without evidence of underlying AD pathology according the NIA-Reagan criteria for AD diagnosis. Paired one sample t-tests were performed. Tangle and neuronal density expressed per mm^2 and relative tangle density as a percentage.

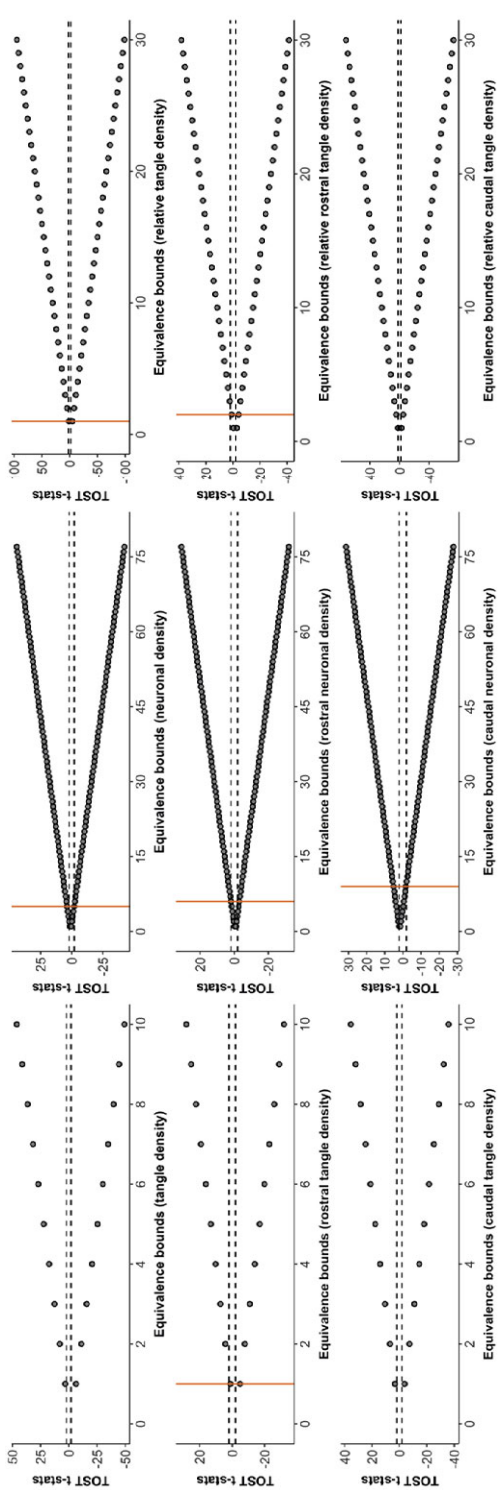

Figure S2. Iterative evaluation of left-right equivalence bounds of LC pathology. Graphs depict the TOST t-statistics (upper and lower) at different equivalence bounds for each LC measure. Equivalence bounds were gradually decreased from the maximum observed difference between left and right to detect the highest bound (red line) where equivalence was no longer significant. Significance thresholds are indicated with the dashed lines at $\alpha = 0.05$. Analyses were run for the entire LC (top row), rostral LC (middle row) and caudal LC (bottom row) and for the tangle density (left column), neuronal density (middle column) and relative tangle density measures (right column).

Table S3. Left-right differences between the rostral and caudal sections of the LC

Hemisphere x section	F-value	p-value	Effect size (partial η^2)
Entire sample (N = 77)			
Tangle density	1.48	0.23	0.019
Neuronal density	2.76	0.10	0.035
Relative tangle density	1.75	0.19	0.023
Sensitivity analyses: Without evidence of AD pathology (N = 30)			
Tangle density	0.59	0.45	0.020
Neuronal density	0.01	0.92	0.000
Relative tangle density	0.95	0.34	0.032
Sensitivity analyses: With evidence of AD pathology (N = 47)			
Tangle density	0.89	0.35	0.019
Neuronal density	4.83	**0.03**	0.095
Relative tangle density	0.90	0.35	0.019

Repeated measures ANOVA with hemisphere (left, right) and section (rostral, caudal) as repeated levels (with Greenhous-Geiser correction) within the entire sample, individuals with and without evidence of underlying AD pathology according the NIA-Reagan criteria for AD diagnosis. Results are adjusted for multiple corrections using Tukey.

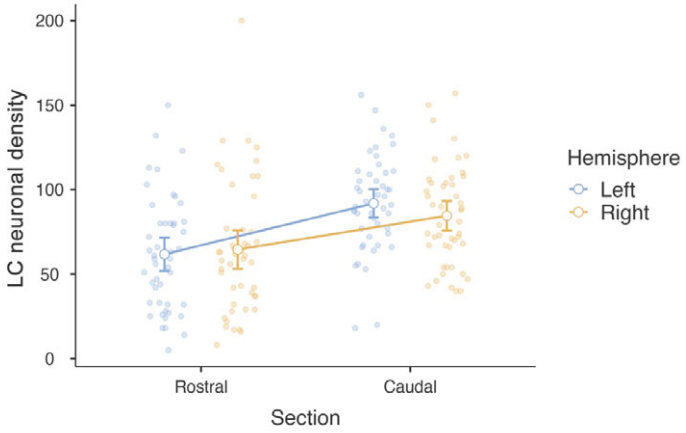

Figure S3. Larger left-right asymmetry in caudal than rostral LC neuronal density in individuals with underlying AD pathology (N = 47). Among individuals with underlying evidence of AD pathology, a larger left-right asymmetry of neuronal density in the caudal section was observed relative to left-right asymmetry in the rostral section of the LC (medium effect size of partial $\eta^2 = 0.095$; Mean neuronal density of rostral LC: left: 61.8, right: 64.6; caudal LC: left: 91.9 and right: 84.6).

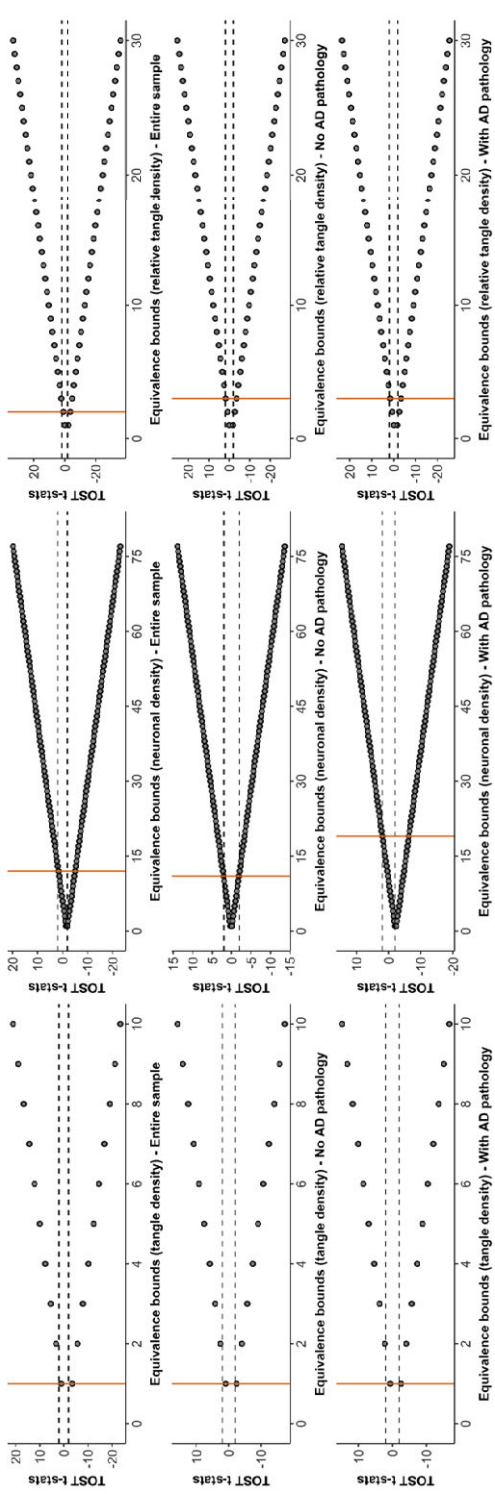

Figure S4. Iterative evaluation of equivalence bands for left-right asymmetry between rostral and caudal LC sections. Graphs depict the TOST t-statistics (upper and lower) at different equivalence bounds for each LC measure (testing whether left-right asymmetry in the rostral portion of the LC is equivalent to that in the caudal portion of the LC). Equivalence bounds were gradually decreased from the maximum observed difference between left and right to detect the highest bound (red line) where equivalence was no longer significant. Significance thresholds are indicated with the dashed lines at $\alpha = 0.05$. Analyses were run for the entire LC, rostral LC and caudal LC and for the tangle density, neuronal density and relative tangle density measures. Top row depicts the entire group, middle row the group without AD pathology (sensitivity analyses) and the bottom row the group with AD pathology (sensitivity analyses).

Part II

Modulating the locus coeruleus function: non-invasive and non-pharmacological interventions

Chapter 4

Impact of light on task-evoked pupil responses during cognitive tasks

Islay Campbell
Elise Beckers
Roya Sharifpour
Alexandre Berger
Ilenia Paparella
Fermin JA Balda
Ekaterina Koshmanova
Nasrin Mortazavi
Siya Sherif
Gilles Vandewalle

Published in Journal of Sleep Research, 2023

ABSTRACT

Light has many non-image-forming (NIF) functions including modulation of pupil size and stimulation of alertness and cognition. Part of these NIF effects may be mediated by the brainstem locus coeruleus (LC). The processing of sensory inputs can be associated with a transient pupil dilation that is likely driven in part by the phasic activity of the LC. In the present study, we aimed to characterize the task-evoked pupil response (TEPR) associated with auditory inputs under different light levels and across two cognitive tasks. We continuously monitored the pupil of 20 young healthy participants (mean [SD] age = 24.05 [4.0] years; 14 women) whilst they completed an attentional and an emotional auditory task whilst exposed to repeated 30–40-s blocks of light interleaved with darkness periods. Blocks could either consist of monochromatic orange light (0.16 melanopic equivalent daylight illuminance (EDI) lux) or blue-enriched white light of three different levels [37, 92, 190 melanopic EDI lux; 6500 K]. For the analysis, 15 and then 14 participants were included in the attentional and emotional tasks, respectively. Generalized linear mixed models showed a significant main effect of light level on the TEPRs triggered by the attentional and emotional tasks ($p \leq 0.0001$). The impact of light was different for the target versus non-target stimulus of the attentional task but was not different for the emotional and neutral stimulus of the emotional task. There is a smaller sustained pupil size during brighter light blocks but, a higher light level triggers a stronger TEPR to auditory stimulation, presumably through the recruitment of the LC.

INTRODUCTION

The non-image-forming (NIF) system (also termed non-visual system) in the human retina detects environmental irradiance to mediate the influences of light on many NIF functions, including circadian entrainment [1], melatonin suppression [2], pupillary light responses [3, 4], and stimulation of alertness and cognitive performance [5]. Light's influence on human alertness and cognition has been reported to be improved by high-intensity white light and short wavelength light, but the impact of light on cognition is complicated by being dependent on several factors, such as time of day, spectral composition, and intensity of the light source [6].

The primary photoreceptors of the NIF system are intrinsically photosensitive retinal ganglion cells (ipRGCs) [7, 8], which express the photopigment melanopsin. Animal studies have established that the ipRGCs project to various subcortical brain regions, including the suprachiasmatic nucleus (SCN) of the hypothalamus, the site of the master circadian clock [9]. The exact brain pathways involved in light's NIF functions for humans is an area of continued and active research. The locus coeruleus (LC), in the brainstem, receives indirect inputs from the SCN, and it is hypothesized that the LC may be involved in mediating light's influence on alertness and cognition [5, 10, 11]. The LC is central to cognition and alertness and a major source of noradrenaline (NA) in the brain [11]. A previous neuroimaging study, using a 3-Tesla magnetic resonance imaging (MRI) apparatus reported that an area of the brainstem consistent with the location of the LC is modulated by the wavelength of light whilst performing a non-visual cognitive task [12]. The LC is a small bilateral nucleus with a cylinder shape, 15 mm long and 2.5 mm in diameter (50.000 neurons in total), located in the brainstem [13]. Due to its small size, and its deep location near the fourth ventricle, in vivo imaging of the LC is challenging such that it is difficult to assess its role in mediating the NIF impacts of light in humans. Here, we emphasize that variation in pupil size may be an accessible means to address this research question.

The autonomic nervous system regulates pupil size through the control of two muscles in the pupil, the iris sphincter muscle that causes the constriction of the pupil, and the dilatory muscle that promotes the dilation

of the pupil [14]. Pupil size is dependent on the sympathovagal balance, with parasympathetic activity promoting pupil constriction through recruitment of the iris sphincter muscle via the midbrain Edinger–Westphal nucleus (EWN). Pupil dilation is dependent on the sympathetic system that starts at the hypothalamus and the LC, leading to the inhibition of the activity of the EWN causing pupil dilation through the constriction of the dilator muscle [14, 15]. However, pupillary dilation can also be caused by inhibiting the parasympathetic constriction pathway, through LC activity inhibiting the EWN, causing relaxation of the constrictor muscles [15, 16]. There is research that suggests that pupil dilation due to cognitive demand is due to inhibition of the parasympathetic pathway [17]. The interplay between the sympathetic and the parasympathetic systems determines the size of the pupil, with environmental irradiance, mental effort, and fatigue influencing the balance between the two systems [14, 17, 18]. Change in pupil size can be described as a baseline response where pupil size is maintained for a longer period of time or a faster phasic response [19].

There is evidence to suggest that fluctuations in pupil size is a proxy measure of the changes in brain arousal during cognitive activity. Specifically, the LC is proposed to be an important region in the control of pupil dilation and changes in pupil diameter have been hypothesized to be a readout of the activity of the NA neurons of the LC [20, 21]. The LC-NA system has two different modes, baseline tonic activity where there is continuous spiking, and phasic activity, characterized by brief bursts of high-frequency activity that can be spontaneous or in response to salient stimuli [11]. Evidence for the link between the LC and pupil size comes from the observation that the neuronal activity of the LC fluctuates almost simultaneously with changes in pupil diameter [11]. Further direct evidence comes from research showing that the spiking activity of the LC and the diameter of the pupil were also correlated during a decision-making task in monkeys [22]. Also, spontaneous LC activity correlated with pupil size in monkeys performing a simple fixation task and an evoked pupil dilation occurred when the LC was electrically microstimulated. In addition, other brain areas (inferior colliculus, superior colliculus, anterior and posterior cingulate cortex) also show a less reliable association between pupil size and spontaneous LC activity, suggesting there is coordinated neuronal activity

in brain areas through LC-mediated arousal [11, 23, 24]. The propagation of LC signal is slow to brain areas due to having unmyelinated projections [25]. Furthermore, human studies combining functional MRI (fMRI) and pupillometry have found activations in the area of the brainstem compatible with the LC were linked to fluctuations in pupil diameter, during resting state and for a novelty detection task [26, 27]. The research highlights that changes in pupil diameter are a relatively reliable means to assess LC activity.

Changes in pupil diameter can also be induced in response to cognitive effort which can be triggered by external stimuli [15, 21]. In response to an external task event, the pupil dilates and then constricts back to baseline. This pupil response to a task event is called the 'task-evoked pupil response' (TEPR). These TEPRs can also be influenced by factors such as the demand of the cognitive task and the performance [11, 28]. The exact mechanism of the link between the size of the pupil and the activity of the LC is still not known. However, studying TEPRs is nevertheless often considered a non-invasive means to determine the ongoing alterations in the LC phasic activity or arousal level during cognitive tasks.

The pupil is well known to adapt to changes in the light environment, with the pupil constricting at higher light levels mainly driven by the parasympathetic system and dilation mainly being driven by the sympathetic system in darkness [14, 21]. This light-induced constriction is maintained by ipRGCs, which innervate the pretectal olivary nucleus, which in turn project to the EWN leading to pupil constriction by parasympathetic drive [21]. However, whether the TEPRs are influenced by light's NIF effects is currently not known. We, therefore, decided to study the TEPRs under different light conditions. We measured pupil diameter during two cognitive tasks and examined the effect of light level, expressed in melanopic (mel) equivalent daytime illuminance (EDI) lux, on the TEPRs to auditory stimuli. We hypothesized that the TEPRs would be greater under higher irradiance levels due to the stimulating NIF impact of light, potentially due to an increase in either sympathetic or parasympathetic drive. To test this hypothesis, we used eye-tracking data from healthy young participants, who completed an attentional and an emotional auditory cognitive task during a fMRI recording whilst exposed to different light conditions.

METHODS

Participants

A total of 20 healthy participants (age (mean ± SD) 24.05 ± 4 years; 14 women) gave their written informed consent to take part in the study, which was approved by the Ethics Committee of the Faculty of Medicine of the University of Liège. The participants were assessed for the exclusion criteria with a semi-structured interview and questionnaires. None of the participants had a history of psychiatric and neurological disorders, sleep disorders, the use of psychoactive drugs or addiction. Participants had no history of night shift work during the last year or recent trans-meridian travel during the last 2 months; excessive caffeine (>4 caffeine units/day) or alcohol consumption (>14 alcohol units/week); and were not taking medication or smoking. Their scores on the 21-item Beck Anxiety Inventory [29] and the Beck Depression Inventory-II [30] were mild or minimal (<17), and minimal (<14), respectively normal. Participants reported no history of ophthalmic disorders or auditory impairments and were screened for color blindness. Due to technical issues (see below), 15 and 14 participants were, respectively, included in the analyses of the attentional and emotional tasks (Table 1).

Table 1. Participants included in the analysis

	Total Participants	Oddball Analysis	Emotional Analysis
Number of participants	20	15	14
Age	24.05 (±4.00)	24.33 (±4.15)	24.07 (±4.41)
Sex (M)	6	5	4
Mood (BDI-II)	6.94 (±5.57)	6.0 (±4.78)	6.83 (±6.01)
Anxiety (BAI)	6.55 (±5.98)	5.71 (±4.06)	7.66 (±6.71)
Sleep quality (PSQI)	4.27 (±2.88)	3.78 (±1.92)	4.41(±3.31)
Seasonality (SPAQ)	1.05 (±0.80)	1 (±0.78)	1.16 (±0.83)
Chronotype (HO)	48.5 (±9.26)	47.42 (±9.72)	47.58 (±6.98)
Daytime sleepiness (ESS)	6.27 (±3.21)	6.35 (±2.79)	6.75 (±3.57)
Years of education	14.35 (±3.12)	14.84 (±2.47)	13.72 (±3.40)

Columns for total number of participants who completed the study, and the number of participants included for each task. Refer to the main text for references. BAI, Beck Anxiety Inventory; BDI-II, Beck Depression Inventory; ESS, Epworth Sleepiness Scale; HO, Horne and Östberg questionnaire; PSQI, Pittsburgh Sleep Quality Index; SPAQ, Seasonal Pattern Assessment Questionnaire.

Participants followed a loose sleep-wake schedule (±1 h from habitual bedtime or wake-up time) during the 7 days preceding the laboratory experiment to maintain realistic entrained life conditions and avoid excessive sleep restriction across all participants. Sleep-wake schedules were verified using wrist actigraphy and sleep diaries. They were asked to refrain from caffeinated and alcohol-containing beverages and excessive exercise for at least 3 days before the experiment. Participants were familiarized with the MRI environment 1 week before the experiment during an MRI session where structural images of the brain were acquired.

Experimental protocol

Most participants (N = 17) arrived at the laboratory 1.5–2 h after habitual wake time, whilst a minority (N = 3) were admitted to the laboratory 1.5–2 h before habitual bedtime. The study will investigate the effect time of day (morning versus evening) has on light exposure on brain functions and behavior in the future. For this paper, all results presented are controlled for time-of-day differences. Participants were first exposed for 5 min to a bright white light (1000 lux) and were then maintained in dim light (<10 lux) for 45

min to standardize participant light history before the fMRI session (Figure 1A). During this period participants were given instructions about the fMRI cognitive tasks and completed practice tasks. The fMRI session consisted of participants completing an executive task (25 min), an attentional task (15 min), and an emotional task (20 min) (Figure 1B-C). Participants always completed the executive task first and then the order of the following two tasks was pseudo-randomized. Only the emotional and the attentional tasks are discussed in the present paper as they consisted of a stream of events, where each sound potential triggers a TEPR.

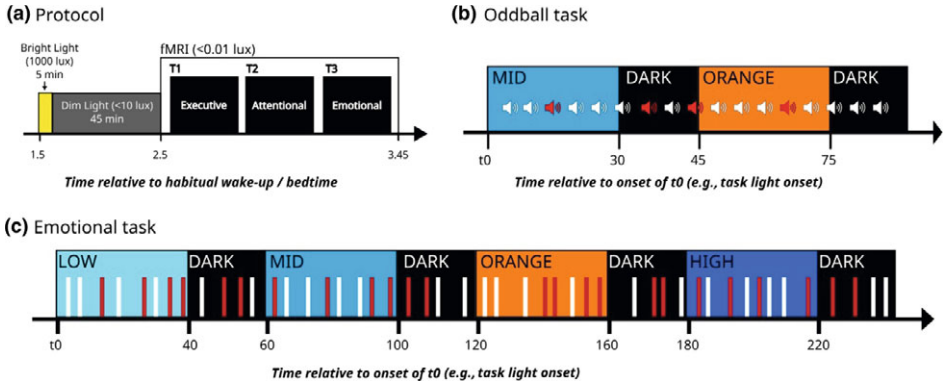

Figure 1. Experimental design. **A)** General protocol. Time relative to scheduled wake-up/bedtime (h). Following standardization of immediate prior light exposure (see Methods), participants performed an executive (not discussed in the present paper), an attentional and emotional task in functional magnetic resonance imaging (fMRI). **B)** Detailed procedures of the attentional task (oddball). Time (s) relative to t0, a time point arbitrarily chosen as the light onset of the session. The task consisted of a stream of standard sounds (80%) and pseudo-randomly interspersed odd sounds (20%); participants were asked to identify the odd stimuli through a button press. Whilst completing the task participants were exposed to blue-enriched white light (BEL; 92 melanopic [mel] equivalent daylight illuminance [EDI] lux; 6500 K) (MID) and a monochromatic orange (0.16 mel EDI lux; 589 nm) light. Light exposures lasted 30 s and were separated by 15-s periods of darkness. Odd (red) and standard (white) stimuli were equally distributed across the two light conditions and darkness. **C)** Detailed procedures of the emotional task. Time (s) relative to t0, a time point arbitrarily chosen as the light onset of the session. The task consisted of a lure gender discrimination of auditory vocalizations of the three pseudo-word types ('goster', 'niuvenci', or 'figotleich') whilst exposed to the alternating white BEL of three different intensities (37, 92, 190 mel EDI lux; 6500 K) (LOW, MID, HIGH) and a monochromatic orange (0.16 mel EDI lux; 589 nm) light. Light exposures lasted 30–40 s and were separated by 15–20-s periods of darkness. Untold to the participants, vocalizations were pronounced with angry (red bars) and neutral (white bars) prosody pseudo-randomly and equally distributed across the three light conditions.

An MRI-compatible light system (Supplementary Figure 1) designed-in-laboratory was developed to ensure relatively uniform and indirect illumination of participants' eyes whilst in the MRI scanner. An 8-m long MRI-compatible dual-branched optic fiber (Setra Systems, MA, USA) transmitted light from a light box (SugarCUBE, Ushio America, CA, USA), that was stored in the MRI control room. The dual end of the optic fiber was attached to a light stand fitted at the back of the MRI coil. This allowed for equal illumination

of the participants' eyes. A filter wheel (Spectral Products, AB300, NM, USA) and optical fiber filters (a monochromatic orange light filter [589 nm; full width at half-maximum: 10 nm] and a UV long bypass [433–1650 nm] filter) were used to create the light conditions needed for the experiment. Participants were asked to keep their eyes open and try not to blink too much during the cognitive tasks.

Both tasks were programmed with OpenSesame (version 3.2.8) [31] and launched from a computer in the MRI control room. Participants heard the auditory stimuli through MR-compatible headphones (Sensimetrics, Malden, MA) and the volume was set by the participant before starting the tasks to ensure a good auditory perception of all the task stimuli. Participants used an MRI-compatible button box to respond to task items (Current Designs, Philadelphia, PA, USA). During the attentional task, participants were exposed to 30 s of light blocks separated by 15 s of darkness (<0.1 lux). The spectra of the lights were assessed at the level of the end of the optic fiber (AvaSpec-2048, Avantes, The Netherlands). Irradiance could not be measured directly in the magnet, but the light source was calibrated (840-C power meter, Newport, Irvine, CA, USA). The light conditions used were a polychromatic, blue-enriched white light emitting diode (LED) light (92 mel EDI lux; 6500 K) and a monochromatic orange light (0.16 mel EDI lux). The light blocks were repeated seven times for each light condition. During the emotional task, participants were exposed to 30–40-s periods of light blocks separated by 20 s of darkness (<0.1 lux). The light conditions used were three different irradiances of a polychromatic, blue-enriched white LED light (37, 92, 190 mel EDI lux; 6500 K) and a monochromatic orange light (0.16 mel EDI lux) (Figure 2; Table 2). The light blocks were repeated five times for each light condition.

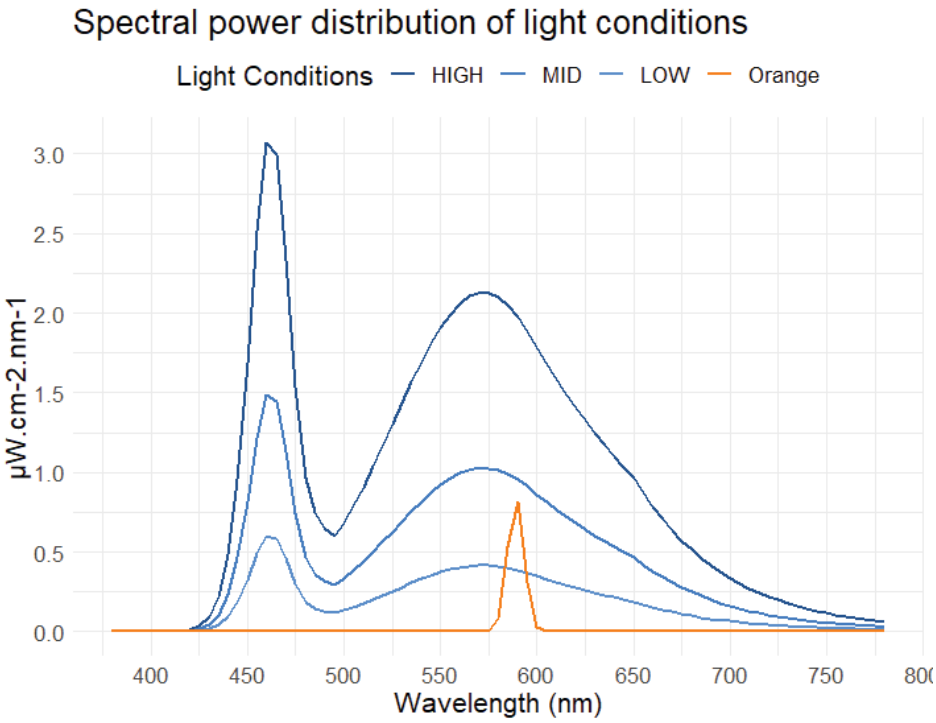

Figure 2. Spectral power distribution of light conditions. Orange: monochromatic orange light, 0.16 melanopic (mel) equivalent daylight illuminance (EDI) lux, 589 nm; blue-enriched white light (BEL) LOW, MID, and HIGH: light of three different intensities (37, 92, 190 mel EDI lux; 6500 K). See Table 2 for additional characteristics.

Table 2. Light characteristics

	Low BEL	Mid BEL	High BEL	Monochromatic light (589 nm)
Photopic illuminance (lux)	47	116	240	7.5
Peak spectral irradiance (nm)	460	460	460	590
Melanopic EDI lux (ipRGCs)	37	92	190	0.16
Rhodopic EDI lux (Rods)	39	97	201	0.94
Cyanopic EDI lux (S-cones)	32	79	163	0
Chloropic EDI lux (M-cones)	44	110	227	5
Erythropic EDI lux (L-cones)	46	113	233	8
Irradiance ($\mu W/cm^2$)	15	36	75	1.4
Photon flux($1/cm^2/s$)	4.12E+13	1.02E+14	2.10E+14	4.24E+12
Log photon Flux (log_{10}) ($1/cm^2/s$)	13.61	14.01	14.32	12.63
Narrowband peak	-	-	-	589
Narrowband FWHM	-	-	-	10

Additional light characteristics of the two light sources used. Blue-enriched white light (BEL) (low, mid, and high) and monochromatic orange light (589 nm). EDI, equivalent daylight illuminance; FWHM, full width at half-maximum; ipRGCs, intrinsically photosensitive retinal ganglion cells.

Attentional task

The attentional task used was a mismatch negativity or oddball task [32]. Participants were asked to detect a rare randomly occurring target (or odd) item in a stream of frequent standard items. They used the keypad to report the detection of the odd items. Stimuli (n = 315) consisted of frequent standard (500 Hz, 100 ms) and odd tones (1000 Hz, 100 ms), presented 80% and 20% of the time, respectively, in a pseudo-randomized order. The interstimulus interval between stimuli was 2 s. Target and standard stimuli were equally distributed across the two light conditions and the separating darkness periods (Figure 1B). The instruction was to prioritize accuracy over rapidity when responding.

Emotional task

The emotional task used was a gender discrimination of auditory vocalizations task [33]. Participants were asked to use the keypad to indicate what they believed the gender of the person pronouncing each token was. The gender

classification was a lure task ensuring participants paid attention to the auditory stimulation. The purpose of the task was to trigger an emotional response as participants were not told that 50% of the stimuli were pronounced with angry prosodies. The 240 auditory stimuli were pronounced by professional actors (50% women) and consisted of three meaningless words ('goster', 'niuvenci', 'figotleich'). The stimuli were expressed in either an angry or neutral prosody, which has been validated by behavioral assessments [33] and in previous experiments [34, 35]. The stimuli were also matched for the duration (750 ms) and mean acoustic energy to avoid loudness effects. During each 30–40-s light block, four angry prosody stimuli and four neutral prosody stimuli were presented in a pseudo-random order and delivered every 3–5 s. A total of 160 distinct voice stimuli (50% angry; 50% neutral) were distributed across the four light conditions. The darkness period separating each light block contained two angry and two neutral stimuli. A total of 80 distinct voice stimuli (50% angry; 50% neutral) were distributed across the darkness periods (Figure 1C). Again, the instruction was to prioritize accuracy over rapidity when responding.

Pupil

The right eye movements and the pupillary size were recorded continuously with an infrared eye-tracking system (Eyelink-1000, SR Research, Osgoode, ON, Canada; sampling rate, 1000 Hz). Pupil data were analyzed using MATLAB R2019b (MathWorks, Natick, MA, USA). Participants with >25% missing or corrupted eye-tracking data were excluded. Blink events were replaced with linear interpolation and the data were smoothed using the '*rlowess*' a robust linear regression function. The total amount of interpolated data included was 21% ± 9% and 22% ± 9% for the attentional and the emotional task, respectively. The transient pupil response was computed as the change in the pupil diameter from before (baseline) and after (maximum) the auditory stimulus presentation. Baseline pupil diameter was computed as the mean pupil diameter over 1 s before stimuli onset. The maximum pupil diameter was defined as the maximum value over a 1.5 s window following sound onset. TEPRs were computed as the ratio between maximum and baseline diameter. For the attentional task, one participant was excluded because they did not complete the entire attentional task and four were excluded as there was >25%

missing or corrupt pupil data. Therefore, we included 15 participants in the analysis of the oddball task (Table 1). For the emotional task, two participants were excluded as there was >25% missing or corrupt pupil data. One participant was excluded because he did not complete the entire emotional task correctly and three were excluded due to problems with the eye-tracking system. Therefore, we included 14 participants in the analysis of the emotional task (Table 1).

Statistical analyses

Statistical analyses were computed using the Statistical Analysis System (SAS) version 9.4 (SAS Institute, Cary, NC, USA) using individual TEPRs segregated per stimulus type and light condition. Values were considered outliers if they were > ± 3 standard deviations (SDs) across the entire dataset and were therefore removed. Analyses consisted of generalized linear mixed models (GLMM) seeking effects of light condition (i.e., mel EDI lux level) on the TEPRs. TEPRs were set as the dependent variable, with subject as a random factor (intercept), and light condition and stimulus type as repeated measures (autoregressive (1) correlation), together with the time of day, age, body mass index and sex as covariates. GLMM were adjusted for the dependent variable distribution. Post hoc contrasts were corrected for multiple comparisons using a Tukey adjustment.

RESULTS

The performance of both tasks was high, with a mean (SD) 96.6% (0.5%) of detection of target sounds during the attentional (oddball) task and 93.9% (7.21%) of button response during the emotional (gender classification) task. In line with the literature [35, 36], for the emotional task, reaction times (RTs) were faster for neutral stimuli with a mean (SD) of 1192 (182.8) ms compared to 1234 (199.8) ms RTs for emotional prosody vocal stimulation ($p = 0.0004$) suggesting that the task was successful in triggering a differential response according to the emotional content. As no response was collected for the standard tone in the oddball task, RTs could not be compared between

stimulus types for the attentional task. Although not relevant to the task and not compromising any emotional effect [34], gender detection accuracy for the emotional task (mean [SD] 79% [11%]) was slightly lower than what has previously been reported for the task [35]. For both tasks, there were no significant main effects of the light level on RTs ($F < 2.1$, $p \geq 0.1$) and accuracy ($F < 2.1$, $p \geq 0.1$), and there was no light exposure by stimulus type interaction for the emotional task ($F_{(4,34.04)} = 0.25$, $p = 0.9$). This was expected, as behavioral performance differences unspecific to light exposure would significantly bias neuroimaging results [37].

It is well established that pupil size changes in response to variations in environmental irradiance. In a joint paper [38], we notably confirmed this and reported that the sustained constriction of the pupil increased with higher light levels in the same sample of participants who completed the same protocol. In contrast to the joint paper [38], here, we consider whether changes in light conditions, as indexed by mel EDI lux, impact the TEPRs for an attentional and emotional task. Both tasks consist of streams of events that putatively trigger TEPRs, and both have two types of auditory stimulations. We hypothesized that the TEPRs would be greater under higher light levels due to the stimulating NIF impact of light.

To characterize the effect of light conditions on TEPRs for the attentional task, an initial GLMM was conducted with TEPRs during the oddball task as the dependent variable. The results yielded significant main effects of stimulus type (target and standard tones; $F_{(1,1548)} = 189.27$, $p \leq 0.0001$) and light condition ($F_{(2,1548)} = 13.71$, $p \leq 0.0001$). Importantly, the GLMM detected a significant interaction between stimulus type and light condition ($F_{(2,1548)} = 3.65$, $p = 0.02$) (Figure 3A). Post hoc analyses first indicated that TEPRs were larger for target versus standard stimuli ($p \leq 0.0001$). They further indicated that TEPRs were smaller during darkness as compared to the blue-enriched white light condition (92 mel EDI lux; $p \leq 0.0001$) but TEPRs during darkness were not significantly different when compared to the orange (0.16 mel EDI lux; $p = 0.1$) light condition. However, TEPRs were significantly larger under the blue-enriched white light (92 mel EDI lux; $p = 0.002$) when compared to the orange light (0.16 mel EDI lux). Finally, post hoc analyses indicated that TEPRs significantly increased with

higher light irradiance for the standard ($p \leq 0.0001$) but not the target stimuli ($p > 0.2$).

The second GLMM, with TEPRs during the emotional task as the dependent variable, led to a significant main effect of light condition ($F_{(4,1072)} = 77.78$, $p \leq 0.0001$). Despite there being a qualitative difference between angry and neutral stimuli, there was no significant main effect of stimulus type ($F_{(1,1072)} = 0.06$, $p = 0.8$) (Figure 3B). In addition, there was no interaction between stimulus type and light condition ($F_{(4,1073)} = 0.5$, $p = 0.7$). Post hoc analysis showed a significant difference between darkness and all four light conditions ($p \leq 0.0001$), as well as between the orange (0.16 mel EDI lux) light and the blue-enriched white light conditions (37, 92, 190 mel EDI lux; $p \leq 0.0001$). There was no significant difference between the blue-enriched white light conditions (37, 92, 190 mel EDI lux; $p \geq 0.7$).

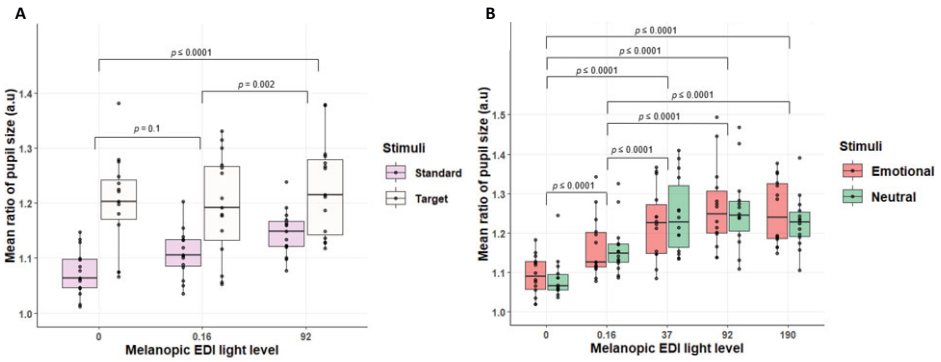

Figure 3. Task-evoked pupil response (TEPRs) across light conditions and stimulus type. **A)** TEPRs under the different light conditions during the attentional (oddball) task (N = 15; mean [SD] age 24.33 [4.15] years; 10 women). Individual average TEPRs were computed per stimulus type and light condition. TEPRs were significantly higher for target versus standard stimulations ($p < 0.0001$), as well as under higher versus lower melanopic equivalent daylight illuminance (EDI) light levels ($p < 0.0001$). A significant light condition by stimulus type was also found ($p = 0.02$) and post hoc analyses indicated that TEPRs significantly increased with higher light irradiance for the standard but not the target stimulations. **B)** TEPRs under different light levels during the emotional task (N = 14; mean [SD] age 24.0 [4.41] years; 10 women). Individual average TEPRs were computed per stimulus type and light condition. There was no significant difference between neutral and emotional stimulations ($p = 0.8$) whilst TEPRs were greater under higher versus lower melanopic light levels ($p < 0.0001$). There was no light condition by stimulus type interaction ($p = 0.7$).

DISCUSSION

The TEPRs consist of transient pupil dilations triggered by the processing of stimulations over diverse cognitive domains. They are considered to be at least in part driven by a transient increase in the phasic activity of the LC-NA system and potentially other brain areas [14, 23]. In the present study, we tested whether the TEPRs evoked by auditory stimulus during two cognitive tasks would be larger under higher ambient light levels, when the parasympathetic drive to the pupil is high, to investigate whether light's NIF impacts on cognitive brain activity could potentially be mediated through the LC. To test this hypothesis, we analyzed eye-tracking data from young healthy participants who completed an attentional and an emotional cognitive task during an fMRI protocol whilst exposed to different light conditions. The results reveal that when there is a smaller sustained pupil size at higher light levels [38], the TEPRs to auditory stimulus were larger under higher light irradiances, as indexed by mel EDI lux. Although this main finding was detected for both the attentional and emotional tasks, we further observed task-specific differences in the impact light irradiance has on the different types of stimuli of each task.

The LC is involved in the processing of salient events through an increase in its phasic activity [39]. The oddball task, which mimics novelty/salience detection has been previously used to assess the phasic activity of the LC [40], whilst the LC is also known to be important for emotional processing [11, 41]. The oddball task was reported to trigger TEPRs (both in the visual and auditory modality) that were larger for the odd target stimuli, which is in line with our findings [27, 42]. Similarly, TEPRs were also reported using emotional tasks [11, 41]. Pupil size depends on the parasympathetic-sympathetic balance and transient pupil dilation is thought to reflect an increase in arousal due to an increase in the sympathetic tone [14]. Although recent investigations have indicated that it is likely not the sole driver of transient pupil dilation, in vivo animal studies support that transient increases in pupil size were directly related to the firing of the neurons of the LC [20]. Our findings could suggest therefore that the phasic activity of the LC related to an ongoing cognitive process is likely to be affected by changes in ambient light level. Light is known to increase arousal and have wake-promoting effects and can cause the

activation of the pupil dilation pathway via the LC, through indirect sympathetic influence by stimulating the SCN, and the dorsomedial hypothalamus [15]. The LC could also cause pupil dilation via sympathetic drive by its projection to the intermediolateral column and potential through projections to the superior colliculus [15, 43]. Alternatively, our results could be interpreted as transient inhibition of the parasympathetic constriction pathway, through EWN inhibition by the LC, leading to an increase in pupil dilation under higher light levels [16]. Transient inhibition of parasympathetic signal may indeed be the primary pathway involved in pupil dilation caused by arousal and cognition [17, 43].

The LC is a good candidate to mediate the impact of light on human alertness and cognition through an effect on other subcortical and cortical structures [11]. The thalamus pulvinar could likely be one of these downstream structures, as it is the most consistently affected by light in previous investigations on the impact of light on non-visual cognitive brain activity [5]. Other structures and nuclei, e.g. within the hypothalamus or basal forebrain, could also be implicated, whilst the recruitment of limbic and cortical areas would depend on the ongoing cognitive processes [44]. Our results indicate that the impact of increasing light level is stronger for standard compared with target stimulation. We interpret this as a ceiling effect for TEPRs elicited by target stimulations that cannot be further increased, whilst the milder TEPRs triggered by standard stimulations in darkness or at lower light levels can continue to be increased under higher ambient light. In line with this interpretation, the impact of light on non-visual cognitive brain activity was previously found to be reduced in the evening during the wake-maintenance zone, when the endogenous circadian signal promoting wakefulness is strong and therefore when alertness could not be further increased by lights influence [45]. In contrast, light's impact was increased in the morning following sleep deprivation, when the circadian signal is weaker but the need for sleep is high due to sleep loss. Therefore, alertness can benefit from the external stimulating impact of light [45]. If our interpretation is correct, this could mean that light can only affect the activity of the LC when it is not already highly recruited by the processing of a salient stimulation. Even though the average TEPR to target stimuli remains stable across light conditions, the variance of TEPR was

larger for target stimuli. We cannot rule out that it contributed to the absence of difference between light conditions for target stimuli.

The situation is different if we consider the emotional task as we find no difference between the TEPRs triggered by the emotional and neutral simulations. This could call into question the emotional valence of the stimuli included in the task. However, the emotional task has been previously extensively validated and was successful in triggering differential brain responses to emotional versus neutral stimulations, including in studies interested in the NIF effects of light [33, 34, 36]. We also find that RTs were significantly slower in response to emotional versus neutral stimulations, which is in line with the literature and supports that the emotional valence of the stimuli was perceived by the participants [35, 36]. Yet, the emotional response may not be strong and/or different enough from the response to neutral stimuli to be detected with 15 subjects. Auditory emotional stimuli are indeed considered to be less effective at provoking an emotional response when compared to visual emotional stimuli [41]. It may also be that the unexpected occurrence of neutral stimulations (stimulations were pseudo-randomly delivered every 3–5 s) triggers a TEPR that is similar to the emotional stimuli. Our results further indicate that given the relatively mild response elicited in darkness or at lower light levels, TEPRs could be increased by increasing light levels. The maximum increase seems to be reached already with the lower level of polychromatic, blue-enriched white light (37 mel EDI lux) to ceiling thereafter. Interestingly, the maximum TEPRs for both the oddball and emotional tasks seem to lay on average around 1.25, i.e. a 25% increase on average in pupil size compared to baseline (cf. Figure 3).

Study limitations

We emphasize that our study has limitations. The light conditions included do not allow for determining which of the human photoreceptors are mostly contributing to the TEPRs. Rods, cones, and ipRGCs could equally be involved with differential recruitment at the different light levels we used [7]. Future research could use metameric light sources with which the wavelength compositions can be manipulated to differentially recruit one photoreceptor type whilst leaving the others relatively similarly recruited [46].

We are also unable to say conclusively to what extent the sympathetic and/or parasympathetic system contributes to the increase in TEPRs under higher light levels. The LC is considered the center point of the NA pupil control pathway and contains sympathetic and parasympathetic premotor neurons [43]. Yet other nuclei may affect pupil size and TEPRs and contribute to our results [23]. We stress that we did not have access to the brain activity associated with TEPRs. The assumptions made regarding the recruitment of the LC can only be verified using the fMRI data acquired simultaneously with the pupil data. Further research using drugs that lead to the alteration of pupil size control, through the modification of the activity/transmission of the sympathetic or parasympathetic NA neurons may elucidate the contribution of sympathetic or parasympathetic systems to increase in TEPRs under higher light levels [16].

Finally, during a goal-oriented task, the phasic activity of the LC facilitates task-related behaviors to optimize performance, and tonic activity is involved in task disengagement and search for alternative behaviors. Switching between these two modes allows to maximize utility [11]. Therefore, it can be hypothesized that we only investigated the phasic activity of the LC, as both tasks used in the study are stream-of-conscious tasks and do not involve the exploration of alternative behaviors at the cost of task performance. However, we cannot rule out the possibility of tonic activity affecting the results.

Conclusion

Overall, this study shows that the NIF impacts of light can be detected when focusing on pupil size with transient pupil dilation induced by increasing light levels. This is true for two different auditory cognitive tasks whilst increased transient pupil dilation may only be possible if TEPRs are not already at maximum. Future research is needed to conclude if it is the sympathetic or parasympathetic drive that is causing the increase in TEPRs under higher light levels. There is a putative link between LC phasic activity and transient pupil dilation [20], alternatively, transient pupil dilation may be due to the transient inhibition of the parasympathetic signal [16]. The results presented here provide further support for the involvement of the LC in the stimulating impact of light on alertness and cognition.

REFERENCES

1. Berson DM, Dunn FA, and Takao M. Phototransduction by retinal ganglion cells that set the circadian clock. *Science*. 2002;295(5557):1070-3.
2. Brainard GC, et al. Action spectrum for melatonin regulation in humans: evidence for a novel circadian photoreceptor. *J Neurosci*. 2001;21(16):6405-12.
3. Gamlin PD, et al. Human and macaque pupil responses driven by melanopsin-containing retinal ganglion cells. *Vision Res*. 2007;47(7):946-54.
4. Hattar S, et al. Central projections of melanopsin-expressing retinal ganglion cells in the mouse. *J Comp Neurol*. 2006;497(3):326-49.
5. Vandewalle G, Maquet P, and Dijk DJ. Light as a modulator of cognitive brain function. *Trends Cogn Sci*. 2009;13(10):429-38.
6. Siraji MA, et al. Effects of Daytime Electric Light Exposure on Human Alertness and Higher Cognitive Functions: A Systematic Review. *Front Psychol*. 2022;12:765750.
7. Mure LS. Intrinsically Photosensitive Retinal Ganglion Cells of the Human Retina. *Front Neurol*. 2021;12:636330.
8. Provencio I, et al. A novel human opsin in the inner retina. *J Neurosci*. 2000;20(2):600-5.
9. Do MTH. Melanopsin and the Intrinsically Photosensitive Retinal Ganglion Cells: Biophysics to Behavior. *Neuron*. 2019;104(2):205-26.
10. Aston-Jones G, et al. A neural circuit for circadian regulation of arousal. *Nat Neurosci*. 2001;4(7):732-8.
11. Aston-Jones G and Cohen JD. An integrative theory of locus coeruleus-norepinephrine function: adaptive gain and optimal performance. *Annu Rev Neurosci*. 2005;28:403-50.
12. Vandewalle G, et al. Brain responses to violet, blue, and green monochromatic light exposures in humans: prominent role of blue light and the brainstem. *PLoS One*. 2007;2(11):e1247.
13. Keren NI, et al. In vivo mapping of the human locus coeruleus. *Neuroimage*. 2009;47(4):1261-7.
14. Larsen RS and Waters J. Neuromodulatory Correlates of Pupil Dilation. *Front Neural Circuits*. 2018;12:21.
15. Mathôt S. Pupillometry: Psychology, Physiology, and Function. *J Cogn*. 2018;1(1):16.
16. Steinhauer SR, Condray R, and Pless ML. Pharmacological Isolation of Cognitive Components Influencing the Pupillary Light Reflex. *J Ophthalmol*. 2015;2015:179542.
17. Steinhauer SR, et al. Sympathetic and parasympathetic innervation of pupillary dilation during sustained processing. *Int J Psychophysiol*. 2004;52(1):77-86.
18. Wang Y, et al. Relations Between Self-Reported Daily-Life Fatigue, Hearing Status, and Pupil Dilation During a Speech Perception in Noise Task. *Ear Hear*. 2018;39(3):573-82.
19. Beatty J. Task-evoked pupillary responses, processing load, and the structure of processing resources. *Psychol Bull*. 1982;91(2):276-92.
20. Costa VD and Rudebeck PH. More than Meets the Eye: the Relationship between Pupil Size and Locus Coeruleus Activity. *Neuron*. 2016;89(1):8-10.

21. Joshi S and Gold JI. Pupil Size as a Window on Neural Substrates of Cognition. *Trends in Cognitive Sciences*. 2020;24(6):466-80.

22. Varazzani C, et al. Noradrenaline and dopamine neurons in the reward/effort trade-off: a direct electrophysiological comparison in behaving monkeys. *J Neurosci*. 2015;35(20):7866-77.

23. Joshi S, et al. Relationships between Pupil Diameter and Neuronal Activity in the Locus Coeruleus, Colliculi, and Cingulate Cortex. *Neuron*. 2016;89(1):221-34.

24. Nassar MR, et al. Rational regulation of learning dynamics by pupil-linked arousal systems. *Nat Neurosci*. 2012;15(7):1040-6.

25. Aston-Jones G, Foote SL, and Segal M. Impulse conduction properties of noradrenergic locus coeruleus axons projecting to monkey cerebrocortex. *Neuroscience*. 1985;15(3):765-77.

26. de Gee JW, et al. Dynamic modulation of decision biases by brainstem arousal systems. *Elife*. 2017;6.

27. Murphy PR, et al. Pupil diameter covaries with BOLD activity in human locus coeruleus. *Hum Brain Mapp*. 2014;35(8):4140-54.

28. Kahneman D and Beatty J. Pupil diameter and load on memory. *Science*. 1966;154(3756):1583-5.

29. Beck AT, et al. An inventory for measuring clinical anxiety: psychometric properties. *J Consult Clin Psychol*. 1988;56(6):893-7.

30. Beck AT, et al. An inventory for measuring depression. *Arch Gen Psychiatry*. 1961;4:561-71.

31. Mathôt S, Schreij D, and Theeuwes J. OpenSesame: An open-source, graphical experiment builder for the social sciences. *Behavior Research Methods*. 2012;44(2):314-24.

32. Kiehl KA and Liddle PF. Reproducibility of the hemodynamic response to auditory oddball stimuli: a six-week test-retest study. *Hum Brain Mapp*. 2003;18(1):42-52.

33. Banse R and Scherer KR. Acoustic profiles in vocal emotion expression. *J Pers Soc Psychol*. 1996;70(3):614-36.

34. Grandjean D, et al. The voices of wrath: brain responses to angry prosody in meaningless speech. *Nat Neurosci*. 2005;8(2):145-6.

35. Sander D, et al. Emotion and attention interactions in social cognition: brain regions involved in processing anger prosody. *Neuroimage*. 2005;28(4):848-58.

36. Vandewalle G, et al. Spectral quality of light modulates emotional brain responses in humans. *Proc Natl Acad Sci U S A*. 2010;107(45):19549-54.

37. Paparella I, et al. Light modulates task-dependent thalamo-cortical connectivity during an auditory attentional task. *Commun Biol*. 2023;6(1):945.

38. Beckers E, et al. Impact of repeated short light exposures on sustained pupil responses in an fMRI environment. *J Sleep Res*. 2023:e14085.

39. Berridge CW and Waterhouse BD. The locus coeruleus-noradrenergic system: modulation of behavioral state and state-dependent cognitive processes. *Brain Res Brain Res Rev*. 2003;42(1):33-84.

40. Rajkowski J, Kubiak P, and Aston-Jones G. Locus coeruleus activity in monkey: phasic and tonic changes are associated with altered vigilance. *Brain Res Bull*. 1994;35(5-6):607-16.

41. Bradley MM, et al. The pupil as a measure of emotional arousal and autonomic activation. *Psychophysiology*. 2008;45(4):602-7.

42. Gilzenrat MS, et al. Pupil diameter tracks changes in control state predicted by the adaptive gain theory of locus coeruleus function. *Cogn Affect Behav Neurosci*. 2010;10(2):252-69.

43. Szabadi E. Functional Organization of the Sympathetic Pathways Controlling the Pupil: Light-Inhibited and Light-Stimulated Pathways. *Front Neurol*. 2018;9:1069.

44. Gaggioni G, et al. Neuroimaging, cognition, light and circadian rhythms. *Front Syst Neurosci*. 2014;8:126.

45. Vandewalle G, et al. Effects of light on cognitive brain responses depend on circadian phase and sleep homeostasis. *J Biol Rhythms*. 2011;26(3):249-59.

46. Viénot F, et al. Domain of metamers exciting intrinsically photosensitive retinal ganglion cells (ipRGCs) and rods. *J Opt Soc Am A Opt Image Sci Vis*. 2012;29(2):A366-76.

SUPPLEMENTARY MATERIAL

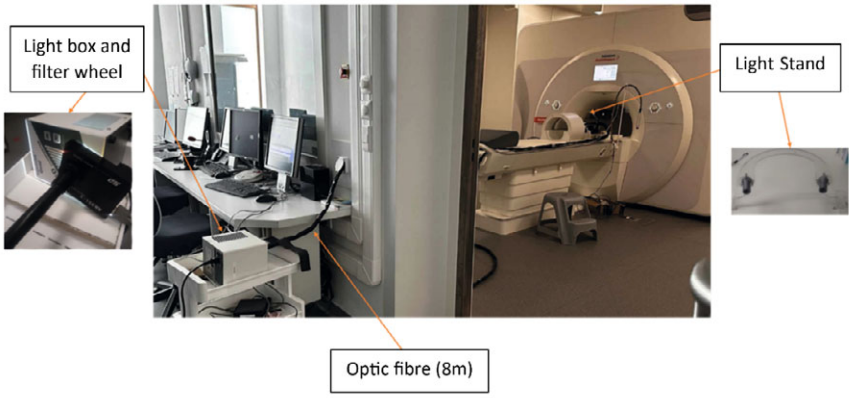

Figure S1. MRI-compatible light system. An 8-m long MRI-compatible dual-branched optic fiber transmitted light from a light box that was stored in the MRI control room. The dual end of the optic fiber was attached to a light stand fitted at the back of the MRI coil. A filter wheel and optical fiber filters (a monochromatic orange light filter (589 nm; full width at half maximum: 10 nm) and a UV long bypass (433 - 1650 nm) filter) were used to create the light conditions needed for the experiment.

Chapter 5

Impact of repeated short light exposures on sustained pupil responses in an fMRI environment

Elise Beckers
Islay Campbell
Roya Sharifpour
Ilenia Paparella
Alexandre Berger
Fermin JA Balda
Ekaterina Koshmanova
Nasrin Mortazavi
Puneet Talwar
Siya Sherif
Heidi IL Jacobs
Gilles Vandewalle

Published in Journal of Sleep Research, 2023

ABSTRACT

Light triggers numerous non-image-forming (NIF), or non-visual, biological effects. The brain correlates of these NIF effects have been investigated, notably using magnetic resonance imaging (MRI) and short light exposures varying in irradiance and spectral quality. However, it is not clear whether NIF responses estimation may be biased by having light in sequential blocks, for example, through a potential carry-over effect of one light onto the next. We reasoned that pupil light reflex (PLR) was an easy readout of one of the NIF effects of light that could be used to address this issue. We characterized the sustained PLR in 13 to 16 healthy young individuals under short light exposures during three distinct cognitive processes (executive, emotional and attentional). Light conditions pseudo-randomly alternated between monochromatic orange light [0.16 melanopic equivalent daylight illuminance (mel EDI) lux] and polychromatic blue-enriched white light of three different levels (37, 92, 190 mel EDI lux). As expected, higher melanopic irradiance was associated with larger sustained PLR in each cognitive domain. This result was stable over the light sequence under higher melanopic irradiance levels compared with lower ones. Exploratory frequency-domain analyses further revealed that sustained PLR was more variable under lower melanopic irradiance levels. Importantly, sustained PLR varied across tasks independently of the light condition pointing to a potential impact of light history and/or cognitive context on sustained PLR. Together, our results emphasize that the distinct contribution and adaptation of the different retinal photoreceptors influence the NIF effects of light and therefore potentially their brain correlates.

INTRODUCTION

Besides its visual function, light affects numerous so-called non-imaging-forming (NIF) or non-visual biological processes, such as the entrainment of circadian rhythms, the regulation of body temperature, the constriction of the pupil, the secretion of hormones, and the stimulation of alertness and cognition [1-4]. The intrinsically photosensitive retinal ganglion cells (ipRGCs), expressing the photopigment melanopsin, constitute a distinct class of retinal photoreceptors heavily involved in mediating the NIF impacts of light [5, 6]. Depending on the light level, ipRGCs also receive inputs from rods and cones that are added to their intrinsic response to modulate the activity of their brain projections [7]. The sensitivity of melanopsin is maximal for blue wavelength light, at about 480 nm, such that the overall sensitivity of ipRGCs and NIF responses is shifted toward the shorter wavelength portion of the visible light spectrum, around 460–480 nm [8, 9].

The diversity of the NIF impacts of light is reflected in the widespread and complex projections of ipRGCs to numerous subcortical regions, including the suprachiasmatic nucleus (SCN), site of the master circadian clock, the ventrolateral preoptic nucleus (VLPO) involved in sleep regulation, and the olivary pretectal nucleus (OPN) playing a key role in pupil light reflex (PLR) [10]. These projections were mainly identified in rodents and translation to humans is not straightforward, making the exact neural mechanisms underlying the NIF impacts of light still insufficiently understood in humans. Over the past two decades, non-invasive techniques such as functional magnetic resonance imaging (fMRI) have started elucidating part of the brain mechanisms underlying the stimulating effect of blue wavelength light on human cognition. These studies led to the idea that this activating effect was mediated through subcortical areas involved in alertness and sleep regulation, and cortical brain regions, in a time- and task-dependent manner [11, 12]. Most of these fMRI studies used repeated short light exposures (1 min or less) alternating between different spectral compositions [13-17]. Whether the effect of light in one block carries over the next one, thus potentially biasing these fMRI results, remains unclear (e.g. exposure to 40 s of monochromatic blue light following 20 s of darkness following 40 s of monochromatic green light).

Here, we addressed this issue by simultaneously acquiring fMRI and pupillometry data. PLR consists of the constriction of the pupil in response to an increased illumination of the retina and constitutes therefore an easy readout of a NIF impact of light. PLR is driven by the combined contribution of rods, cones, and ipRGCs intrinsic response [4]. Rods and cones play a primary role at low irradiance levels and/or over the earliest part of the illumination, while the intrinsic response of ipRGCs has a dominant contribution under relatively higher irradiance levels and/or following the initial period of illumination [18]. While pupil constriction is robustly affected by light, it shows signs of progressive adaptation with a gradual pupil dilation in continuous exposure with a rate of change dependent on the irradiance level [18].

Importantly, the diameter of the pupil can also fluctuate over prolonged periods independently from changes in luminance through ongoing cognitive activity, e.g. increase in pupil size in the high-reward versus low-reward condition, or during emotionally arousing stimuli compared to neutral ones [19-21]. However, whether these prolonged fluctuations impact PLR as a function of the cognitive context is not known. Interestingly, these non-luminance fluctuations may be driven in part by the tonic activity of the locus coeruleus (LC)-noradrenergic system, which is suggested as an important region of the brainstem mediating part of the NIF impacts of light [22, 23]. Quantification of these fluctuations under various light exposures may therefore inform on the activity of the LC underlying the NIF responses to light.

In the present study, we sought to characterize the sustained pupil response during an fMRI protocol including different cognitive tasks under short light exposures. Participants were exposed to pseudo-randomly alternating short blocks of different irradiance levels, expressed in melanopic (mel) equivalent daytime illuminance (EDI) lux: darkness (< 0.1 lux), exposed to a low-level monochromatic orange light (0.16 mel EDI lux), or 3 intensities of blue-enriched polychromatic white light (6500 K; 37, 92, and 190 mel EDI lux). While under light, participants completed executive, emotional, and attentional tasks, respectively lasting 25, 20 and 15 min. We aimed to replicate the larger sustained PLR under higher irradiance levels and to assess whether sustained PLR was stable across tasks and time. Under higher melanopic irradiance levels, we expected a stronger sustained PLR not modulated by cognitive processes or

protocol time. We also conducted exploratory frequency-domain analyses on sustained PLR variability under different light conditions and cognitive contexts to potentially relate them to LC activity [24].

METHODS

The data used in this paper arise from a large study that is leading to [25, 26] and will lead to several publications. While the main goals of the larger study deal with fMRI data and aspects, pupil measures were included for secondary intermediate objectives focusing on the pupil data themselves (as in the present paper and in [25]) as well as for other objectives putting together pupil and MRI data [26]. The assumptions, objectives and hypotheses of the different papers are as independent as possible to reduce statistical inference issues across manuscripts.

Participants

In total, twenty-two healthy young adults (15 females; age (mean ± SD) 23.3 ± 4.3 years) were recruited to take part in this study after providing written informed consent. All participants were screened via semi-structured interviews and clinical questionnaires to assess exclusion criteria such as history of major psychiatric or neurological disorders, sleep disturbances and extreme chronotypes. They scored within normal ranges on the 21-item Beck Anxiety Inventory [27], the Beck Depression Inventory II [28], the Epworth Sleepiness Scale [29], the Horne-Östberg questionnaire [30], the Pittsburgh Sleep Quality Index [31], and the Seasonal Pattern Assessment Questionnaire [32].

All participants were non-smokers, eligible for MRI scanning, and free of psychoactive medications. Although no thorough ophthalmologic examination was performed, none of the participants reported ophthalmic disorders or color blindness. All participants reported normal hearing abilities. We excluded participants with a body mass index (BMI) above 28 kg/m^2, excessive caffeine (>4 caffeine units per day) or alcohol consumption (>14 alcohol units per week), travelling through more than one time zone during the last 2 months or working

on non-regular office hours. Women were not pregnant or breastfeeding. Due to the exclusion of data sets with bad or missing data, the analyses of the executive, emotional and attentional tasks included 16, 13 and 16 participants, respectively. A summary of participants' characteristics respective to each task can be found in Table 1. The protocol was approved by the Ethics Committee of the Faculty of Medicine of the University of Liège and all participants received monetary compensation for their participation.

Table 1. Study sample characteristics

	Total sample (N = 22)	**Executive task (N = 16)**	**Emotional task (N = 13)**	**Attentional task (N = 16)**
Age (years)	23.27 ± 4.33	23.25 ± 4.7	23.92 ± 4.66	24.13 ± 4.1
BMI (kg/m²)	21.38 ± 2.52	20.93 ± 2.34	21.48 ± 1.65	21.68 ± 2.31
Education (years)	14.2 ± 3.14	14.2 ± 3.45	14.45 ± 2.58	15.07 ± 2.43
BAI	6.25 ± 5.79	5.93 ± 6.17	8.36 ± 6.58	6.33 ± 4.59
BDI-II	6.7 ± 5.53	5.53 ± 5.8	7.45 ± 5.89	6.73 ± 5.42
ESS	6.4 ± 3.1	5.93 ± 3.06	7.09 ± 3.53	6.33 ± 2.69
HO	47.45 ± 9.34	48.07 ± 8.06	46.64 ± 6.47	48.13 ± 9.76
PSQI	4.4 ± 2.76	4.27 ± 2.89	4.73 ± 3.29	4.4 ± 3.02
SPAQ	0.95 ± 0.83	1 ± 0.85	1.09 ± 0.83	1 ± 1.07
Sex	15 F – 7 M	11 F – 5 M	9 F – 4 M	11 F – 5 M

Characteristics of the total study sample, and of the participants included in the executive, emotional, and attentional tasks, respectively. Average value ± standard deviation (SD). BMI: body mass index. The education level is computed as the number of successful years of study. Scores of the BAI (Beck Anxiety Inventory), BDI-II (Beck Depression Inventory II), ESS (Epworth Sleepiness Scale), HO (Horne-Ostberg), PSQI (Pittsburgh Sleep Quality Index) and SPAQ (Seasonal Pattern Assessment Questionnaire). F: Female, M: Male.

Protocol

All participants followed a loose sleep-wake schedule for a 7-day period preceding the experiment at their habitual sleep and wake-up time (± 1 h) to avoid excessive sleep restriction while maintaining uniform realistic life conditions. Adhesion to the pre-defined schedule was verified through wrist actimetry (AX3 accelerometer, Axivity, United Kingdom) and sleep diaries.

Participants were asked not to take nap during this period. Volunteers were requested to refrain from all caffeine and alcohol-containing beverages, and extreme physical activity for at least 3 days before participating in the study. The experiment took place either in the morning (N = 18) or in the evening (N = 4) intending to investigate the time-of-day effect of light exposure on brain functions and behavior in the future. Although controlled for in statistical analyses, the later time-of-day aspect will not be considered in the present paper. Data acquisitions took place between December 2020 and May 2022. On the day of the experiment, participants arrived in the laboratory 1.5 to 2 h after their habitual wake-up time or 1.5 to 2 h before their habitual bedtime and were exposed to 5 min of bright white light (~1000 lux) followed by 45 min of dim light (<10 lux) to control for recent light history. During the dim light adaptation period, detailed instructions were given regarding the study, MRI environment and cognitive tasks to be performed in the MR scanner (Figure 1). Task practices were also completed on a laptop with low-mode luminance level (<10 lux at eye level) aiming for an accuracy score of at least 75%.

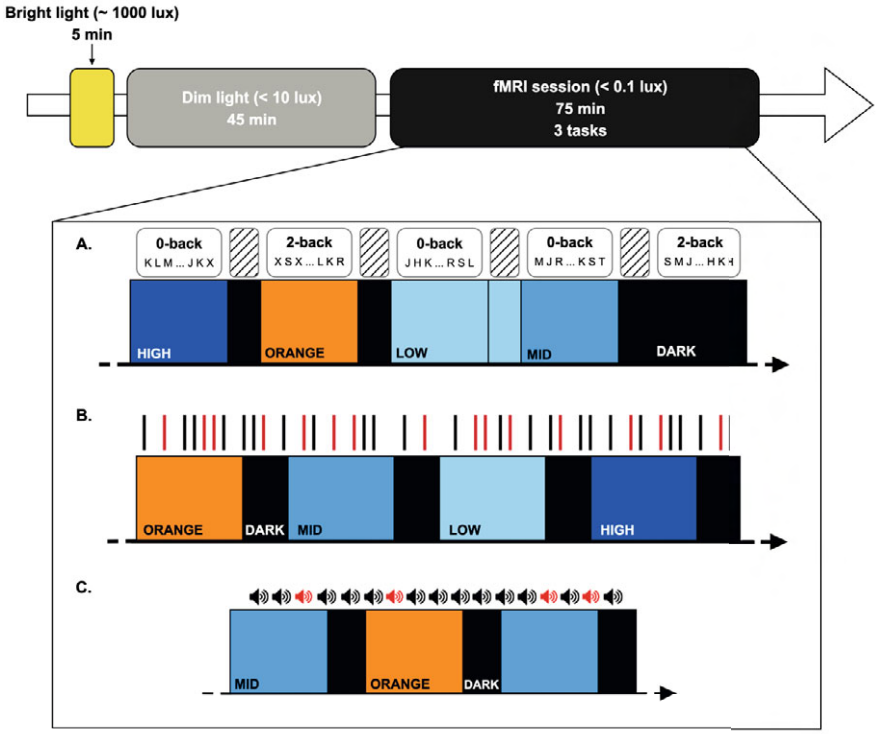

Figure 1. Graphical representation of the experimental protocol. Following a 7-day period of loose sleep–wake schedule (verified through wrist actimetry and sleep diaries), participants arrived at the laboratory 1.5-2 h after their wake-up time, or 1.5-2 h before their bedtime. After a light adaptation period (5 min of bright light [~1000 lux] followed by 45 min of dim light [<10 lux]), participants completed three auditory cognitive tasks during a functional magnetic resonance imaging (fMRI) session. Tasks, respectively, probed executive, emotional and attentional processes. While the protocol always started with the executive task, the order of the emotional and attentional tasks was counter-balanced across participants. **A)** Detailed experimental design for the executive task. The task consisted of a two-level variant of the n-back task: 0- and 2-back. Participants had to detect whether the current item matched the predefined letter "K" (0-back), or whether the current item was identical to the letter presented two items earlier (2-back). Task blocks included 15 items, lasted 30 s, and were interleaved with 10-s rest periods (represented by dashed areas). While performing the task, participants were exposed to pseudo-randomly alternating polychromatic white light of three different intensities (LOW: 37; MID: 92; HIGH: 190 mel EDI lux; 6500 K) and a monochromatic orange light (0.16 mel EDI lux; 589 nm). In total, 11 blocks for each light condition were included. Each light block lasted 30–40 s. **B)** Detailed experimental design for the emotional task. The task consisted of a pure gender discrimination of auditory vocalizations while being exposed to the pseudo-randomly alternating polychromatic white light of three different intensities (LOW: 37; MID: 92; 8 HIGH: 190 mel EDI lux; 6500 K) and a monochromatic orange (0.16 mel EDI lux; 589 nm) light. Five blocks of each light condition were included.

Each light block lasted 30–40 s and was followed by a 20-s period of darkness. Untold to the participants, vocalizations were pronounced with angry (red bars) and neutral (black bars) prosody, pseudo-randomly and equally distributed across the four light conditions. **C)** Detailed experimental design for the attentional task. The task consisted of the detection of rare deviant tones (20%), within a stream of frequent standard tones (80%). Whilst completing the task, participants were pseudo-randomly exposed to a polychromatic white light (MID: 92 mel EDI lux; 6500 K) and a monochromatic orange light (0.16 mel EDI lux; 589 nm). Seven blocks for both light conditions were included. Each block lasted 30 s, and was followed by a 15-s period of darkness. Standard (black) and deviant (red) stimuli were equally distributed across the two light conditions. Mel EDI lux, melanopic equivalent daytime illuminance lux.

Light exposure

In the MRI, light was administered through a computer-controlled MR-compatible set-up designed in-lab and consisting of 3 main parts. First, a polychromatic blue-enriched white LED light source (SugarCUBE, Ushio America, CA, USA) with various intensities; second, a motor-driven filter wheel (AB300-Series, Spectral Products, NM, USA) allowing the automated changes in light conditions respectively using an Ultra Violet (UV) long bypass filter (433–1650 nm) or a monochromatic orange light filter (589 nm); third, an 8-m long metal-free dual-end optic fiber (Setra Systems, MA, USA) transmitting the light to participants' eyes. A stand placed at the back of the head coil allowed the reproducible fixation and orientation of the optic fiber ends toward the inside of the coil and created a relatively uniform and indirect illumination toward participants' eyes.

While performing functional tasks in the MR environment, participants were either maintained in darkness (<0.1 lux) or exposed to short light blocks which could be of 4 types, varying in irradiance level and spectral composition. Light pseudo-randomly alternated between a monochromatic orange light ($4.24x10^{12}$ photons/cm^2/s; 589 nm, 10 nm at full width half-maximum; 0.16 mel EDI lux) and a polychromatic LED light enriched in blue wavelengths of three different irradiance levels (6500 K; 37, 92 and 190 mel EDI lux). Spectra of the lights were assessed at the level of the end of the optic fiber (AvaSpec-2048, Avantes, The Netherlands). Irradiance could not be measured directly in the magnet, but the light source was calibrated (840-C power meter, Newport, Irvine, CA). Light spectra and light characteristics can be found in Figure 2 and Table 2, respectively.

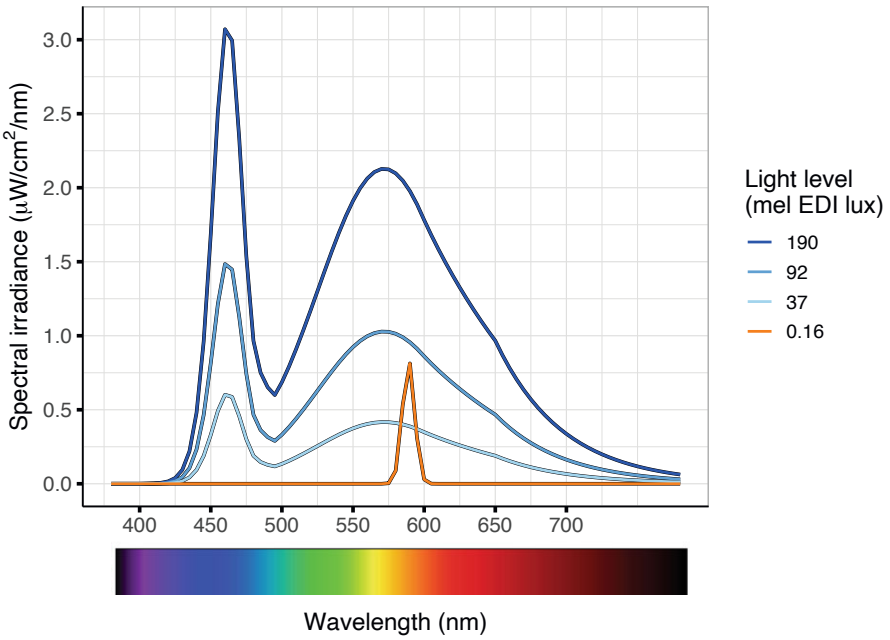

Figure 2. Spectrum power distribution of the four different light conditions. Monochromatic orange light (0.16 mel EDI lux), 589 nm; Polychromatic white LED light enriched in blue wavelengths of three distinct irradiance levels (37, 92, 190 mel EDI lux; 6500 K). Mel EDI lux, melanopic equivalent daytime illuminance lux. Adapted from Campbell et al., 2023 [25] .

Table 2. Light characteristics of the four light conditions

	Low	Mid	High	Orange
Photopic illuminance (lux)	47	116	240	7.5
Peak spectral irradiance (nm)	460	460	460	590
Melanopic EDI lux (ipRGCs)	37	92	190	0.16
Rhodopic EDI lux (Rods)	39	97	201	0.94
Cyanopic EDI lux (S-cones)	32	79	163	0
Chloropic EDI lux (M-cones)	44	110	227	5
Erythropic EDI lux (L-cones)	46	113	233	8
Irradiance (μW/cm²)	15	36	74	1.4
Photon flux (1/cm²/s)	4.12E+13	1.02E+14	2.10E+14	4.24E+12
Log photon flux (log_{10}) (1/cm²/s)	13.61	14.01	14.32	12.63
Narrowband peak	-	-	-	589
Narrowband FWHM	-	-	-	10

Characteristics of polychromatic blue-enriched white light of 3 irradiance levels (Low: 37 mel EDI lux, Mid: 92 mel EDI lux, High: 190 mel EDI lux) and monochromatic orange light (589 nm). FWHM, full width at half-maximum; ipRGCs, intrinsically photosensitive retinal ganglion cells; mel EDI lux, melanopic equivalent daytime illuminance lux.

Auditory cognitive tasks

The fMRI session included 3 auditory tasks probing cognitive functions such as executive, emotional, and attentional processes lasting about 25, 20, and 15 min, respectively. Figure 1 depicts an overview of the global protocol. The executive task consisted of an auditory variant version of the n-back task [33] with two levels presented in distinct blocks: 0-back and 2-back. Participants had to detect whether the current item matched the predefined letter "K" (0-back), or whether the current item was identical to the letter presented 2 items earlier (2-back). Each task block lasted 30 s and therefore included 15 items. Task blocks were interleaved with 10-s rest period. Blocks and task levels were pseudo-randomly presented across all light conditions. Overall, the executive task included 11 blocks of each of the 4 melanopic irradiance levels. Light blocks lasted between 30 and 40 s.

During the emotional task, participants were asked to indicate the gender of meaningless auditory vocalizations, while ignoring the negative

and neutral prosodies of these stimuli [34]. In total, 240 auditory stimuli were pronounced by professional actors (50% female). Tasks events were pseudo-randomly and equally spread over the four light conditions. The emotional task included 5 blocks for each of the four melanopic irradiance levels. Blocks of light lasted 30 to 40 s and were interleaved by 20 s of darkness.

The attentional task was a mismatch negativity, or oddball task [35]. Participants had to report the detection of rare deviant tones (20%, 1000 Hz, 100 ms) within a stream of frequent standard tones (80%, 500 Hz, 100 ms). To maintain task duration acceptable for the participants and below 15 min, only two light conditions were included in the attentional task: one level of polychromatic, blue-enriched LED light (6500 K; 92 mel EDI lux), and the monochromatic orange light. In total, 315 tasks events were pseudo-randomly spread over the two melanopic irradiance levels. The attentional task included 7 blocks for both light conditions. Participants were exposed to 30 s of light blocks interleaved by 15 s of darkness.

The executive task being the longest and the most demanding, the protocol always started with the latest to minimize the effect of time in the overall experiment and fatigue on this particular task. The order of the emotional and attentional tasks was counter-balanced across participants. Auditory stimuli and instructions were delivered through MR-compatible earplugs (Sensimetrics, Malden, MA) controlled via a computer running OpenSesame software (version 3.2.8) [36]. Prior to the start of the experiment, a volume check was performed to ensure the scanner noise was not undermining a proper perception of auditory stimuli. Responses to fMRI tasks were collected through an MR-compatible button box (Current Design, Philadelphia, PA) placed in the participants' dominant hand. At the end of each task, participants stayed in near darkness for about 5 min which were used to acquire a control MRI sequence, recalibrate the eye-tracking system, and repeat instructions to the participant.

Data acquisition

Data were acquired while participants were lying in a 7T MAGNETOM Terra MR scanner (Siemens Healthineers, Erlangen, Germany) with a 32-channel receiver and 1-channel transmit head coil (Nova Medical, Wilmington, MA, USA). Pupil

size was continuously measured using an MR-compatible infrared eye-tracking system at a sampling rate of 1000 Hz (EyeLink 1000Plus, SR Research, Ottawa, Canada) with a monocular recording (right pupil was used). The eye-tracking system returned pupil area as an arbitrary unit, i.e. the number of pixels considered part of the detected pupil. Before the execution of each task, a pupil calibration was performed. Besides acquiring pupil data, the eye-tracking system enabled the constant monitoring of participants' sleepiness.

Pupil signal preprocessing

Pupil data analyses were conducted offline in MATLAB R2019b (MathWorks, MA, USA) where the data was cleaned at first. Identified blinks were replaced using linear interpolation and data were smoothed using the *rlowess* built-in robust linear regression function. Data sets with more than 25% of missing or corrupted data were excluded from the analysis.

Since we were interested in sustained PLR, the first 2 s of each light block were discarded prior to averaging pupil value per light block. Pupil size averages were normalized with respect to the average pupil size during the darkness periods prior to averaging per light condition. For frequency domain analyses, power spectral density (PSD) was estimated via Welch's method through the built-in *pwelch* function on 4-s rectangular windows with a 50% overlap, excluding missing values. In line with previous studies, the frequency band of interest was set between 0.5 and 4 Hz with 0.5-Hz sensitivity [22, 37, 38]. Total power per light condition between 0.5 and 4 Hz was first computed by summing PSD values in this frequency range, prior to being normalized to the total power under darkness periods, and then converted to dB through a $\log_{10}$ scaling.

Statistics

Generalized linear mixed models (GLMM) implemented in SAS 9.4 (SAS Institute Inc, NC, USA) were used with averaged normalized sustained pupil value as the dependent variable, subject as random effect, and melanopic irradiance, task, and block order (when applicable) as repeated measures [autoregressive (1) correlation]. As the literature suggests that the NIF impacts of light vary with sex, time of day, and within the age range of our sample, we included

these as covariates of the models [15, 39]. We further included BMI as a proxy measure of overall health/fitness status. The statistical significance threshold was set at $\alpha < 0.05$. The distribution of the dependent variable was assessed prior to each model and the GLMM was set accordingly. Cook's distance > 1 was used as cut-off to detect outlier values. No outliers were detected in the analyses of the executive, emotional and attentional tasks. Partial R^2 (R^2*) values were computed to estimate the effect sizes of significant effects in each model [40]. Interactions and main effect always consisted of confirmatory tests while unplanned post hoc contrasts consisted of exploratory tests.

The first implemented model tested for simple effects, along with interaction effects, of melanopic irradiance and task nature on the total averaged normalized pupil size while considering the three tasks altogether, i.e. M1: Total averaged normalized pupil size ~ melanopic x task + sex + age + BMI + time-of-day. Post hoc analyses were conducted on the task nature while using a Tukey adjustment. Then, a second model tested for simple effects of melanopic irradiance in each task separately and post hoc analyses were conducted on melanopic irradiance levels, i.e. M2: Total averaged normalized pupil size ~ melanopic + sex + age + BMI + time-of-day. In order to investigate the sustained pupil response stability across the light sequence for each task, the averaged normalized pupil size from the first and the last block of each light condition were tested in a third model for simple effects and interaction against melanopic irradiance and block order, i.e. M3: Block averaged normalized pupil size ~ melanopic x block order + sex + age + BMI + time-of-day. Post hoc analyses were conducted on this interaction and results were corrected for multiple comparisons using a Tukey adjustment.

In the scope of exploratory frequency-domain analyses, a fourth GLMM was implemented with total normalized PSD as the dependent variable, subject as random effect, and melanopic irradiance as a repeated measure [autoregressive (1) correlation], while adjusting for sex, age, BMI, and time of day, i.e. M4: Total normalized PSD ~ melanopic + sex + age + BMI + time-of-day. For the executive task, one dataset was reported as an outlier. As a consequence, the analysis of the executive, emotional and attentional tasks included 15, 13 and 16 participants, respectively. Results from models including and excluding the outlier were not differing. This model tested for simple effects

of melanopic irradiance on the total normalized PSD in the 0.5–4-Hz frequency range. Post hoc analyses were conducted on melanopic irradiance levels and results were corrected for multiple comparisons using a Tukey adjustment.

RESULTS

Melanopic EDI lux level-dependent sustained pupil response

Sustained averaged pupil response was first related to melanopic irradiance levels (0.16, 37, 92 and 190 mel EDI lux) considering all cognitive contexts together (M1 model, see Methods). The GLMM yielded a significant main effect of the irradiance level ($F_{(3,37)} = 530.6$, $p < 0.0001$, $R^2* = 0.98$), such that higher melanopic irradiance level was associated with larger sustained PLR. Importantly, a significant main effect of the task ($F_{(2,52)} = 3.8$, $p = 0.03$, $R^2* = 0.13$) was detected, but, critically, no evidence for a significant interaction effect between task and melanopic irradiance ($F_{(4,37)} = 0.85$, $p = 0.5$). Post hoc analyses revealed no evidence of significant difference in pupil response between the attentional and the emotional tasks ($t_{55} = -0.09$, $p = 0.996$), while statistical trends were observed between the executive task and both the emotional ($t_{63} = 2.38$, $p = 0.053$) and attentional tasks ($t_{55} = 2.1$, $p = 0.099$) such that the PLR was suggested to be reduced in the executive task as compared to the two other tasks (Supplementary Table 1).

Then, taking each task individually (M2 model), a significant main effect of the melanopic irradiance level was also observed (Executive: $F_{(3,15)} = 289.8$, $p < 0.0001$, $R^2* = 0.98$; Emotional: $F_{(3,12)} = 165.1$, $p < 0.0001$, $R^2* = 0.98$; Attentional: $F_{(1,6)} = 332.5$, $p < 0.0001$, $R^2* = 0.98$), such that higher melanopic irradiance was associated with higher PLR for each cognitive context (Figure 3; Supplementary Table 2). No effect of sex, age, BMI, or time of day was detected (Executive: $F_{(1,11)} < 1.07$, $p > 0.32$; Emotional: $F_{(1,8)} < 1.36$, $p > 0.28$; Attentional: $F_{(1,10)} < 1.56$, $p > 0.24$). For each task, significant differences ($p < 0.002$) were observed between each pair of melanopic irradiance levels.

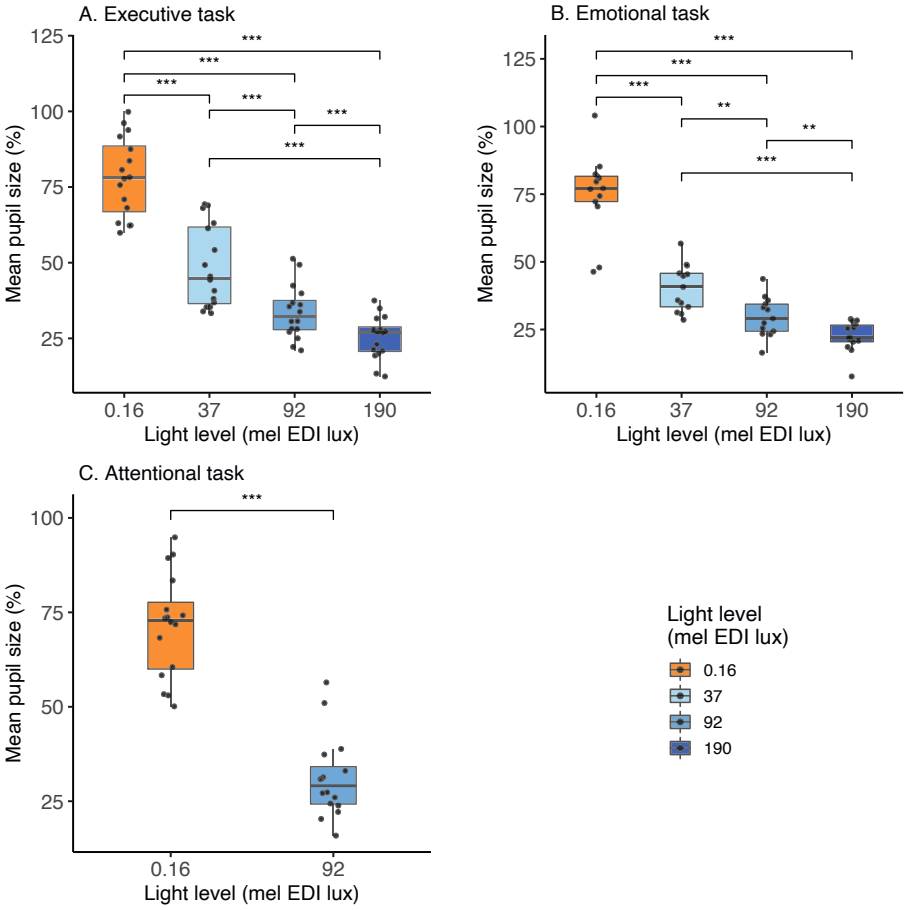

Figure 3. Sustained pupil light reflex across mel EDI lux levels and tasks. Darkness-normalized mean pupil size under each light level (0.16, 37, 92, 190 mel EDI lux) for the **A)** executive, **B)** emotional and **C)** attentional tasks. Statistical significance on the post hoc analysis after Tukey adjustment (***: $p < 0.0001$, **: $p < 0.002$). Mel EDI lux: melanopic equivalent daytime illuminance lux.

Sustained pupil response stability

The effect of time in protocol and light block sequence was evaluated on the sustained pupil response stability in each task separately (Figure 4). Sustained PLR was compared during the first versus last block of each melanopic irradiance level (Figure 4A,C,E). GLMM analysis (M3 model) revealed a significant

interaction between irradiance level and light block order while controlling for sex, age, BMI, and time of day for the executive task only ($F_{(3,33)}$ = 4.8, p = 0.007, R^{2}* = 0.3). We failed to find significant interactions between melanopic irradiance level and block order for the emotional and attentional tasks ($F_{(3,26)}$ = 1.03, p = 0.4, and $F_{(1,16)}$ = 1.96, p = 0.18, respectively). Post hoc analyses compared light block order against each irradiance level in the executive task, but also in the other tasks. These post hoc analyses yielded significant differences between the first and last light blocks for 0.16 and 37 mel EDI lux levels, for all three tasks [0.16 mel EDI lux: t_{33} = -2.26, p = 0.031 (Executive), t_{26} = -2.37, p = 0.025 (Emotional), t_{16} = -3.11, p = 0.007 (Attentional); 37 mel EDI lux: t_{33} = -3.26, p = 0.003 (Executive), t_{26} = -2.66, p = 0.013 (Emotional)]. No evidence of significant difference was detected between the first and last blocks for the 92 and 190 mel EDI lux conditions for all three tasks (p > 0.17; Supplementary Table 3). Taken together, these results revealed smaller sustained PLR over the last block compared to the first block when considering lower melanopic irradiance levels.

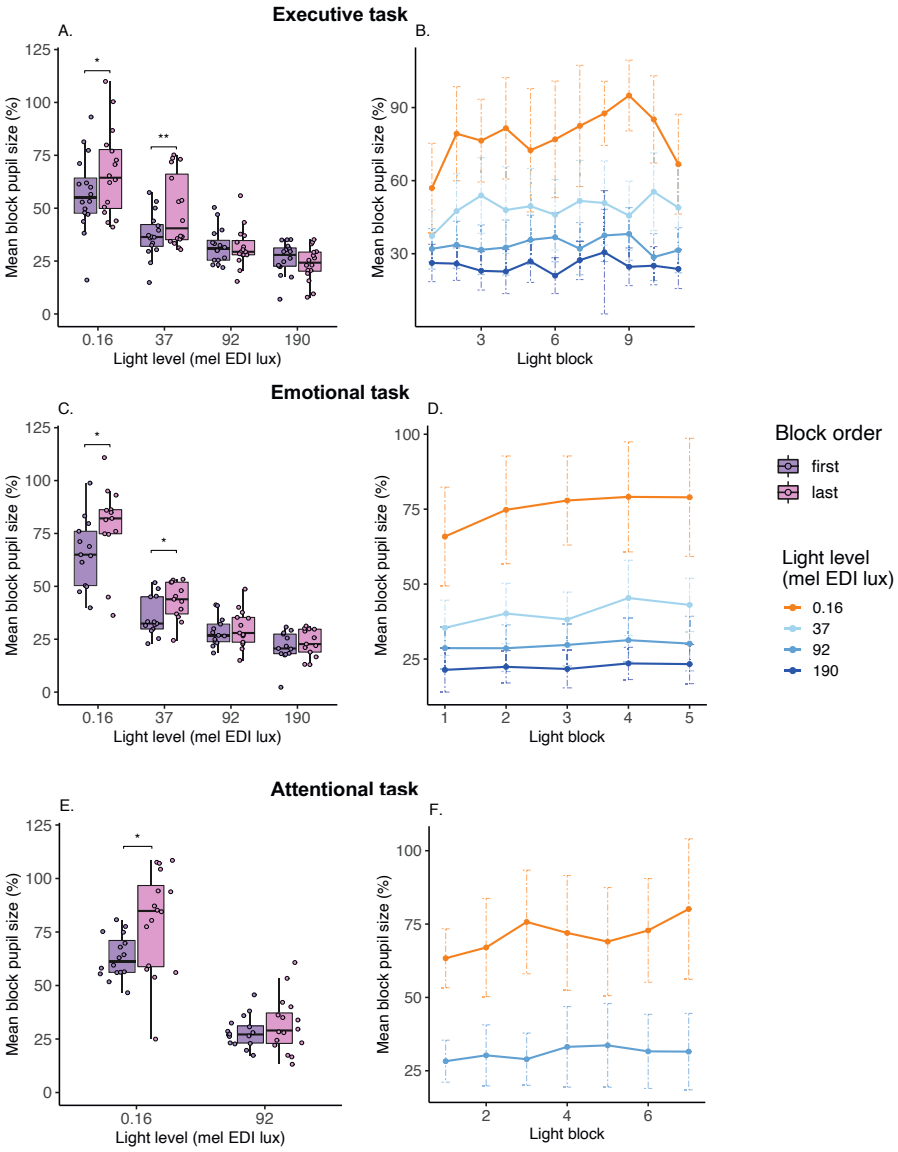

Figure 4. Pupil light reflex stability across light blocks. **Left:** darkness-normalized mean pupil size during the first and last block of each light level for all three cognitive tasks. Statistical significance on the post hoc analysis after Tukey adjustment (**: $p < 0.005$, *: $p < 0.05$). **Right:** for illustrative purposes, complete evolution of darkness-normalized mean pupil size per block under each light level for the three cognitive tasks. **A-B)** Executive task, 0.16, 37, 92, 190 mel EDI lux. **C-D)** Emotional task, 0.16, 37, 92, 190 mel EDI lux. **E-F)** Attentional task, 0.16, 92 mel EDI lux. Mel EDI lux, melanopic equivalent daytime illuminance lux.

Frequency analysis of sustained pupil response

To better characterize the influence of melanopic irradiance level on pupil response variability, exploratory frequency-domain analyses were performed on the PSD of sustained PLR in the 0.5–4-Hz frequency range for each task separately (Figure 5). The GLMM with total power as dependent variable (M4 model) yielded a significant main effect of melanopic irradiance level for all three tasks (Executive: $F_{(3,13)} = 23.7$, $p < 0.0001$, $R^2* = 0.85$; Emotional: $F_{(3,16)} = 130.75$, $p < 0.0001$, $R^2* = 0.96$; Attentional: $F_{(1,5)} = 40.2$, $p = 0.0011$, $R^2* = 0.89$), such that greater PSD is observed under lower melanopic irradiance level. Post hoc analyses on irradiance levels highlighted significant differences in the emotional and attentional tasks for all light levels ($p < 0.0011$). Interestingly, for the executive task, all light levels were significantly different from one another ($p < 0.041$), except the lowest and the highest melanopic irradiance level that showed no evidence of the effect ([0.16–37 mel EDI lux]: $t_{13} = 2.22$, $p = 0.17$; [92–190 mel EDI lux]: $t_{13} = 2.59$, $p = 0.093$; Supplementary Table 4).

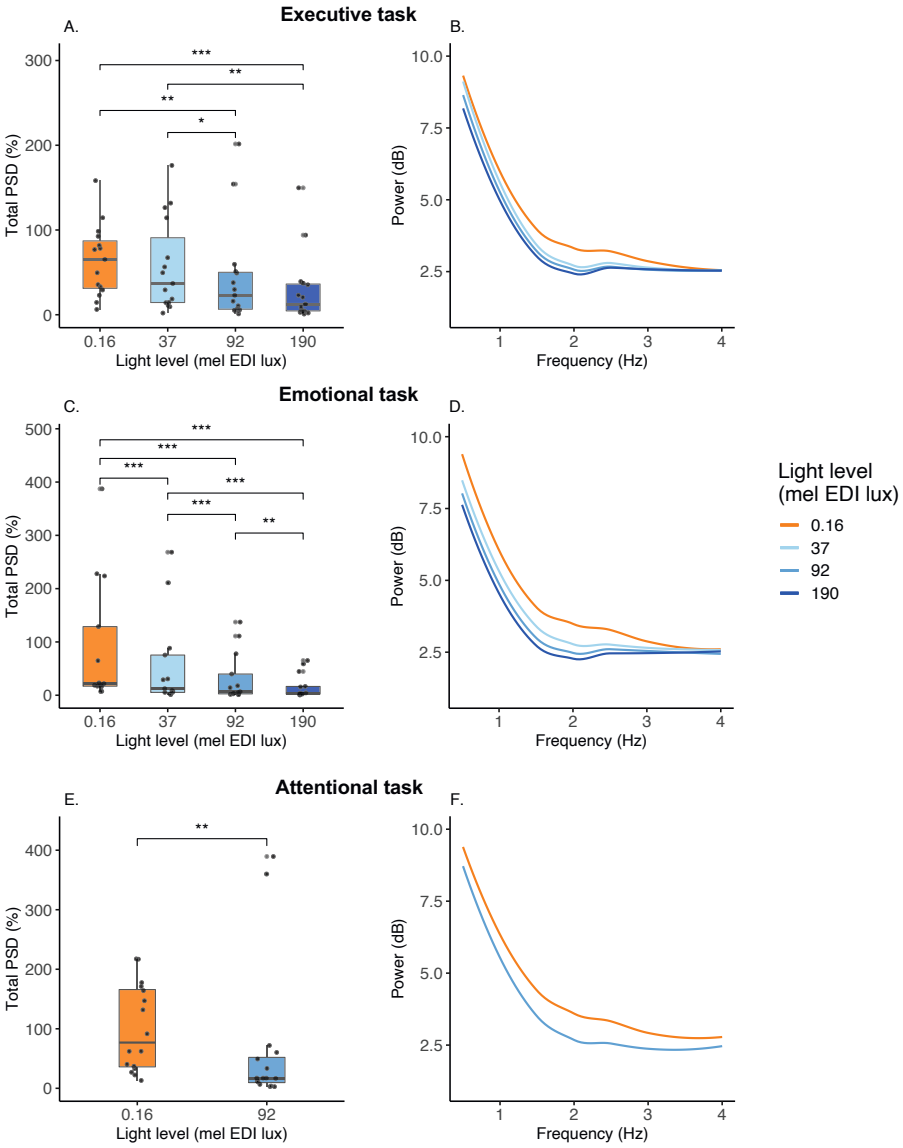

Figure 5. Pupil size oscillations across light conditions. **Left:** dark-normalized total power spectrum density of pupil size across light levels for all three cognitive tasks. Statistical significance on the post hoc analysis after Tukey adjustment (***< 0.0001, **< 0.005 and *< 0.05**). Right:** dark-normalized power spectrum density under various light conditions for all three cognitive tasks. For clarity's sake, standard error areas are not displayed. **A-B)** Executive task, 0.16, 37, 92, 190 mel EDI lux. **C-D)** Emotional task 0.16, 37, 92, 190 mel EDI lux. **E-F)** Attentional task, 0.16, 92 mel EDI lux. Mel EDI lux, melanopic equivalent daytime illuminance lux.

DISCUSSION

We characterized sustained PLR under different cognitive domain and light conditions. Thirteen to 16 healthy young individuals completed 3 different cognitive tasks while in an MRI apparatus and being exposed to repeated pseudo-randomly alternating short light blocks of different melanopic irradiance, as indexed by mel EDI lux. We replicated that a higher melanopic irradiance level leads to a larger sustained PLR. Our analyses further show that this effect is consistent across all three cognitive domains, taken separately. Across each task, sustained PLR was stable in time for higher irradiance levels (92 and 190 mel EDI lux), while sustained PLR decreased from the first until the last block for lower irradiance ones (0.16 and 37 mel EDI lux). To further characterize the variability of the sustained PLR in terms of slow oscillation power density, we found that sustained PLR variability within the 0.5 to 4-Hz range was lower under higher melanopic irradiance. Finally, sustained PLR may vary between the executive and both the attentional and emotional tasks irrespectively of the current light condition.

Although protocols can vary substantially, PLR assessments most often used exposures lasting one to a few minutes separated by a relatively long period of darkness or constant exposure, which allows for readaptation of all retinal photoreceptors to the ambient light level [41-43]. So far, it was unclear whether a neuroimaging protocol where light exposures are shorter (1 min or less) and interleaved with short 10 to 20-s periods in darkness would affect sustained PLR. We used light levels similar to many previous PLR studies [41-43] and first confirm, as expected, that sustained PLR is stronger under higher melanopic irradiance.

Light adaptation mechanisms affect retinal photoreceptors and their associated neural circuits over the course of light exposure to optimize their sensitivity according to the ambient light levels [44]. Since the executive task was always administered first – following 45 min under a dim light – while the other two tasks were following the executive task and its light exposures in a counter-balanced design, one could have expected a progressive reduction in PLR across the protocol. We find however a statistical trend suggesting a reduced sustained PLR during the executive task compared to the following emotional

and attentional tasks, while there was no evidence for a difference between the latter two tasks. The dim light condition and associated adaptation preceding the executive task may have therefore contributed to a lower sensitivity to light, although we do not observe a difference in baseline sustained pupil size under complete darkness between tasks ($p > 0.27$; data not shown). The nature of the ongoing cognitive task may also have influenced sustained PLR since pupil size is influenced by the cognitive context [19]. The trends we observe should be verified in a larger sample allowing to fully separate the light history from the cognitive context. We emphasize that, despite overall changes in sustained PLR across tasks, we found no evidence of an existing relationship between tasks and irradiance light levels. The putative light adaptation mechanisms do not seem therefore to significantly affect the relative variations in sustained PLR with irradiance levels across tasks. It remains therefore appropriate to compare tasks with respect to the relative changes in corneal irradiance levels, despite the fact that the attentional task only included two irradiance levels preventing a complete comparison across the tasks.

Overall, our results emphasize that, together with cognitive context, recent light history may influence sustained PLR assessment and should therefore be carefully taken into account. Our findings question the appropriateness of the light history standardization period that was implemented in the protocol, with 5 min of bright (1000 lux) light exposure followed by 45 min under dim light (<10 lux). Both human and rodent data suggest that melanopsin-dependent photoreception is the main driver of NIF responses to light under more naturalistic conditions, i.e. not following dim light or dark adaptation [44]. Standardization using higher ambient light levels (and potentially over shorter periods of time) would simplify experimental procedures and reduce the glare effect most participants experience during the first block(s) of exposure to light while maintaining, or potentially improving, the sensitivity to melanopsin-driven photoreception. This warrants future investigations comparing different pre-recording standardization procedures.

The fact that sustained PLR was reduced from the first to the last block of light for mel EDI lux levels inferior and equal to 37 mel EDI lux suggests that light adaptation did affect the sensitivity of photoreceptor-mediated pupil responses over time within a task. Since rods and cones contribute more than

melanopsin-dependent photoreception to PLR at lower light levels [18, 45-47], we suspect that light adaptation of either rods or cones, or both, could contribute to a reduction in PLR over time. At higher melanopic irradiance levels, PLR is more heavily driven by the intrinsic melanopsin-dependent photoreception of ipRGCs which show a much slower adaptation to the ambient light level [18]. Our data support therefore that the intrinsic photoreception of ipRGCs drives the relatively stable PLR we observe from the beginning until the end of each task for melanopic irradiance of ~90 mel EDI lux or higher. We stress, however, that this remains hypothetical as we did not measure directly rod, cone or ipRGC function and light adaptation.

Studies assessing neural correlates of NIF effects light often used repeated alternating short light exposures with varying irradiances and spectral compositions [11, 13, 15-17]. Although light characteristic descriptions were not always exhaustive, these studies seem to have mostly used melanopic irradiance levels higher than ~90 and up to ~330 mel EDI lux, except for a few cases which also included a light condition of ~20 mel EDI lux in addition to higher irradiances [15-17]. Hence, the present results support that these studies did not suffer from important bias related to photoreceptor-mediated pupil responses over short exposures (1 min or less) separated by brief periods of darkness. The fMRI data associated with the present study will nevertheless need to account for potential photoreceptors' adaptation, especially at low irradiance level, if not in their analysis, i.e. by including averaged sustained pupil size per block as covariate (or regressor), at least in the interpretation of the results.

The finding that higher melanopic irradiance is associated with lower power density over the 0.5–4-Hz frequency band may appear surprising as it shows that pupil response oscillations (over 0.25 to 2-s periods) were less important at higher irradiances. This could indeed imply a reduced tonic activity of the LC when light is known to stimulate alertness and higher alertness is associated with higher LC activity [48]. Previous research reported, however, higher power densities of fast pupil size oscillation under lower background luminance [24, 37, 38]. In addition, increasing arousal is associated first with a higher rate of tonic LC firing, and then with a switch to a phasic firing of the LC activity [48]. The reduced power density could therefore be the consequence

of a change in the firing pattern of the LC. It could also result from a change in the frequency of the fast oscillations in pupil diameter outside the frequency band we considered. In a companion paper, we focus on transient changes in pupil size that are arguably related to the phasic activity of the LC [25]. Yet, the transient dilations of the pupil are induced by the auditory stimulations included in the cognitive task recorded in fMRI [49]. We are therefore not in a position to assess a putative LC phasic activity that would not be related to the sensory stimulations and contribute to changes in power density of pupil size variations. Importantly also, since pupil size is not governed by the LC but rather influenced by it, our findings could be driven by other brain structures.

We stress that our research bears some limitations. First, we included 4 distinct melanopic irradiance levels, preventing the establishment of a true action spectrum of the PLR under the conditions of our experiments [50]. In addition, two distinct spectral qualities or colors were used so that visual responses to the perception of a control orange exposure could be subtracted from the response to the active blue-enriched polychromatic light in the analyses of fMRI data [14, 17]. This implies that part of our findings regarding PLR may be related to spectral differences and not only to irradiance levels. Given the relative homogeneity of our findings across tasks, we remain confident that the significant differences we find are robust. In addition, as our primary interest was to relate sustained PLR to melanopic irradiance levels, we did not consider the initial phasic portion of PLR over the first 2 s of the exposure which is known to rely more heavily on rods and/or cone photoreception [18]. Hence, we cannot exclude that changes in the sensitivity of these photoreceptors impacted this initial portion of the PLR. Finally, we emphasize that a pseudo-random sequence of block of light as in the present study does not allow isolating a true carry over effect but rather allows assessing whether it may or may not bias the results of the study.

Light is an important environmental factor affecting brain functions, behavior, health and well-being. Given the expansion of artificial light usage, a detailed understanding of its NIF impacts is timely. With this study, we emphasize that PLR is an easy readout of one of the multiple NIF effects of light and that it can be used as a window to the underlying brain mechanisms. We provided information on the association between sustained PLR and

melanopic irradiance levels under the specific context of an fMRI protocol. We show that depending on the experimental conditions, photoreceptor-mediated pupil responses may or may not significantly affect the NIF responses of interest. We further suggest that the light adaptation period may influence PLR. Since PLR can be easily characterized across different species, our results will contribute to the translation of animal findings to human beings and vice-versa [46].

REFERENCES

1. Cajochen C, et al. High sensitivity of human melatonin, alertness, thermoregulation, and heart rate to short wavelength light. *J Clin Endocrinol Metab*. 2005;90(3):1311-6.
2. Fisk AS, et al. Light and Cognition: Roles for Circadian Rhythms, Sleep, and Arousal. *Front Neurol*. 2018;9:56.
3. Lok R, et al. Light, Alertness, and Alerting Effects of White Light: A Literature Overview. *J Biol Rhythms*. 2018;33(6):589-601.
4. Gamlin PD, et al. Human and macaque pupil responses driven by melanopsin-containing retinal ganglion cells. *Vision Res*. 2007;47(7):946-54.
5. Berson DM, Dunn FA, and Takao M. Phototransduction by retinal ganglion cells that set the circadian clock. *Science*. 2002;295(5557):1070-3.
6. Lucas RJ, et al. Measuring and using light in the melanopsin age. *Trends in Neurosciences*. 2014;37(1):1-9.
7. Güler AD, et al. Melanopsin cells are the principal conduits for rod-cone input to non-image-forming vision. *Nature*. 2008;453(7191):102-5.
8. Brainard GC, et al. Action spectrum for melatonin regulation in humans: evidence for a novel circadian photoreceptor. *J Neurosci*. 2001;21(16):6405-12.
9. Thapan K, Arendt J, and Skene DJ. An action spectrum for melatonin suppression: evidence for a novel non-rod, non-cone photoreceptor system in humans. *J Physiol*. 2001;535(Pt 1):261-7.
10. Hattar S, et al. Central projections of melanopsin-expressing retinal ganglion cells in the mouse. *J Comp Neurol*. 2006;497(3):326-49.
11. Gaggioni G, et al. Neuroimaging, cognition, light and circadian rhythms. *Front Syst Neurosci*. 2014;8:126.
12. Vandewalle G, Maquet P, and Dijk DJ. Light as a modulator of cognitive brain function. *Trends Cogn Sci*. 2009;13(10):429-38.
13. McGlashan EM, et al. Afraid of the dark: Light acutely suppresses activity in the human amygdala. *PLoS One*. 2021;16(6):e0252350.
14. Vandewalle G, et al. Brain responses to violet, blue, and green monochromatic light exposures in humans: prominent role of blue light and the brainstem. *PLoS One*. 2007;2(11):e1247.
15. Vandewalle G, et al. Effects of light on cognitive brain responses depend on circadian phase and sleep homeostasis. *J Biol Rhythms*. 2011;26(3):249-59.
16. Vandewalle G, et al. Spectral quality of light modulates emotional brain responses in humans. *Proc Natl Acad Sci U S A*. 2010;107(45):19549-54.
17. Daneault V, et al. Aging reduces the stimulating effect of blue light on cognitive brain functions. *Sleep*. 2014;37(1):85-96.
18. Gooley JJ, et al. Melanopsin and rod-cone photoreceptors play different roles in mediating pupillary light responses during exposure to continuous light in humans. *J Neurosci*. 2012;32(41):14242-53.
19. Joshi S and Gold JI. Pupil Size as a Window on Neural Substrates of Cognition. *Trends in Cognitive Sciences*. 2020;24(6):466-80.
20. Cole L, et al. Tonic and phasic effects of reward on the pupil: implications for locus coeruleus function. *Proc Biol Sci*. 2022;289(1982):20221545.

21. Partala T and Surakka V. Pupil size variation as an indication of affective processing. *International Journal of Human-Computer Studies*. 2003;59(1):185-98.

22. Joshi S, et al. Relationships between Pupil Diameter and Neuronal Activity in the Locus Coeruleus, Colliculi, and Cingulate Cortex. *Neuron*. 2016;89(1):221-34.

23. Megemont M, McBurney-Lin J, and Yang H. Pupil diameter is not an accurate real-time readout of locus coeruleus activity. *eLife*. 2022;11:e70510.

24. Nguyen KT, et al. Time-frequency analysis of pupil size modulated by global luminance, arousal, and saccade preparation signals using Hilbert-Huang transform. *Int J Psychophysiol*. 2022;176:89-99.

25. Campbell I, et al. Impact of light on task-evoked pupil responses during cognitive tasks. *J Sleep Res*. 2023;33(4):e14101.

26. Paparella I, et al. Light modulates task-dependent thalamo-cortical connectivity during an auditory attentional task. *Commun Biol*. 2023;6(1):945.

27. Beck AT, et al. An inventory for measuring clinical anxiety: psychometric properties. *J Consult Clin Psychol*. 1988;56(6):893-7.

28. Beck AT, et al. An inventory for measuring depression. *Arch Gen Psychiatry*. 1961;4:561-71.

29. Johns MW. A new method for measuring daytime sleepiness: the Epworth sleepiness scale. *Sleep*. 1991;14(6):540-5.

30. Horne JA and Ostberg O. A self-assessment questionnaire to determine morningness-eveningness in human circadian rhythms. *Int J Chronobiol*. 1976;4(2):97-110.

31. Buysse DJ, et al. The Pittsburgh Sleep Quality Index: a new instrument for psychiatric practice and research. *Psychiatry Res*. 1989;28(2):193-213.

32. Rosenthal N. Seasonal pattern assessment questionnaire. *Journal of Affective Disorders*. 1984.

33. Collette F, et al. Exploration of the neural substrates of executive functioning by functional neuroimaging. *Neuroscience*. 2005;139(1):209-21.

34. Banse R and Scherer KR. Acoustic profiles in vocal emotion expression. *J Pers Soc Psychol*. 1996;70(3):614-36.

35. Stevens AA, et al. Event-related fMRI of auditory and visual oddball tasks. *Magn Reson Imaging*. 2000;18(5):495-502.

36. Mathôt S, Schreij D, and Theeuwes J. OpenSesame: An open-source, graphical experiment builder for the social sciences. *Behavior Research Methods*. 2012;44(2):314-24.

37. Nakayama M and Shimizu Y. Frequency Analysis of Task Evoked Pupillary Response and Eye Movement. In: Nakayama M, Shimizu Y, editors. Pupil Reactions in Response to Human Mental Activity. Singapore: Springer Singapore; 2021. p. 89-103.

38. Peysakhovich V, et al. Frequency analysis of a task-evoked pupillary response: Luminance-independent measure of mental effort. *Int J Psychophysiol*. 2015;97(1):30-7.

39. Campbell I, Sharifpour R, and Vandewalle G. Light as a Modulator of Non-Image-Forming Brain Functions—Positive and Negative Impacts of Increasing Light Availability. *Clocks & Sleep*. 2023;5(1):116-40.

40. Jaeger BC, et al. An R2 statistic for fixed effects in the generalized linear mixed model. *Journal of Applied Statistics*. 2017;44(6):1086-105.

41. Prayag A, et al. Dynamics of Non-visual Responses in Humans: As Fast as Lightning? *Frontiers in Neuroscience*. 2019;13.

42. Rukmini AV, et al. Pupillary responses to short-wavelength light are preserved in aging. *Sci Rep*. 2017;7:43832.

43. Daneault V, et al. Does pupil constriction under blue and green monochromatic light exposure change with age? *J Biol Rhythms*. 2012;27(3):257-64.

44. Lucas RJ, et al. Chapter 1 - How rod, cone, and melanopsin photoreceptors come together to enlighten the mammalian circadian clock. In: Kalsbeek A, Merrow M, Roenneberg T, Foster RG, editors. Progress in Brain Research. 199: Elsevier; 2012. p. 1-18.

45. Do MT, et al. Photon capture and signalling by melanopsin retinal ganglion cells. *Nature*. 2009;457(7227):281-7.

46. Lucas RJ, et al. Diminished pupillary light reflex at high irradiances in melanopsin-knockout mice. *Science*. 2003;299(5604):245-7.

47. McDougal DH and Gamlin PD. The influence of intrinsically-photosensitive retinal ganglion cells on the spectral sensitivity and response dynamics of the human pupillary light reflex. *Vision Res*. 2010;50(1):72-87.

48. Aston-Jones G and Bloom FE. Norepinephrine-containing locus coeruleus neurons in behaving rats exhibit pronounced responses to non-noxious environmental stimuli. *J Neurosci*. 1981;1(8):887-900.

49. Murphy PR, et al. Pupil diameter covaries with BOLD activity in human locus coeruleus. *Hum Brain Mapp*. 2014;35(8):4140-54.

50. Mure LS. Intrinsically Photosensitive Retinal Ganglion Cells of the Human Retina. *Front Neurol*. 2021;12:636330.

SUPPLEMENTARY MATERIAL

Table S1. Post hoc analyses (model M1) assessing the difference in sustained PLR according to tasks' nature

Task		t-value	Uncorrected p-value	Corrected p-value
Executive	Attentional	2.10	**0.0406**	0.0994
Executive	Emotional	2.38	**0.0202**	0.0527
Attentional	Emotional	-0.09	0.9325	0.9960

Correction for multiple comparisons was computed using a Tukey adjustment. Significant p-values are highlighted in bold. Model M1: Total averaged normalized pupil size ~ melanopic x task + sex + age + BMI + time-of-day.

Table S2. Post hoc analyses (model M2) assessing, for each cognitive task, the difference in sustained PLR across each irradiance light levels

Light level		t-value	Uncorrected p-value	Corrected p-value
		Executive task		
0.16	37	12.00	**<0.0001**	**<0.0001**
0.16	92	20.76	**<0.0001**	**<0.0001**
0.16	190	27.95	**<0.0001**	**<0.0001**
37	92	8.76	**<0.0001**	**<0.0001**
37	190	15.95	**<0.0001**	**<0.0001**
92	190	7.19	**<0.0001**	**<0.0001**
		Emotional task		
0.16	37	10.69	**<0.0001**	**<0.0001**
0.16	92	16.14	**<0.0001**	**<0.0001**
0.16	190	21.21	**<0.0001**	**<0.0001**
37	92	5.46	**0.0001**	**<0.0006**
37	190	10.52	**<0.0001**	**<0.0001**
92	190	5.06	**0.0002**	**0.0012**
		Attentional task		
0.16	92	18.23	**<0.0001**	**<0.0001**

Correction for multiple comparisons was computed using a Tukey adjustment. Significant p-values are highlighted in bold. Model M2: Total averaged normalized pupil size ~ melanopic + sex + age + BMI + time-of-day.

Table S3. Post hoc analyses (model M3) assessing, for each cognitive task and for each irradiance light levels, the difference in sustained PLR from the first to the last light block

Light level	Block order		t-value	Uncorrected p-value	Corrected p-value
			Executive task		
0.16	First	Last	-2.26	**0.0308**	**0.0308**
37	First	Last	-3.28	**0.0025**	**0.0025**
92	First	Last	0.36	0.7224	0.7224
190	First	Last	1.40	0.1707	0.1707
			Emotional task		
0.16	First	Last	-2.37	**0.0253**	**0.0253**
37	First	Last	-2.66	**0.0132**	**0.0132**
92	First	Last	-0.46	0.6459	0.6459
190	First	Last	-1.28	0.2125	0.2125
			Attentional task		
0.16	First	Last	-3.11	**0.0067**	**0.0067**
92	First	Last	-1.13	0.2735	0.2735

Correction for multiple comparisons was computed using a Tukey adjustment. Significant p-values are highlighted in bold**.** M3: Block averaged normalized pupil size ~ melanopic x block order + sex + age + BMI + time-of-day.

Table S4. Post hoc analyses (model M4) assessing, for each cognitive task, the difference in total PSD across each irradiance light level

Light level		t-value	Uncorrected p-value	Corrected p-value
		Executive task		
0.16	37	2.22	**0.0453**	0.1703
0.16	92	5.27	**0.0002**	**0.0006**
0.16	190	7.86	**<0.0001**	**<0.0001**
37	92	3.05	**0.0095**	**0.0413**
37	190	5.64	**<0.0001**	**0.0004**
92	190	2.59	**0.0228**	0.0926
		Emotional task		
0.16	37	7.46	**<0.0001**	**<0.0001**
0.16	92	13.46	**<0.0001**	**<0.0001**
0.16	190	18.81	**<0.0001**	**<0.0001**
37	92	6.00	**<0.0001**	**<0.0001**
37	190	11.35	**<0.0001**	**<0.0001**
92	190	5.35	**<0.0001**	**0.0003**
		Attentional task		
0.16	92	6.34	**0.0011**	**0.0011**

Correction for multiple comparisons was computed using a Tukey adjustment. Significant p-values are highlighted in bold. M4: Total normalized PSD ~ melanopic + sex + age + BMI + time-of-day.

Chapter 6

The effect of transcutaneous vagus nerve stimulation on sustained attention is dependent on locus coeruleus integrity in responders

Elise Beckers
Prokopis C Prokopiou
Maxime Van Egroo
Gilles Vandewalle
Heidi IL Jacobs

In preparation

ABSTRACT

Transcutaneous vagus nerve stimulation (tVNS) is a neuromodulatory technique that is promising in targeting the locus coeruleus-norepinephrine (LC-NE) system, which regulates several cognitive and behavioral functions. While several studies explored the therapeutic effects of tVNS in neurodegenerative and psychiatric diseases, recent studies have investigated its modulating effect on cognition in healthy populations. Importantly, findings in healthy individuals demonstrate considerable heterogeneity in their outcomes. Accurately identifying characteristics of individuals who are more likely to benefit from the stimulation would help developing more effective and personalized interventions related to cognition. Here, we hypothesized that the inter-individual variability in the effect of tVNS could be explained, at least in part, by the structural integrity of the LC, assessed in vivo using 7T MRI. We enrolled 27 healthy older individuals into a single-blind sham-controlled randomized cross-over fMRI study consisting of a sham/active tVNS followed by a sustained attention task. Our main findings indicated that compared to the sham condition, tVNS enhanced suboptimal attentional performance in responder individuals, in particular when integrity values of the LC are higher. Our results provide evidence that considering LC integrity in evaluating tVNS-induced attention outcomes in healthy older individuals might offer a new approach in population stratification and ultimately guide toward more precise and personalized prevention or treatment approaches.

INTRODUCTION

The locus coeruleus (LC) is a small brainstem nucleus which constitutes the primary source of norepinephrine (NE) in the brain [1]. The LC-NE neurons project extensively to cortical and subcortical brain regions and are involved in the modulation of multiple behavioral and cognitive processes, including arousal, attention and memory [2, 3]. Autopsy studies revealed that LC alterations may be part of the earliest stages of Alzheimer's disease (AD) neuropathology, as it is one of the first regions to accumulate hyperphosphorylated tau proteins several decades prior to the typical onset of clinical symptoms [4]. Furthermore, animals and human studies have consistently demonstrated that the dysregulation of the noradrenergic LC system can contribute to cognitive dysfunction [5-8]. Thus, balancing activity of the LC-NE system could be a relevant target for interventions aiming at improving cognition but also at preventing cognitive decline.

Transcutaneous vagus nerve stimulation (tVNS) is a neuromodulatory technique that has received increased attention for targeting the LC-NE system in a non-invasive and non-pharmacological manner. The vagus nerve is the longest of the 12 cranial nerves with vagal afferents primarily innervating the nucleus tractus solitaris (NTS), which in turn send projections to brainstem nuclei, including the LC [9]. In rodents, invasive vagus nerve stimulation (VNS) resulted in direct and intensity-dependent activation of LC neurons [10, 11], accompanied with a transient NE concentration increase in LC target brain regions such as the hippocampus and amygdala [12, 13]. In humans, VNS is a well-established therapy for several neurological disorders including refractory epilepsy [14] and major depression [15]. Furthermore, despite heterogeneity in the findings, evidence points toward a potential beneficial effect of VNS on cognition, alertness and memory among patients with neurodegenerative disorders including AD [16-20]. In parallel, tVNS was suggested to activate brain structures along the vagal afferent [21] and to induce similar therapeutic effects to its invasive counterpart by reducing symptoms in epilepsy [22], depressive disorder [23], stroke [24], tinnitus [25] and chronic pain [26]. Through the modulatory role of the LC-NE system on numerous cognitive functions, tVNS was also proposed to positively modulate overall cognition

in healthy individuals [27, 28]. Improvement following tVNS was observed in healthy adults over multiple facets of cognition including associative and working memory [29, 30], cognitive flexibility [31], emotion recognition [32], conflict resolution [33], action control [34], arousal measured through post-error slowing [35] and attention [36, 37]. However, inconsistencies in the findings have also been reported, [38-40], emphasizing the importance of better understanding inter-individual differences that can interact with the effect of tVNS.

Recent work by O'Callaghan and colleagues (2021) reported that measures of the LC structural integrity explained part of the heterogeneity in the response to pharmacological treatment targeting the LC-NE system in Parkinson's disease patients [41]. Advancements in ultra-high field (UHF) magnetic resonance imaging (MRI) have enabled the detailed in vivo visualization and structural quantification of the LC with high precision [42]. A growing body of evidence indicated that the variability in MRI-derived LC structural integrity was associated with differences in performance across various cognitive domains [6, 43-49], further supporting this proxy measure of LC integrity as a relevant marker for later-life cognition.

The LC-NE system plays a critical role in regulating attention, which is a fundamental component of overall cognitive functioning and one of the first cognitive domains to decline with age [50]. In particular, optimal sustained attention supports overall cognitive performance, and its decline can negatively impact other cognitive functions [51]. Given the involvement of the LC-NE system in tVNS-mediated neural pathways, we investigated the impact of tVNS on sustained attention and hypothesized that the individual variability in the benefits of tVNS on sustained attention in healthy older individuals could be explained, at least in part, by the structural integrity of the LC-NE system. Being able to stratify the population based on inter-individual differences in brain integrity, particularly of the LC, could enhance our understanding of tVNS efficacy, facilitate the identification of target populations, and ultimately inform personalized prevention or treatment approaches. To investigate this hypothesis, we combined measurements at UHF MRI of LC integrity and activity with performance on a sustained attentional task following tVNS intervention in a cohort of healthy older individuals..

METHODS

Participants

Twenty-seven healthy older individuals (age (mean ± SD) 68.63 ± 4.16 years, 13 women) were recruited from the Dutch (N = 12) and the Belgian (N = 15) population through local advertisements in the South of the Netherlands and in the East of the French-speaking region of Belgium. All participants were cognitively healthy based on the country-specific age-, sex- and education-adjusted scores on the Mini-Mental State Examination (MMSE) and the Logical Memory test, right-handed, non-smokers, with a body mass index < 28 kg/m^2, had at least 12 years of education and normal or corrected-to-normal visual acuity. Exclusion criteria included any contraindications for UHF MRI scanning, history of major psychiatric or neurological disorders, history of major cardiovascular disorders, use of drugs or psychoactive medication, excessive alcohol consumption (>15 units/week), night shift work, recent trans-meridian travel (<2 months) and unstable hypo-/hyper-tension or hypo-/hyper-thyroidism. All participants received monetary compensation for their participation and provided written informed consent. Approvals of the experimental protocol were obtained from both the local Medical Ethics Committees of the Maastricht University Medical Center and of the Faculty Hospital Ethics Committee of the University of Liège.

Experimental design

The present study falls within a larger international research project between Maastricht and Liège Universities. Here, only the data acquired in Maastricht and investigating the effect of tVNS on an attentional task is analyzed and discussed. Participants completed a randomized single-blind cross-over study design involving two similar MRI scan sessions alternating between tVNS and sham conditions. The order of administration of the stimulation condition was counterbalanced across participants. The experiment took place in the morning in Maastricht, on two distinct days separated by at least two weeks to avoid carry-over effects. Each MRI session started with the acquisition of structural scans for about 25 minutes, was followed by the administration of the stimulation condition for 6 minutes prior to the realization of a 7-min

attentional fMRI task (Figure 1). During the 7-day period preceding each session, participants were asked to follow a loose sleep-wake schedule at their habitual sleep and wake-up time (± 1 h) and to not take naps. Adhesion to the pre-defined schedule was assessed through actigraphy recording (Axivity AX3 device, Axivity Ltd, Newcastle, UK) worn on the non-dominant wrist, and the completion of sleep diaries. Participants were asked to refrain from all caffeinated and alcohol-containing beverages, and unusual physical activity for at least 3 days before the experiment.

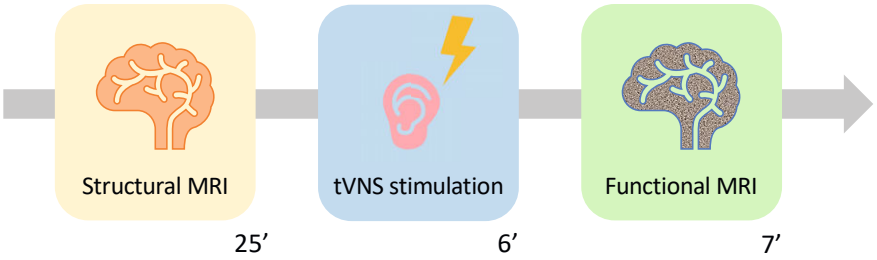

Figure 1. Schematic representation of the experimental MRI protocol.

Psychomotor vigilance task

Sustained attention and its neural correlates were assessed in the MR scanner by a psychomotor vigilance task (PVT) [52] implemented in the E-Prime 2.0 software (Psychology Software Tools, Pittsburgh, PA, USA). For each session, participants completed the task in the morning, 4 to 6 h after their wake-up time. A white fixation cross on a black background was displayed in the middle of the screen for a pseudo-random duration varying between 2 and 8 s. Next, a 10-s countdown clock with millisecond precision appeared, and participants were asked to stop the counter by key pressing the response button box (Current Designs, Inc., Philadelphia, USA) as quickly as possible, while discouraged to do anticipations. The response time (RT) was then displayed in milliseconds for a 1-s period. In total, 64 clock stimuli were shown over a task duration of approximately 7 minutes. Before entering the scanner, participants practiced the task on a 5-min version of the PVT allowing to assess their proper understanding of the instructions. Sustained attentional performance was

assessed by measuring the RT to each stimulus and categorizing them as follow: anticipations (defined as RT ≤ 100 ms) and lapses (defined as RT ≥ 500 ms) were counted and excluded from the dataset. The remaining RTs were divided into the 10% fastest, the 10% slowest and the middle 80%. These categorized RTs were averaged and further used in the analyses, following the methodology reported literature [53].

Transcutaneous vagus nerve stimulation

For both conditions, two custom-made carbon stimulation electrodes (impedance = 30Ω) were placed with conductive electroencephalogram gel over the cymba conchae of the left ear, an area innervated by the auricular branch of the vagus nerve. We chose the left cymba concha, as the right vagus nerve innervates the sinoatrial node, and the cymba concha is the most densely innervated by the auricular branch of the vagus nerve. The electrodes were connected to the stimulator device (TENStem dental device, Schwa-Medico BV, Woudenberg, the Netherlands) through the penetration panel and its low-pass RF-filter at 10 MHz. Stimulation gating was locked to the exhalation phase of the respiratory cycle, based on previous evidence that this technique improves the targeting of regions highly influenced by respiration, such as the brainstem LC [54]. The respiratory belt was connected to a pressure transducer (PX138-0.3D5V, Omegadyne, Sunbury, USA) and loaded in LabVIEW 9.0 through a DAQ USB 6001 (National Instruments, Austin, USA) where real-time peak inspiration and exhalation was applied to the respiration signal and gated the TENS-stimulator via a relay. Prior to the start of each scanning session, participants' sensory and pain thresholds were tested while they lay on the scanner table. This procedure helped them accommodate to the stimulation sensation and allowed us to set the maximum stimulation current intensity. This maximum value was defined to the participants as the level at which they felt a disturbing but painless sensation.

Stimulation parameters were in line with the literature [21, 55], although there is no clear consensus on the optimal values for effective targeting of the LC [56]: 25 Hz frequency, 500 μs pulse width, and a current intensity varying between 4 and 5 mA according to participant tolerance threshold. The expiration-gated stimulation lasted for 6 minutes while the participant was

lying in the scanner fixating a white cross, and directly preceded the execution of the PVT. For the active condition, the stimulation was applied continuously. For the sham condition, the stimulation was turned on for a few seconds at the beginning and at the end of the stimulation period, in order to induce a stimulation sensation to the participants and avoid unblinding. Participants were not informed about the hypothesized outcome effects or the current stimulation condition. At the end of each session, participants were asked to rate potential side effects including headache, neck pain, skin irritations at the ear, tingling sensations, dizziness, tiredness, nausea, concentration and mood changes. The proportion of reported side effects did not differ across stimulation conditions, as summarized in the Supplementary Figure 1. No serious side effects were reported.

Imaging parameters

The imaging protocol was performed using a 7T MAGNETOM whole-body MR system (Siemens Healthineers, Erlangen, Germany) with a 32-channel (1TX/32RX) head coil (Nova Medical, Wilmington, MA, USA). A whole-brain structural T1-weighted image was acquired using a Magnetization Prepared 2 Rapid Gradient Echoes (MP2RAGE) sequence [57] (TR = 5000 ms, TE = 2.47 ms, flip angle = 5°/3°, voxel size = 0.7 mm isotropic, number of slices = 240). The LC was imaged at high resolution with an in-house developed magnetization transfer-weighted turbo flash (MT-TFL) sequence [42], consisting of a multi-shot 3D readout (TR, varying from 538 to 544 ms, TE = 4.08, flip angle = 8°, voxel size = 0.4 x 0.4 x 0.5 mm^3, number of slices = 60) with center-out k-space sampling, preceded by 20 long off-resonant Gaussian sinc pulses (pulse length = 5.12 ms, bandwidth = 250 Hz, B_1 = 0.25 μT). The field of view of the MT-TFL sequence was placed perpendicular to the dorsal surface of the pons and covered an area between the inferior colliculi and the caudal border of the pons. A multiband gradient-echo echo-planar imaging (EPI) sequence [58, 59] was acquired for the high-resolution blood-oxygen-level dependent (BOLD) fMRI images (TR = 2200 ms, TE = 19 ms, voxel size = 1.25 mm isotropic, number of slices = 82, multi-band acceleration factor = 2, GRAPPA R = 3). Because of our focus on the brainstem, the field of view of the fMRI images excluded the most dorsal portion of the fronto-parietal lobe and was placed at 45° to the pons, which

tends to reduce the effect of physiological movement around this region [60]. BOLD fMRI scan was followed by the acquisition of five additional volumes with reversed phase encoding direction to facilitate distortion correction.

Structural MRI data preprocessing

Anatomical whole-brain T1-weighted images were first prepared using the *Presurfer* toolbox (https://github.com/srikash/presurfer) before being preprocessed in FreeSurfer version 7.4.1 [61] using the default automated reconstruction protocol as previously described [62], with the appropriate configuration for 7T data, i.e. including the "*-highres*" flag and the expert options file. In brief, this preprocessing pipeline entails bias field correction, skull stripping, intensity normalization, detection of white and pial surfaces, and parcellation of cortical and subcortical areas. All processed images were visually inspected for over- or under-estimation of the white and pial surfaces boundaries and, if necessary, manually corrected.

The MT-TFL images were preprocessed following our in-house developed 7T LC pipeline, as described previously [63]. All LC scans were intensity-normalized using the subject-specific mean intensity of a 10x10 voxels reference region located in the pontine tegmentum. A study-specific template was created using an iterative diffeomorphic warp estimate in ANTs version 2.1.0 (*buildtemplateparallel* function) based on all individual intensity-normalized MT-TFL images. The LC mask was then manually delineated on the resulting template by an expert (EB), based on voxel intensities and prior knowledge on LC anatomy. Each individual intensity- and spatially- normalized MT-TFL images to the template space were manually checked for accurate anatomical registration. Subject-specific median LC MRI signal intensity values were extracted slice-wise across each hemisphere by applying the LC mask onto each individual intensity- and spatially-normalized image and finally averaged bilaterally across the entire LC length.

For the following fMRI analyses, the study-specific LC mask was spatially-normalized to the MNI space (ICBM152 2009c Nonlinear Asymmetric 1mm resolution) in a unified step by applying subject-specific transformation matrices using the *antsApplyTransforms* function in ANTs. These subject-specific transformation matrices were either retrieved from previous steps

or created as described below. First, the linear and non-linear transformation files linking the study-specific MT-TFL template to the individual MT-TFL images were retrieved from the template creation process previously mentioned. Next, individual MT-TFL images were realigned to their respective T1-weigthed images using *bbregister* from FreeSurfer and the resulting affine transformation files were extracted. A visual evaluation of the anatomical registration revealed that 3 subjects had poor quality registration of their MT-TFL to T1-weighted image. For these 3 subjects, the registration was successfully performed using *antsRegistration* function in ANTs. Then, the preprocessed T1-weighted images were wrapped to the MNI space using linear and non-linear transformations in *antsRegistration* function in ANTs. A visual quality check confirmed the accuracy of this registration step. Finally, the study-specific LC mask was warped to the MNI space for each subject by applying the set of generated transformation matrices using the *antsApplyTransforms* function in ANTs. A study-specific LC probabilistic atlas was created by averaging the individual LC mask wrapped to the MNI space. Following Ye et al. (2021), an arbitrary threshold of 25% was applied to obtain a template specific to the LC core [64].

BOLD fMRI data preprocessing

The BOLD fMRI data was preprocessed using fMRIPrep 21.0.1 [65], which is based on Nipype 1.6.1 [66]. In brief, each functional run was corrected for B_0 inhomogeneity using corresponding field maps, slice-time corrected, and normalized to the standard MNI152NLin2009cAsym 1mm resolution template. Nuisance regressors, including white matter signal, cerebrospinal fluid signal and motion parameters were estimated and used for data denoising. We subsequently applied high-pass temporal filtering, correction for motion artifacts estimated by the ICA-AROMA toolbox and spatial smoothing with a custom ellipsoid Gaussian kernel (full width at half-maximum = 1.5 mm), matching the minimum LC width to enhance the detection of such elongated structure [67].

ROI-based fMRI analyses

After visual inspection of the preprocessed fMRI data, first-level general linear models were computed for each run with *FEAT* from FSL version 6.0.6.5

(https://fsl.fmrib.ox.ac.uk/fsl/fslwiki/FSL). Our regressors of interest were the RTs classified in the slow, middle and fast categories. Contrasts associated to each individual regressors were created to investigated the effect of tVNS on LC activity associated with each type of events. The median activity estimates (betas) were subsequently extracted from the generated contrast maps by applying the study-specific LC probabilistic atlas thresholded at 25% using the *featquery* option in FSL. Because of no prior hypotheses on potential lateralization, we averaged the mean beta activity estimates across the left and right LC.

Statistical analysis

All statistical analyses were performed using R statistical software (version 4.1.2, http://www.r-project.org/). Group characteristics are presented as mean and standard deviation for continuous variables and proportions for dichotomous variables. The statistical threshold for significance was set to $\alpha < 0.05$.

Behavior, LC activity and LC intensity

We first explored the simple effects of tVNS on behavioral and brain measures, and the univariate associations between these behavioral and brain measures. Welch paired two-sample t-tests investigated the difference in behavioral performance or in LC activity across tVNS conditions. Repeated measures correlations were used to explore the association between behavior and LC activity across both measurements.

We then aimed to examine which factors contributed to tVNS-related effects on attentional performance. First, we computed the relative changes from the sham to stimulation condition in PVT score and in median LC activity estimates for each RT category (slow, middle and fast). Zero-order correlations assessed associations between age and sex on our variables of interest (LC intensity, relative changes in PVT score and relative changes in LC activity for all three RT categories). Given the non-normality of (part of) the data, LC intensity associations were further evaluated using linear regression models with bootstrapped standard errors (5,000 iterations) on each of our dependent variables: the relative change in RT and in median LC activity estimates from

the sham to stimulation condition in each of the three RT categories. Models were controlled for age, sex and education.

Responders versus non-responders

Participants were subsequently classified per RT category as responders (R), if they were showing improvement of their attentional performance, i.e. decreased RTs from the sham to the tVNS session, or non-responders (NR, no improvement or worsening in RTs from the sham to the tVNS session). Across all 3 RT categories, we counted 16 responders in the middle RT category, 15 for the slow RT category and 12 for the fast RT category. We examined differences between R and NR groups on each of the relative changes in PVT score or in LC activity using bootstrapped linear regression models (5,000 iterations). In a second step, we examined whether potential group differences were dependent on LC intensity, age or sex by including the interactions. Models were controlled for age, sex and education, when appropriate.

RESULTS

Demographics and descriptive statistics

A total of 27 healthy older individuals (mean MMSE score: 29.41) participated in the present study, on average aged of 68.63 years and including 13 females (Table 1).

Table 1. Sample characteristics

	Mean (SD)
N	27
Age (years)	68.63 (4.16)
Sex (No. female, %)	13 (48.15)
Education (years)	16.06 (2.92)
MMSE (score)	29.41 (0.75)
LC intensity (a.u.)	0.17 (0.04)

MMSE = Mini-Mental State Examination

Global participants' performance on the PVT, excluding the lapses and anticipations, was on average of 319.24 ms for the sham session, and of 314 ms for the tVNS session (Table 2). There was no significant difference between both stimulation conditions for the global PVT score (t_{26} = 1.38, p = 0.18). The categorized PVT scores per slow, middle and fast RT categories together with the associated estimated LC activity values did not show any significant difference across stimulation conditions (Table 2, Supplementary Figure 2).

Table 2. Descriptive statistics across stimulation conditions

	Sham	**tVNS**	**Condition difference**	
	Mean (SD)	**Mean (SD)**	**t-value**	**p-value**
Global PVT score (ms)	319.24 (32.87)	314 (31.70)	1.38	0.18
Anticipations (N)	0.15 (0.36) [range: 0-1]	0.19 (0.40) [range: 0-1]	-0.33	0.75
Lapses (N)	1.96 (2.71) [range: 0-12]	2.11 (2.41) [range: 0-11]	-0.24	0.81
PVT score - Slow (ms)	417.67 (38.15)	413.68 (37.72)	0.60	0.55
PVT score - Middle (ms)	315.65 (34.02)	309.79 (32.78)	1.49	0.15
PVT score - Fast (ms)	251.04 (29.75)	249.56 (27.14)	0.36	0.72
LC activity – Slow (a.u.)	-1.28 (158.28)	30.09 (127.74)	-0.83	0.41
LC activity – Middle (a.u.)	11.99 (103.34)	26.19 (139.15)	-0.46	0.65
LC activity – Fast (a.u.)	37.31 (257.81)	-3.91 (292.39)	0.50	0.62

The t- and p-values correspond to paired two-sample t-tests between stimulation conditions.

Repeated measures correlations did not reveal any association between changes in PVT scores and their respective LC activity across measurements for each of the slow (r = -0.02, p = 0.92), middle (r = -0.18, p = 0.36), and fast (r = -0.10, p = 0.61) RT category.

Zero-order correlations suggested a trend level relationship between the relative change in LC activity across stimulation conditions in the slow RT category and sex, suggesting that compared to sham, LC activity levels after tVNS were decreasing in men while increasing in women (r = 0.38, p = 0.05). There were no other significant correlations observed between our variables

of interest (LC intensity, relative changes in PVT score and in LC activity per RT category) and age or sex (all $p > 0.1$, Supplementary Table 1).

There was no significant association between LC intensity and the relative changes in PVT score or LC activity, for each of the three RT categories while controlling for age, sex and level of education (range: $p = [0.14; 0.99]$).

Responders versus non-responders

For each RT category, visualization of the sham versus tVNS changes in PVT score revealed variability in behavior among participants (Figure 2). A negative slope (i.e., decrease in RT) was considered an improvement in performance during the tVNS session compared to the sham. Participants showing this type of behavior were classified as "Responders" (R) (N = 15 for slow RT, N = 16 for middle RT, and N = 12 for fast RT categories). In contrast, positive slopes in the task performance from the sham to the tVNS session (i.e., increase in RT) were associated with participants not showing improvement in their performance related to the intervention. These participants were classified as "Non-responders" (NR) (N = 12 for slow RT, N = 11 for middle RT, and N = 15 for fast RT categories). Overall, 37.04% of our sample was assigned to the same group across all 3 RT categories. Group characteristics are presented in Supplementary Table 2. Responders in the middle RT category were significantly older compared to non-responders.

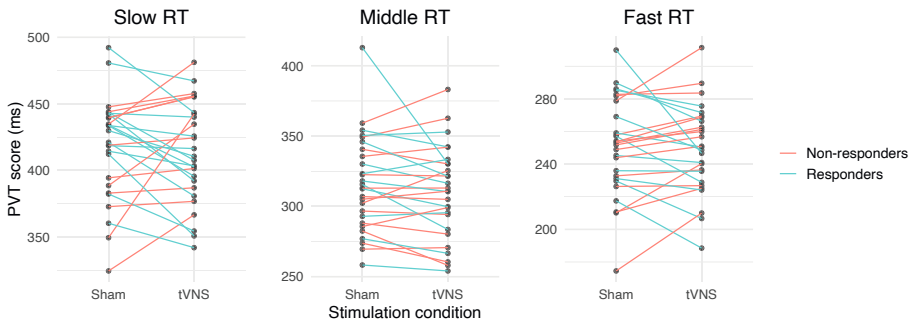

Figure 2. Visualization of responders versus non-responders based on PVT scores across stimulation conditions. Evolution of PVT scores from the sham to the tVNS stimulation condition for each RT category (slow, middle and fast). Each line represents the repeated measures per participant.

As expected, after classifying participants as responders or non-responders based on their relative change in task RTs, we observed a significant main effect of the group (R versus NR) on the relative change in PVT score. Specifically, this effect was present in the slow RT (β = -12.75, CI = [-17.32; -8.41], p = 0.0002), middle RT (β = -8.27, CI = [-11.99; -4.35], p = 0.0002), and fast RT categories (β = -12.41, CI = [-16.20; -8.50], p = 0.0002) after adjusting for covariates. However, no significant effect was detected on the relative change in LC activity (range: p = [0.10; 0.20]).

Further characterizing the differences between responders and non-responders, we found that the interaction between group (R versus NR) and age was associated with the relative change in PVT score in the middle RT category (β = 0.91, CI = [0.05; 1.75], p = 0.041, Figure 3A). No other interaction effects between age and group were observed for the other metrics of interest (range: p = [0.12; 0.61]). In addition, the interaction between R-NR group and sex revealed a trend-level association on the relative change in PVT score for the middle RT category (β = 6.11, CI = [0.37; 12.60], p = 0.041), but this effect disappeared when controlling for covariates (β = 5.15, CI = [-0.85; 11.76], p = 0.102). No other sex interactions were observed for the PVT score in the slow and fast RT categories or any of the LC activity metrics (range: p = [0.24; 0.87]).

Finally, we found a significant interaction between the R-NR group and LC intensity on the relative change in PVT score in the slow RT category (β = -127.16, CI = [-251.41; -5.50], p = 0.042). In responders, higher LC intensity was associated with decreased RTs to the task, i.e. better performance, in the tVNS compared to the sham session (Figure 3B). No other significant interaction was observed for relative changes in PVT score in the middle and fast RT categories, or for any of the three LC activity metrics (range: p = [0.22; 0.96]).

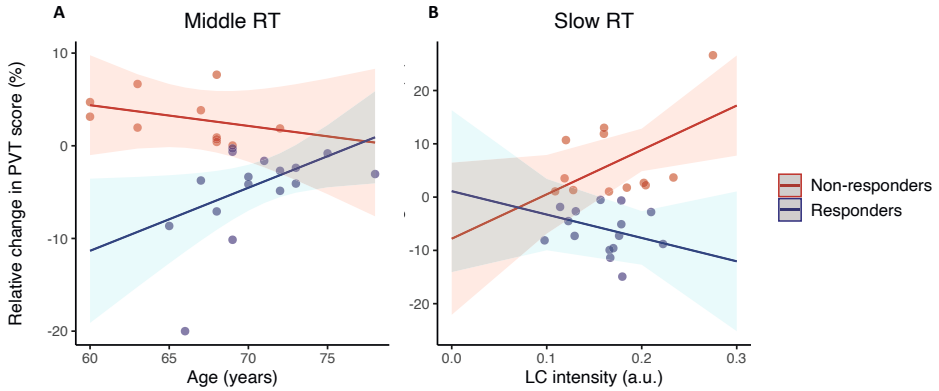

Figure 3. Associations between relative change in PVT score with LC intensity or age is dependent on responders and non-responders. Raw data points are overlayed to the predicted regression lines.

DISCUSSION

In recent years, tVNS has gained increasing interest for its potential in targeting the LC-NE system and modulating several cognitive processes, including attention [36, 37, 68]. To date, studies yielded heterogeneous results among healthy and clinical populations, emphasizing the need for indicators that can signal who is likely to benefit from tVNS. Here, we aimed to evaluate whether inter-individual differences in the integrity of the LC-NE system, indexed by an in vivo MRI-measure of LC intensity, may help to explain the variability observed in the effect of tVNS on sustained attentional processes in healthy older adults. We provided in vivo evidence that the degree of improvement or decline in attentional task performance following tVNS is dependent on LC integrity. These results highlight the importance of better understanding the variability in tVNS effects and the associated markers in order to help developing more precise and personalized clinical trials, with the ultimate goal to boost cognition or prevent cognitive decline.

We did not observe a direct impact of tVNS on behavioral or LC neural measures. Recent literature reported mixed-findings on the effect of tVNS on

attention in healthy individuals. In terms of behavior, tVNS was associated with shorter RTs to attentional tasks [36, 37]. However, other studies with comparable sample sizes failed to observed tVNS-related improvements on an auditory oddball task [68] or on a PVT in a sleep deprived cohort [30]. Additionally, Villani and colleagues (2022) even found an increase in RTs associated with tVNS [39]. At the electrophysiological level, Rufener and colleagues (2018) and Chen and colleagues (2023) both observed that tVNS resulted in higher amplitude of the P3, a specific event-related potential also suggested to involve the LC-NE system [37, 68]. Finally, one fMRI study investigated the neural correlates of tVNS on attentional processes and, similar to us, found no significant change in brain activation pattern, despite a positive effect observed on behavioral performance [36]. Together, these mixed-findings argue for a better understanding of the factors underlying important variability in the effect of tVNS on attention.

As with many clinical trials, not everyone responds to the intervention. However, identifying those who do respond and understanding their characteristics is critical for assessing treatment efficacy and defining the target population. While we did not observe significant differences between groups across all three RT categories, we found that in the slow RT category, higher LC integrity was associated with improved PVT performance in responders following tVNS, but with worsening of PVT performance in non-responders. Importantly, this association was not detected in the entire sample. As the LC-NE system is one of the established targets along the vagal nerve stimulation pathway and is also highly involved in the regulation of attentional processes, it is possible that alterations in this structure might interfere with the hypothesized effect of tVNS in individuals benefiting from the intervention. Degeneration of LC neurons leads to a decrease in NE release, in turn impacting the modulation of attentional and other cognitive processes. It is possible that when the LC is too much affected, the effect of tVNS on the LC-NE system is no longer optimal.

Interestingly, responders did not differ on average in terms of LC integrity from non-responders, suggesting that other processes contributing to overall LC health may be determining the effect of tVNS. Variability in LC integrity in older individuals has been attributed to the presence of underlying AD

pathology [46], cognitive reserve [44] and lifestyle factors, such as nocturnal awakenings [63]. While we adjusted our analyses for education, and controlled sleep-wake patterns before scanning, we cannot exclude that some of our individuals harbor incipient late-life pathology. It will be important for future studies to determine the effect of neurodegenerative pathologies on tVNS-related attentional performance. Importantly, because of the small sample size, caution is needed when interpreting these associations. Whether this tVNS-related pattern translates to clinical population with presumably greater damage to their LC health will require additional longitudinal research in larger healthy and clinical cohorts.

Critically, the modulating effect of tVNS on PVT performance in responders was only detected for the 10% slowest RT. Sustained attention is not constant in time, but rather fluctuates between suboptimal and optimal states, as reflected by behavior and brain activity [69]. While lapses (RT≥500ms) are deemed indicative of attentional failure, the slowest RTs (<500ms) are considered to reflect less optimal attentional processes compared to the middle or fast RT categories, corresponding to normal to optimal states. Our cohort is composed of healthy individuals, which are likely to perform already close to their maximum, even without external stimulation. Therefore, the slowest RTs would be the most likely to reflect differences given the potential opportunity window to improve these suboptimal performances.

Finally, we observed that individuals at lower ages within the age range of the cohort (60-80 years) benefited more from tVNS, as reflected in improved PVT scores for the middle RT events. Age is known to exert important negative effects on RT [70]. Over the entire group, we did not observe a direct effect of age on PVT performance or LC activity across stimulation conditions, probably because of the narrow age range of our cohort. However, in responders, older age was associated with reduced improvement in their behavioral performance following tVNS. Interestingly, responders were reported as significantly older than non-responders in this specific middle RT category. Given that we did not find an effect of age on LC intensity in our cohort, this result is not likely to be driven by age-related changes in LC intensity values. Including more individuals on a larger age range together with the measurements of additional biomarkers would allow for a more precise characterization of the responder versus non-

responder groups, and facilitate the selection of individuals in future clinical trials.

Attention is one of the first cognitive functions to decline with age [50]. This decline can manifest in several ways, including reduced ability to sustain focus, increased susceptibility to distractors and slower processing speeds [71]. In addition, previous research showed that the ongoing attentional state has a profound impact on cognition through the activation of the LC-NE system [72]. Although NE release is typically triggered by external stimuli, it is plausible that an increase in tVNS-induced NE levels arising from the LC could enhance attention. This heightened attention could, in turn, improve other cognitive functions by facilitating greater focus on the ongoing task. However, we are not in the position to confirm these mechanisms as our study did not measure NE levels, nor did we measure performance to another cognitive task following tVNS.

There are several limitations to our study to be mentioned. First, the absence of a relationship between tVNS and LC activity measures in our study may be due to limited statistical power, as other studies have reported changes in LC activity following tVNS [54, 68, 73-75]. This indicates that future studies should consider to recruit larger cohorts to detect potential effects more reliably. It is also possible that the effect of tVNS is reduced in healthy individuals compared to clinical populations. However, it is not clear how disease-related brain alterations would interact with or potentially limit the effect of tVNS on attention. Our findings suggest that a structurally more intact LC may be associated with better attentional outcomes. What this exactly means for individuals with higher burden of pathologies or for AD patients requires further investigation. Second, the PVT is known for its high sensitivity to fatigue-related changes rather than to early age-related changes in sustained attention. Other type of attentional task paradigms, visual and auditory, could therefore be investigated as the tVNS effects might be too subtle to be detected by the PVT in a healthy cohort of well-rested individuals. Third, there is actually no clear consensus on the optimal set of tVNS parameters or the sham configuration to use. Indeed, there is variability in studies regarding the choice of electrode location during the sham, but also tVNS parameters such as stimulation duration, frequency, current intensity,

and pulse width. Future studies are encouraged to better understand the relationship between different parameters and neural or behavioral outcomes in different populations, and at the same time work toward a harmonization of the tVNS settings to improve the comparability of their results.

In conclusion, our results suggest that LC integrity could explain, at least in part, the inter-individual variability observed in tVNS efficacy on attentional behavioral outcomes among responders, and therefore might contribute to the optimization of future research in healthy and clinical populations with the ultimate goal to inform on a more personalized non-invasive and non-pharmacological treatment approach targeting the LC-NE system.

REFERENCES

1. Poe GR, et al. Locus coeruleus: a new look at the blue spot. Nat Rev Neurosci. 2020;21(11):644-59.
2. Aston-Jones G and Cohen JD. An integrative theory of locus coeruleus-norepinephrine function: adaptive gain and optimal performance. Annu Rev Neurosci. 2005;28:403-50.
3. Sara SJ. The locus coeruleus and noradrenergic modulation of cognition. Nat Rev Neurosci. 2009;10(3):211-23.
4. Braak H, et al. Stages of the pathologic process in Alzheimer disease: age categories from 1 to 100 years. J Neuropathol Exp Neurol. 2011;70(11):960-9.
5. Jacobs HIL, et al. Waning locus coeruleus integrity precedes cortical tau accrual in preclinical autosomal dominant Alzheimer's disease. Alzheimers Dement. 2023;19(1):169-80.
6. Dahl MJ, et al. The integrity of dopaminergic and noradrenergic brain regions is associated with different aspects of late-life memory performance. Nat Aging. 2023;3(9):1128-43.
7. Wilson RS, et al. Neural reserve, neuronal density in the locus ceruleus, and cognitive decline. Neurology. 2013;80(13):1202-8.
8. Galgani A, et al. The degeneration of locus coeruleus occurring during Alzheimer's disease clinical progression: a neuroimaging follow-up investigation. Brain Struct Funct. 2024;229(5):1317-25.
9. Ruffoli R, et al. The chemical neuroanatomy of vagus nerve stimulation. J Chem Neuroanat. 2011;42(4):288-96.
10. Groves DA, Bowman EM, and Brown VJ. Recordings from the rat locus coeruleus during acute vagal nerve stimulation in the anaesthetised rat. Neurosci Lett. 2005;379(3):174-9.
11. Hulsey DR, et al. Parametric characterization of neural activity in the locus coeruleus in response to vagus nerve stimulation. Exp Neurol. 2017;289:21-30.
12. Raedt R, et al. Increased hippocampal noradrenaline is a biomarker for efficacy of vagus nerve stimulation in a limbic seizure model. J Neurochem. 2011;117(3):461-9.
13. Roosevelt RW, et al. Increased extracellular concentrations of norepinephrine in cortex and hippocampus following vagus nerve stimulation in the rat. Brain Res. 2006;1119(1):124-32.
14. Berger A, et al. How Is the Norepinephrine System Involved in the Antiepileptic Effects of Vagus Nerve Stimulation? Front Neurosci. 2021;15:790943.
15. Rush AJ, et al. Effects of 12 months of vagus nerve stimulation in treatment-resistant depression: a naturalistic study. Biol Psychiatry. 2005;58(5):355-63.
16. Sun L, et al. Vagus nerve stimulation improves working memory performance. J Clin Exp Neuropsychol. 2017;39(10):954-64.
17. Merrill CA, et al. Vagus nerve stimulation in patients with Alzheimer's disease: Additional follow-up results of a pilot study through 1 year. J Clin Psychiatry. 2006;67(8):1171-8.
18. Sjögren MJ, et al. Cognition-enhancing effect of vagus nerve stimulation in patients with Alzheimer's disease: a pilot study. J Clin Psychiatry. 2002;63(11):972-80.

19. Broncel A, et al. Vagal nerve stimulation as a promising tool in the improvement of cognitive disorders. Brain Res Bull. 2020;155:37-47.

20. van Bochove ME, et al. Reduced distractor interference during vagus nerve stimulation. Int J Psychophysiol. 2018;128:93-9.

21. Yakunina N, Kim SS, and Nam EC. Optimization of Transcutaneous Vagus Nerve Stimulation Using Functional MRI. Neuromodulation. 2017;20(3):290-300.

22. Bauer S, et al. Transcutaneous Vagus Nerve Stimulation (tVNS) for Treatment of Drug-Resistant Epilepsy: A Randomized, Double-Blind Clinical Trial (cMPsE02). Brain Stimul. 2016;9(3):356-63.

23. Fang J, et al. Transcutaneous Vagus Nerve Stimulation Modulates Default Mode Network in Major Depressive Disorder. Biol Psychiatry. 2016;79(4):266-73.

24. Baig SS, et al. Transcutaneous vagus nerve stimulation (tVNS) in stroke: the evidence, challenges and future directions. Auton Neurosci. 2022;237:102909.

25. Lehtimäki J, et al. Transcutaneous vagus nerve stimulation in tinnitus: a pilot study. Acta Otolaryngol. 2013;133(4):378-82.

26. Straube A and Eren O. tVNS in the management of headache and pain. Auton Neurosci. 2021;236:102875.

27. Naparstek S, Yeh AK, and Mills-Finnerty C. Transcutaneous Vagus Nerve Stimulation (tVNS) applications in cognitive aging: a review and commentary. Front Aging Neurosci. 2023;15:1145207.

28. Ridgewell C, et al. The effects of transcutaneous auricular vagal nerve stimulation on cognition in healthy individuals: A meta-analysis. Neuropsychology. 2021;35(4):352-65.

29. Jacobs HI, et al. Transcutaneous vagus nerve stimulation boosts associative memory in older individuals. Neurobiol Aging. 2015;36(5):1860-7.

30. Zhao R, et al. Transcutaneous auricular vagus stimulation (taVNS) improves human working memory performance under sleep deprivation stress. Behav Brain Res. 2023;439:114247.

31. Borges U, et al. Transcutaneous Vagus Nerve Stimulation May Enhance Only Specific Aspects of the Core Executive Functions. A Randomized Crossover Trial. Front Neurosci. 2020;14:523.

32. Colzato LS, Sellaro R, and Beste C. Darwin revisited: The vagus nerve is a causal element in controlling recognition of other's emotions. Cortex. 2017;92:95-102.

33. Fischer R, et al. Transcutaneous vagus nerve stimulation (tVNS) enhances conflict-triggered adjustment of cognitive control. Cogn Affect Behav Neurosci. 2018;18(4):680-93.

34. Jongkees BJ, et al. Transcutaneous Vagus Nerve Stimulation (tVNS) Enhances Response Selection During Sequential Action. Front Psychol. 2018;9:1159.

35. Sellaro R, et al. Transcutaneous Vagus Nerve Stimulation Enhances Post-error Slowing. J Cogn Neurosci. 2015;27(11):2126-32.

36. Klaming R, et al. Effects of Noninvasive Cervical Vagal Nerve Stimulation on Cognitive Performance But Not Brain Activation in Healthy Adults. Neuromodulation. 2022;25(3):424-32.

37. Chen Y, et al. Modulatory effects of transcutaneous auricular vagus nerve stimulation (taVNS) on attentional processes. Gen Psychiatr. 2023;36(6):e101176.

38. Mertens A, et al. Transcutaneous Vagus Nerve Stimulation Does Not Affect Verbal Memory Performance in Healthy Volunteers. Front Psychol. 2020;11:551.

39. Villani V, et al. Event-related transcutaneous vagus nerve stimulation modulates behaviour and pupillary responses during an auditory oddball task. Psychoneuroendocrinology. 2022;140:105719.

40. Verkuil B and Burger AM. Transcutaneous vagus nerve stimulation does not affect attention to fearful faces in high worriers. Behav Res Ther. 2019;113:25-31.

41. O'Callaghan C, et al. Locus coeruleus integrity and the effect of atomoxetine on response inhibition in Parkinson's disease. Brain. 2021;144(8):2513-26.

42. Priovoulos N, et al. High-resolution in vivo imaging of human locus coeruleus by magnetization transfer MRI at 3T and 7T. Neuroimage. 2018;168:427-36.

43. Dahl MJ, et al. Rostral locus coeruleus integrity is associated with better memory performance in older adults. Nat Hum Behav. 2019;3(11):1203-14.

44. Clewett DV, et al. Neuromelanin marks the spot: identifying a locus coeruleus biomarker of cognitive reserve in healthy aging. Neurobiol Aging. 2016;37:117-26.

45. Hämmerer D, et al. Locus coeruleus integrity in old age is selectively related to memories linked with salient negative events. Proc Natl Acad Sci U S A. 2018;115(9):2228-33.

46. Jacobs HIL, et al. In vivo and neuropathology data support locus coeruleus integrity as indicator of Alzheimer's disease pathology and cognitive decline. Sci Transl Med. 2021;13(612):eabj2511.

47. Liu KY, et al. Noradrenergic-dependent functions are associated with age-related locus coeruleus signal intensity differences. Nat Commun. 2020;11(1):1712.

48. Elman JA, et al. MRI-assessed locus coeruleus integrity is heritable and associated with multiple cognitive domains, mild cognitive impairment, and daytime dysfunction. Alzheimers Dement. 2021;17(6):1017-25.

49. Bell TR, et al. Rostral-middle locus coeruleus integrity and subjective cognitive decline in early old age. J Int Neuropsychol Soc. 2023;29(8):763-74.

50. Murman DL. The Impact of Age on Cognition. Semin Hear. 2015;36(3):111-21.

51. Parasuraman R, Nestor P, and Greenwood P. Sustained-attention capacity in young and older adults. Psychol Aging. 1989;4(3):339-45.

52. Dinges DF and Powell JW. Microcomputer analyses of performance on a portable, simple visual RT task during sustained operations. Behavior Research Methods, Instruments, & Computers. 1985;17(6):652-5.

53. Basner M and Dinges DF. Maximizing sensitivity of the psychomotor vigilance test (PVT) to sleep loss. Sleep. 2011;34(5):581-91.

54. Sclocco R, et al. The influence of respiration on brainstem and cardiovagal response to auricular vagus nerve stimulation: A multimodal ultrahigh-field (7T) fMRI study. Brain Stimul. 2019;12(4):911-21.

55. Yap JYY, et al. Critical Review of Transcutaneous Vagus Nerve Stimulation: Challenges for Translation to Clinical Practice. Front Neurosci. 2020;14:284.

56. Ludwig M, et al. Current challenges in reliably targeting the noradrenergic locus coeruleus using transcutaneous auricular vagus nerve stimulation (taVNS). Auton Neurosci. 2021;236:102900.

57. Marques JP, et al. MP2RAGE, a self bias-field corrected sequence for improved segmentation and T1-mapping at high field. Neuroimage. 2010;49(2):1271-81.

58. Moeller S, et al. Multiband multislice GE-EPI at 7 tesla, with 16-fold acceleration using partial parallel imaging with application to high spatial and temporal whole-brain fMRI. Magn Reson Med. 2010;63(5):1144-53.

59. Setsompop K, et al. Blipped-controlled aliasing in parallel imaging for simultaneous multislice echo planar imaging with reduced g-factor penalty. Magn Reson Med. 2012;67(5):1210-24.

60. Brooks JC, et al. Physiological noise in brainstem FMRI. Front Hum Neurosci. 2013;7:623.

61. Fischl B. FreeSurfer. Neuroimage. 2012;62(2):774-81.

62. Dale AM, Fischl B, and Sereno MI. Cortical Surface-Based Analysis: I. Segmentation and Surface Reconstruction. NeuroImage. 1999;9(2):179-94.

63. Van Egroo M, van Hooren RWE, and Jacobs HIL. Associations between locus coeruleus integrity and nocturnal awakenings in the context of Alzheimer's disease plasma biomarkers: a 7T MRI study. Alzheimers Res Ther. 2021;13(1):159.

64. Ye R, et al. An in vivo probabilistic atlas of the human locus coeruleus at ultra-high field. Neuroimage. 2021;225:117487.

65. Esteban O, et al. fMRIPrep: a robust preprocessing pipeline for functional MRI. Nat Methods. 2019;16(1):111-6.

66. Gorgolewski K, et al. Nipype: a flexible, lightweight and extensible neuroimaging data processing framework in python. Front Neuroinform. 2011;5:13.

67. Prokopiou PC, et al. Lower novelty-related locus coeruleus function is associated with Aβ-related cognitive decline in clinically healthy individuals. Nat Commun. 2022;13(1):1571.

68. Rufener KS, et al. Modulating auditory selective attention by non-invasive brain stimulation: Differential effects of transcutaneous vagal nerve stimulation and transcranial random noise stimulation. Eur J Neurosci. 2018;48(6):2301-9.

69. Fortenbaugh FC, DeGutis J, and Esterman M. Recent theoretical, neural, and clinical advances in sustained attention research. Ann N Y Acad Sci. 2017;1396(1):70-91.

70. Wilkinson RT and Allison S. Age and simple reaction time: decade differences for 5,325 subjects. J Gerontol. 1989;44(2):P29-35.

71. Salthouse TA. The processing-speed theory of adult age differences in cognition. Psychol Rev. 1996;103(3):403-28.

72. Sara SJ and Bouret S. Orienting and reorienting: the locus coeruleus mediates cognition through arousal. Neuron. 2012;76(1):130-41.

73. Garcia RG, et al. Modulation of brainstem activity and connectivity by respiratory-gated auricular vagal afferent nerve stimulation in migraine patients. Pain. 2017;158(8):1461-72.

74. Sharon O, Fahoum F, and Nir Y. Transcutaneous Vagus Nerve Stimulation in Humans Induces Pupil Dilation and Attenuates Alpha Oscillations. J Neurosci. 2021;41(2):320-30.

75. Zhang Y, et al. Transcutaneous auricular vagus nerve stimulation at 1 Hz modulates locus coeruleus activity and resting state functional connectivity in patients with migraine: An fMRI study. Neuroimage Clin. 2019;24:101971.

SUPPLEMENTARY MATERIAL

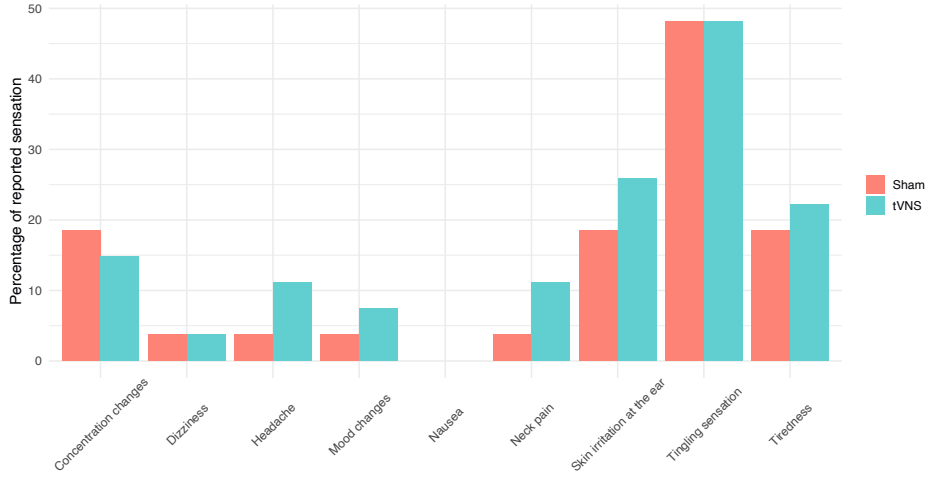

Figure S1. Types and percentage of reported side effects during the sham and tVNS sessions. The most reported side effect was the tingling sensation at the electrode location. No significant difference in reported side effects was observed between the sham and tVNS condition. tVNS = transcutaneous vagus nerve stimulation.

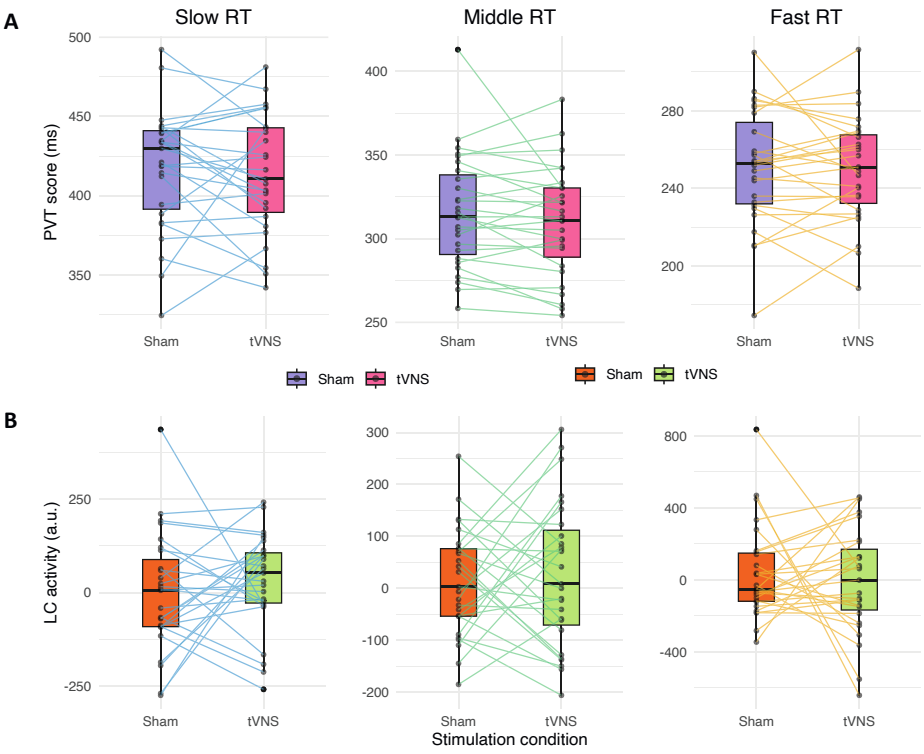

Figure S2. PVT performance and LC activity across stimulation conditions. Colored lines represent the repeated measures for each subject across stimulation conditions (sham and tVNS) for each variable of interest (**A**: PVT score, **B**: LC activity) and across the three RT categories (slow, middle and fast). Horizontal lines within the box plots represent the median values. No differences between conditions were observed on any of the outcome measures (tested with paired two-sample tests). LC = locus coeruleus, PVT = Psychomotor Vigilance Task, tVNS = transcutaneous vagus nerve stimulation.

Table S1. Zero-order correlations between demographics and variables of interest

		Age	Sex
		r (p)	r (p)
LC intensity (a.u.)		0.02 (0.92)	-0.28 (0.15)
Relative changes in:	**PVT score - Slow**	-0.32 (0.1)	0.04 (0.86)
	PVT score – Middle	-0.22 (0.27)	-0.01 (0.98)
	PVT score - Fast	0.23 (0.25)	-0.07 (0.73)
	LC activity - Slow	-0.02 (0.93)	0.38 (0.05)$^{\#}$
	LC activity - Middle	-0.02 (0.91)	0.02 (0.91)
	LC activity - Fast	0.004 (0.98)	0.19 (0.35)

Pearson product-moment correlation coefficients (r, continuous variable) or point-biserial correlation coefficients (r, dichotomous variable). Relative changes represent the changes in the variable of interest from the sham to active stimulation condition. Significance threshold indicated as $^{\#}$: $p < 0.1$, *: $p < 0.05$. LC = locus coeruleus, PVT = Psychomotor Vigilance Task.

Table S2. Characteristics of responders versus non-responders

	Responders	Non-responders	Group difference	
	Mean (SD)	Mean (SD)	t-value	p-value
Slow RT				
N	15	12	-	-
Age (years)	68.8 (2.24)	68.42 (5.87)	-0.23	0.82
Sex (No. female, %)	7 (46.67)	6 (50)	0.17	0.87
Education (years)	15.73 (2.99)	16.46 (2.9)	0.63	0.53
MMSE (score)	29.4 (0.74)	29.42 (0.79)	0.06	0.96
LC intensity (a.u.)	0.16 (0.04)	0.17 (0.05)	0.72	0.48
Rel. change in PVT score (%)	-6.35 (4.23)	6.63 (7.7)	5.58	<0.001
Rel. change in LC activity (%)	84.81 (224.38)	-24.57 (154.41)	-1.44	0.16
Middle RT				
N	16	11	-	-
Age (years)	70.44 (3.37)	66 (3.9)	-3.16	0.004
Sex (No. Female, %)	6 (37.5)	7 (63.64)	1.33	0.2
Education (years)	15.25 (2.35)	17.23 (3.36)	1.8	0.08
MMSE (score)	29.44 (0.73)	29.36 (0.81)	-0.25	0.81
LC intensity (a.u.)	0.17 (0.04)	0.16 (0.05)	-0.45	0.66
Rel. change in PVT score (%)	-4.85 (4.9)	2.9 (2.58)	4.79	<0.001
Rel. change in LC activity (%)	204.6 (747.95)	-60.53 (311.37)	-1.11	0.28
Fast RT				
N	12	15	-	-
Age (years)	68.58 (3.48)	68.67 (4.76)	0.05	0.96
Sex (No. Female, %)	6 (50)	7 (46.67)	-0.17	0.87
Education (years)	15.75 (2.26)	16.3 (3.41)	0.48	0.64
MMSE (score)	29.42 (0.67)	29.4 (0.83)	-0.06	0.96
LC intensity (a.u.)	0.17 (0.03)	0.17 (0.05)	0.05	0.96
Rel. change in PVT score (%)	-7.27 (5.77)	5.63 (5.65)	5.84	<0.001
Rel. change in LC activity (%)	123.88 (328.62)	-112.87 (351.94)	-1.79	0.09

The t- and p-values correspond to the two-sample t-tests between groups. LC = locus coeruleus, MMSE = Mini-Mental State Examination, PVT = Psychomotor Vigilance Task.

Chapter 7

General discussion

RATIONALE

Aging is an inevitable and gradual process which is accompanied by important structural and functional changes in the brain, including in the brainstem locus coeruleus (LC). Through its extensive network of projections, the LC releases norepinephrine (NE) and modulates brain-wide neural activity of several cognitive and behavioral functions. Accumulating evidence suggests that the maintenance of the integrity of the LC-NE system is a key determinant for preserving late-life cognition [1, 2] and supporting brain health [3-5], notably through its effect on neuroinflammatory processes [6, 7]. In parallel, the LC is also specifically vulnerable to Alzheimer's disease (AD)-related pathology. From early in adulthood, the LC is one of the first brain structure to accumulate hyperphosphorylated tau and it undergoes extensive neural degeneration as the disease progresses [8, 9]. Thus, the LC-NE system may be a promising target against age-related cognitive decline or for disease-modifying interventions starting from the very early stages, prior to the occurrence of irreversible pathological processes. As such, future novel LC-focused interventions may represent an alternative path to the currently developed disease-modifying treatments.

The main focus of this thesis was to contribute to a better understanding of LC structural and functional properties in healthy aging and along the AD continuum, and to further test the effectiveness of non-invasive and non-pharmacological stimulating techniques in modulating LC function (Figure 1). Our findings will contribute to the larger effort of developing LC-focused interventions to boost cognition in aging, and for preventing or delaying AD progression. In this final chapter, we discuss the main findings reported in this thesis, the strengths and limitations of the studies conducted and their implications for future research and clinical translation.

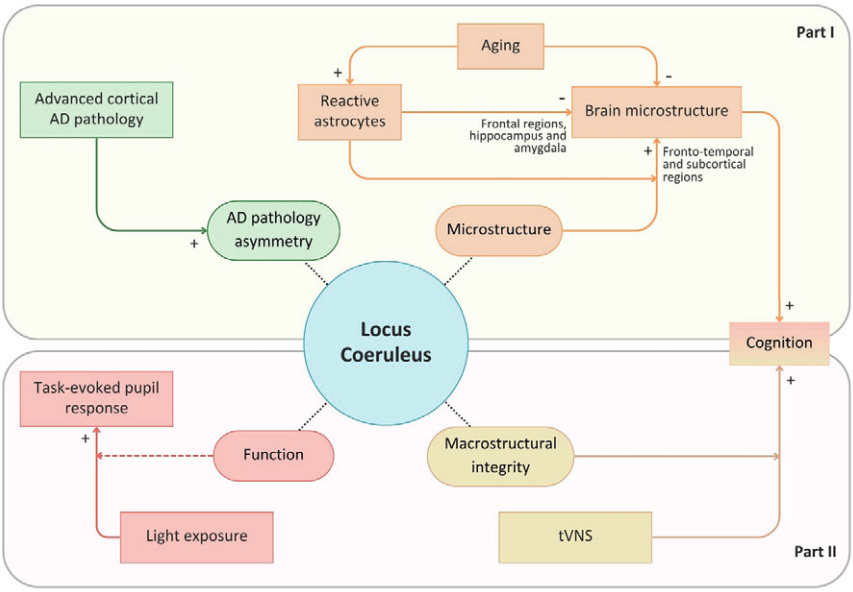

Figure 1. Schematic overview of the main findings in this thesis. **Part I** focused on the microstructural properties of the LC in healthy aging or along AD continuum, and **Part II** focused on the modulation of LC function via non-invasive and non-pharmacological interventions. The colored arrows indicate the relationships found for each chapter. The directionality of each relationship is indicated by a '+' in case of positive association, and by a '-' in case of a negative association. The dashed arrow represents a hypothesized relationship.

OUR MAIN FINDINGS

Part I. In vivo and ex vivo quantifications of the locus coeruleus structure

State-of-the-art magnetic resonance imaging (MRI) approaches at ultra-high field (UHF) combined with dedicated LC sequences have revealed their potential in visualizing the LC structure with great precision and detail [10]. MRI-derived LC structural integrity is increasingly investigated and reported as

a potential marker of several late-life processes, including changes in cognition, structural brain health, and early AD-related processes [3, 11-13]. However, the exact biological contributions to the MRI signal, including potential changes in the microstructural architecture of LC during advanced brain aging and neurodegenerative processes, remain unclear.

In **Chapter 2**, we took advantage of neurite orientation dispersion and density imaging (NODDI), an advanced model of diffusion-weighted imaging providing measures of neurites density and dendritic arborization complexity, and set out to evaluate the associations between LC, cortical and subcortical microstructure in a cohort of healthy adults throughout the lifespan. Considering the established crucial regulatory role of the LC in neuroinflammation [14], we further aimed to evaluate the modifying effect of astrocyte reactivity on the above-mentioned microstructural relationships. Our results indicated that higher astrocyte reactivity is related to microstructural brain damage, evidenced by reduced neurite density in the hippocampus, amygdala and frontal cortical regions. These findings are consistent with previous AD literature [15-17] and further expand it to the healthy lifespan, as these regions are known to be vulnerable to the aging process. Furthermore, in the presence of elevated astrocyte reactivity, lower LC neurite arborization was associated with lower arborization in neurites of several subcortical and fronto-temporal cortical regions. Interestingly, individuals presenting higher levels of arborization in the LC exhibited higher levels of arborization in these subcortical and fronto-temporal cortical regions, despite the presence of elevated astrocyte reactivity. Hence, our results align with animal studies [18] and suggest a dynamic interaction between LC cells and astrocytes, where LC dendritic arborization might exert either a neuroprotective or detrimental effect on brain microstructure across the lifespan. Specifically, this interaction appears in cortical and subcortical regions that are highly vulnerable to the earliest stages of AD, highly connected to and regulated by the LC-NE system [19, 20].

To our knowledge, this is the first study relating astrocyte reactivity and LC microstructural NODDI properties to microstructural properties in cortical and subcortical brain regions in a healthy adult lifespan cohort. While our findings support the notion that the LC is able to provide neural resilience,

it does not allow us to infer causality. Additional studies are necessary to elucidate the exact underlying mechanisms and the temporal sequence of these processes. Together, these findings highlight the relevance of maintaining LC neuronal health in aging and stress that LC microstructural properties, as indexed by NODDI, may hold the potential to signal more subtle and very early age-related neurodegenerative changes, occurring prior to the more apparent macrostructural changes.

Effectively differentiating the age-related from the AD-related changes in LC microstructure remains an important challenge for a better understanding of the aging process but also for the optimization of early diagnosis and the development of successful treatment. While neuronal degeneration in the LC occurs as the disease progresses, it is preceded by pathological tau accumulation. Asymptomatic individuals reported higher left compared to right LC MRI-derived integrity, a measure proposed to reflect, at least in part, neuronal density and tau accumulation [9, 21]. However, inconsistencies have been reported in the AD literature [22, 23].

To evaluate whether these MRI observations reflect pathological asymmetries, we investigated in **Chapter 3** whether there were asymmetric patterns of LC neuronal and tangle density in older individuals with and without evidence of AD pathology. Across 77 autopsy cases, we established that tangle density was equivalent across the left-right LC in individuals with and without underlying AD pathology, suggesting a homogeneous, symmetrical spreading pattern of pathological tau in the LC during the course of the disease. Our results further indicated that individuals with evidence of AD pathology displayed higher left than right LC neuronal density along the caudal section, relative to the rostral part. While specific to the caudal LC, these results are consistent with the observed increase in left-right differences in LC neuronal count during AD progression [24]. The caudal LC section has been related to autonomic and motor functions due to its descending projections to the cerebellum, brainstem and spinal cord. We could speculate that, while the rostral section is reported to be more vulnerable to neuronal damage in aging and AD [25], asymmetric caudal LC neurodegeneration may signal the

progression to a more advanced disease stage, also reflected by the late-stage symptoms of autonomic and motor-related dysfunction in AD.

Together, these results indicated that separately investigating LC neuronal loss across hemispheres and along its different sections is crucial in individuals with more advanced AD-related pathology, whereas this level of detail might not be required when assessing tangle density or tangle-related measures. These findings hold important implications for future in vivo studies, although caution is advised when translating these post-mortem results.

Overall, Part I of the thesis emphasizes the importance of characterizing LC microstructure in aging and AD-related processes. This characterization is crucial for identifying individuals following detrimental trajectories and for enhancing our knowledge on the biological processes that impact LC health and influence the LC MRI-signal.

Part II. Modulating the locus coeruleus function: non-invasive and non-pharmacological interventions

Pharmacological interventions targeting the LC-NE system are currently explored as treatments for AD and other neurological disorders. However, these are often accompanied with negative side effects likely due to the broad action of NE in the central nervous system. Thus, exploring non-pharmacological and non-invasive techniques for modulating the LC function offers a promising alternative path for enhancing cognition or slowing down cognitive decline. The second part of the thesis focused on the investigation of two hypothesized non-invasive, non-pharmacological and cost-effective stimulation techniques targeting the LC-NE system: the exposure to blue-enriched light and transcutaneous vagus nerve stimulation (tVNS).

Light is known to exert important non-image-forming (NIF) effects on the brain, including the pupillary light response and the modulation of alertness and cognition. The widespread neural pathways of the NIF system primary involves the intrinsically photosensitive retinal ganglion cells (ipRGCs) which in turn project to various subcortical brain regions. Through these projections, it is hypothesized that the LC may be involved, indirectly, in mediating the

enhancing effects of light on alertness and cognition [26]. Moreover, stimulus-related transient pupil variations are considered to be related, at least in part, to the ongoing changes in LC phasic activity during a cognitive engagement [27].

In **Chapter 4**, following the suggested contributions of the LC-NE system to these transient pupillary and NIF light-induced processes, we investigated the effect of light on task-evoked pupil response (TEPR) to auditory cognitive tasks in 20 healthy young adults. Our results revealed that higher light irradiances resulted in larger TEPRs on both attentional and emotional cognitive contexts. In line with in vivo animals studies relating transient variation in pupil size to LC neuronal firing [28], we could speculate that changes in light levels impact the phasic LC activity related to the ongoing cognitive process, further reflected by a transient variation in pupil size. Moreover, other studies have shown that both the attentional oddball and the emotional tasks are sensitive paradigms to measure LC activity [29-31]. Consistent with previous research [32, 33], target stimuli on the attentional task elicited larger TEPRs compared to neutral stimuli. Although similar effects have been observed in emotional tasks [29, 30], our study did not replicate this pattern in the emotional paradigm. This absence of effect is unlikely to arise from the emotional nature of the task itself, as both behavioral performance and stimulus valence were consistent with other studies [34, 35], but may be a consequence of the small sample size.

Overall, it is important to keep in mind that the LC is not the sole driver of transient pupil response but is part of a larger network of subcortical structures that regulates pupil size variations [36, 37]. Thus, the observed effects may arise from the combined influence of other nuclei directly involved in the NIF effects of light, which impact pupil regulation and share projections with the LC. While this study initially focused on pupillometry data, our future objective is to explore the brain correlates of these effects, particularly the impact of light on subcortical brainstem structures including the LC, using the associated fMRI data. Conducting this research on a larger, healthy cohort, along with including in vivo brain measures will deepen our understanding of the mechanisms underlying the influence of light on cognitive processes during aging. This knowledge could further facilitate the translation of these

findings to older adults and clinical populations, and aid in the development of light-based techniques for targeting the LC-NE system.

While the investigation of the exact brain pathways of the NIF impact of light is an active field of research, light protocols considerably differ across studies therefore limiting the direct comparison of their outcomes. In addition, most of these fMRI studies used repeated short light exposures alternating between different spectral compositions [38-40] and it is not clear whether the effect of one light block carries over onto the next ones, thus potentially biasing these fMRI results.

In **Chapter 5**, we took advantage of pupillometry as an easy and accessible method to assess the NIF effects of light. We aimed to characterize the sustained pupil response during an fMRI protocol including alternating short light blocks varying in irradiance levels and during different cognitive tasks. Our results demonstrated that, as expected, higher light irradiance levels led to larger sustained pupil light responses (PLR), consistently observed across all three cognitive contexts. Notably, this pattern was not stable throughout the protocol under lower light levels, for which smaller PLR was observed over the last compared to the first light blocks. We did not find evidence for such a difference at higher light levels (above ~90 melanopic equivalent daylight illuminance (EDI) lux). In addition, the overall sustained PLR during the first administered task was reduced compared to the two subsequent randomized tasks. Further research is needed to elucidate whether the nature of the cognitive tasks interacts with this relationship. However, it is plausible that the dim light adaptation period preceding the fMRI protocol temporarily affected the sensitivity of retinal photoreceptors to light during the initial part of the experiment. In **Chapter 4**, this impact is likely minimized as the reported results are derived from tasks not directly following the light adaptation period. However, caution is warranted when interpreting results from future investigation of the associated brain correlates, as they may still be biased at their lower light levels. Overall, our findings emphasize that cognitive context, light levels and recent light history may influence sustained PLR assessment and should be further accounted for in the analysis and/or the interpretation of fMRI data.

Transcutaneous vagus nerve stimulation (tVNS) is an emerging neuromodulatory technique that has garnered the interest of the scientific field for its ability to target the LC-NE system in a non-invasive, non-pharmacological and cost-effective manner. Despite multiple studies investigating tVNS-induced responses in both healthy individuals and patients with varying diagnoses, notable inconsistencies in its efficacy have been reported so far [41-44]. These variations may indicate that tVNS-related pathways interact or are affected differently across diverse scenarios or populations.

In **Chapter 6**, we set out to evaluate whether the structural integrity of the LC-NE system could account for some of the variability in tVNS effects on attentional processes in 27 healthy older individuals. Our results revealed that MRI-derived LC integrity interacts with tVNS-induced responses, such that higher LC integrity was associated with higher performance following tVNS. Importantly, this pattern was only observed under suboptimal attention and in a group of responders, i.e. individuals who demonstrated enhanced performance after tVNS compared to the sham condition. These findings further suggest that the mixed tVNS-related outcomes reported in the literature might result from the lack of specificity in the targeted population. Interestingly, responders and non-responders were not differing in their LC integrity measures, indicating that factors beyond LC structural integrity, potentially related to overall LC health or other processes, may be involved in determining the tVNS-induced responses on attentional processes. Finally, no associations were found between tVNS and LC neural activity, which may reflect a statistical power issue as other studies reported changes in LC activity following tVNS [45, 46]. Future research with larger sample sizes including the measurement of various LC-related properties is needed to confirm these findings. Such studies should aim to better characterize the populations that benefits the most from tVNS and explore the potential for translating this technique into clinical practice for targeting the LC-NE system.

Overall, this second part contributes to the growing knowledge on the mechanisms underlying light-related and tVNS techniques, with the ultimate goal to modulate the LC-NE system effectively and to translate these non-pharmacological and non-invasive methods into clinical applications.

METHODOLOGICAL CONSIDERATIONS

Strengths and limitations

Within this thesis, we were able to assess our LC-focused research questions in diverse cohorts, including healthy individuals across the entire lifespan and AD autopsy cases. However, the generalizability of our findings may be limited by several factors. Research at 7T MRI, beside its important technical advantages, is often accompanied with a selection bias inherent to the scanning contraindications. In addition, the studies presented in this thesis involved complex experimental designs with strict exclusion criteria regarding health, cognition and lifestyle. Therefore, it is plausible that our sample, and specifically in the older age range, is healthier and not entirely representative of the average population. Similarly, **Chapter 3** is likely to suffer from a survival bias inherent to the older age range of autopsy data, which limits the translation of these findings to the younger population. Finally, although our sample sizes were considered as moderate given the inclusion criteria, as well as the complexity and burden of the protocols on participants, some results and conclusions from **Chapters 4 and 6** are likely to be limited due to statistical power issue. This prevented further exploration of subgroups or higher-order interactions. Altogether, these limitations emphasize the need for larger cohorts including both healthy individuals and patients along the AD continuum. Longitudinal study designs are also crucial for opening up opportunities to examine the evolution of our findings over time.

Even though not everyone is eligible to undergo 7T MR-imaging, the combined use of in-house developed LC-dedicated sequences together with advanced UHF MRI techniques was critical for addressing our research questions and is a major strength of this thesis. UHF imaging facilitates the measurement of small structures through its inherent increased signal to noise ratio and spatial resolution. Nevertheless, imaging tiny brainstem structures such as the LC remains challenging as they are highly sensitive to motion and physiological artifacts, including respiration and flow pulsatility. In **Chapter 6**, we worked to mitigate these factors by using advanced processing methods such as the implementation of image denoising and motion regression on the fMRI data,

and the use of expiration-gated stimulation technique known to enhance LC targeting [46]. It is also important to note that the blood-oxygen level dependent fMRI signal does not directly measure neuronal activity, but rather the oxygenated and deoxygenated blood level variations which are likely to interact with other mechanisms, including blood volume and flow. Therefore, we cannot rule out the presence of non-neural contributions and our results should be interpreted with this caveat in mind.

In addition, the measure of LC structural integrity is derived from the MRI signal intensity at the anatomical location of the LC and contrasting with its surroundings on LC-specific sequences. Just as with any MRI measure or proxy of a process, it is important to be cognizant of its limitations. Firstly, the nature of the biological mechanisms underlying this hyperintense signal remains a topic of debate, making it hard to interpret its variations relative to a unique and specific biological process. While the LC MRI signal strongly correlates with AD-related processes [13], other mechanisms, such as inflammation, water content, copper and lipids have also been suggested to contribute to the signal variability [47]. Secondly, these LC-imaging sequences do not capture the entire length of the LC, excluding the most caudal portion due to its more diffuse nature. Thirdly, when imaging the brain, scientists must balance spatial and temporal resolution, requiring trade-offs that can impact the precision and detail of the images.

In **Chapter 2**, we opted for a reduced field of view in our diffusion-weighted scans to achieve smaller voxel sizes. However, this choice prevented us from exploring LC to cortical association in some fronto-parietal regions. The recently developed Connectome 2.0 scanners for diffusion MRI offer significant technological advancements, including higher spatial resolution, greater sensitivity to microstructural changes and reduced scan times [48]. Replicating our findings and further expanding it to whole-brain cortical associations using this state-of-the-art MRI technology could provide crucial insights into the LC-brain microstructural interactions with astrocyte reactivity. Importantly, our results are not generalizable to the entire astrocyte population as our GFAP blood-marker only quantifies a sub-population of astrocytes measured in the periphery. It is also important to note that astrocytes can exhibit different reactive profiles, both pro-inflammatory

and anti-inflammatory. Due to their hypertrophic morphology and altered metabolism, reactive astrocytes can also be quantified in vivo at the brain level through the detection of myo-inositol, an intra-astrocyte metabolite, using magnetic resonance spectroscopy (MRS) [49, 50], and by employing astrocyte-specific positron emission tomography (PET) tracers [51]. Thus, replicating our findings with additional astrocytes biomarkers derived from MRS and PET in vivo modalities may further inform on the specificity and sensitivity of the observed interactions.

Lastly, the acquisition of the pupillometry data (**Chapters 4 and 5**) was challenging due to the complexity of the MRI-integrated light setup, which resulted in a limited number of participants with high-quality data suitable for analysis. The MR-compatible infrared eye-tracking system, positioned behind the MRI head coil and fixated to the table, was susceptible to the gradient coil vibrations. In addition, optimal calibration of the eye-tracking system to the pupil diameter was hampered by the dark ambient lighting, and the quality of pupil detection during the scans varied with light conditions, such as lower light levels led to poorer measurements. It is important to recognize that pupil dynamics are affected by a wide variety of factors, including light exposure, environmental conditions, emotional states and cognitive engagement. Moreover, pupil changes involve the complex interaction of multiple brain structures that are not yet fully understood. Consequently, interpretating these changes in pupil size in relation to specific processes is not straightforward. To address these challenges, efforts are needed to integrate eye-tracking systems more effectively within MRI environments and further ensure the acquisition of reliable measurements. Additionally, combining pupil data with other physiological and behavioral metrics can provide a more comprehensive understanding of the underlying processes, with the ultimate goal to address more complex research questions.

Both stimulation techniques investigated in this thesis come with their own limitations. On the one hand, light sequences were restricted to only four distinct illuminance levels and included two different spectral colors. The design of the light protocol restricted our ability to establish a complete light action spectrum, to properly differentiate between spectral and irradiance effects

and to further assess the specific involvement of each photoreceptor in pupil response [52]. Future neuroimaging studies could overcome these limitations by using metameric lights, which offer the ability to vary in spectral composition without altering light color perception, and to further target specific types of photoreceptors more accurately [53]. Moreover, while **Chapters 4 and 5** hypothesized the involvement of the LC in the observed pupillary response, the contribution of other nuclei to these complex NIF effects of light cannot be ruled out. To achieve a comprehensive understanding of the underlying mechanisms, future in vivo studies need to focus on the LC alongside other relevant subcortical structures using dedicated imaging methods.

On the other hand, a major limitation of tVNS is the lack of clear consensus on the optimal set of parameters -such as duration, frequency, current intensity, and pulse width- or on the appropriate sham configuration [54] (**Chapter 6**). Whether these parameters need to be adapted depending on the population or on the stimulation target remains unknown, highlighting an important need for standardization in the field. A recent international group of tVNS researchers encouraged future studies to be more comprehensive and transparent in reporting procedures and parameters [55]. Such efforts are crucial to facilitate our understanding of the mechanisms, protocols and potential clinical implications of this stimulation technique.

The LC is a small yet fascinating nucleus, with its approximately 50,000 neurons playing a key role in various behaviors and diseases. While the methodological considerations discussed in this thesis are important, they should not discourage other scientists from exploring the LC, but instead provide valuable suggestions for future research directions and goals.

CLINICAL IMPLICATIONS AND FUTURE DIRECTIONS

The multifaceted and complex role of the LC in the daily functioning along with its involvement in aging and neurodegenerative processes has heightened curiosity for this brainstem nuclei within both research and clinical practice. This growing interest is further reflected by the extensive literature exploring

LC-related processes and providing valuable insights into the underlying mechanisms. In vivo, the LC is most commonly characterized through its macrostructural integrity, a marker increasingly related to processes occurring in aging and along AD, and a promising indicator for identifying individuals at risk of disease progression. However, microstructural properties of the LC remain mostly unexplored in vivo.

Our results in **Chapter 2** point toward an important role of LC neurites architecture along with reactive astrocytes in shaping neuroprotective or detrimental microstructural brain pathways in healthy aging. Microstructural NODDI diffusion metrics have been highlighted as more sensitive brain health indicators capturing earlier neurodegenerative changes compared to morphometric measurements both in aging and in AD [56]. In line with this, our results suggest an important role of the LC microstructure in detecting subtle and very early brain changes in asymptomatic older individuals. Given the vulnerability of the LC reported from the earliest stages of AD, future studies should investigate the temporal evolution of LC microstructural properties using longitudinal designs across the disease spectrum.

Specifically, our findings indicate that reactive astrocytes closely interact with LC cells, playing a critical role in shaping brain health. While astrocytes are shown to become reactive with age [57], astrocytes dysfunction has also been related to neurodegenerative changes in AD [58]. More recently, astrocyte reactivity in humans has been proposed as an early process in preclinical AD, through its close relationship with amyloid-beta in triggering tau pathology among cognitively unimpaired individuals [59]. Since astrocyte reactivity is likely to reflect AD pathology upstream of early tau phosphorylation [60], it could hold great implication for the hypothesized biomarker models [61] and biological definitions [62] of AD. Therefore, it is crucial to elucidate the temporal sequence of the interaction between LC microstructure and reactive astrocytes, and to integrate this understanding within the larger framework of the biomarker modeling of AD. Future longitudinal studies along the disease continuum should leverage NODDI, an easily accessible and highly sensitive technique for detecting early AD processes, in combination with LC-dedicated MRI sequences, astrocytes and AD-related biomarkers. Moreover, including cerebrospinal fluid (CSF) biomarkers of neuroinflammation would

be informative to discern whether these relationships are directly linked to neuroinflammatory brain processes, or reflect other peripheral mechanisms. Ultimately, this information could help in determining whether LC NODDI microstructure can act as a potential marker for very early neurodegenerative processes and indicate individuals at increased risk of developing AD.

Most of the LC research examines its in vivo structure as a whole rather than separated in its left and right parts. Autopsy studies, on the other hand, typically focus on only one hemisphere of the brain. In **Chapter 3**, we provide ex vivo evidence for an asymmetrical left-right pattern in neuronal density across the rostro-caudal LC in individuals with underlying AD pathology. Given that the MRI-derived in vivo LC integrity measure is thought to reflect neuronal density and tau-related processes [13, 47], our findings suggest that the in vivo examination of LC integrity in individuals at later stages of the disease should consider both sides separately and across different LC sections. So far, only a few studies reported inconsistencies regarding LC integrity asymmetry in AD cohorts [22, 23]. Interestingly, these mixed results do not align with our ex vivo findings, suggesting that additional biological mechanisms, such as copper, lipids and water, may interact with LC neuronal density over time to influence the MRI signal intensity. Similarly, our results of a homogeneous and symmetrical spreading pattern of pathological tau along the disease do not exclude the possibility that tau, which also impacts the LC MRI signal intensity, contributes to the asymmetrical pattern observed in LC neurons density. Further exploring the biological contributions of the MRI-derived LC integrity would facilitate the translation of these post-mortem results to in vivo contexts. To achieve this, future research could focus on longitudinal studies design across the disease spectrum, acquiring bilateral measurements of LC structural integrity along its rostro-caudal extent, alongside AD-related biomarkers and cognitive data. When these individuals pass away, the longitudinal MRI data together with the pathophysiological and cognitive diagnosis at time of death can then be correlated with post-mortem neuronal density in the left and right LC. Overall, these finding holds important implications for in vivo LC-focused studies involving clinical population, providing insights on the level of

detail required when examining LC neurodegenerative changes or tau-related measures.

There is a growing interest in the use of in vivo measurement of LC integrity in clinical settings, given its potential as biomarker from the earliest stages of the disease. Although less explored, LC microstructural properties also appear as promising indicators of more subtle neurodegenerative changes associated with aging, while future research should determine if this pattern extends to AD population. Overall, brain micro- and macro-structural properties are intricately linked, each influencing the other and contributing to the global brain health and function. Currently, the interaction between these metrics at the level of the LC remains unclear. Considering the dynamic and complex processes the LC undergoes along the disease spectrum, its micro- and macro-structural properties likely reflect distinct aspects of the AD pathophysiological cascade. A joint measurement of these properties, combined with multimodal phenotyping of individuals in longitudinal studies across different stages of the disease could offer a more precise and comprehensive understanding of the evolution of age- and AD-related neurodegenerative changes. In clinical settings, the integrated assessment of these metrics could facilitate the early diagnosis and the identification of individuals at risk of developing AD and further contribute to the development of personalized treatment strategies.

Dysfunction of the LC-NE system is observed in neurodegenerative diseases including AD, and in age-related cognitive decline. Developing non-invasive, non-pharmacological, cost-effective and easily accessible interventions targeting the noradrenergic system is an important step toward the establishment of a valuable AD-related therapeutic approach. These interventions hold the potential to alleviate cognitive symptoms and possibly slow down disease progression. However, further research is required to better understand their underlying mechanisms, optimize their implementation and design personalized approaches, with the aim to fully realize their potential in clinical practice.

Sleep-wake disruption [63] and cognitive decline are two common characteristics of AD. Light exposure, known for its NIF effects including the regulation of sleep-wake cycles and several cognitive functions, has recently been studied for its hypothesized therapeutic effect in AD patients. Overall, little and mixed results regarding the effectiveness of light therapy on cognitive function have been reported in AD population [64-66]. Critically, the brain pathways underlying these NIF effects of light in humans remain poorly understood. In rodents, ipRGCs-related brain pathways have been established as diverse and complex, projecting to numerous subcortical and cortical brain regions [67]. Neuroimaging studies attempting at translating these animal findings have highlighted several brain regions modulated by light, including an area compatible with the anatomical location of the LC [38].

Within this thesis, **Chapters 4 and 5** provided additional insights into the NIF impact of light during cognitive engagement on pupillary response, which is suggested to reflect light-modulated LC activity. While our current results do not provide clear in vivo evidence for the LC involvement in light-induced TEPR in healthy young adults (**Chapter 4)**, we plan to explore the brain correlates underlying these associations in the future by using the available UHF fMRI data. With these results in combination with pupillometry, we hope to further inform on the impact of light on the LC during TEPRs and to better understand the neural correlates of light in humans.

Importantly, the LC is not directly innervated by ipRGCs, but receives notably indirect inputs from the suprachiasmatic nucleus (SCN) of the hypothalamus, a major target of ipRGCs (see Figure 3 from Chapter 1). It is therefore likely that the observed light impact on LC-related measures arise from a synergistic effect from one or multiple subcortical structures involved in the NIF brain pathways. While there is currently no evidence supporting this hypothesis, here we discuss a subcortical structure that may be theoretically relevant to this scenario. A recent study from our group showed a stimulating effect of light on the activity of the posterior part of the hypothalamus [68]. Interestingly, this area encompasses the lateral hypothalamus (LH), which is reported to be innervated by ipRGCs in rodents [67] and further support its potential in being influenced by light illuminance. The LH is highly interconnected to the LC [20], exerting direct orexinergic activation on the LC-NE

system [69]. This suggests that the LH may play an early role in light-related stimulation pathways, subsequently modulating LC activity and its associated mechanisms. Animal models examining the effect of localized lesions of the LH could further inform on the specificity of the hypothesized light-induced pathways. Notably, the LH has also been recognized as a neuromodulatory nucleus that accumulates tau pathology early in the disease progression, prior to its appearance in cortical regions [70], highlighting an additional potentially therapeutic pathway that could be relevant to light exposure strategies.

Future work on the NIF effects of light is encouraged to avoid investigating irradiance levels below approximately 90 melanopic EDI lux (**Chapter 5)** to minimize the potential bias introduced by the light protocol. Instead, studies should explore higher irradiances levels to work toward the establishment of a comprehensive light action spectrum. Metameric light research is also an important path to explore, as it holds the potential to inform on the specific involvement of photoreceptors in response to varying light irradiance levels while keeping participants blind to their spectral composition. Future research would highly benefit from studies involving large cohorts to overcome statistical power limitations. Including healthy older individuals would help determine whether our findings apply to this population, as they have been shown to be less sensitive to light than younger adults [71]. Ultimately, extending these studies to AD patients is essential for the development and optimization of light therapy in moderating AD symptoms. This therapeutic approach has the potential to improve sleep-wake cycles, cognition and overall quality of life, and offers the advantages of being non-invasive, harmless and easily affordable.

The growing need for interventions addressing early neurodegenerative processes has highlighted tVNS as a promising technique for modulating the LC-NE system in both aging and AD contexts. However, there is a current challenge in precisely evaluating the effects of tVNS in human research, as evidenced by the considerable inconsistencies in tVNS-induced responses reported in the literature. **Chapter 6** suggests that MRI-derived LC integrity measure determines the effects of tVNS on suboptimal attention in responders and that it could explain, at least in part, the variability observed in tVNS-related changes in cognition in healthy older individuals. Interestingly, we

were not able to differentiate responders from non-responders based on their demographics or in vivo brain measures. This suggests that other factors related to the LC health may interact with its integrity when determining the effect of tVNS. Consequently, future research should focus on the identification of biological or cognitive markers reflecting the efficacy of tVNS on the LC-NE system.

Beside exploring the tVNS effects on the LC-NE system via fMRI, studies could benefit from the investigation of other proxies of LC activity. These could include pupillometry, measurements of NE and its metabolites in blood or CSF, and salivary alpha-amylase levels. Moreover, the establishment of an optimal stimulation protocol is crucial for accurately evaluating tVNS responses. This process could benefit from translational approaches using animal models to refine the stimulation parameters and guide the development of the protocol. Additional studies should attempt to validate our results in larger cohorts to address potential issues related to statistical power. Finally, given the early vulnerability of the LC in AD and the potential of tVNS to target the noradrenergic system and modulate cognition, future research should investigate these effects in cognitively impaired individuals along the disease spectrum. Specifically, it remains unclear to what extent the underlying neurodegenerative processes of AD affecting LC properties might interfere with the tVNS-induced response on cognition.

Overall, our findings will help stratify the population based on their likelihood to benefit from the intervention. This will facilitate participants selection for future clinical trials and ultimately contribute to developing highly personalized and effective non-invasive, non-pharmacological treatments aiming at boosting cognition or preventing cognitive decline.

CONCLUDING REMARKS

Within this thesis, we emphasized the critical role of LC microstructure in shaping brain health along the lifespan and its vulnerability to AD-related processes, as evidenced by the asymmetrical pattern in LC neurodegeneration observed in the later stages of the pathology. These microstructural properties,

combined with other common markers of LC health, may be crucial for identifying individuals at risk of AD, starting in the preclinical phase. This early detection is essential for the development of successful and effective therapeutic approaches.

Moreover, we provided in vivo evidence that light exposure and tVNS are promising candidates for modulating LC function, as reflected in TEPRs and attentional processes in healthy individuals. However, important work remains to establish these stimulation techniques as accessible, low-cost and non-invasive interventions in clinical population.

Future longitudinal studies spanning the disease spectrum, including information on AD pathology, are needed to confirm and translate our findings throughout the AD pathophysiological cascade. Altogether, the results presented in this thesis provide strong directions for future research that hopefully will lead to safe and effective preventive and therapeutic LC-focused interventions in the future.

REFERENCES

1. Mather M and Harley CW. The Locus Coeruleus: Essential for Maintaining Cognitive Function and the Aging Brain. *Trends Cogn Sci*. 2016;20(3):214-26.
2. Sara SJ. The locus coeruleus and noradrenergic modulation of cognition. *Nat Rev Neurosci*. 2009;10(3):211-23.
3. Bachman SL, et al. Locus coeruleus MRI contrast is associated with cortical thickness in older adults. *Neurobiol Aging*. 2021;100:72-82.
4. Elman JA, et al. Associations between MRI-assessed locus coeruleus integrity and cortical gray matter microstructure. *Cereb Cortex*. 2022;32(19):4191-203.
5. Engels-Domínguez N, et al. Lower in vivo locus coeruleus integrity is associated with lower cortical thickness in older individuals with elevated Alzheimer's pathology: a cohort study. *Alzheimers Res Ther*. 2024;16(1):129.
6. Braun D, Madrigal JL, and Feinstein DL. Noradrenergic regulation of glial activation: molecular mechanisms and therapeutic implications. *Curr Neuropharmacol*. 2014;12(4):342-52.
7. Heneka MT, et al. Locus ceruleus controls Alzheimer's disease pathology by modulating microglial functions through norepinephrine. *Proceedings of the National Academy of Sciences*. 2010;107(13):6058-63.
8. Braak H, et al. Stages of the pathologic process in Alzheimer disease: age categories from 1 to 100 years. *J Neuropathol Exp Neurol*. 2011;70(11):960-9.
9. Jacobs HIL, et al. Waning locus coeruleus integrity precedes cortical tau accrual in preclinical autosomal dominant Alzheimer's disease. *Alzheimers Dement*. 2023;19(1):169-80.
10. Priovoulos N, et al. High-resolution in vivo imaging of human locus coeruleus by magnetization transfer MRI at 3T and 7T. *Neuroimage*. 2018;168:427-36.
11. Clewett DV, et al. Neuromelanin marks the spot: identifying a locus coeruleus biomarker of cognitive reserve in healthy aging. *Neurobiol Aging*. 2016;37:117-26.
12. Dahl MJ, et al. Rostral locus coeruleus integrity is associated with better memory performance in older adults. *Nat Hum Behav*. 2019;3(11):1203-14.
13. Jacobs HIL, et al. In vivo and neuropathology data support locus coeruleus integrity as indicator of Alzheimer's disease pathology and cognitive decline. *Sci Transl Med*. 2021;13(612):eabj2511.
14. Evans AK, Defensor E, and Shamloo M. Selective Vulnerability of the Locus Coeruleus Noradrenergic System and its Role in Modulation of Neuroinflammation, Cognition, and Neurodegeneration. *Front Pharmacol*. 2022;13:1030609.
15. Benedet AL, et al. Differences Between Plasma and Cerebrospinal Fluid Glial Fibrillary Acidic Protein Levels Across the Alzheimer Disease Continuum. *JAMA Neurol*. 2021;78(12):1471-83.
16. Bettcher BM, et al. Astrogliosis and episodic memory in late life: higher GFAP is related to worse memory and white matter microstructure in healthy aging and Alzheimer's disease. *Neurobiol Aging*. 2021;103:68-77.

17. Spotorno N, et al. Diffusion MRI tracks cortical microstructural changes during the early stages of Alzheimer's disease. *Brain*. 2023.

18. Bekar LK, He W, and Nedergaard M. Locus coeruleus alpha-adrenergic-mediated activation of cortical astrocytes in vivo. *Cereb Cortex*. 2008;18(12):2789-95.

19. Chandler DJ, Gao WJ, and Waterhouse BD. Heterogeneous organization of the locus coeruleus projections to prefrontal and motor cortices. *Proc Natl Acad Sci U S A*. 2014;111(18):6816-21.

20. Samuels ER and Szabadi E. Functional neuroanatomy of the noradrenergic locus coeruleus: its roles in the regulation of arousal and autonomic function part I: principles of functional organisation. *Curr Neuropharmacol*. 2008;6(3):235-53.

21. Engels-Domínguez N, et al. State-of-the-art imaging of neuromodulatory subcortical systems in aging and Alzheimer's disease: Challenges and opportunities. *Neurosci Biobehav Rev*. 2023;144:104998.

22. Betts MJ, et al. In vivo MRI assessment of the human locus coeruleus along its rostrocaudal extent in young and older adults. *Neuroimage*. 2017;163:150-9.

23. Cassidy CM, et al. Association of locus coeruleus integrity with Braak stage and neuropsychiatric symptom severity in Alzheimer's disease. *Neuropsychopharmacology*. 2022;47(5):1128-36.

24. Chan-Palay V and Asan E. Alterations in catecholamine neurons of the locus coeruleus in senile dementia of the Alzheimer type and in Parkinson's disease with and without dementia and depression. *J Comp Neurol*. 1989;287(3):373-92.

25. German DC, et al. Disease-specific patterns of locus coeruleus cell loss. *Ann Neurol*. 1992;32(5):667-76.

26. Vandewalle G, Maquet P, and Dijk DJ. Light as a modulator of cognitive brain function. *Trends Cogn Sci*. 2009;13(10):429-38.

27. Joshi S and Gold JI. Pupil Size as a Window on Neural Substrates of Cognition. *Trends in Cognitive Sciences*. 2020;24(6):466-80.

28. Costa VD and Rudebeck PH. More than Meets the Eye: the Relationship between Pupil Size and Locus Coeruleus Activity. *Neuron*. 2016;89(1):8-10.

29. Aston-Jones G and Cohen JD. An integrative theory of locus coeruleus-norepinephrine function: adaptive gain and optimal performance. *Annu Rev Neurosci*. 2005;28:403-50.

30. Bradley MM, et al. The pupil as a measure of emotional arousal and autonomic activation. *Psychophysiology*. 2008;45(4):602-7.

31. Rajkowski J, Kubiak P, and Aston-Jones G. Locus coeruleus activity in monkey: phasic and tonic changes are associated with altered vigilance. *Brain Res Bull*. 1994;35(5-6):607-16.

32. Gilzenrat MS, et al. Pupil diameter tracks changes in control state predicted by the adaptive gain theory of locus coeruleus function. *Cogn Affect Behav Neurosci*. 2010;10(2):252-69.

33. Murphy PR, et al. Pupil diameter covaries with BOLD activity in human locus coeruleus. *Hum Brain Mapp*. 2014;35(8):4140-54.

34. Grandjean D, et al. The voices of wrath: brain responses to angry prosody in meaningless speech. *Nat Neurosci*. 2005;8(2):145-6.

35. Vandewalle G, et al. Spectral quality of light modulates emotional brain responses in humans. *Proc Natl Acad Sci U S A*. 2010;107(45):19549-54.

36. DiNuzzo M, et al. Brain Networks Underlying Eye's Pupil Dynamics. *Front Neurosci*. 2019;13:965.

37. Joshi S, et al. Relationships between Pupil Diameter and Neuronal Activity in the Locus Coeruleus, Colliculi, and Cingulate Cortex. *Neuron*. 2016;89(1):221-34.

38. Vandewalle G, et al. Brain responses to violet, blue, and green monochromatic light exposures in humans: prominent role of blue light and the brainstem. *PLoS One*. 2007;2(11):e1247.

39. Daneault V, et al. Aging reduces the stimulating effect of blue light on cognitive brain functions. *Sleep*. 2014;37(1):85-96.

40. McGlashan EM, et al. Afraid of the dark: Light acutely suppresses activity in the human amygdala. *PLoS One*. 2021;16(6):e0252350.

41. Jacobs HI, et al. Transcutaneous vagus nerve stimulation boosts associative memory in older individuals. *Neurobiol Aging*. 2015;36(5):1860-7.

42. Klaming R, et al. Effects of Noninvasive Cervical Vagal Nerve Stimulation on Cognitive Performance But Not Brain Activation in Healthy Adults. *Neuromodulation*. 2022;25(3):424-32.

43. Mertens A, et al. Transcutaneous Vagus Nerve Stimulation Does Not Affect Verbal Memory Performance in Healthy Volunteers. *Front Psychol*. 2020;11:551.

44. Villani V, et al. Event-related transcutaneous vagus nerve stimulation modulates behaviour and pupillary responses during an auditory oddball task. *Psychoneuroendocrinology*. 2022;140:105719.

45. Garcia RG, et al. Modulation of brainstem activity and connectivity by respiratory-gated auricular vagal afferent nerve stimulation in migraine patients. *Pain*. 2017;158(8):1461-72.

46. Sclocco R, et al. The influence of respiration on brainstem and cardiovagal response to auricular vagus nerve stimulation: A multimodal ultrahigh-field (7T) fMRI study. *Brain Stimul*. 2019;12(4):911-21.

47. Priovoulos N, et al. Unraveling the contributions to the neuromelanin-MRI contrast. *Brain Struct Funct*. 2020;225(9):2757-74.

48. Huang SY, et al. Connectome 2.0: Developing the next-generation ultra-high gradient strength human MRI scanner for bridging studies of the micro-, meso- and macro-connectome. *Neuroimage*. 2021;243:118530.

49. Ligneul C, et al. Diffusion-weighted magnetic resonance spectroscopy enables cell-specific monitoring of astrocyte reactivity in vivo. *Neuroimage*. 2019;191:457-69.

50. Spotorno N, et al. Astrocytic function is associated with both amyloid-β and tau pathology in non-demented APOE 4 carriers. *Brain Commun*. 2022;4(3):fcac135.

51. Liu Y, et al. PET imaging of reactive astrocytes in neurological disorders. *Eur J Nucl Med Mol Imaging*. 2022;49(4):1275-87.

52. Gamlin PD, et al. Human and macaque pupil responses driven by melanopsin-containing retinal ganglion cells. *Vision Res*. 2007;47(7):946-54.

53. Viénot F, et al. Domain of metamers exciting intrinsically photosensitive retinal ganglion cells (ipRGCs) and rods. *J Opt Soc Am A Opt Image Sci Vis*. 2012;29(2):A366-76.

54. Ludwig M, et al. Current challenges in reliably targeting the noradrenergic locus coeruleus using transcutaneous auricular vagus nerve stimulation (taVNS). *Auton Neurosci*. 2021;236:102900.

55. Farmer AD, et al. International Consensus Based Review and Recommendations for Minimum Reporting Standards in Research on Transcutaneous Vagus Nerve Stimulation (Version 2020). *Front Hum Neurosci*. 2020;14:568051.

56. Yu X, et al. NODDI in gray matter is a sensitive marker of aging and early AD changes. *Alzheimers Dement (Amst)*. 2024;16(3):e12627.

57. Palmer AL and Ousman SS. Astrocytes and Aging. *Front Aging Neurosci*. 2018;10:337.

58. Acosta C, Anderson HD, and Anderson CM. Astrocyte dysfunction in Alzheimer disease. *J Neurosci Res*. 2017;95(12):2430-47.

59. Bellaver B, et al. Astrocyte reactivity influences amyloid-β effects on tau pathology in preclinical Alzheimer's disease. *Nat Med*. 2023;29(7):1775-81.

60. Johansson C, et al. Plasma biomarker profiles in autosomal dominant Alzheimer's disease. *Brain*. 2023;146(3):1132-40.

61. Jack CR, Jr., et al. Tracking pathophysiological processes in Alzheimer's disease: an updated hypothetical model of dynamic biomarkers. *Lancet Neurol*. 2013;12(2):207-16.

62. Jack CR, Jr., et al. NIA-AA Research Framework: Toward a biological definition of Alzheimer's disease. *Alzheimers Dement*. 2018;14(4):535-62.

63. Van Egroo M, et al. Sleep-wake regulation and the hallmarks of the pathogenesis of Alzheimer's disease. *Sleep*. 2019;42(4).

64. Kim SJ, et al. Positive effect of timed blue-enriched white light on sleep and cognition in patients with mild and moderate Alzheimer's disease. *Sci Rep*. 2021;11(1):10174.

65. Fontana Gasio P, et al. Dawn-dusk simulation light therapy of disturbed circadian rest-activity cycles in demented elderly. *Exp Gerontol*. 2003;38(1-2):207-16.

66. Riemersma-van der Lek RF, et al. Effect of bright light and melatonin on cognitive and noncognitive function in elderly residents of group care facilities: a randomized controlled trial. *Jama*. 2008;299(22):2642-55.

67. Do MTH. Melanopsin and the Intrinsically Photosensitive Retinal Ganglion Cells: Biophysics to Behavior. *Neuron*. 2019;104(2):205-26.

68. Campbell I, et al. Regional response to light illuminance across the human hypothalamus. *Elife*. 2024;13.

69. Horvath TL, et al. Hypocretin (orexin) activation and synaptic innervation of the locus coeruleus noradrenergic system. *J Comp Neurol*. 1999;415(2):145-59.

70. Stratmann K, et al. Precortical Phase of Alzheimer's Disease (AD)-Related Tau Cytoskeletal Pathology. *Brain Pathol*. 2016;26(3):371-86.

71. Duffy JF, Zeitzer JM, and Czeisler CA. Decreased sensitivity to phase-delaying effects of moderate intensity light in older subjects. *Neurobiol Aging*. 2007;28(5):799-807.

Addendum

SUMMARY

Global aging of the population is accompanied with increasing prevalence rates of Alzheimer's disease (AD) and important challenges for the healthcare system. While recently discovered disease-modifying drugs are getting approved, there is currently no indication for a widely available treatment free of adverse side effects and also targeting the early asymptomatic stages of the disease. During the last decades, the locus coeruleus (LC) has been identified as a promising preclinical marker of AD, reflected by its specific vulnerability to early AD-related processes starting in the pre-symptomatic phase. Therefore, the LC has been considered as a favorable target and potential alternative path for disease-modifying interventions starting from the very early neuropathological stages of the disease. In addition, the LC has also been shown to undergo alterations in healthy aging such that maintaining its integrity can be essential for preventing age-related neurodegenerative changes, including cognitive decline. Thus, being able to better characterize and differentiate age-related from AD-related neurodegenerative changes occurring within the LC will pave the way toward an earlier identification of detrimental processes and will contribute to the larger effort in developing interventions targeting the pre-symptomatic stages of the disease. Within this thesis, we aimed to, firstly, expand on the current knowledge regarding the LC structure in aging and along the AD continuum (**Part I**); and secondly, to assess the effectiveness of two non-invasive and non-pharmacological stimulation techniques, the exposure to blue-enriched light and transcutaneous vagus nerve stimulation (tVNS), in modulating LC function in healthy cohorts (**Part II**).

Part I. In vivo and ex vivo quantifications of the LC structure

In **Chapter 2**, we investigated the associations between the microstructural properties in the LC, cortical and subcortical grey matter, measured through 7T MRI in combination with neurite orientation dispersion and density imaging (NODDI) diffusion models, in a healthy adult lifespan cohort. Because the LC-norepinephrine (NE) system plays a key role in supporting brain health along the lifespan, notably through its modulatory effects on neuroinflammation, we examined the modulatory effect of reactive astrocytes on these microstructural

associations. We found that higher astrocyte reactivity was associated with lower neurite density in the amygdala, hippocampus and frontal cortex, which are regions vulnerable to aging processes. Furthermore, in the presence of elevated astrocyte reactivity, lower arborization in LC neurites was associated with lower neurites arborization in fronto-temporal cortical and several subcortical regions. Interestingly, individuals presenting higher levels of arborization in the LC exhibited higher levels of arborization in these cortical and subcortical regions, despite the presence of elevated astrocyte reactivity. Together, these results suggest that the interaction between LC-NE cells and astrocytes can signal a detrimental or neuroprotective pathway on brain microstructure, specifically in brain regions highly vulnerable to the earliest stages of AD, connected to and regulated by the LC-NE system. Our findings further support the importance of maintaining LC neuronal health in aging, and stress the potential of LC NODDI microstructural properties to signal subtle and very early age-related neurodegenerative changes occurring prior to the more apparent macrostructural changes.

In **Chapter 3**, we examined the potential asymmetrical pattern in tangle and neuronal density within the LC in 77 autopsy cases along the AD continuum. Our results showed left-right equivalence for tangle density across individuals with and without AD pathology. However, asymmetry in neuronal density along the LC rostro-caudal axis was observed among individuals presenting evidence of AD pathology, with higher left than right neuronal density in the caudal section, relative to the rostral part. These results further suggest the relevance of the asymmetry in LC neuronal density as a potential signal for advanced disease progression and to consider this measure in future AD in vivo neuroimaging studies of LC neurodegeneration.

Part II. Modulating the LC function: non-invasive and non-pharmacological interventions

In **Chapter 4**, we aimed to characterize the non-image-forming (NIF) impact of distinct light exposure varying in illuminance on task-evoked pupil response (TEPR) associated with the auditory inputs of attentional and emotional tasks in healthy young adults. As hypothesized, we observed that TEPRs were modulated by the stimulating impact of light in both cognitive tasks. We further

observed task-specific differences in the impact of light levels on stimulus type such that higher TEPR was observed during the target stimuli of the attentional task compared to the neutral ones, while TEPRs were not significantly differing across stimulus type in the emotional task. Overall, our findings emphasize that higher light levels trigger larger TEPR to auditory stimulus, despite the inherent smaller sustained pupil size (**Chapter 5**). This effect presumably reflects the indirect involvement of the LC in the stimulating impact of light on alertness and cognition, although additional neuroimaging studies are required to further confirm this hypothesis.

In **Chapter 5**, we evaluated the potential bias introduced in functional MRI (fMRI) studies investigating the NIF impacts of light on brain correlates by their light protocols, i.e. repeated short light exposures alternating between different spectral composition. In order to elucidate whether the effect of light in one block carries over the next one, thus potentially biasing the fMRI results, we characterized the sustained pupil response of healthy young adults to various short light exposures during an fMRI protocol including distinct auditory cognitive tasks. While replicating previous studies by showing that higher illuminance results in smaller sustained pupil size, we further informed on the stability of this effect in time under higher melanopic irradiance levels compared to lower ones. Importantly, sustained pupil light response varied across tasks independently of the light condition, potentially reflecting the impact of prior light history and/or the ongoing cognitive context. Together, these results emphasize that the distinct contribution and adaptation of the different retinal photoreceptors influence the NIF effects of light and therefore potentially their brain correlates.

In **Chapter 6**, we investigated the effect of tVNS on behavioral and LC neural correlates of sustained attention in healthy older individuals, and assessed whether the variability in tVNS-induced response could be explained in part by our MRI-derived LC integrity measure. Our results showed that higher LC integrity was associated with higher performance during suboptimal attentional processes following tVNS. Importantly, this pattern was only valid in individuals responding to the tVNS, as non-responders with higher LC integrity did not show any improvement in their behavioral performance. These findings contribute to our understanding of the inter-individual variability in

tVNS-induced effects on sustained attention, partly explained by LC integrity measure, with the ultimate goal to inform and develop more personalized non-invasive and non-pharmacological interventions targeting the LC-NE system.

Finally, **Chapter 7** provides a summary and discusses of our main findings in light with the current literature, together with the associated methodological considerations, clinical implications and future research directions.

RÉSUMÉ EN FRANÇAIS

Le vieillissement de la population mondiale s'accompagne d'une augmentation de la prévalence de la maladie d'Alzheimer (MA), posant ainsi des défis majeurs pour les systèmes de santé. Bien que de récents médicaments modificateurs de la maladie soient en cours d'approbation, il n'existe actuellement aucun traitement largement accessible, sans effets secondaires et ciblant les premiers stades asymptomatiques de la maladie. Au cours des dernières décennies, le locus coeruleus (LC) a été identifié comme un marqueur préclinique prometteur de la MA, reflété par la vulnérabilité spécifique de cette structure aux processus précoces liés à la maladie, dès la phase présymptomatique. Par conséquent, le LC est considéré comme une cible prometteuse et une voie alternative potentielle pour les interventions visant à modifier l'évolution de la maladie, dès les premiers stades neuropathologiques. En outre, il a également été démontré que le LC subit des altérations lors du vieillissement sain, de sorte que le maintien de l'intégrité de cette structure pourrait être essentiel pour prévenir les changements neurodégénératifs liés à l'âge, y compris le déclin cognitif. Dès lors, mieux caractériser et distinguer les changements neurodégénératifs se produisant dans le LC liés à l'âge de ceux liés à la MA pourrait favoriser une détection plus précoce des processus pathologiques et contribuer au développement d'interventions ciblant les stades présymptomatiques de la maladie. Dans cette thèse, notre objectif était, premièrement, d'élargir les connaissances actuelles sur la structure du LC au cours du vieillissement sain et de la MA (**Partie I**) ; et deuxièmement, d'évaluer l'efficacité de deux techniques de stimulation non invasives et non pharmacologiques, à savoir l'exposition à la lumière enrichie en bleu et la stimulation transcutanée du nerf vague (tVNS), dans la modulation de la fonction du LC au sein de cohortes saines (**Partie II**).

Partie I. Quantifications in vivo et ex vivo de la structure du LC

Dans le **Chapitre 2**, nous avons étudié les associations entre les propriétés microstructurales du LC, de la matière grise corticale et sous-corticale, mesurées par imagerie par résonance magnétique (IRM) 7 Tesla en combinaison avec des modèles de diffusion NODDI (neurite orientation dispersion and density imaging), dans une cohorte d'adultes sains. Le système

LC-norépinephrine (NE) jouant un rôle clé dans le maintien de la santé cérébrale au cours de la vie, notamment par ses effets modulateurs sur les processus de neuroinflammation, nous avons examiné l'impact de la réactivité astrocytaire sur ces associations microstructurales. Nous avons observé qu'une réactivité astrocytaire plus élevée était associée à une densité neuritique plus faible au niveau de l'amygdale, de l'hippocampe et du cortex frontal, des régions particulièrement vulnérables aux processus de vieillissement. De plus, en présence d'une réactivité astrocytaire élevée, une arborisation neuritique plus faible dans le LC était associée à une arborisation neuritique réduite dans certaines régions cortico-frontales et temporales, ainsi que dans plusieurs régions sous-corticales. Il est intéressant de noter que les individus présentant des niveaux d'arborisation plus élevés dans le LC montraient également une arborisation neuritique plus importante dans ces régions corticales et sous-corticales, malgré une réactivité astrocytaire élevée. Ces résultats suggèrent que l'interaction entre les cellules du système LC-NE et les astrocytes pourrait signaler une voie délétère ou neuroprotectrice pour la microstructure du cerveau, en particulier dans les régions cérébrales très vulnérables durant les premiers stades de la MA et hautement connectées et régulées par le système LC-NE. Nos résultats confirment l'importance du maintien de l'intégrité neuronale du LC avec l'âge et mettent en évidence le potentiel des propriétés microstructurales NODDI du LC pour signaler des changements neurodégénératifs subtils et très précoces liés au vieillissement sain, survenant avant des changements macrostructuraux plus apparents.

Dans le **Chapitre 3**, nous avons examiné 77 cas d'autopsie de personnes saines et atteintes de la MA afin de déterminer si la densité des enchevêtrements neurofibrillaires et des neurones dans LC présentait une éventuelle asymétrie. Nos résultats ont montré que la densité des enchevêtrements du côté gauche et droit du LC était équivalente chez les individus atteints ou non de la MA. Cependant, nous avons observé une asymétrie de la densité neuronale le long de l'axe rostro-caudal du LC chez les individus atteints de la MA, de telle sorte que la densité neuronale de la partie caudale étant plus élevée à gauche qu'à droite, par rapport à la partie rostrale. Ces résultats suggèrent que l'asymétrie de la densité neuronale dans le LC pourrait servir d'indicateur potentiel d'un stade plus avancé de la maladie, et que cette mesure pourrait

être prise en compte dans de futures études de neuroimagerie in vivo sur la neurodégénérescence du LC.

Partie II. Modulation de la fonction du LC : interventions non invasives et non pharmacologiques

Dans le **Chapitre 4**, nous avons examiné l'impact dit « sans formation d'image » (NIF) de différents niveaux de lumière sur la réponse pupillaire évoquée par la tâche (TEPR) associée aux stimuli auditifs de tâches attentionnelles et émotionnelles chez de jeunes adultes en bonne santé. Comme supposé, nous avons observé que les TEPR étaient modulées par l'impact de la lumière dans les deux tâches cognitives. Nous avons également observé des différences spécifiques aux tâches dans l'impact de la lumière sur le type de stimulus, de sorte que des TEPR plus élevées ont été observées pendant les stimuli cibles de la tâche attentionnelle par rapport aux stimuli neutres, tandis que les TEPR n'étaient pas significativement différentes selon le type de stimulus dans la tâche émotionnelle. Dans l'ensemble, nos résultats soulignent que des niveaux de lumière plus élevés induisent des TEPR plus importantes pendant les stimuli auditifs, malgré une taille de pupille soutenue plus petite (**Chapitre 5**). Cet effet reflète potentiellement l'implication indirecte du LC dans l'impact de la lumière sur la vigilance et la cognition, bien que des recherches supplémentaires neuroimagerie soient nécessaires pour confirmer cette hypothèse.

Dans le **Chapitre 5**, nous avons évalué le biais potentiel introduit dans les études d'IRM fonctionnelle (IRMf) portant sur l'impact NIF de la lumière sur les corrélats cérébraux par leurs protocoles de lumière, c'est-à-dire de courtes expositions à la lumière répétées et alternant entre différentes compositions spectrales. Afin de déterminer si l'effet de la lumière dans un bloc se répercute sur le suivant, ce qui pourrait fausser les résultats en IRMf, nous avons caractérisé la réponse soutenue de la pupille à diverses expositions lumineuses de courte durée pendant un protocole d'IRMf comprenant différentes tâches cognitives auditives chez des jeunes adultes sains. Tout en reproduisant des études antérieures en montrant que des niveaux de lumière plus élevés entraînaient une diminution de la taille de la pupille, nous avons fourni plus d'information quant à la stabilité de cet effet dans le temps,

en particulier à des niveaux de lumière plus élevés comparés aux niveaux plus faibles. Il est important de noter que la réponse soutenue de la pupille à la lumière variait d'une tâche à l'autre indépendamment de la condition lumineuse, ce qui pourrait refléter l'impact d'une exposition lumineuse antérieure et/ou du contexte cognitif en cours. Ces résultats soulignent que les différentes contributions et adaptations des photorécepteurs rétiniens pourraient influencer les effets NIF de la lumière et donc potentiellement leurs corrélats cérébraux.

Dans le **Chapitre 6**, nous avons étudié l'effet de la tVNS sur l'activité neuronale du LC lors de processus d'attention soutenue et sur la performance dans cette tâche chez des personnes âgées en bonne santé. En outre, nous avons évalué si la variabilité de la réponse induite par la tVNS pouvait être partiellement expliquée par notre mesure d'intégrité du LC, mesurée à l'aide d'images IRM. Nos résultats ont montré qu'une plus grande intégrité du LC était associée à une meilleure performance pendant les processus attentionnels suboptimaux suivant directement la tVNS. Il est important de noter que cette tendance n'a été observée que pour les personnes répondant à la tVNS, étant donné que les individus ayant une intégrité du LC plus élevée et non-répondants à la tVNS n'ont pas montré d'amélioration de leur performance. Ces résultats contribuent à notre compréhension de la variabilité interindividuelle des effets induits par la tVNS sur l'attention soutenue, partiellement expliquée par la mesure de l'intégrité du LC, et permettent d'informer et de développer des interventions non invasives et non pharmacologiques plus personnalisées ciblant le système LC-NE.

Enfin, le **Chapitre 7** résume et discute nos principaux résultats à la lumière de la littérature actuelle, ainsi que les considérations méthodologiques associées, les implications cliniques et les futures directions de recherche

NEDERLANDSE SAMENVATTING

De wereldwijde vergrijzing van de bevolking gaat gepaard met een toenemende prevalentie van de ziekte van Alzheimer (AD), wat belangrijke uitdagingen met zich meebrengt voor het gezondheidszorgsysteem. Hoewel recentelijk ontdekte ziektemodificerende medicijnen worden goedgekeurd, is er momenteel geen toegankelijke behandeling zonder bijwerkingen beschikbaar die ook gericht is op de vroege, asymptomatische stadia van de ziekte. In de afgelopen decennia is de locus coeruleus (LC) geïdentificeerd als een veelbelovende preklinische marker van AD, wat wordt weerspiegeld door de specifieke kwetsbaarheid van deze structuur voor vroege AD-gerelateerde processen die al in de presymptomatische fase beginnen. Daarom wordt de LC beschouwd als een kansrijk doelwit en een potentieel alternatief pad voor ziektemodificerende interventies, te beginnen bij de presymptomatische stadia van de ziekte. Daarnaast is aangetoond dat de LC ook veranderingen ondergaat tijdens het gezond ouder worden, wat suggereert dat het behoud van de integriteit van dit hersengebied essentieel kan zijn voor het voorkomen van leeftijdsgerelateerde veranderingen, waaronder cognitieve achteruitgang. Het beter karakteriseren en onderscheiden van leeftijdsgerelateerde - van AD-gerelateerde neurodegeneratieve veranderingen in de LC zal dan ook de weg vrijmaken voor een eerdere identificatie van schadelijke processen en een belangrijke bijdrage leveren aan de ontwikkeling van interventies gericht op de presymptomatische stadia van de ziekte. In dit proefschrift was ons doel, ten eerste om de huidige kennis over de LC-structuur tijdens veroudering en het AD-continuüm uit te breiden (**Deel I**). Ten tweede, de effectiviteit van twee niet-invasieve en niet-farmacologische stimulatietechnieken, blootstelling aan blauwverrijkt licht en transcutane nervus vagus stimulatie (tVNS) ter modulatie van de LC-functie in gezonde cohorten, te beoordelen (**Deel II**).

Deel I. In vivo en ex vivo kwantificaties van de LC-structuur

In **Hoofdstuk 2** onderzochten we de verbanden tussen de microstructurele eigenschappen van de LC, corticale en subcorticale grijze stof, gemeten door middel van 7T MRI in combinatie met neurite orientation dispersion and density imaging (NODDI) diffusiemodellen, in een cohort van gezonde volwassenen

over de gehele levensduur. Aangezien het LC-noradrenaline (NE)-systeem een belangrijke rol speelt bij het ondersteunen van de hersengezondheid gedurende het leven, met name door de modulerende effecten op neuroinflammatie, onderzochten we het effect van reactieve astrocyten op deze microstructurele verbanden. We ontdekten dat een hogere astrocyten reactiviteit geassocieerd was met een lagere dichtheid van neurieten in de amygdala, hippocampus en frontale cortex, regio's die kwetsbaar zijn voor verouderingsprocessen. Daarnaast, in de aanwezigheid van verhoogde astrocyten reactiviteit, was een verminderde vertakking in LC-neurieten geassocieerd met minder vertakking van neurieten in frontotemporale corticale en verschillende subcorticale regio's. Opmerkelijk is dat individuen met meer vertakkingen van de neuriten in de LC ook meer vertakking in de neurieten van corticale en subcorticale gebieden vertoonden, ondanks de aanwezigheid van verhoogde astrocyten reactiviteit. Deze resultaten suggereren dat de interactie tussen LC-NE-cellen en astrocyten kan wijzen op zowel schadelijke of neuroprotectieve paden voor de hersenmicrostructuur, en waarbij de integriteit van het LC-NE systeem een belangrijke factor kan zijn. Onze bevindingen ondersteunen het belang van het behouden van de neuronale gezondheid van de LC bij veroudering, en benadrukken het potentieel van LC NODDI microstructurele eigenschappen, om subtiele en zeer vroege leeftijdsgerelateerde neurodegeneratieve veranderingen te signaleren, die plaatsvinden voordat de meer zichtbare macrostructurele veranderingen optreden.

In **Hoofdstuk 3** onderzochten we in 77 ex vivo breinen van gezonde mensen en mensen met aanwezigheid van AD pathologie of de dichtheid van neurofibrillaire tau tangles en neuronen in de LC asymmetrisch is. Onze resultaten toonden aan dat de tangle-dichtheid aan de linker- en rechterkant equivalent was voor individuen met en zonder AD-pathologie. Echter, observeerden we asymmetrie in neuronale dichtheid langs de rostro-caudale as van de LC bij individuen met AD-pathologie, waarbij de neuronale dichtheid in het caudale deel hoger was aan de linkerkant dan aan de rechterkant, vergeleken met het rostrale deel. Deze resultaten suggereren dat de asymmetrie in neuronale dichtheid in de LC zou kunnen fungeren als een potentiële indicator voor een meer gevorderde fase van de ziekte, en dat

deze bevinding in overweging genomen zou kunnen worden in toekomstige in vivo AD-neuroimaging studies van LC-neurodegeneratie.

Deel II. Moduleren van de LC-functie: niet-invasieve en niet-farmacologische interventies

In **Hoofdstuk 4** onderzochten we de impact van verschillende niet-beeldvormende (NIF) lichtniveaus op taak-opgewekte pupilreacties (TEPR) tijdens auditieve stimuli van aandachts- en emotionele taken in gezonde, jonge volwassenen. Zoals verwacht, observeerden we dat TEPR's werden gemoduleerd door de stimulerende impact van licht in beide cognitieve taken. We observeerden verder taak-specifieke verschillen in de effecten van lichtniveaus op stimulustype, waarbij hogere TEPR's werden waargenomen tijdens de doelstimuli van de aandachtstaak in vergelijking met de neutrale stimuli, terwijl TEPR's niet verschilden tussen stimulustypes in de emotionele taak. Over het geheel genomen benadrukken onze bevindingen dat hogere lichtniveaus grotere TEPR's veroorzaken bij auditieve stimuli, ondanks de kleinere, aanhoudende pupilgrootte (**Hoofdstuk 5**). Dit effect weerspiegelt vermoedelijk de indirecte betrokkenheid van de LC bij de stimulerende impact van licht op alertheid en cognitie, hoewel meer neuroimaging onderzoek nodig is om deze hypothese verder te bevestigen.

In **Hoofdstuk 5** evalueerden we de mogelijke vertekening geïntroduceerd in functionele MRI (fMRI)-studies die de NIF-impact van licht op hersencorrelaten onderzoeken met hun lichtprotocollen, d.w.z. herhaalde korte blootstellingen aan licht die afwisselen tussen verschillende spectrale composities. Om te verduidelijken of het effect van licht in het ene blok overdraagbaar is op het volgende blok, en zo mogelijk de fMRI-resultaten vertekent, karakteriseerden we de aanhoudende pupilreactie van gezonde jonge volwassenen op verschillende korte lichtblootstellingen tijdens een fMRI-protocol met verschillende auditieve cognitieve taken. Terwijl we eerdere onderzoeken repliceerden door aan te tonen dat hogere verlichtingsniveaus resulteren in kleinere aanhoudende pupilgrootte, geven we verdere informatie over de stabiliteit van dit effect in tijd onder hogere lichtniveaus in vergelijking met lagere. Belangrijk is dat de aanhoudende pupilreactie op licht onafhankelijk van de lichtconditie varieerde per taak, wat mogelijk het effect van eerdere

lichtblootstelling en/of de huidige cognitieve context weerspiegelt. Deze resultaten benadrukken dat de verschillende bijdragen en aanpassingen van de verschillende retinale fotoreceptoren de NIF-effecten van licht beïnvloeden en daarom mogelijk zowel hun hersencorrelaten beïnvloeden.

In **Hoofdstuk 6** onderzochten we het effect van niet-invasieve tVNS op de neuronal activiteit van de LC tijdens volgehouden aandacht en op de prestatie op die taak bij gezonde oudere individuen. Daarnaast beoordeelden we of de variabiliteit in tVNS-geïnduceerd respons gedeeltelijk verklaard kan worden door de integriteit van de LC, gemeten met MRI beelden. Onze resultaten toonden aan dat hogere LC-integriteit geassocieerd was met betere prestaties tijdens suboptimale aandachtsprocessen na tVNS. Belangrijk is dat dit patroon alleen geobserveerd werd bij individuen die reageerden op de tVNS. Deze bevindingen dragen bij aan ons begrip van de interindividuele variabiliteit in tVNS-geïnduceerde effecten op volgehouden aandacht, en het informeren en ontwikkelen van meer gepersonaliseerde niet-invasieve en niet-farmacologische interventies gericht op het LC-NE-systeem.

Tot slot geeft **Hoofdstuk 7** een samenvatting en bespreking van onze belangrijkste bevindingen in het licht van de huidige literatuur, samen met de bijbehorende methodologische overwegingen, klinische implicaties en toekomstige onderzoekslijnen.

IMPACT PARAGRAPH

In this thesis, we aimed to expand the field's knowledge by offering novel insights into the structure of the locus coeruleus (LC) in the context of healthy aging and the Alzheimer's disease (AD) continuum (**Part I**). Additionally, we explored the effectiveness of non-invasive and non-pharmacological techniques for modulating LC function (**Part II**), with the ultimate goal to contribute to the larger effort of developing LC-focused interventions aiming at maintaining cognitive health in aging and mitigating the impact of AD. This impact paragraph highlights the scientific and societal relevance of our findings, as well as opportunities of application.

Main findings

In **Part I**, we demonstrated that astrocyte reactivity was associated with brain microstructural damage in regions susceptible to the aging process. In addition, we found that LC microstructure closely interacts with astrocyte reactivity, influencing whether brain microstructure follows a neuroprotective or detrimental pathway along the lifespan. This interaction was evident in a set of regions particularly vulnerable to the early stages of AD. Furthermore, we observed an asymmetrical pattern in LC neuronal density in autopsy cases at advanced stages of AD and specific to the caudal LC section compared to the rostral part.

In **Part II**, we showed that non-invasive techniques such as the exposure to blue-enriched light and transcutaneous vagus nerve stimulation (tVNS) may hold the potential to modulate cognition in healthy individuals through their hypothesized indirect impact on the LC. First, higher light illuminance levels resulted in larger task-evoked pupil responses related to the auditory attentional and emotional stimuli. This effect presumably reflects the indirect involvement of the LC, as the variations in pupil size are thought to be a reliable proxy of LC activity. Second, our results emphasized that MRI-derived LC integrity could explain part of the variability observed in the effects of tVNS on attention. In responders only, higher LC integrity was associated with higher performance on the suboptimal attentional task events following tVNS. Interestingly, non-responders did not significantly differ from the responders in

their LC integrity measure, further suggesting that other factors related to LC health may be involved in determining the efficacy of tVNS-induced responses on attention.

Scientific impact

The LC is a tiny yet remarkable nucleus playing a crucial role in a variety of behavioral and cognitive functions. Its dysfunction is also implicated in neurodegenerative processes related to both aging and AD, making it a key target for research. Recent technological advancements in magnetic resonance imaging (MRI) have successfully addressed the challenge of visualizing this small nucleus in vivo with great detail, enhancing our ability to explore its structural and functional aspects. While MRI-derived LC integrity is increasingly investigated and reported as a potential marker of several late-life and AD-related processes, the precise relationship between changes in LC microstructure and MRI signal intensity remains unclear. Understanding this relationship is crucial for accurately interpreting MRI findings across the different stages of the disease and driving innovative research forward.

Our findings indicate that in more advanced stages of the disease, LC neuronal density is differentially impacted across hemispheres, specifically in the caudal section. This asymmetry highlights the need for a nuanced approach in evaluating MRI-derived LC integrity, encouraging the incorporation of separate bilateral assessments of the LC into in vivo imaging studies involving AD cohorts. Such an approach will allow researchers to map more precisely the extent of LC neurodegeneration within the broader pathophysiological cascade of AD. Furthermore, this underscores the need for refining imaging techniques to effectively capture these asymmetries in vivo, particularly considering the challenge in visualizing the more diffuse caudal section of the LC.

We also provide relevant evidence that diffusion-weighted neurite orientation dispersion and density imaging (NODDI) at the level of the LC is a sensitive technique for signaling very subtle and early age-related neurodegenerative changes. These findings suggest that NODDI could complement classical LC structural integrity, providing a more comprehensive understanding of LC health and its alterations in aging and AD. Altogether, these structural findings could potentially contribute to the integration of LC metrics

into the existing AD biological models, thereby enhancing our understanding of the disease progression and improving predictive frameworks.

Finally, our results are relevant for the initial development of non-invasive, non-pharmacological therapeutic strategies aiming at targeting the LC, such as light exposure and tVNS. Our research underscores the critical role of the LC in the efficacy of these interventions, while also acknowledging that other subcortical structures and biological processes are likely involved. Firstly, we recommend future light-based research to use light sources with high irradiance levels, specifically above 90 melanopic equivalent daylight illuminance lux, to maximize their impact. Secondly, our results indicate that LC integrity is a critical determinant of the effectiveness of tVNS on attentional outcomes, although other mechanisms related to LC health may also contribute. These insights are crucial for the optimization of future research designs by potentially enhancing the effectiveness of these interventions, enabling more precise selection of participant populations, and ultimately reducing the time, costs and number of participants required.

Overall, this thesis provides novel and important directions for future LC-focused research and underlies the importance of addressing these critical research questions through the investigation of large datasets with longitudinal designs across the disease spectrum. Considering the complexity for researchers and the burden for participants in acquiring such datasets, we strongly encourage researchers to share and take advantages of existing datasets. This collaborative approach will facilitate the exploration of these vital research goals and potentially lead to more rapid and efficient solutions.

Societal impact

Global aging of the population comes with important challenges, with one of the most alarming being the increase in the prevalence of AD. This neurodegenerative disorder not only affects millions of individuals worldwide but also imposes a substantial burden on their families, caregivers and healthcare systems. While the recent FDA approval of disease-modifying treatments represents an important milestone in the fight against AD, its moderated clinical benefit and associated side effects limit its ability to offer a solution for widespread implementation to many patients. It is increasingly

recognized that interventions are more likely to succeed in altering the course of the disease by targeting its earlier pre-symptomatic phases, prior to the occurrence of irreversible brain damage. The LC is a subcortical structure particularly vulnerable to the earliest neuropathological stages of AD, as it is suggested to be one of the first brain regions to accumulate tau pathology, starting from the first decades of life. Therefore, developing biomarkers that can detect LC-related changes and treatments that specifically target this nucleus could be crucial in impacting the disease early on, thereby preventing or delaying its progression.

Our findings support the potential of MRI-derived measures of LC structural properties as indicators of age- and AD-related processes. In particular, we emphasize the value of advanced diffusion-weighted techniques such as NODDI in providing a more detailed and nuanced assessment of LC microstructural integrity, which could enable the earlier and more accurate identification of neurodegenerative processes. Incorporating NODDI with LC imaging into standard clinical MRI protocols could enhance clinicians' ability to identify individuals at risk for AD before the onset of clinical symptoms. However, achieving this integration will require harmonizing of diffusion data methodologies and ensuring their comparability across different sites and MRI manufacturers. In addition, efforts should focus on better understanding the clinical interpretation of NODDI values and establishing cut-off values that indicate when further examination is necessary. Ultimately, this will be an opportunity for researchers and clinicians to work closely together in better understanding the sensitivity and specificity of NODDI metrics to clinical symptoms and disease progression. Importantly, while NODDI shows promise, it should not be considered a standalone diagnostic tool. Instead, it has the potential to serve as a supplementary measure alongside traditional diagnostic approaches, such as clinical interviews, neuropsychological tests and biomarkers assessments, thereby providing a more comprehensive evaluation of an individuals' condition. Currently, applying this approach in most clinical settings is challenging due to the limitations of lower magnetic fields, and their inherent reduced resolutions preventing the precise visualization of the LC. Therefore, efforts must be directed toward the effective translation of these methods across different magnetic field strengths. However, as technological

innovations continue, UHF MRI scanners may become more widespread and affordable, potentially enhancing the precision and the clinical use of these diagnosis tools. Finally, further research is needed to advance MRI-derived LC measures as reliable clinical biomarkers of AD pathology. Clinicians must be able to translate the biological processes and associated potential mechanisms underlying the LC MRI signal to the individual patient, and to distinguish AD-related changes from other processes affecting the LC, such as healthy aging and other neurodegenerative diseases.

The world-wide neuromodulatory devices market is experiencing substantial growth, driven by the advancements in technology and medicine, as well as the increasing prevalence of neurological or psychiatric disorders. Currently, light therapy is recognized as an effective treatment in mood disorders and several tVNS devices are FDA-approved for the treatment of migraine and pain from irritable bowel syndrome in adolescents, depression, anxiety and epilepsy. This thesis emphasizes the emerging potential of light exposure and tVNS as non-invasive and non-pharmacological treatment opportunities for AD. As they seem to effectively target the LC and modulate its function, these techniques are promising paths to explore for boosting cognition and preventing cognitive decline along the AD continuum. Neuromodulatory devices companies may therefore find important opportunities in the development of these interventions to offer innovative prevention or therapeutic solutions for AD patients. We could envision a future where AD treatment involves connected technologies such as light-emitting glasses or wireless stimulation earplugs, controlled by an interface easily accessible on a smartphone. These interventions could revolutionize AD healthcare by offering a cost-effective, easily accessible and well-tolerated approach, making it more patient-friendly and integrated into everyday life. However, ethical considerations including safety, privacy and accessibility must be carefully addressed by all stakeholders to ensure the responsible development and use of these technologies. In addition, an important amount of research is still needed to fully establish these neuromodulation techniques as effective AD treatment enhancing cognition. This includes a deeper understanding of their underlying mechanisms as well as the optimization of stimulation protocols to maximize their efficacy.

Disseminations activities

The findings reported in this thesis were disseminated to both the scientific community and the general public through various channels and on multiple occasions. Our work was published in several scientific journals, including the *Journal of Sleep Research* (2023, **Chapters 4 and 5**), *Journal of Alzheimer's Disease* (2024, **Chapter 3**) and *Cerebral Cortex* (2024, **Chapter 2**). All code developed for the associated analyses was either shared with the research team, or made available on open-access platforms to promote transparency and facilitate broader accessibility. In addition, results were disseminated internationally via oral presentations at the European Sleep Research Society (ESRS) 2022 (Athens, Greece), as well as poster presentations at the Alzheimer's Association international Conference (AAIC) 2022 (San Diego, USA) and 2023 (Amsterdam, The Netherlands), and the meeting of the Society for Light Treatment and Biological Rhythms (SLTBR) 2023 (Lausanne, Switzerland), where the Best Poster Prize was awarded for the work discussed in Chapter 5. Other oral presentations of our work were given as an invited speaker at a Neurex meeting in June 2022 (Strasbourg, France) and at one of the Tiny Dots meetings 2023 organized by the ISTAART Neuromodulatory Subcortical Systems PIA, targeting a broader early-career scientific audience. Furthermore, findings were presented at local scientific events including the GIGA Day 2022 and the MHeNs Research Days 2022-2024. Through teaching and supervisory activities, our work was shared and discussed with bachelor and master students from Liège and Maastricht Universities, spanning various disciplines including medicine, psychology, biology and engineering. Finally, we shared insights form this thesis with the general community through oral presentations at the *Université du Troisième Age* of Liège and during a bi-weekly meeting of the Rotary Club of Liège, through publications of simplified take-home messages on social media platforms such as LinkedIn and the ACL website, and through a brief interview for Healio, a medicine web journal.

This thesis is part of the Imaging Valley collaboration between the University of Liège and Maastricht University, aiming to share scientific knowledge and strengthen collaborative ties between research institutes. This joint PhD program facilitated the exchange of expertise, resources, and innovative ideas, fostering a multidisciplinary approach through the access to diverse methodologies and further enhancing the quality and impact of our research.

LIST OF PUBLICATIONS

This dissertation

Beckers, E., Van Egroo, M., Ashton, N. J., Blennow, K., Vandewalle, G., Zetterberg, H., Poser, B. A., & Jacobs, H. I. L. (2024). Microstructural associations between locus coeruleus, cortical, and subcortical regions are modulated by astrocyte reactivity: a 7T MRI adult lifespan study. *Cereb Cortex, 34*(6). https://doi.org/10.1093/cercor/bhae261

Beckers, E., Riphagen, J. M., Van Egroo, M., Bennett, D. A., & Jacobs, H. I. L. (2024). Sparse Asymmetry in Locus Coeruleus Pathology in Alzheimer's Disease. *J Alzheimers Dis, 99*(1), 105-111. https://doi.org/10.3233/jad-231328

Campbell, I., **Beckers, E.**, Sharifpour, R., Berger, A., Paparella, I., Aizpurua, J. F. B., Koshmanova, E., Mortazavi, N., Sherif, S., & Vandewalle, G. (2023). Impact of light on task-evoked pupil responses during cognitive tasks. *J Sleep Res, 33*(4), e14101. https://doi.org/10.1111/jsr.14101

Beckers, E., Campbell, I., Sharifpour, R., Paparella, I., Berger, A., Aizpurua, J. F. B., Koshmanova, E., Mortazavi, N., Talwar, P., Sherif, S., Jacobs, H. I. L., & Vandewalle, G. (2023). Impact of repeated short light exposures on sustained pupil responses in an fMRI environment. *J Sleep Res*, e14085. https://doi.org/10.1111/jsr.14085

Other work

Campbell, I., Sharifpour, R., Balda, F., **Beckers, E.**, Paparella, I., Berger, A., Koshmanova, E., Mortazavi, N., Read, J., Zubkov, M., Talwar, P., Collette, F., Sherif, S., Phillips, C., Lamalle, L., & Vandewalle, G. (2024). Regional response to light illuminance across the human hypothalamus. *eLife, 13*, RP96576. https://doi.org/10.7554/eLife.96576.3

Sharifpour, R., Balda, F., Paparella, I., Read, J., Leysens, Z., Letot, S., Campbell, I., **Beckers, E.**, Collette, F., Phillips, C., Zubkov, M., & Vandewalle, G. (2024). Cortical Excitability is Affected by Light Exposure-Distinct Effects in Adolescents and Young Adults. *bioRxiv (Preprint)*, pp.2024-08. https://doi.org/10.1101/2024.08.21.608922

Mortazavi, N., Talwar, P., Koshmanova, E., Sharifpour, R., **Beckers, E.**, Berger, A., Campbell, I., Paparella, I., Balda, F., Hamzaoui, I.D., & Berthomier, C. (2024). REM sleep quality is associated with balanced tonic activity of the locus coeruleus during wakefulness. *bioRxiv (Preprint)*, pp.2024-07. https://doi.org/10.1101/2024.07.12.603275

Campbell, I., Balda, F., Sharifpour, R., Paparella, I., **Beckers, E.**, Berger, A., Koshmanova, E., Mortazavi, N., Read, J., Phillips, C., Collette, F., Sherif, S., Talwar, P., Zubkov, M., Lamalle, L., & Vandewalle, G. (2024). Exposure to light supresses the activity of the medial and superior amygdala during emotional processing. *bioRxiv (Preprint)*, pp.2024-04. https://doi.org/10.1101/2024.04.25.591085

Berger, A., **Beckers, E.**, Joris, V., Duchêne, G., Danthine, V., Delinte, N., Cakiroglu, I., Sherif, S., Morrison, E. I. G., Sánchez, A. T., Macq, B., Dricot, L., Vandewalle, G., & El Tahry, R. (2024). Locus coeruleus features are linked to vagus nerve stimulation response in drug-resistant epilepsy. *Front Neurosci, 18*, 1296161. https://doi.org/10.3389/fnins.2024.1296161

Koshmanova, E., Berger, A., **Beckers, E.**, Campbell, I., Mortazavi, N., Sharifpour, R., Paparella, I., Balda, F., Berthomier, C., Degueldre, C., Salmon, E., Lamalle, L., Bastin, C., Van Egroo, M., Phillips, C., Maquet, P., Collette, F., Muto, V., Chylinski, D., Jacobs, H. I., Talwar, P., Sherif, S., & Vandewalle, G. (2023). Locus coeruleus activity while awake is associated with REM sleep quality in older individuals. *JCI Insight, 8*(20). https://doi.org/10.1172/jci.insight.172008

Paparella, I., Campbell, I., Sharifpour, R., **Beckers, E.**, Berger, A., Aizpurua, J. F. B., Koshmanova, E., Mortazavi, N., Talwar, P., Degueldre, C., Lamalle, L., Sherif, S., Phillips, C., Maquet, P., & Vandewalle, G. (2023). Light modulates task-dependent thalamo-cortical connectivity during an auditory attentional task. *Commun Biol, 6*(1), 945. https://doi.org/10.1038/s42003-023-05337-5

Berger, A., Koshmanova, E., **Beckers, E.**, Sharifpour, R., Paparella, I., Campbell, I., Mortazavi, N., Balda, F., Yi, Y. J., Lamalle, L., Dricot, L., Phillips, C., Jacobs, H. I. L., Talwar, P., El Tahry, R., Sherif, S., & Vandewalle, G. (2023). Structural and functional characterization of the locus coeruleus in

young and late middle-aged individuals. *Front Neuroimaging, 2*, 1207844. https://doi.org/10.3389/fnimg.2023.1207844

Sharifpour, R., Campbell, I., **Beckers, E.**, Balda, F., Mortazavi, N., Koshmanova, E., Paparella, I., Sherif, S., Phillips, C., & Vandewalle, G. (2022). Pitfalls in recording BOLD signal responses to light in small hypothalamic nuclei using Ultra-High-Field 7 Tesla MRI. *Proc Natl Acad Sci U S A, 119*(49), e2212123119. https://doi.org/10.1073/pnas.2212123119

Sharifpour, R., Campbell, I., Paparella, I., Balda, F., **Beckers, E.**, Mortazavi, N., Koshmanova, E., Colette, F., Phillips, C., Talwar, P., Lamalle, L., Zubkov, M., & Vandewalle, G. Light impact on thalamo-cortical connectivity during executive cognitive task: effect of time of day and developmental age. *In prep*

Van Egroo, M., **Beckers, E.**, Ashton, N. J., Blennow, K., Zetterberg, H., & Jacobs, H. I. Sex differences in the relationships between 24-h rest-activity patterns and plasma markers of Alzheimer's disease pathology. *Submitted*

ACKNOWLEDGMENTS

Completing a PhD is to the doctoral candidate what reaching the mountain summit is to the climber: a joyful mix of relief and gratitude, knowing that every step of the adventure has been worth it for the incredible view at the top. As I stand at this peak, I realize that this accomplishment is not just about reaching the destination or holding this finished book in my hands; it is about the transformative journey of the past four years, a time marked by dedicated work and challenges but also personal growth, enriching learning experiences and authentic human connections. Throughout this chapter, I was privileged to be surrounded by so many incredible people—colleagues, family and friends—whose guidance and encouragement have made this milestone possible. This section is dedicated to all of you who inspired me, generously offered your time, encouragement and unwavering support, whether near or far. Thank you for being an essential part of this journey.

To begin, I would like to thank my promotion team, **Dr. Heidi Jacobs** and **Dr. Gilles Vandewalle**, for their constant support, availability and impressive expertise. Together, we created an ideal balance, which provided me with the freedom to grow as a scientist while providing strong guidance whenever I needed it.

Heidi, I am grateful to have crossed paths with you, almost by chance, and to have learned so much from your endless passion for LC research. You have been a constant source of inspiration to me, both scientifically and personally. Despite the distance between us, you were always available to address any of my concerns, whether big or small, and to celebrate every milestone along the way. Your advices during the most stressful periods always felt wise and reassuring. It will definitely feel strange not having our bi-weekly online meetings to chat and discuss exciting science! Thank you for guiding me through this adventure, I truly loved working with you.

Gilles, tout a commencé lorsque tu as assisté à ma défense de mémoire de master en ingénierie. À l'époque, étudier le cerveau d'un point de vue

neuroscientifique était un mystère pour moi. Qui aurait pu imaginer que quatre ans plus tard, tu jouerais un rôle si crucial dans mon parcours académique en m'offrant ce poste de doctorat et en me fournissant l'accompagnement nécessaire pour atteindre ce point ? Merci de m'avoir donné l'opportunité d'éveiller ma curiosité pour le cerveau et ses structures les plus intrigantes. Travailler avec l'équipe pour développer le pipeline IRM 7T a été une expérience incroyablement gratifiante. Nous avons tous tant appris des défis rencontrés, ainsi que de notre travail d'équipe et de notre collaboration. Merci pour ces quatre années d'exploration scientifique tellement enrichissantes!

I am also thanking to the members of the assessment committee, **Prof. Dr. Walter Backes**, **Prof. Dr. Alexander Sack**, **Prof. Dr. Dorothea Hämmerer**, **Prof. Dr. Sander Nieuwenhuis**, **Dr. Christine Bastin** and **Dr. Christophe Phillips**, for their time in reading, evaluating and discussing this thesis.

Engaging in a joint doctorate program has been incredibly rewarding, especially for the chance to work with an even larger network of amazing colleagues. To all my (former) **colleagues from CRC and ACL**: thank you for the unforgettable moments we shared, from the Christmas dinners and summer BBQ to our conference trips. I enjoyed every moments of working together, from our thought-provoking debates to all the valuable insights and encouragement you shared, which kept me motivated every step of the way. I can't wait to stay connected and hopefully cross paths again soon!

In particular, to my **Big Office buddies**, **Islay**, **Stella**, **Soodeh**, **Florence**, **Nawël**, **Solène**, **Lindsay**, **Harry**, thank you for all the tea breaks, calming chats and amazing shorebreads. Sharing that space meant so much more than just being officemates, it became a place of trust, support and friendship. I couldn't be happier to have both contributed to and benefited from that mutual encouragement.

Islay, your calm presence was a true anchor. Even if it may not have always felt that way to you, I deeply appreciated it. Thank you also for bringing me into the HILIGHT adventure—I truly loved working with you on this project.

Florence, tu as été mon repère durant mon doctorat, une année devant moi et toujours là pour me montrer la bonne direction. Merci pour ta présence, nos conversations, nos rires, et ton amitié.

Nawël, ta passion pour la recherche m'a toujours impressionnée et inspirée. De ton organisation sans faille à ta capacité à mener 36 études en parallèle avec succès, tu es la définition même de la Girl Boss. Je suis tellement heureuse d'avoir partagé ces premières années avec toi dans notre coin de bureau.

Moving offices isn't always easy, but joining the **Striatum office** was a gift: thank you to **Grégory**, **Emma** and **Raphaël**. Même si nos emplois du temps rendaient parfois le bureau un peu vide, je suis reconnaissante d'avoir rencontré des personnes aussi passionnées par leur travail et bienveillantes.

To **Yuliya**, **Maxime**, **Roy** and **Linda**, thank you for creating such an amazing spirit in our MRI office!

Yuliya, I truly appreciated your willingness to listen to (and share) the drama stories along the way, it was comforting to feel understood! You are a true source of inspiration and your strength from life challenges is exceptional. I wish you all the best in the future.

Maxime, dès notre premier meeting Zoom, tu as fait preuve d'une générosité, d'une écoute et de conseils incroyables. Tu étais le seul à comprendre parfaitement la situation dans laquelle je me trouvais, entre Liège et Maastricht. Tu n'imagines pas à quel point je suis reconnaissante d'avoir eu un guide comme toi tout au long de mon doctorat, mais aussi d'avoir pu développer cette amitié. Tu es une véritable source d'inspiration et j'espère que tu continueras à mener le domaine LC-sommeil encore longtemps. Merci pour les heures passées ensemble à débugger les scripts et examiner les images IRM, ou encore à remplir nos déclarations fiscales (on pourrait même envisager une carrière dans la comptabilité maintenant). Tes encouragements, surtout vers la fin, m'ont permis d'arriver ici de manière (presque) sereine.

Roy, your help in acquiring the eyetracker data during some critical moments was a blessing. Thank you for your availability and your presence, but most of all, for sharing the name of your cover designer with me, she is a gem!

Linda, despite the mess on your desk, you didn't lack of organizational skills. Thank you for giving me such a warm welcome at my arrival and for helping understand the Dutch procedures. You always amazed me and were a true inspiration to me!

Very importantly, I want to share my gratitude for some other amazing souls.

Ilenia, when I think of a genuinely kind and extraordinary person, I think of you. Always there to help and listen, your strength of character is truly inspiring. Your friendship has been my place of trust and confidence during my PhD, and I am so grateful for every moments we shared, especially the ones outside of work. You have no idea how much our discussions have meant to me. I can't wait to see your next dance show, but I know we will catch up before that!

Marine et **John**, votre authenticité et amitié sont incomparables ! Seul, on va plus vite, à plusieurs, on va plus loin ; c'est ce qui me vient à l'esprit quand je pense à vous et à nos discussions autour de nos sandwichs ou de notre soupe de midi. C'est en se serrant les coudes et en se motivant dans les moments faciles mais aussi plus difficiles que l'on parvient au bout du chemin. Alors ne lâchez rien, vous êtes formidables!

To the **HILIGHT team**, **Islay**, **Roya** and **Fermin**, I really enjoyed working alongside each of you on this massive project. From our sleepless nights at the MRI and countless hours in monthly meetings, to the endless coding session in Matlab, I am grateful for every moments. But most of all, thank you for your constant support and teamwork on this shared project.

Next, I want to thank everyone in **Gilles' lab**, from interns, PhDs and postdocs to study coordinators and nurses. It was our effective collaboration, bridging

our diverse backgrounds, that allowed us to lift each other up and reach where we stand today. Wishing each of you all the best for the future!

Nina, I am so grateful to have met you on this PhD journey. It is amazing how close I feel to your path, even with thousands of kilometers between us. Especially towards the end, sharing each step together was such a comfort, and your help with your (so nicely documented!) R codes was invaluable. I will never forget the first time we met: me already fast asleep and jet-lagged in a San Diego hotel, and you arriving to share the room, quietly trying to reach your bed without waking me—a perfect stranger at the time. Our friendship grew quickly, and you are truly one of the extraordinary people I have met along the way. I will miss AAIC, mostly because it was our time together. Thank you for every encouraging WhatsApp message and for always sharing your positivity.

To my dear **Boston colleagues**, including the one that I had never the chance to meet, but who were always congratulating me via Teams on my milestones, thank you for this wonderful opportunity to learn from your work across the ocean and for all the laughs and support!

Joost, **Chris** and **Prokopis**, I feel lucky to have connected and learned from each of you. Your expertise has been invaluable, with each of you providing unique insights that have deepened my understanding—from R statistics and data visualization to tVNS and fMRI analysis. I am truly grateful for the time and knowledge you have shared, which has had a lasting impact on my work. Thank you for helping me grow in ways I couldn't have anticipated.

Sometimes, having two offices also means having twice as much problems. However, someone was always present to solve it. To all the **administrative, support and technical staff** that made it possible to work within a nice environment, from cleaning to fixing the heat system, booking MRIs or solving IT related problems, thank you for your help!

Thank you also to the Master students, **Dennis**, **Julia** and **Théo**, that accompanied the project from different perspectives, from the recruitment

and cognitive assessment to MRI scanning. This project could not have been completed without your hard work.

I would also like to express my gratitude to the **participants of the BOOSTMEM study**, who generously lent me their brain and precious time. Without your patience and dedication, this work would not have been possible.

J'ai également la chance d'être entourée d'une famille et d'amis en or, des personnes extraordinaires qui n'ont jamais hésité à me soutenir et sans qui rien n'aurait été possible. Que ce soit en relisant mes textes, en m'écoutant parler des défis liés à mes analyses, en partageant mes moments de joie ou de tristesse, en me sortant de mon bureau pour prendre l'air, ou simplement en profitant des petits moments de la vie, ils ont toujours été présents.

« Ils », ce sont de nombreuses personnes remarquables qui comptent plus que tout au monde pour moi.

« Ils », ce sont ma mamy **Simone**, mes parents **Marie-Pierre** et **Jacques**, ma belle-mère **Françoise**, mon frère **Laurent** et sa femme **Céline**, ma sœur **Cyrielle**, ma demi-sœur **Émilie** et son mari **Lionel**, mon demi-frère **Jérémy**, ainsi que mon adorable filleule **Lucille**, mes neveux **Samuel** et **Valentin**, et ma nièce de cœur **Louise**. Chacun d'eux a contribué à faire de moi la personne que je suis aujourd'hui. Sans oublier ceux qui sont partis trop tôt et qui ne peuvent pas lire ces mots, en particulier mon Grand-Père **Jules** et ma Mamou **Jeanne**, qui auraient été si fiers de voir le chemin parcouru.

« Ils », ce sont aussi la **Tihange Family**, **Geneviève**, **Jean-Luc**, **Béné** et **Antoine**, ma deuxième famille, tellement généreuse et soutenante, qui m'inspire chaque jour.

« Ils », ce sont aussi ces amis à qui vous pourriez confier votre vie, **Rourou**, **Delphine**, **Sarah**, **les Ingénis,** ou encore **les amis de Huy**. Merci pour les sorties et les rires partagés.

Pour finir, « ils » c'est aussi **Jean-Baptiste**, qui m'a accompagné au quotidien dans cette aventure en l'illuminant de son amour, de sa bonne humeur et de son humour débordant. Tes ambitions m'inspirent, ton optimisme me rend plus légère et ton soutien m'aide à surmonter n'importe quelle difficulté. Je suis tellement heureuse d'avoir vécu ce travail à tes côtés et je suis impatiente de réaliser nos projets futurs ensemble. Merci de m'avoir supportée aux cours de ces années, et pour longtemps encore, je l'espère.

"It always seems impossible until it is done" – Nelson Mandela

ABOUT THE AUTHOR

Elise Beckers was born on July 6th, 1998, in Liège, Belgium. She studied Biomedical Engineering at the University of Liège, with a specialization in Electronics, and graduated *Magna cum laude* in 2020. During her Master's program, she developed a keen interest in medical imaging techniques, particularly MRI, gaining valuable hands-on experience during an internship at the Wellcome Centre for Human Neuroimaging, University College London. Under the supervision of Prof. Dr. Martina Callaghan and Dr. Christophe Phillips, she worked on optimizing the MRI visualization of the locus coeruleus, which ignited her research enthusiasm for this tiny yet remarkable brain structure.

After completing her Master's, she embarked on a joint PhD program between Maastricht University and the University of Liège, under the supervision of Dr. Heidi Jacobs and Dr. Gilles Vandewalle. Supported by the Liège-Maastricht Imaging Valley grant, her doctoral research explored various aspects of the locus coeruleus, investigating its structure and function using advanced 7T MRI, with a particular focus on its role in aging and Alzheimer's disease. A significant part of her PhD involved the design and implementation of the international BOOSTMEM study, where she explored the modulatory effects of light exposure and transcutaneous vagus nerve stimulation on the locus coeruleus.